Understanding and Controlling Exchange Spin Coupling: Insights from First-Principles Calculations

Torben Steenbock

Dissertation

with the aim of achieving a doctoral degree

at the Faculty of Mathematics, Informatics and Natural Sciences

Department of Chemistry

University of Hamburg

September, 2016

The present work was carried out in the period from September 2013 to September 2016 in the Institute of Inorganic and Applied Chemistry at the University of Hamburg in the group of Prof. Dr. Carmen Herrmann.

Dissertation accepted on the recommendation of

Prof. Dr. Carmen Herrmann

Prof. Dr. Gabriel Bester

Date of admission: 09/15/2016

Date of submission: 09/02/2016

Date of oral defence: 10/28/2016

Approval of dissertation: 01/17/2017

"Learn from yesterday, live for today, hope for tomorrow. The important thing is not to stop questioning."

-Albert Einstein (1879-1955)

In memory of my beloved grandmother Sonja Frenzel.

Contents

Appendix 173

I. Zusammenfassung

Die Vorhersage und das Verständnis von Austauschkopplung zwischen Spinzentren in offenschaligen Molekülen sind wichtige Aufgaben der theoretischen Chemie. Für spintronische Anwendungen ist es notwendig, diese Austauschwechselwirkungen mit externen Stimuli, wie zum Beispiel elektrischen und magnetischen Feldern oder Licht, zu kontrollieren. Eine weitere wichtige Voraussetzung für diese Anwendungen ist die Stabilität der magnetischen Systeme auch bei höheren Temperaturen. Die Ziele dieser Arbeit sind daher, einen Weg zum Verständnis von Austauschpfaden in Form von Molekülorbitalen zu finden und Möglichkeiten zur Kontrolle der Austauschwechselwirkungen durch externe Stimuli oder strukturelle Modifikationen zu untersuchen.

Im ersten Teil der Arbeit wird die Anwendbarkeit eines Green's-Funktions-basierten Ansatzes untersucht, der ursprünglich aus der Festkörperphysik stammt und im Rahmen dieser Arbeit unter Verwendung von lokalen Projektionsoperatoren neu abgeleitet wurde, für die Beschreibung von Spinwechselwirkungen in chemisch relevanten Systemen. Der Ansatz wird mit dem normalerweise in der Quantenchemie verwendeten Broken-Symmetry-Ansatzes im Rahmen der Kohn–Sham-Dichtefunktionaltheorie verglichen. Der auf Green's-Funktionen basierende Ansatz gibt weiterhin die Möglichkeit, die Kopplungskonstanten in Beiträge von Paaren von besetzten und unbesetzten Molekülorbitalen zu zerlegen. Diese Eigenschaft wird zunächst verwendet, um Austauschpfade in verschiedenen literaturbekannten Übergangsmetallkomplexen zu evaluieren und wird schließlich auf eine Reihe von Komplexen angewendet, für die bisher noch keine Austauschpfade in der Literatur analysiert wurden. Dabei liegt ein besonderes Augenmerk auf der Unterscheidung zwischen Through–Space und Through–Bond Beiträgen zur Spinkopplung in diesen Systemen.

Im zweiten Teil dieser Arbeit werden eine Reihe von, in der Arbeitsgruppe Heck, synthetisierten und charakterisierten metallocen-substituierten photochromen Schaltern untersucht. Diese Systeme können unter Bestrahlung mit Licht einer bestimmten Wellenlänge zwischen zwei isomeren Formen, einer offenen und einer geschlossenen, transformiert werden. Die Einführung von paramagnetischen Metallocenen bietet die Möglichkeit die Stärke der Spinwechselwirkungen zwischen den beiden Zentren mit Licht zu schalten, was für potentielle Anwendungen in spintronischen Bauteilen von Interesse sein könnte. In diesem Teil wurde das Schaltverhalten dieser Verbindungen mit zeitabhängiger Dichtefunktionaltheorie untersucht und mit den analogen chlorsubstituierten Schaltern, die für ihr gutes Schaltverhalten bekannt sind, verglichen. Außerdem wurden die

magnetostrukturellen Korrelationen in der geschlossenen Form von verschiedenen magnetischen photochromen Schaltern untersucht, für die eine offenschalige und eine geschlossenschalige Singulett–Resonanzstruktur existiert. Wegen dieser Resonanzstrukturen stellen diese Systeme eine Herausforderung für die Dichtefunktionaltheorie dar. Des Weiteren wurden diese Moleküle auch als Testfälle für den auf Green's-Funktionen basierenden Ansatz verwendet, mit einem speziellen Fokus auf dem Einfluss der Definition der Spinzentren auf die erhaltenen Kopplungskonstanten.
Im dritten Teil wird der Einfluss der Einführung von radikalischen Brücken auf die Spinkopplung in Donor–Akzeptor-Diradikalen untersucht. Das ist von Interesse, da die zusätzlichen Spinwechselwirkungen zwischen der Brücke und den radikalischen Gruppen zu einer zusätzlichen Stabilisierung des Grundzustandes gegenüber den angeregten Spinzuständen führen könnten. Auch der Green's-Funktions-Ansatz wurde wieder zum Vergleich verwendet, da diese Systeme aufgrund der Delokalisierung des Spins von den radikalischen Gruppen auf die Brücke eine Herausforderung für diesen Ansatz darstellen.
Insgesamt konnten also neue Ansätze zur theoretischen Analyse von Spinwechselwirkungen entwickelt werden, und die Grenzen der Steuerbarkeit dieser Wechselwirkungen für Dithienelyethenschalter und radikalische Brücke genauer als bisher etabliert werden. Beides ist relevant für die theoretische Beschreibung potentieller molekularer Bausteine für spintronische Anwendungen, wie zum Beispiel molekülbasierte Spins auf Oberflächen.

II. Abstract

The prediction and understanding of exchange spin coupling between spin centers in open-shell molecules is an important task in theoretical chemistry. Moreover, for spintronic applications it is necessary to control spin coupling by external stimuli, as for example light or magnetic fields. A second requirement is that the strength of the spin coupling is large enough so that the system is stable at sufficiently high temperatures. The aims of this thesis are therefore to develop an understanding of spin exchange pathways in terms of molecular orbitals, and to investigate how the spin coupling can be altered by external stimuli and structural modifications.

In Part I, a Green's-function approach originally developed in solid-state physics and rederived in this work using local projection operators is systematically tested as a tool for the prediction of spin coupling constants for chemically relevant compounds by comparing it to the Broken-Symmetry approach usually used in theoretical chemistry, in combination with Kohn–Sham density functional theory. The Green's-function approach further provides the opportunity to decompose the coupling constants into contributions arising from different pairs of occupied and virtual molecular orbitals. This property is used to evaluate the exchange pathways in different transition-metal complexes known from the literature and in a series of complexes for which no studies on the exchange pathways had been reported so far. Special emphasis is put on the discrimation between through-space and through-bond contributions to exchange spin coupling.

In Part II, a series of metallocene-substituted photochromic dithienylethene switches is studied. These systems are able to undergo transformations between two isomeric forms by irradiation with light of an appropriate wavelength. The introduction of paramagnetic metallocenes promises the opportunity to switch the strength of the spin coupling by irradiation with light, making these systems potentially interesting for spintronic applications. The switching behavior of these compounds is investigated by employing time-dependent density functional theory and by comparing the results to a bare chlorine-substituted switch which is known to show good switching behavior. Finally, the magneto–structural correlations in the closed form of the photochromic switches are evaluated, which is challenging due to the two different possible resonance structures, one open-shell and one closed-shell. The goal is to analyze if density functional theory is able to give an unambiguous description of the open-shell character in these compounds. These systems are also used as test cases for the Green's-function

approach, with special emphasis on the choice of the spin center definition required in that method.
Part III finally discusses the influence of the introduction of radical bridges on the spin coupling in donor–acceptor diradicals. This is interesting because the additional spin interactions between the bridge and the radical moieties could lead to an additional stabilization with respect to spin-flip excitations of the ground state compared with closed-shell brides. The Green's-function approach is also compared to the results obtained from the BS approach to see if it gives reliable results for these systems, which might be challenging because of the higher degree of spin delocalization onto the bridge.
Overall, new methods for the theoretical analysis of spin–spin interactions are developed, and the limits of controlling these interactions for dithienylethene switches and radical bridges is established. Both is relevant for the theoretical description of potential molecular building blocks for spintronic applications, as for example chains of molecule-based spins on surfaces.

Introduction

Spintronics deals with the storage [1, 2], the transport [3], and the procession of information [4, 5] in terms of the spin degree of freedom [6] and could help to overcome two essential problems of modern computer architectures.

The first problem is that in the past the focus was often on performance rather than on power efficiency. The second problem in modern computer architectures is the difference between the speed of calculations and that of information transfer from memory which is often referred to as "memory wall". According to Moore's Law [7], the number of transistors in an integrated circuit doubles every two years [1], while the speed in memory technologies increases more slowly. This gap is closed by complex memory hierarchies that automatically transfer frequently used data from slower to faster memories [9], which is not a long-term solution because the speed of logical operations in the central processing units (CPU) increases too strongly in comparison [6].

To overcome these problems, one could for example think about integrating logic elements into the memory, which would lead to a reduced information transfer between CPUs and memory and would therefore be less power-consuming. Such logic elements could be composed of spin-polarized nanoscale objects such as molecules, which are able to perform logic operations by inducing spin crossovers [10–12] or by varying the spin coupling between two spin centers by external stimuli. This would lead to a reduced information transfer between CPUs and memory and would therefore be less power-consuming. An important configuration for these purposes is the arrangement of local spins on a surface to form all-spin based logic gates. These local spins could be spin-polarized atoms as realized by Khajetoorians and coworkers [3] in the framework of the SFB 668 at the University of Hamburg. They formed two atomic spin leads from iron atoms connected to an output atom and to two ferromagnetic input islands, which can be manipulated by an external magnetic field and read out by a spin-polarized STM tip. But also molecular spins could be used for this purpose. Molecules are (in principle) able to self-assemble on surfaces, and most often the exchange spin coupling is assumed to be stronger than the Ruderman-Kittel-Kasuya-Yoshida (RKKY) interactions mediated by the surface [13]. In general, such spin-based elements are promising because pure spin transport along chains produces less heat than charge transport due to the smaller energy needed to manipulate the spins. Therefore, it is important to understand the

[1] Note, however, that Moore's Law has been proclaimed to be nearing its end very recently [8].

spin coupling in such building blocks and to be able to chemically control these systems. In addition, the effects of the surface on the spin–spin interactions needs to be understood and controlled.

Several experimental studies were carried out for spin-polarized manganese [14], iron [15,16], and cobalt atoms [15,17] on metal surfaces in order to explore their magnetic properties in the presence of the surface. In some studies, an insulating interlayer was introduced between the atoms and the metallic surface [18] in order to minimize the spin transfer from the atoms to the surface. Molecules were also successfully brought onto metallic surfaces [13,19,20]. In this context, theory is an important complement to provide deeper insights into the observed properties and to predict systems with desired properties.

The theoretical description of such systems is most often carried out using density functional theory (DFT) for slab models or under periodic boundary conditions [20–23]. Although sophisticated ab-initio wave-function methods are in principle more accurate and have a larger predictive power, the advantage of DFT is the possibility to describe systems up to thousands of atoms while sacrificing some of this predictive power. Noodleman's Broken-Symmetry approach [24] is by far the most popular method to describe the spin-state energetics and the Heisenberg coupling constants within DFT (see also Section 2.3).

There are many important tasks in the theoretical description of spin-polarized molecules for spintronic applications. First of all, an understanding of the spin–spin interactions in isolated systems is crucial in order to develop molecules with tailored magnetic properties. Furthermore, for spintronic applications the spins need to be controlled and manipulated by external stimuli, as for example light [10, 25–27], magnetic and electric fields [28–31], or an applied voltage. In addition, the molecules in an experiment interact with their environment (e.g. molecule–surface interactions) which can also heavily affect their properties. Some of these problems can be tackled by existing theoretical methods, while for other purposes a development of new methods is necessary. An example is an approach derived in solid-state physics by Alexander Lichtenstein (University of Hamburg) and coworkers [32] which holds promise for the analysis of spin coupling pathways and thus could be employed for the decomposition of the spin coupling into contributions from the surface and the molecule. This approach is based on the idea of introducing a small spin rotation from which the coupling constant can be calculated by a Green's-function expression employing the local force theorem. This approach was never formulated in a way in which it is suitable for the exchange pathway analysis, which is done in this work. Furthermore, it was never systematically studied if this approach can be used in quantum chemistry. In the author's Master's thesis [33] the Green's-function approach was implemented in a Löwdin-transformed basis into the program package Artaios [34]. This work was finalized and extended in this thesis.

The aim of this work is to develop new methods for the theoretical calculation and analysis of spin coupling in molecules that can be applied to both isolated molecules and those on surfaces. It is divided into three parts, dealing with

different aspects of spin coupling.

Part I is devoted to the prediction and understanding of spin coupling in transition-metal complexes by the Green's-function method. In a first step, the BS approach derived by Noodleman and frequently employed in quantum chemistry [24] is compared to the Green's-function approach [32] for a large number of diradicals and dinuclear transition-metal complexes to evaluate if the latter approach is able to make meaningful predictions, which is an important prequisite for using it as an automated method for the analysis of exchange pathways. In a next step, one of the fundamental properties of the Green's-function approach, the decomposition of the coupling constant into contributions from molecular orbitals, is used to analyze the exchange pathways in different transition-metal complexes, and the results are compared to cases from the literature. Then, the Green's-function approach is applied to a series of π-stacked bis(metallocene) complexes synthesized in the group of Jürgen Heck at the University of Hamburg, being highly relevant in the context of the SFB 668, because they could be used as molecular analogues of the iron atoms employed for the all-spin logic gate by Khajetoorians *et al.* [3] and were successfully brought onto a gold surface and partially studied by spinpolarized STM.

As mentioned above, a second important requirement for spintronic devices is the control of spin coupling by external stimuli. In Part II of this work, a series of metallocene-substituted photochromic dithienylethene switches is studied as synthesized and characterized in the Heck group in Hamburg with the aim of obtaining DTE molecules with paramagnetic metallocenes, in which the spin coupling can be controlled by irradiation with light of an appropriate wavelength. However, depending on the metallocene substituent, large differences in the switching behavior are found experimentally. Time-dependent density functional theory (TDDFT) is used in order to rationalize the photoswitching behavior in these compounds. Furthermore, the magnetism in these systems is studied in further depth by using the BS and the Green's-function approach with a special focus on the magneto–structural correlations in the closed form, which is challenging in DFT because two resonance structures can be drawn, one being an open-shell and the second one being a closed-shell singlet state.

Another important aspect that must be considered for spintronic applications is the stability of a device at operating temperatures. This thermal stability strongly depends on the energetic stabilization of the spin ground state against the excited spin states. One way of solving this problem is the introduction of radical bridges that could lead to a stabilization of the ground state by the additional spin–spin interactions between the bridge and the radical moieties. In the author's Bachelor's thesis [35], a series of meta-substituted donor–acceptor model di- and triradicals had been studied. However, the di- and triradicals chosen in that work would not be stable under experimental conditions, and therefore these findings were compared in Part III to a potentially realizable molecule to systematically study how far the conclusions are transferable to

such systems. This type of systems is also interesting because the spin coupling can be tuned by the degree of spin delocalization within the radical bridge. Before discussing these aspects of theoretical insight into systems for molecular spintronics, a brief outline of some theoretical background is given.

Theoretical Background

In this part, the theoretical methods and concepts used in this work are briefly discussed, starting in Section 2.1, with the basics of DFT which, is used throughout this work. In experiment, the spin coupling is most often obtained by fitting magnetic susceptibility data with the Heisenberg–Dirac–Van Vleck (HDvV) Hamiltonian describing the isotropic interactions between two spin vectors. This Hamiltonian is discussed in more detail in Section 2.2. However, there are also alternatives to the Heisenberg Hamiltonian, as for example the Ising Hamiltonian which only considers the z direction of the spin [36]. The central property in both Hamiltonians is the spin coupling constant J, which can also be evaluated theoretically. In DFT, these coupling constants are usually calculated by the so-called BS formalism (Section 2.3). This approach approximates the low-spin state by a determinant with artificial spin density on both spin centers. Although artificial, local spins can be calculated from it in order to control, if the calculation converged to the correct open-shell solution or if perhaps a closed-shell solution is obtained. Therefore, the concept of local spins in Section 2.4 is discussed. Another aspect besides the correct prediction of spin coupling, is the understanding of these interactions by chemical concepts. In Section 2.5, two measures for aromaticity are discussed. Aromaticity was found to correlate with the open-shell character in polyhydrocarbons [37]. These correlations in magnetic photochromic switches are probed by comparing their aromaticities to the diradical characters discussed in Section 2.6.

2.1 Density Functional Theory

The fundamentals of density functional theory will be shortly discussed [38, 39] here, because it is used throughout the whole work. While in Hartree-Fock and post-Hartree Fock methods, the wavefunction is the central quantity, the description of the system in DFT is based on the electron density. The advantages of using the electron density are that it depends only on three Cartesian coordinates and that it is an experimental observable. The first practical DFT method was the so-called Thomas-Fermi model, which employs an energy functional derived from the homogeneous electron gas. This description turned out to be inadequate for molecules due to the highly inhomogeneous electron density in those systems. An additional problem arose for the description of the kinetic energy, for which no accurate expressions could be found. In 1964, Kohn and Sham solved this problem by employing a reference system of non-interacting

fermions with the same ground-state electron density as the interacting system. KS-DFT is based on the two Hohenberg-Kohn theorems. The first theorem shows that there is one-to-one mapping between the ground state electron density and the external potential (and thus ground-state wave function). The second Hohenberg-Kohn theorem proofs the variation principle of DFT and states that the energy obtained as a functional of a trial electron density is always larger than (or equal to) the energy obtained for the true ground-state electron density. Employing a reference system of non-interacting fermions also solves the basic problem of finding expressions for the kinetic energy, because the total kinetic energy of such a system is just equal to the sum over all single-particle kinetic energies, which gives the largest contributions to the overall kinetic energy in the interacting system. Corrections to the kinetic energy as well as the exchange- and the correlation-energy contributions are included in the exchange-correlation functional.
Although the existence of the exact exchange–correlation functional was proven, nothing is said about how to construct it. Therefore in practice many different approximate exchange-correlation functionals were designed, which can be ordered into different classes based on specific characteristics. The earliest functional was the so-called Local Density Approximation (LDA) [38,40], which only considers the electron density as a variable. The next class are the so-called GGA functionals [41–43] which include the gradient of the electron density with respect to the spatial coordinates. Meta-GGAs [44] include also the second derivative of the electron coordinates in order to improve the description of the kinetic energy. Compared to the previously discussed classes, hybrid functionals [45] add a fraction of Hartree-Fock exchange to the DFT exchange. Range-separated functionals [46] use different amounts of Hartree-Fock exchange for different electron-electron separations. The class of double-hybrid functionals uses hybrid functional DFT and a subsequent MP2 step in order to improve the correlation energy [47].

2.2 The Heisenberg Hamiltonian

The Heisenberg-Dirac-van Vleck (HDvV) Hamiltonian is an effective Hamiltonian which describes magnetic exchange coupling in chemical compounds and solids and is formulated as the sum over pairs of spin centers A, B, ...

$$\begin{aligned} \hat{H}_{\mathrm{HDvV}} &= -2\sum_{A<B} J_{AB}\hat{\mathbf{S}}_A\hat{\mathbf{S}}_B = -2\sum_{A<B} J_{AB}S_AS_B\hat{\mathbf{e}}_{\mathrm{A}}\hat{\mathbf{e}}_{\mathrm{B}} \\ &= -2\sum_{A<B} J_{AB}S_AS_B\cos\left(\theta_{AB}\right), \end{aligned} \tag{2.1}$$

where J_{AB} are the coupling constants and $\hat{\mathbf{S}}_A$ and $\hat{\mathbf{S}}_B$ local spin vectors on different atoms A and B. In Equation (2.1) the local spin vectors can be decomposed into the magnitude S_{A} and a vector of unit length $\hat{\mathbf{e}}_A$ describing

the spin orientation,

$$\hat{\mathbf{S}}_A = S_A \hat{\mathbf{e}}_A. \tag{2.2}$$

The product of these unit vectors is equal to the cosine of the angle between the spin vectors on both spin centers, θ_{AB}. The spin centers can be, in principle, atoms or groups of atoms. J_{AB} is positive for ferromagnetically coupled spins (parallel alignment) and negative for antiferromagnetically coupled ones (antiparallel alignment). Equation (2.1) for the Heisenberg-Dirac-Van Vleck Hamiltonian is only valid for insulators and semiconductors where the spin is localized [48, 49]. For metals a Hamiltonian containing spin operators $\hat{\mathbf{e}}_A$ with unit length is employed instead [48–50],

$$\hat{H}^{\text{Unit}}_{\text{HDvV}} = -\sum_{A<B} 2J^{\text{unit}}_{AB} \hat{\mathbf{e}}_A \hat{\mathbf{e}}_B. \tag{2.3}$$

This form of the Hamiltonian is later used in the derivation of the expression used in the Green's-function approach. The coupling constants for two cases are thus related by

$$J_{\text{AB}} = \frac{J^{\text{unit}}_{AB}}{S_A S_B}. \tag{2.4}$$

In the following, the local spin vectors are assumed to be ideal, that is, S_A is one-half the number of formally unpaired electrons on A (which may in practice be diminished by spin delocalization).

2.3 Noodleman's Broken-Symmetry Approach to Spin Coupling

In quantum chemistry, usually a method for evaluating spin coupling proposed by Noodleman is employed [24], in which the coupling constant is calculated based on spin projection for two spin centers from the energy difference between the high-spin or ferromagnetically coupled (F) and the Broken-Symmetry (BS) determinants,

$$J_{\text{BS,projected}} = -\frac{E^{\text{F}} - E^{\text{BS}}}{S^2_{\text{F}}}. \tag{2.5}$$

The subscript AB is omitted here and in the following for better readability. S_{F} is the total spin quantum number in the ferromagnetic state. The BS determinant is an approximation to the low-spin state, whose description is not straight-forward in effective one-determinant methods as KS-DFT. In the case of a singlet low-spin state in a diradical and in the context of wave-function theory, the BS determinant is an equal admixture of a pure triplet and a pure singlet state, with α (or spin-up or majority) spin density on one and β (or spin-down

or minority) spin density on the other spin center. The energy of the singlet state is extracted by employing spin-projection techniques. Additionally to the artificial spin densities also the $\langle \hat{S}^2 \rangle$ expectation value differs from its expectation value $M_S\,(M_S+1)$. These deviations are known as spin contamination. It can be understood by the formula used for the calculation of $\langle \hat{S}^2 \rangle$ values in Slater determinants,

$$O_{ij}^{\beta\alpha} = \langle \psi_i^{\beta} \mid \psi_j^{\alpha} \rangle, \tag{2.6}$$

$$\langle \hat{S}^2 \rangle = M_S\,(M_S+1) + N^{\beta} - \sum_{i,j}^{N^{\alpha}N^{\beta}} \left(O_{ij}^{\beta\alpha} \right)^2, \tag{2.7}$$

where $O_{ij}^{\beta\alpha}$ is the overlap between the spatial parts of different α and β spin orbitals $\mid \phi_j^{\alpha} \rangle$ and $\mid \phi_i^{\beta} \rangle$. In the limit of the closed-shell singlet the α and β spin orbitals have exactly the same shape and consequently Equation (2.7) reduces to the exact $\hat{S}^2$ expectation value of zero.
Although spin contamination appears to make a spin projection necessary, Perdew and coworkers [51, 52] suggested by an alternative interpretation of spin density functional theory, that the artificial spin density is there in order to obtain the right behavior of the exchange–correlation hole density $n_{xc,\lambda}\,(\mathbf{r},\mathbf{r}')$ which can be defined by the pair density $P_{\lambda}\,(\mathbf{r},\mathbf{r}')$,

$$P_{\lambda}\,(\mathbf{r},\mathbf{r}') = n\,(\mathbf{r})\,[n\,(\mathbf{r}') + n_{xc,\lambda}\,(\mathbf{r},\mathbf{r}')]\,. \tag{2.8}$$

$P_{\lambda}\,(\mathbf{r},\mathbf{r}')\,d^3r d^3r'$ gives the probability to finding an electron in a volume element d^3r and a second one in a volume elemt d^3r' in space, $n\,(\mathbf{r})$ is the electron density (obtained as $n\,(\mathbf{r}) = n_{\uparrow}\,(\mathbf{r}) + n_{\downarrow}\,(\mathbf{r})$). The λ refers to an interpolation between the non-interacting system (λ=0) and the fully interacting system (λ=1) [52–54]. By the calculation of the atomization energies of the H_2 molecule from its dissociation curve it turned out that the true spin-unpolarized densities on separate atoms give a significant larger error than the self-consistent local-spin density (LSD) or GGA spin densities [51]. The breaking of the spin symmetry is not only observed for H_2 with stretched bonds, but also for open-shell molecules at equilibrium distances, as *e.g.* C_2 and Cr_2. Perdew and coworkers [51] explained these findings by an alternative pair-density interpretation of LSD and GGA calculations, using the spin densities $n_{\uparrow}\,(\mathbf{r})$ and $n_{\downarrow}\,(\mathbf{r})$ as auxiliary quantities, from which the on-top pair density $P_{\lambda=1}\,(\mathbf{r},\mathbf{r})$ can be constructed,

$$P_{\lambda=1}\,(\mathbf{r},\mathbf{r}) = P_{\lambda=1}^{\mathrm{unif}}\,(n_{\uparrow}\,(\mathbf{r})\,, n_{\downarrow}\,(\mathbf{r})\,; u=0)\,, \tag{2.9}$$

where $P_{\lambda=1}^{\mathrm{unif}}\,(n_{\uparrow}\,(\mathbf{r})\,, n_{\downarrow}\,(\mathbf{r})\,; u=0)$ refers to the on-top pair density of the uniform electron gas. The on-top pair density is a special case of the pair density in Equation (2.8) which refers to the probability of finding two electrons at same position $\mathbf{r}$ in space. The u refers to the distance between the two electrons at $\mathbf{r}$ and $\mathbf{r}'$, $u = |\mathbf{r}-\mathbf{r}'|^2$. Perdew and coworkers concluded therefore that the

[2] u is zero in this case because the two electrons are at the same position $\mathbf{r}$ in space.

exchange–correlation energy only indirectly depends on the magnetization $m(\mathbf{r})$ but directly on the on-top pair density $P_{\lambda=1}(\mathbf{r},\mathbf{r})$, or the exchange-correlation hole density $n_{xc,\lambda}(\mathbf{r},\mathbf{r})$ [51, 52]. Therefore, we will compare with coupling constants which assume that the BS determinant gives the correct energy of the singlet state,

$$J_{\mathrm{BS,unprojected}} = -\frac{E^{\mathrm{F}} - E^{\mathrm{BS}}}{S_{\mathrm{F}}\left(S_{\mathrm{F}}+1\right)}. \tag{2.10}$$

From now Equation (2.5) will be referred to as the projected Noodleman equation and to Equation (2.10) as the unprojected Noodleman equation. The above equations only hold for systems including two magnetic sites, but they can be easily extended to systems with more than two magnetic sites by setting up a system of linear equations (one for each spin configuration) and deriving equations for the different coupling constants [55]. However, one bottleneck of this method is that with increasing number of spin centers the problem is quickly overdetermined so that one finds more than one expression for one coupling constant including different spin-configuration energies which consequently can lead to inconsistent results depending on the exact configurations used in the calculations.

2.4 Local Spins

When using the Heisenberg Hamiltonian, one assumes that the magnitude of the local spins is the same in different spin states. This is an assumption that needs to be checked in KS-DFT calculations. Therefore often a local spin analysis is carried out which gives the local contributions $\langle \hat{S}_{zA} \rangle$ from an atom or fragment A to the expectation value of the z component of the total spin operator, $\hat{S}_z$. $\langle \hat{S}_{zA} \rangle$ can be calculated as one-half the difference of the local populations of α and β electrons, N_A^α and N_A^β, as

$$\langle \hat{S}_{zA} \rangle = \frac{1}{2}\left(N_A^\alpha - N_A^\beta\right). \tag{2.11}$$

This equation provides a connection between local spins and population analysis. The first schemes for the population analysis were derived by Löwdin [56] and Mulliken [57]. In this work, only used the latter is used for evaluating local spins, as the local partitioning scheme was shown to have little influence on local spins (in contrast to population analysis) and Mulliken partitioning is implemented in virtually any electronic structure code due to its simplicity [58]. Within the Mulliken local partitioning scheme, the number of electrons on a center A is calculated from matrix elements of the product of the density matrix $\mathbf{P}$ for α and β electrons, respectively, and the elements of the overlap matrix $\mathbf{S}$ between pairs of atom-centered basis functions μ and ν [59],

$$N_A^\sigma = \sum_{\mu \in A} \left(\mathbf{P}^\sigma \mathbf{S}\right)_{\mu\mu}, \tag{2.12}$$

with $\sigma \in \{\alpha, \beta\}$. The sum runs only over basis functions located on A.

2.5 Theoretical Measures of Aromaticity

Different criteria can be employed to investigate the degree of aromaticity in a system by means of DFT. Since we investigate the correlations between the aromaticity and the open-shell characters (found for polyhydrocarbons [37]) in Chapter 12 for a series of magnetic photochromic switches. Energetic criteria can be applied [60–62], which are closely related to reactivity-based criteria [63–68]. Also magnetic [69–73], as well as structural parameters [74–78] can be taken into account. Due to the manifold of criteria only the measures employed here are discussed. First, the harmonic oscillator model of heterocyclic electron density (HOMHED) [79] is employed, which calculates the aromaticity by comparing the structural parameters of an underlying structure with reference values from ideally aromatic structures and is therefore simple to calculate (Section 2.5.1). In complement to the structural effects, also effects on the electronic structure can be observed. Therefore, the HOMO–LUMO gap gap is used as a measure of stability, which is discussed in Section 12.2.2. An extended discussion of the characterization of aromatic systems within the framework of DFT is given by De Proft and Geerlings [80].

2.5.1 Harmonic Oscillator Model of Heterocyclic Electron Density

The harmonic oscillator model of heterocyclic electron density (HOMHED) [79] enables the description of aromaticity by taking into account the bond lengths involved in the π system under investigation. The difference between the bond length R_i (i refers to the bond index) between a pair of two atoms X and Y and an optimal value $R\left(\mathrm{XY}\right)_{\mathrm{Opt}}$, obtained as the average over several hundred of experimentally described aromatic structures, is used to calculate the HOMHED index,

$$\begin{aligned}\mathrm{HOMHED} = 1 - \frac{1}{n}\Bigg\{ & \alpha_{\mathrm{CC}} \sum_i \left[R\left(\mathrm{CC}\right)_{\mathrm{Opt}} - R_i\right]^2 + \alpha_{\mathrm{CX}} \sum_i \left[R\left(\mathrm{CX}\right)_{\mathrm{Opt}} - R_i\right]^2 \\ & + \alpha_{\mathrm{CY}} \sum_i \left[R\left(\mathrm{CY}\right)_{\mathrm{Opt}} - R_i\right]^2 + \alpha_{\mathrm{XY}} \sum_i \left[R\left(\mathrm{XY}\right)_{\mathrm{Opt}} - R_i\right]^2 \Bigg\},\end{aligned} \tag{2.13}$$

where α is a bond type specific normalization constant and n refers to the total number of bonds considered. For the calculation a computational tool was written and the parameters from Ref. [79] were employed in the course of this thesis.

2.5.2 HOMO–LUMO Gaps and the Concept of Global Hardness

The global hardness η is a quantity first defined by Parr and Pearson as the second derivative of the energy E with respect to the number of electrons N in a constant external potential $v(\mathbf{r})$ [81],

$$\eta = \left(\frac{\delta^2 E}{\delta N^2}\right)_{v(\mathbf{r})}, \tag{2.14}$$

which was later used for the so-called hard and soft acids and bases (HSAB) principle [82–84]. The global hardness is an energy-based measure of the aromaticity in a system, since it represents the energy changes according to the changes in the total number of electrons (by adding or removing electrons to the system). In other words, it is a measure of the stability according to nucleophilic or electrophilic addition reactions. By employing a finite difference approximation the hardness can be expressed as the energy difference between the ionization energy IE and the electron affinity IA [80] so that one obtains in combination with Koopman's theorem [59],

$$\eta = \mathrm{IE} - \mathrm{EA} = \epsilon_{\mathrm{LUMO}} - \epsilon_{\mathrm{HOMO}}, \tag{2.15}$$

where ϵ_{LUMO} and ϵ_{HOMO} are the MO energies of the LUMO and HOMO respectively. In this work we will use the HOMO-LUMO gap as an approximate measure for the aromaticity.

2.6 Diradical Characters

The diradical character y can be understood as the deviation of the electronic structure from being a closed-shell singlet. In KS-DFT open-shell and closed-shell singlets can be distinguished by the artificial spin density in the BS determinant, which is zero anywhere in space in true singlet states. The diradical character influences structural parameters, as *e.g.* the bond lengths [85–90]. In the literature different methods were introduced to evaluate the diradical character of chemical compounds [91–93]. In this work, the diradical characters are calculated according to Kamada and coworkers [94]. This method employs the natural orbital occupations n of the HOMO (bonding linear combination of the magnetic orbitals) and the LUMO orbitals (antibonding linear combination of the magnetic orbitals),

$$y = \frac{(1-T)^2}{1+T^2}, \tag{2.16}$$

$$T = \frac{n_{HOMO} - n_{LUMO}}{2}. \tag{2.17}$$

It should be noticed that according to the literature, DFT underestimates the diradical characters calculated according to Equations (2.16) and (2.17) [91],

but nevertheless it depends also on the employed exchange-correlation functional which relativizes the preceding statement. Furthermore, the focus lies on trends and it is assumed that the underlying error by employing Equation (2.16) is of the same order for all structures.

Part I: Analyzing Spin Coupling Pathways

Exchange coupling between electron spins is important in many compounds, especially in polynuclear transition metal complexes with partially filled *d*-orbitals [95,96] and in organic polyradicals [97]. In addition to direct exchange coupling between two metal centers, it is possible that closed-shell bridging ligands between two metal centers mediate the coupling. This is referred to as superexchange [98, 99]. Exchange-coupled molecular compounds are candidates for molecular spintronics [100, 101] and are extensively studied in the field of molecular magnetism [96]. Spin coupling is also important in biological systems, in particular in the active sites of enzymes such as methane monooxygenase, which contains a di-μ-oxo-diiron core exhibiting magnetic coupling between the iron centers via the oxo ligands [102, 103]. Spin coupling is equally relevant for a range of synthetic homogeneous catalysts [104, 105]. It can be regarded as an example of a more general phenomenon, communication through molecular bridges [106–108].

Experimentally, the nature (ferromagnetic vs. antiferromagnetic) and strength of exchange coupling is usually determined by the temperature dependence of the magnetic susceptibility. The resulting curves are fitted to a spin Hamiltonian (see Equation (2.1) below), resulting in an exchange spin coupling constant J [109–114]. Sometimes an unambiguous fit is not possible experimentally, so theoretical calculations are a very valuable complement to experiment. Furthermore, such calculations offer a more detailed understanding of chemical mechanisms behind spin coupling, and can help to design new compounds with desired magnetic properties. Due to the typical size of the systems under study here, Kohn-Sham density functional theory (KS-DFT) [38] is by far the most popular electronic structure method in this context. In 1981 Noodleman derived the Broken-Symmetry (BS) formalism, which enables the calculation of J from the energy difference between the high-spin and a BS determinant [24] by applying spin projection. The BS determinant describes the antiferromagnetically coupled state as having local spins with the same magnitudes, but opposite signs on both magnetic sites (for a system with two identical spin centers). Although this description introduces an artificial spin density which is not present in a real singlet state, it has been successfully applied to a variety of systems [39, 102, 115–118][3]. Noodleman's approach may be considered today's standard method for evaluating exchange coupling constants in quantum chemistry.

[3]Also note that the proper evaluation of $\langle \hat{S}^2 \rangle$ in KS-DFT is still under debate [24, 51, 52, 119].

Another approach for calculating J based on Green's functions comes from solid-state physics. It was first published by Lichtenstein in 1984 for the description of Ruderman-Kittel-Kasuya-Yoshida (RKKY) coupling of impurity atoms in metals [49]. It was derived by comparing the energy change due to a small rotation of a local spin vector between a Green's function energy expression and the Heisenberg model [32], using the local force theorem. Han, Ozaki, and Yu have implemented a version of this approach in the program OPENMX [120], where it can be used in combination with unrestricted KS-DFT [121]. This version is conceptually interesting since it can be written as the sum of contributions from pairs of molecular orbitals occupied by electrons of opposing spins. This suggests using this method as a tool for understanding magnetic coupling in terms of exchange pathways [116, 122].

A conceptually related approach has been published by Peralta and coworkers [123, 124], in which all magnetic exchange couplings of a molecule are calculated from derivatives of the energy with respect to spin rotations in the high-spin configuration based on a perturbative approach within non-collinear density functional theory. It was applied to various transition-metal complexes, and the obtained magnetic exchange coupling constants were in a very good agreement with Noodleman's BS approach. While this approach employs an iterative coupled-perturbed Kohn–Sham scheme, the Green's function approach employed here is a simple post-processing method (possibly at the cost of reduced accuracy).

While the Green's function approach has been used to describe atomic adsorbates on surfaces [125,126] and magnetic solids [127–129], applications to molecules are rare and, include manganese and vanadium complexes only [121,130]. Therefore the goal is to check systematically if the Green's-function approach gives reliable results compared with Noodleman's approach for chemically relevant compounds. Note that the reference is not the experiment, but DFT in combination with the BS approach: If DFT+BS fails to reproduce the measured spin coupling (either because of methodological shortcomings or because of neglected intermolecular interactions), the Green's-function approach should fail in the same way.

In Chapter 3, the derivation of the Han–Ozaki–Yu version of the Green's-function approach employing local projection operators as frequently used in population analysis and other local partitioning methods in quantum chemistry [131] is discussed. Further, it is discussed how the coupling constant within this method can be decomposed into molecular orbital (MO) contributions and how these contributions relate to the antiferromagnetic contributions to the coupling constants based on MO energy differences according to a model derived by Hay and coworkers [95].

The resulting equation has been implemented in the in-house program for post-processing electronic-structure calculations, ARTAIOS [34], and is applied to a series of molecular structures in Chapter 4.

Numerous studies were carried out to understand underlying spin coupling mechanisms by using molecular orbitals (MOs) [132–135]. In practice, such

approaches often rely on visual inspection of the MOs, and do not provide quantitative measures for the importance of the individual MOs.
The Green's-function approach allows to decompose the coupling constant into contributions from pairs of occupied and virtual spin orbitals. This property is used here to create a new automated analysis tool which automatically filters out the largest contributions to the coupling. In Chapter 5, this method is tested by evaluating the exchange pathways in the dinuclear Cu(II) complex investigated by Hay [95] and coworkers and its dependence on the Cu(II)-O-Cu(II) angle. Further, the dinuclear Mn(III) complex described by Brunhold and coworkers [122] is considered to see if the exchange pathways found by the Green's-function approach agree with the exchange pathways identified by visual inspection of the MOs.
In Chapter 6, the Green's-function approach is then applied to a number of 1,8-bis(metallocenyl)naphthalene derivatives differing in the metal centers of the metallocenes (M=Co(II) [136], Ni(II) [111], V(II) [137]), as synthesized in the Heck group in the framework of the SFB 668. This is interesting because in many cases it was shown that the choice of the metal centers in di- and polynuclear systems affects the kind and strength of exchange spin coupling [133, 138–140]. Besides the variation of the metal centers, also the naphthalene bridge was successfully replaced by acenaphthylene- and acenaphthalene bridges [141]. These systems are studied here, and compared with a tetranuclear cobaltocene analogue of the 1,8-bis(cobaltocene)naphthalene complex in order to investigate if the Green's-function approach is able to describe metallocene systems with more than two spin centers. These systems are also interesting because of their possible applications as molecular spin leads in all spin-based logic elements suggested by Khajetoorians and coworkers [3]. The first step was already realized, and 1,8-bis(cobaltocenyl)naphthalene molecules were successfully brought onto a Au(111) surface, where they formed chains suitable for such purpose [142]. In order to understand the behavior of such compounds the first step is to understand the spin coupling in the isolated complexes. This is a challenging task, because there are two competitive exchange pathways, a through-bond and through-space pathway. Although DFT calculations were carried out in all earlier studies [111, 136], the mechanisms were mainly proposed based on spin density arguments, and the contributions from both mechanisms were not be evaluated quantitatively, or systematically compared. Therefore, these systems are an ideal test case for the Green's-function method, which is used here in order to gain deeper insights in the exchange spin coupling mechanism in these compounds.

3. Molecular-Orbital Based Understanding of Spin Coupling

This section is dedicated to the concepts developed in order to rationalize spin coupling in terms of molecular orbital energies and shapes. In Section 3.1, the key concept of superexchange and the Goodenough-Kanamori rules, providing a relation between the symmetry of the orbitals and the contribution to the coupling constant, are presented. In Section 3.2, the mechanism of spin polarization is shortly discussed, which is used in the discussion of the spin density distribution in the cobaltocene-substituted systems in Chapter 11. In Section 3.3 then, the approach by Hay and Hoffmann [95] is described, who formulated these relations in terms of expressions, which depend on the energy difference between bonding and antibonding linear combinations of the magnetic orbitals.

3.1 Superexchange: The Goodenough–Kanamori Rules

Superexchange is a concept which describes the exchange-spin coupling in compounds where the electron spins on two or more spin centers interact with each other via closed-shell ions or ligands. This mechanism was first described by Kramer in 1934 by mixing small contributions from excited states with unpaired electrons on the closed-shell bridge into the ground state [143]. It was further discussed in detail by Anderson [144], relating the symmetry of the magnetic orbitals to the sign of the exchange integral. A set of rules, often referred to as Goodenough–Kanamori rules, was first expressed by Goodenough [145,146] and later improved by Kanamori [147], and Anderson [48]. According to Anderson, superexchange between local spins on transition-metal atoms arises from the overlap of the metal d orbitals with filled s and p orbitals of the closed-shell bridge, and therefore the spin-carrying orbitals are no longer strictly localized on the metal center. The Anderson theory distinguishes between two contributions, arising from orbital overlap and orthogonality [148].
Instead of using canonical MOs, Anderson's theory relies on the concept of magnetic orbitals, which are orthogonal, and mainly localized on the spin centers. In DFT they can be obtained by the corresponding orbital transformation (COT) developed by Neese [149]. Often, canonical orbitals may be identified which, even though not exactly corresponding to magnetic orbitals, are sufficiently close in shape to be useful for quantitative interpretation as such. A considerable overlap between two magnetic orbitals gives rise to antiferromagnetic contributions, and

the resulting energy difference between the ferromagnetic and antiferromagnetic spin orientations is

$$\Delta E\,(\mathrm{AF}-\mathrm{F}) = -2\frac{b_{ij}^2}{U} \tag{3.1}$$

The matrix elements b_{ij} are transfer integrals between the magnetic orbitals ϕ_i and ϕ_j, and U refers to the "Hubbard U" representing Coulomb interaction on a given spin center. Anderson referred to this exchange as "kinetic exchange" [148]. The argumentation in this context is often based on orbital overlaps rather than on the transfer integrals themselves, because the overlap between orbitals is an approximation to the transfer integrals, as was first introduced by Mulliken and coworkers [150].
If the magnetic orbitals, on the other hand, are orthogonal to each other, ferromagnetic contributions are obtained ("potential exchange"). Anderson distinguished three different cases. In the first case, the orthogonal magnetic orbitals reside on different atoms, in which case the potential exchange is always positive, and ferromagnetic coupling occurs. In some cases, the orthogonal magnetic orbitals share a component on the same bridging ligand, which, following Hund's rule, results in ferromagnetic coupling. The third kind of ferromagnetic contribution results from the overlap of magnetic orbital with an empty d orbital on the other metal center [148].

3.2 Spin Polarization Mechanism

Besides superexchange, spin coupling can also be mediated by a spin polarization mechanism, which appears in the discussion of the spin density in the cobaltocene-substituted switch in Chapter 11. A good overview on the spin polarization mechanism based on the description within density functional theory was provided by Adamo and coworkers [151].

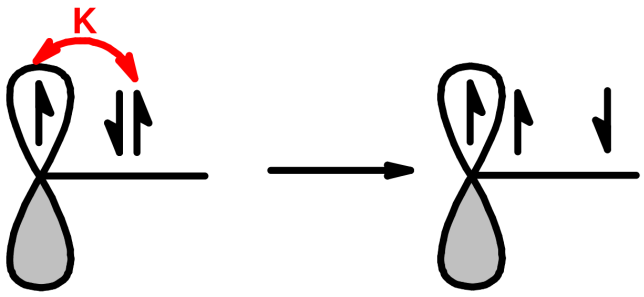

Figure 3.1: Scheme for the spin polarization mechanism, where K refers to the exchange integral.

They pointed out that the spin polarization consists of two contributions, one resulting from the singly occupied molecular orbital (SOMO), and the second one resulting from the fact that the unpaired electron interacts differently with the electrons of a σ spin-paired bond, because the exchange interaction is operative only for electrons of the same spin. The latter effect results in a shorter average distance between electrons of the same spin compared to the electrons of opposite spin and consequently to an induction of net spin density of opposite sign on the neighboring carbon atom with respect to the atom under investigation (Figure 3.1).

3.3 Understanding Spin Coupling by Molecular Orbital Energies

Hay and Hoffmann [95] derived an approach for understanding the spin coupling constants in dinuclear transition-metal complexes in the form of molecular orbital energies, which will be briefly summarized in the following. They used the antibonding and the bonding linear combination of the magnetic orbitals, which are in the case of an dinuclear Cu(II) complex, dominated by the singly occupied $d_{x^2-y^2}$ Cu orbitals, centered on the two copper atoms A and B. These orbitals refer approximately to the highest singly occupied α (or majority) spin orbitals in the high-spin state,

$$\phi_1 = d^A_{x^2-y^2} + d^B_{x^2-y^2},$$
$$\phi_2 = d^A_{x^2-y^2} - d^B_{x^2-y^2},$$

with the orbital energies ϵ_1 and ϵ_2. By considering all different configurations of the two electrons in the two molecular orbitals ϕ_1 and ϕ_2, it is possible to evaluate the energy differences triplet and singlet states,

$$E_\mathrm{S} - E_\mathrm{T} = 2K_{AB} - \frac{(\epsilon_1 - \epsilon_2)^2}{J_{AA} - J_{AB}}, \tag{3.2}$$

where J_{AA} and J_{AB} refer to the two-electron Coulomb repulsion between two electrons in the same and in two different magnetic orbitals, respectively, and K_{AB} is the exchange integral between electrons in two magnetic orbitals. Hay and coworkers argumented that the changes in the denominator $J_{AA} - J_{AB}$ are small compared to the molecular orbital difference in the numerator of Equation (3.2) when the molecular structure is varied, as typically $J_{AA} >> J_{AB}$. The (always positive) exchange integral K_{AB} gives ferromagnetic contributions, while the second term gives antiferromagnetic contributions. In the derivation of Equation (3.2), several approximations were made. In some cases contributions were neglected by comparing the order of magnitude of different elements.
Comparing Equation (3.1) and the antiferromagnetic contributions to Equation (3.2), one can identify $J_{AA} - J_{AB}$ with U and the transfer integral b_{ij}

with one half the energy difference between bonding and antibonding orbital combinations.
In Ref. [95], it was also shown that Equation (3.2) can be easily extended to the general case of m unpaired electrons on each spin center, in which the ferromagnetic J_{F} and antiferromagnetic contributions J_{AF} to the coupling constant are obtained by expressions similar to Equation (3.2),

$$J_{\mathrm{F}} = \frac{1}{m^2} \sum_{i \in A} \sum_{j \in B} K_{ij} \tag{3.3}$$

$$J_{\mathrm{AF}} = -\frac{1}{m^2} \sum_{i=1}^{m} \frac{\frac{1}{2} \left(\epsilon_{2i} - \epsilon_{2i-1}\right)^2}{J_{Ai,Ai} - J_{Ai,Bi}}. \tag{3.4}$$

Equation (3.2) was successfully applied to understand the angular dependence of spin coupling in two dinuclear copper(II) complexes, one bridged by one chloro, and the other one bridged by two chloro ligands, by visual inspection of the molecular orbital shapes (including the MO contributions from the bridging ligands), and the associated changes in the molecular orbital energies due to the increase or decrease of their antibonding character.

3.4 Green's-Function Approach

An alternative ansatz for the evaluation of magnetic exchange coupling constants was derived by Lichtenstein and coworkers [32] by comparing the energy change due to a small spin rotation between a Green's-function energy expression and the Heisenberg model [32], using the local force theorem.

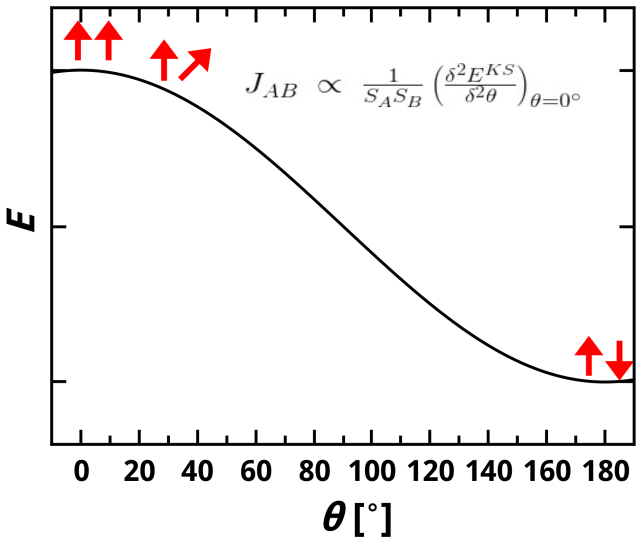

Figure 3.2: Relation between the relative angle between the local spins and the exchange spin coupling constant.

The energy is assumed to have a cosine dependence on the relative angle between the local spins, and since in this case the energy splitting between ferro- and antiferromagnetically coupled states can be obtained from the second derivative of the energy with respect to rotation of one spin vector (see Figure 3.2), the electronic structure of only one spin state needs to be known. The final expression for the Heisenberg exchange coupling constant $J^{\text{unit}}_{\text{Green}}$ (F) for local spin vectors of unit length (Equation (2.3)) calculated from the ferromagnetically (F) coupled state is obtained as the imaginary part of an integral over the trace of products of the Green's functions for α and β spins and so-called on-site potentials $\hat{V}_A$ and $\hat{V}_B$ of the two magnetic sites,

$$J^{\text{unit}}_{\text{Green}}\ (\text{F}) = -\frac{1}{4\pi}\text{Im}\int_{-\infty}^{\epsilon_F} \text{d}\epsilon\ \text{Tr}\left[\hat{V}_A \hat{G}^{\alpha}\, \hat{V}_B \hat{G}^{\beta}\right]. \tag{3.5}$$

The on-site potentials can be expressed as the difference between the Coulomb potentials for α and β electrons, $\hat{U}^{\alpha}_A$ and $\hat{U}^{\beta}_A$,

$$\hat{V}_A = \hat{U}^{\alpha}_A - \hat{U}^{\beta}_A, \tag{3.6}$$

which refer to a Hubbard-like term that describes the repulsion between α and β electrons on a given magnetic site A. In Section 3.4.1, the derivation of the final Equation 3.23 implemented in Artaios outgoing from Equation 3.5, derived by Lichtenstein and coworkers 1987 [32], is given. In Section 3.4.2, it is discussed into which contributions the coupling constants can be decomposed, before it is discussed in Section 3.4.3 how to signs of these contributions can be understood.

3.4.1 The Green's-function Approach in Terms of Local Projection Operators

A short derivation of the Green's-function approach was given in the author's master's thesis [33], nevertheless important steps in the derivation were missing and therefore in the following a complete derivation of the Han–Ozaki–Yu version of Equation (3.5) [121], which left out some aspects of the derivation, is given featuring local projection operators. This allows for employing different local partitioning schemes available in quantum chemistry to be used for the definition of the on-site potentials.
Equation (3.5) can be reformulated by considering that $\text{Im}\,(AB) = \text{Im}\,(A)\,\text{Re}\,(B) + \text{Re}\,(A)\,\text{Im}\,(B)$,

$$\begin{aligned} J^{\text{unit}}_{\text{Green}}\ (\text{F}) = \ & - \ \frac{1}{4\pi}\int_{-\infty}^{\epsilon_F} \text{d}\epsilon\ \text{Tr}\left[\hat{V}_A \text{Im}\left(\hat{G}^{\alpha}\right)\, \hat{V}_B \text{Re}\left(\hat{G}^{\beta}\right)\right. \\ & + \ \left.\hat{V}_A \text{Re}\left(\hat{G}^{\alpha}\right)\, \hat{V}_B \text{Im}\left(\hat{G}^{\beta}\right)\right]. \end{aligned} \tag{3.7}$$

The Green's functions are expressed in a Kohn-Sham molecular orbital (MO) basis $\{|\,\phi^{\sigma}_i\rangle\}$ by using the definition

$$\hat{G}^{\sigma}(\epsilon) = \lim_{\delta \to 0+}\left(\epsilon - \hat{h}^{\sigma} + \text{i}\delta\right)^{-1}, \tag{3.8}$$

where the effective single-particle (or here Kohn–Sham) Hamiltonian in the basis of molecular orbitals is

$$\hat{h}^{\sigma} = \sum_{i} |\phi_i^{\sigma}\rangle \epsilon_i^{\sigma} \langle \phi_i^{\sigma}| \,, \tag{3.9}$$

and where ϵ_i^{σ} refers to the energy of MO $|\,\phi_i^{\sigma}\rangle$ with spin $\sigma \in \{\alpha, \beta\}$. Equation (3.9) is inserted into Equation (3.8) to obtain the final expressions for the Green's functions in the Kohn-Sham orbital basis,

$$\hat{G}^{\sigma}(\epsilon) = \sum_{i} \frac{|\phi_i^{\sigma}\rangle\langle\phi_i^{\sigma}|}{\epsilon - \epsilon_i^{\sigma} + \mathrm{i}\delta}, \tag{3.10}$$

Within an integral the denominator of Equation (3.10) can be rewritten as

$$\frac{1}{\epsilon - \epsilon_i^{\sigma} + \mathrm{i}\delta} = \mathrm{P}\frac{1}{\epsilon - \epsilon_i^{\sigma}} - \mathrm{i}\pi\delta\left(\epsilon - \epsilon_i^{\sigma}\right), \tag{3.11}$$

where P refers to the Cauchy principal part. According to Equation (3.11) the imaginary and real parts of the Green's function are given as

$$\mathrm{Im}\left(\hat{G}^{\sigma}\right) = -\pi \sum_{i} |\phi_i^{\sigma}\rangle\langle\phi_i^{\sigma}|\, \delta\left(\epsilon - \epsilon_i^{\sigma}\right), \tag{3.12}$$

$$\mathrm{Re}\left(\hat{G}^{\sigma}\right) = \sum_{i} \frac{|\phi_i^{\sigma}\rangle\langle\phi_i^{\sigma}|}{\epsilon - \epsilon_i^{\sigma}}. \tag{3.13}$$

By inserting (3.12) and (3.13) into (3.7), the following equation is obtained:

$$\begin{aligned} J_{\mathrm{Green}}^{\mathrm{unit}}(\mathrm{F}) = \quad & -\frac{1}{4}\int^{\epsilon_F} \mathrm{d}\epsilon \mathrm{Tr}\left[\sum_{i,j} \hat{V}_A\, |\phi_i^{\alpha}\rangle\langle\phi_i^{\alpha}|\, \delta\left(\epsilon - \epsilon_i^{\alpha}\right) \hat{V}_B \frac{\left|\phi_j^{\beta}\rangle\langle\phi_j^{\beta}\right|}{\epsilon - \epsilon_j^{\beta}}\right. \\ & \left. + \hat{V}_A \frac{|\phi_i^{\alpha}\rangle\langle\phi_i^{\alpha}|}{\epsilon - \epsilon_i^{\alpha}} \hat{V}_B \left|\phi_j^{\beta}\rangle\langle\phi_j^{\beta}\right| \delta\left(\epsilon - \epsilon_j^{\beta}\right)\right]. \end{aligned} \tag{3.14}$$

Employing the properties of the Dirac distribution,

$$\int_{-\infty}^{\infty} \mathrm{d}\epsilon\; f(\epsilon)\, \delta\left(\epsilon - \epsilon_i^{\sigma}\right) = f\left(\epsilon_i^{\sigma}\right), \tag{3.15}$$

the following equation is obtained,

$$\begin{aligned} J_{\mathrm{Green}}^{\mathrm{unit}}(\mathrm{F}) = \; & -\frac{1}{4}\mathrm{Tr}\left[\sum_{i\in\mathrm{occ},j} \hat{V}_A\, |\phi_i^{\alpha}\rangle\langle\phi_i^{\alpha}|\, \hat{V}_B \frac{\left|\phi_j^{\beta}\rangle\langle\phi_j^{\beta}\right|}{\epsilon_i^{\alpha} - \epsilon_j^{\beta}}\right. \\ & \left. + \sum_{j\in\mathrm{occ},i} \hat{V}_A \frac{|\phi_i^{\alpha}\rangle\langle\phi_i^{\alpha}|}{\epsilon_j^{\beta} - \epsilon_i^{\alpha}} \hat{V}_B \left|\phi_j^{\beta}\rangle\langle\phi_j^{\beta}\right|\right]. \end{aligned} \tag{3.16}$$

The two terms appearing in Equation (3.16) differ in the order of the molecular orbital energy differences. Since the Fermi energy constitutes the upper bond of integration, the sums are restricted to occupied α spin-orbitals in the first term, and to occupied β spin orbitals in the second term.

The on-site potentials can be defined with local projection operators $\hat{p}_A$, which are chosen in the following according to Löwdin's partitioning scheme,

$$\hat{p}_A = \sum_{\mu \in A} |\mu\rangle\langle\mu| \,, \tag{3.17}$$

where the $|\mu\rangle$ are symmetrically orthogonalized atom-centered one-particle basis functions, resulting in

$$\hat{V}_A = \hat{p}_A \left(\hat{h}^\alpha - \hat{h}^\beta\right) \hat{p}_A = \sum_{\{\mu,\nu\} \in A} |\mu\rangle\langle\mu| \left(\hat{h}^\alpha - \hat{h}^\beta\right) |\nu\rangle\langle\nu| \,. \tag{3.18}$$

The advantage of this partitioning scheme is that the overlap matrix is fully neglected. This definition of the on-site potentials leads to an expression for J that is consistent with the one given by Ozaki and coworkers [121]. It should be noted that this definition of the on-site potentials is not unique (which is discussed in the Supporting Information). By inserting Equation (3.18) into Equation (3.16) one gets

$$\begin{aligned} J^{\text{unit}}_{\text{Green}}\ (\text{F}) = \ - \ & \frac{1}{4}\text{Tr}\left[\sum_{i \in \text{occ},j} \sum_{\substack{\{\mu,\nu\} \in A \\ \{\mu',\nu'\} \in B}} |\mu\rangle\langle\mu| \left(\hat{h}^\alpha - \hat{h}^\beta\right) |\nu\rangle\langle\nu|\, \phi_i^\alpha\rangle \right. \\ & \langle\phi_i^\alpha \,|\, \mu'\rangle\langle\mu' \,|\, \left(\hat{h}^\alpha - \hat{h}^\beta\right) |\nu'\rangle\langle\nu'|\, \phi_j^\beta\rangle\langle\phi_j^\beta \,|\, \frac{1}{\epsilon_i^\alpha - \epsilon_j^\beta} \\ & + \sum_{j \in \text{occ},i} \sum_{\substack{\{\mu,\nu\} \in A \\ \{\mu',\nu'\} \in B}} |\mu\rangle\langle\mu| \left(\hat{h}^\alpha - \hat{h}^\beta\right) |\nu\rangle\langle\nu|\, \phi_i^\alpha\rangle \\ & \left. \langle\phi_i^\alpha \,|\, \mu'\rangle\langle\mu' \,|\, \left(\hat{h}^\alpha - \hat{h}^\beta\right) |\nu'\rangle\langle\nu'|\, \phi_j^\beta\rangle\langle\phi_j^\beta \,|\, \frac{1}{\epsilon_j^\beta - \epsilon_i^\alpha}\right] . \end{aligned} \tag{3.19}$$

Evaluating the trace and exploiting that the Löwdin basis functions are or-

thonormal, one obtains

$$
\begin{aligned}
J^{\text{unit}}_{\text{Green}}\ (\text{F}) = \ - \ \frac{1}{4}\Bigg[& \sum_{i\in\text{occ},j} \sum_{\substack{\{\mu,\nu\}\in A \\ \{\mu',\nu'\}\in B}} \langle\mu\,|\left(\hat{h}^{\alpha}-\hat{h}^{\beta}\right)|\nu\rangle\langle\nu|\,\phi_i^{\alpha}\rangle \\
& \langle\phi_i^{\alpha}\,|\,\mu'\rangle\langle\mu'\,|\left(\hat{h}^{\alpha}-\hat{h}^{\beta}\right)|\nu'\rangle\langle\nu'|\,\phi_j^{\beta}\rangle\langle\phi_j^{\beta}\,|\,\mu\rangle\frac{1}{\epsilon_i^{\alpha}-\epsilon_j^{\beta}} \\
+ & \sum_{j\in\text{occ},i} \sum_{\substack{\{\mu,\nu\}\in A \\ \{\mu',\nu'\}\in B}} \langle\mu\,|\left(\hat{h}^{\alpha}-\hat{h}^{\beta}\right)|\nu\rangle\langle\nu|\,\phi_i^{\alpha}\rangle \\
& \langle\phi_i^{\alpha}\,|\,\mu'\rangle\langle\mu'\,|\left(\hat{h}^{\alpha}-\hat{h}^{\beta}\right)|\nu'\rangle\langle\nu'|\,\phi_j^{\beta}\rangle\langle\phi_j^{\beta}\,|\,\mu\rangle\frac{1}{\epsilon_j^{\beta}-\epsilon_i^{\alpha}}\Bigg]
\end{aligned}
\tag{3.20}
$$

The matrix elements $\langle\mu\,|\left(\hat{h}^{\alpha}-\hat{h}^{\beta}\right)|\,\nu\rangle$ can be rewritten as the difference between elements of the α and β Fock matrices $F^{\alpha}_{\mu\nu}-F^{\beta}_{\mu\nu}$ in a Löwdin- (or symmetrically orthogonalized) basis, resulting in

$$
\begin{aligned}
J^{\text{unit}}_{\text{Green}}\ (\text{F}) = \ - \ \frac{1}{4}\Bigg[& \sum_{i\in\text{occ},j} \sum_{\substack{\{\mu,\nu\}\in A \\ \{\mu',\nu'\}\in B}} C^{\alpha}_{\nu i}\left(F^{\alpha}_{\mu\nu}-F^{\beta}_{\mu\nu}\right)C^{\beta *}_{\mu j} \\
& C^{\alpha *}_{\mu' i}\left(F^{\alpha}_{\mu'\nu'}-F^{\beta}_{\mu'\nu'}\right)C^{\beta}_{\nu' j}\frac{1}{\epsilon_i^{\alpha}-\epsilon_j^{\beta}} \\
+ & \sum_{j\in\text{occ},i} \sum_{\substack{\{\mu,\nu\}\in A \\ \{\mu',\nu'\}\in B}} C^{\alpha}_{\nu i}\left(F^{\alpha}_{\mu\nu}-F^{\beta}_{\mu\nu}\right)C^{\beta *}_{\mu j} \\
& C^{\alpha *}_{\mu' i}\left(F^{\alpha}_{\mu'\nu'}-F^{\beta}_{\mu'\nu'}\right)C^{\beta}_{\nu' j}\frac{1}{\epsilon_j^{\beta}-\epsilon_i^{\alpha}}\Bigg]
\end{aligned}
\tag{3.21}
$$

with the (Löwdin) MO coefficients $C^{\sigma}_{\nu i}=\langle\nu\,|\,\phi_i^{\sigma}\rangle$. The sum over occupied molecular orbitals can be reformulated by employing Fermi functions at a temperature of zero Kelvin,

$$
\lim_{T\to 0} f_i^{\alpha}(T) = \lim_{T\to 0}\frac{1}{\exp^{\frac{\epsilon_i^{\alpha}-\mu}{kT}}+1} = \begin{cases} 1 & \forall \quad \epsilon_i^{\alpha}<\mu \\ 0 & \forall \quad \epsilon_i^{\alpha}>\mu. \end{cases}, \tag{3.22}
$$

Assuming real molecular orbitals and exploiting the symmetry of the Fock matrix one gets the final expression for the coupling constant (compare a related

expression by Antropov and coworkers [152]),

$$J^{\text{unit}}_{\text{Green}}\ (\text{F}) = \frac{1}{4}\Bigg[\sum_{i,j}\sum_{\{\mu,\nu\}\in A}\sum_{\{\mu',\nu'\}\in B}\frac{f_i^\alpha - f_j^\beta}{\epsilon_j^\beta - \epsilon_i^\alpha} C^\alpha_{\mu i}\left(F^\alpha_{\mu\nu} - F^\beta_{\mu\nu}\right) C^\beta_{\nu j} \quad (3.23)$$
$$C^\alpha_{\mu' i}\left(F^\alpha_{\mu'\nu'} - F^\beta_{\mu'\nu'}\right) C^\beta_{\nu' j}\Bigg].$$

This expression will be used in the following. The final equations are in general applicable to the ferromagnetically coupled (high-spin) state and to the BS determinant modelling the antiferromagnetically coupled state. Because of the assumed cosine dependence of the energy on relative spin orientations, the sign of Equation (3.5) and Equations (3.7) through (3.23) changes when applied on the BS determinant,

$$J^{\text{unit}}_{\text{Green}}\ (\text{AF}) = -J^{\text{unit}}_{\text{Green}}\ (\text{F}). \quad (3.24)$$

As pointed out in Chapter 4, this relation is not fulfilled in practice. While the Green's-function approach when applied to a ferromagnetically coupled determinant ($J^{\text{unit}}_{\text{Green}}$ (F)) is qualitatively consistent with Noodleman's BS approach, it gives inconsistent and at times wildly varying results when applied to a BS determinant modeling the antiferromagnetically coupled state.
For completeness, it should also be noted that the term "(Noodleman's) BS approach" is used to denote the approach described in Section 2.3. Since the Green's-function approach can in principle also be applied to a BS determinant, a more exact expression for the BS approach in this context would be "total-energy difference approach". To be consistent with the quantum chemistry literature, the term "Broken-Symmetry approach" will be used in the following.

3.4.2 Analyzing Exchange Pathways with the Green's-Function Method

Starting from the ansatz by Lichtenstein and coworkers [32,49] the expression of Ozaki and coworkers [127], implemented in the OpenMX program package [120], was rederived by employing local projection operators in the previous section,

$$\begin{aligned} J_{\text{Green}}\ (\text{F}) = & -\tfrac{1}{4S_AS_B}\sum_{\substack{i\in\text{occ}\\ j\in\text{virt}}}\sum_{\substack{\{\mu,\nu\}\in A\\ \{\mu',\nu'\}\in B}} C^\alpha_{\nu i}\left(F^\alpha_{\mu\nu} - F^\beta_{\mu\nu}\right) C^{\beta *}_{\mu j} \quad (3.25)\\ & C^{\alpha *}_{\mu' i}\left(F^\alpha_{\mu'\nu'} - F^\beta_{\mu'\nu'}\right) C^\beta_{\nu' j}\frac{1}{\epsilon_i^\alpha - \epsilon_j^\beta}\\ & -\tfrac{1}{4S_AS_B}\sum_{\substack{j\in\text{occ}\\ i\in\text{virt}}}\sum_{\substack{\{\mu,\nu\}\in A\\ \{\mu',\nu'\}\in B}} C^\alpha_{\nu i}\left(F^\alpha_{\mu\nu} - F^\beta_{\mu\nu}\right) C^{\beta *}_{\mu j}\\ & C^{\alpha *}_{\mu' i}\left(F^\alpha_{\mu'\nu'} - F^\beta_{\mu'\nu'}\right) C^\beta_{\nu' j}\frac{1}{\epsilon_j^\beta - \epsilon_i^\alpha}, \end{aligned}$$

with $F^{\sigma}_{\mu'\nu'}$ referring to the elements of the Fock matrices, and $C^{\sigma}_{\nu i}$ referring to the molecular orbital coefficients for a given spin σ in a Löwdin transformed basis. S_A and S_B refer to the local spins on the magnetic sites A and B.
The resulting Equation (3.25), can be reduced to contributions $j_{\text{Green}}(i,j)$ depending on pairs of α and β orbitals (Equation (3.26)), where one spin orbital is occupied and one is unoccupied.

$$j_{\text{Green}}(i,j) = \frac{q}{4S_AS_B} \sum_{\substack{\{\mu,\nu\}\in A \\ \{\mu',\nu'\}\in B}} C^{\alpha}_{\nu i}\left(F^{\alpha}_{\mu\nu} - F^{\beta}_{\mu\nu}\right) C^{\beta *}_{\mu j} \; C^{\alpha *}_{\mu' i}\left(F^{\alpha}_{\mu'\nu'} - F^{\beta}_{\mu'\nu'}\right) C^{\beta}_{\nu' j} \frac{1}{\epsilon^{\alpha}_i - \epsilon^{\beta}_j} \begin{cases} i \in \text{occ}, j \in \text{virt} & q = -1 \\ j \in \text{occ}, i \in \text{virt} & q = 1 \end{cases} \tag{3.26}$$

In the following $j_{\text{Green}}(i,j)$ values will be referred to as the contributions from spin-flip excitations. The contributions can be further reduced by adding up all contributions $j^{\sigma}_{\text{Green,MO}}(i)$ arising from spin-flip excitations from a given occupied spin orbital with all unoccupied spin orbitals with spin σ,

$$j^{\sigma}_{\text{Green,MO}}(y) = \sum_{x\in\text{virt}} j_{\text{Green}}(i,j) \begin{cases} \text{if } \sigma = \alpha & \text{then } x = j \text{ and } y = i \\ \text{if } \sigma = \beta & \text{then } x = i \text{ and } y = j \end{cases} \tag{3.27}$$

In the same spirit, it is possible to calculate the contributions for virtual spin orbitals $j^{\sigma}_{\text{Green,MO(virt)}}(i)$,

$$j^{\sigma}_{\text{Green,MO(virt)}}(y) = \sum_{x\in\text{occ}} j_{\text{Green}}(i,j) \begin{cases} \text{if } \sigma = \alpha & \text{then } x = j \text{ and } y = i \\ \text{if } \sigma = \beta & \text{then } x = i \text{ and } y = j \end{cases}.$$

In the following, the largest spin-orbital contributions will be reported $j^{\sigma}_{\text{Green,MO}}(i)$ and the spin-flip excitations giving the largest contributions $j_{\text{Green}}(i,j)$ to those selected $j^{\sigma}_{\text{Green,MO}}(i)$ are discussed in order to obtain insight into the occupied MO contributions. In Chapter 6, additionally the virtual $j^{\sigma}_{\text{Green,MO(virt)}}(i)$ MO contributions are employed.

3.4.3 Dihydrogen in a Minimal Basis: How to Understand the Sign of Contributions from Spin-Flip Excitations?

To understand the magnitudes and signs of contributions arising from different spin-flip excitations, defined according to Equation (3.26), the dihydrogen molecule is studied with B3LYP in a minimal STO-3G basis. The spin-flip excitations are calculated with the Green's-function approach, and further decomposed into the contributions from MO coefficients and Fock matrix elements (Table 3.1).

Table 3.1: Spin-flip excitations and their different contributions from Equation (3.26), for H_2 at a bond distance of 2.5 Å calculated from the electronic structure of the high-spin state calculated (B3LYP/STO-3G). The differences between the Fock matrices for diffent spins are equal to $\left(F_{11}^{\alpha} - F_{11}^{\beta}\right) = \left(F_{22}^{\alpha} - F_{22}^{\beta}\right)$ for basis functions 1 and 2 corresponding to the $1s$ atomic orbitals. The contributions from the spin-flip excitations are given in cm^{-1}, and all other contributions are given in atomic units.

i	j	$j_{\mathrm{Green}}(i,j)$	$C_{1i}^{\alpha} C_{1j}^{\beta *} C_{2i}^{\alpha *} C_{2j}^{\beta}$	$(\epsilon_i^{\alpha} - \epsilon_j^{\beta})^{-1}$	$\left(F_{11}^{\alpha} - F_{11}^{\beta}\right)$
HOMO-1$^{\alpha}$	LUMO$^{\beta}$	20722.3	0.25	−1.98	−0.52
HOMO-1$^{\alpha}$	LUMO+1$^{\beta}$	−17779.7	−0.25	−1.76	−0.52
HOMO$^{\alpha}$	LUMO$^{\beta}$	−23391.6	−0.25	−2.15	−0.52
HOMO$^{\alpha}$	LUMO+1$^{\beta}$	19709.5	0.25	−1.90	−0.52

The differences between α and β Fock matrix elements $\left(F_{11}^{\alpha} - F_{11}^{\beta}\right)$ and $\left(F_{22}^{\alpha} - F_{22}^{\beta}\right)$ both have a negative sign, which always leads to positive factor. The reason for this is that in a simple 2-electrons-in-2-orbitals picture, the diagonal elements of the single-particle Hamiltonian matrix (in a local basis) will determine the energetic location of the "energetic center" of the two resulting MOs, and the off-diagonal elements will determine the energetic splitting of the MOs, that is, their energetic distance from that center.

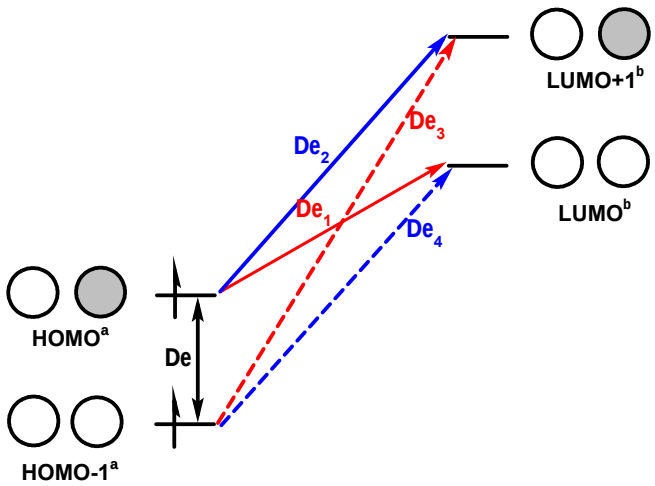

Figure 3.3: Spin-up (α) and spin-down (β) MO shapes and energy levels of the dihydrogen molecule in an unrestricted Kohn-Sham DFT framework in the triplet state, using a minimal basis. The black double arrow describes the energy difference between the HOMO$^{\alpha}$ and and the HOMO-1$^{\alpha}$, $\Delta\epsilon$, referring to the bonding and antibonding linear combinations of the $1s$ orbitals, which is used to calculate the antiferromagnetic contributions according to the Hay approach [95] (Equation (3.2)). The red single arrows refer to the MO differences $\Delta\epsilon_1$, and $\Delta\epsilon_3$ (giving antiferromagnetic contributions), and the blue single arrows refer to the MO differences $\Delta\epsilon_2$, and $\Delta\epsilon_4$ (giving ferromagnetic contributions), and enter the Green's-function approach (Equation (3.26)) in the denominator.

There is no reason to expect the splitting to be substantially different for spin-up (α) and spin-down (β) orbitals, but the location of their "energy center" is expected to be much higher in energy for β than for α orbitals, as illustrated by Figure 3.3. This implies that the diagonal elements of $\mathbf{F}^{\beta}$ are higher than those of $\mathbf{F}^{\alpha}$, leading to the negative difference.

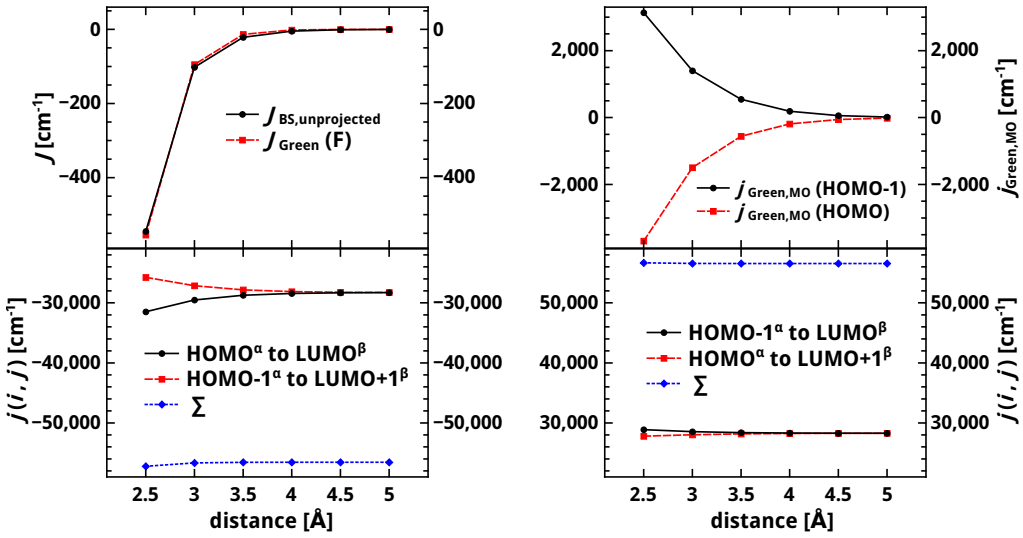

Figure 3.4: Coupling constants calculated with the unprojected BS approach and the Green's-function approach (top-left panel), the contributions from occupied α orbitals $j^{\alpha}_{\mathrm{Green,MO}}(i)$ (top-right panel) the antiferromagnetic (bottom-left panel) and ferromagnetic contributions (bottom-right panel) from spin-flip excitations $j_{\mathrm{Green}}(i,j)$ (B3LYP/STO-3G) for different bond distances.

The inverse of the MO energy differences $\epsilon^{\alpha}_{i} - \epsilon^{\beta}_{j}$ are always negative, because here, the β MOs are always higher in energy than any α MOs, so that they cannot be decisive for the kind of contribution (F vs. AF). While the sign stays the same, it is the only quantity which differs in its magnitude from one spin-flip excitation to another, causing the changes in the overall contributions from the different spin-flip excitations. It turns out that the products over the four MO coefficients differ in their sign, and therefore play the decisive role for the kind of contribution. This difference can be explained by the shape of the MOs. For the spin-flip excitation from the HOMO-1$^{\alpha}$ to the LUMO$^{\beta}$, both MOs have bonding character (Figure 3.3), and consequently the MO coefficients always have the same signs, resulting in a positive value and thus in a ferromagnetic contribution. For the spin-flip excitation between the HOMO-1$^{\alpha}$ and the LUMO+1$^{\beta}$, a negative sign and thus an antiferromagnetic contribution is found, because the coefficients have a different sign on both hydrogen atoms in the LUMO+1$^{\beta}$ (Figure 3.3). This observation can be generalized to a rule that pairs of two bonding or pairs of two antibonding orbitals lead to ferromagnetic contribution $j_{\mathrm{Green}}(i,j)$, while pairs of bonding and antibonding orbitals lead

to antiferromagnetic contributions. Even though the signs of the other may not be as clear-cut as in this simple example, this rule will be found applicable in all examples studied in this work.

The Green's-function approach and the model of Hay and Hoffmann [95] (Section 3.3), both depend on MO energy differences. However, in the Green's-function approach the energy differences between occupied and unoccupied orbitals of different spin are considered, while in the Hay model the energy differences between the occupied bonding and antibonding linear combinations of the localized magnetic orbitals is taken into account. Also the form in which they appear for both approaches differs. While they enter the Green's-function approach in the denominator, in the Hoffmann model the square of the energy differences between the occupied high-spin MOs are considered in the numerator. The energy differences considered in both models, and the way they enter Equations (3.26) and (3.2), are illustrated in Figure 3.3.

To elucidate the relations between these energy differences, the spin coupling and the different contributions to the coupling constant ($j^{\alpha}_{\mathrm{Green,MO}}(i)$ and $j_{\mathrm{Green}}(i,j)$) are given in Figure 3.4 as a function of the bond distance. Further the contributions to the $j^{\alpha}_{\mathrm{Green,MO}}(i)$ (Equation (3.27)) and $j_{\mathrm{Green}}(i,j)$ (Equation (3.26)) are decomposed into the absolute values of the products of coefficients, $|C^{\alpha}_{1i}C^{\beta *}_{1j}C^{\alpha *}_{2i}C^{\beta}_{2j}|$, which are equal in magnitude for all spin-flip excitations (bottom-right panel in Figure 3.5), the differences in the Fock matrix elements $\left(F^{\alpha}_{11}-F^{\beta}_{11}\right)$, and different MO orbital energy difference contributions to the Green's-function approach (top and bottom-left in Figure 3.5).

It should be noted that all signs are included in the MO energy difference terms. The MO energy difference contributions to the antiferromagnetic spin-flip excitation contributions $j_{\mathrm{Green}}(i,j)$ ($1/\Delta\epsilon_1+1/\Delta\epsilon_3$; bottom-right), the occupied orbital contributions $j^{\alpha}_{\mathrm{Green,MO}}(i)$ of the HOMO$^{\alpha}$ ($1/\Delta\epsilon_1-1/\Delta\epsilon_2$; top-left in Figure 3.5), and of the HOMO-1$^{\alpha}$ ($1/\Delta\epsilon_3-1/\Delta\epsilon_4$; top-right in Figure 3.5), along with the MO energy distributions of the approach of Hay et al. [95] are given in Figure 3.5 (top-left and bottom-left).

The coupling constants are calculated with the Green's-function approach (red curve), and the BS approach (black curve) using the STO−3G minimal basis set, and are in very good agreement with each other (Figure 3.5; top-left panel). Both contributions from occupied MOs have opposite signs (antiferromagnetic for the HOMO$^{\alpha}$ and ferromagnetic contributions for the HOMO-1$^{\alpha}$). The absolute values of these contributions decrease with increasing bond distance. The antiferromagnetic (ferromagnetic) spin-flip contributions are larger for the HOMO$^{\alpha}$→LUMO$^{\beta}$ (HOMO-1$^{\alpha}$→LUMO$^{\beta}$) than for the HOMO-1$^{\alpha}$→LUMO+1$^{\beta}$ (HOMO$^{\alpha}$→LUMO+1$^{\beta}$) spin-flip excitation, but approach each other for larger bond distances.

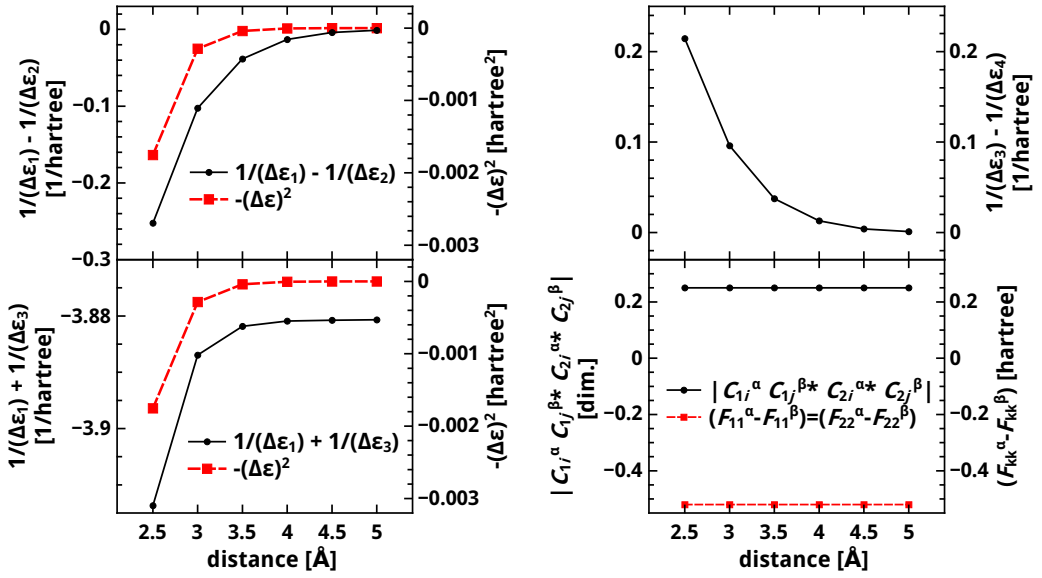

Figure 3.5: MO energy difference contributions to the occupied MO contributions $j^{\alpha}_{\mathrm{Green,MO}}(i)$ (Figure 3.4) to the coupling constant from the HOMO$^{\alpha}$ ($1/\Delta\epsilon_1 - 1/\Delta\epsilon_2$; top-left), the HOMO-1$^{\alpha}$ ($1/\Delta\epsilon_3 - 1/\Delta\epsilon_4$; top-right), and the MO energy difference contributions from the spin-flip excitations $j_{\mathrm{Green}}(i,j)$ giving antiferromagnetic contributions ($1/\Delta\epsilon_1 + 1/\Delta\epsilon_3$; bottom-left) obtained from the Green's-function approach, along with the antiferromagnetic MO contributions from the Hay model [95] (top-left and bottom-left). The differences between the Fock matrix elements for different spins $\left(F^{\alpha}_{11} - F^{\beta}_{11}\right)$ (again $\left(F^{\alpha}_{11} - F^{\beta}_{11}\right) = \left(F^{\alpha}_{11} - F^{\beta}_{11}\right)$ for all distances) and absolute values for the products of the coefficients $-C^{\alpha}_{1i} C^{\beta *}_{1j} C^{\alpha *}_{2i} C^{\beta}_{2j}|$ (exactly the same values for all orbital pairs; the sign is included in the MO differences).

In order to justify an analysis of the spin coupling by MO energies only, it is necessary to check if the other parameters stay constant with increasing bond length. The differences between the Fock matrices $\left(F^{\alpha}_{11} - F^{\beta}_{11}\right) = \left(F^{\alpha}_{22} - F^{\beta}_{22}\right)$, as well as the absolute of the products of the different MO coefficients $C^{\alpha}_{1i} C^{\beta *}_{1j} C^{\alpha *}_{2i} C^{\beta}_{2j}$ are not changed with increasing distance (bottom-right panel in Figure 3.5). Consequently, the changes in the spin coupling must result from changes in the MO energy differences. The trends for the MO energy contribution from the Hay approach ($-(\Delta\epsilon)^2$) [95] correlates with the trends obtained for the antiferromagnetic contributions to the spin-flip excitations ($1/\Delta\epsilon_1 + 1/\Delta\epsilon_3$ in Figure 3.5), and the contributions from the HOMO$^{\alpha}$ ($1/\Delta\epsilon_1 - 1/\Delta\epsilon_2$ in Figure 3.5). However, the spin-flip excitations giving antiferromagnetic contributions do not decrease and are also very large at larger distances, while the contributions from the HOMO$^{\alpha}$ approach zero for larger distances, as also observed for the Hay model [95]. However, the $1/\Delta\epsilon_1 - 1/\Delta\epsilon_2$ is smoother than the $-(\Delta\epsilon)^2$) curve, which is in better agreement with the total coupling constant. From this, it can be concluded, that the contributions of the Hay model refer to the sum of

all four spin-flip excitations (or both occupied MO contributions) referring to the total coupling constant in the case of H_2 in a minimal basis. However, it should be noted that for larger basis sets or systems there should be more of these kind of contributions.

4. Validation of a Green's-Function Approach to Exchange Spin Coupling

In this initial study, the spin center is defined as the formally spin-carrying atom only rather than including ligand atoms on which the spin may be delocalized, to check whether this simple approach allows for qualitative accuracy. First, simple model systems for exchange and superexchange, H_2 and H−He−H, are studied which is used to evaluate the importance of the choice of exchange–correlation functional and basis set (Section 14.1). Then several dinuclear transition metal complexes and *para*- and *meta*-connected dimethyl benzene radicals are investigated, which are grouped according to whether the spin density is mainly localized on the formally spin-carrying atoms (Section 4.2) or not (Section 4.3). Also the importance of structural relaxation in the different spin states is discussed. In Section 4.4, finally qualitative trends as a function of bridging angle for systems with delocalized spins, dinuclear hydroxo-bridged copper(II) complexes as investigated by Hoffmann and coworkers [95], are evaluated. In Section A.5 non-collinear DFT calculations are carried out for a series of systems in order to verify the assumption of the Heisenberg Hamiltonian, that the energy follows a cosine behavior with respect to the angle between the spins (see Section 2.2).

4.1 Parameter Study on Small Systems

For examination of the implementation of Lichtenstein's Green's-function approach in ARTAIOS, the hydrogen dimer is chosen as a very simple model of direct exchange spin coupling, and the H−He−H model system for superexchange coupling, where the spin-carrying hydrogen atoms are bridged by a helium atom which is modeling a closed-shell bridge.

4.1.1 Dihydrogen Molecule

In this section the magnetic exchange coupling in the dihydrogen molecule is studied as a function of the distance between the hydrogen atoms (Figure 4.1). In this system each hydrogen carries one unpaired electron, resulting in a triplet high-spin and a singlet low-spin state. To investigate the influence of the basis set and the exchange–correlation functional, the pure functional BP86 and the hybrid functional B3LYP, and basis sets of different size (SVP, TZVP and QZVP) are employed. The local spins are plus-minus one half for all parameters

and distances (Figure A.1 in Appendix A).

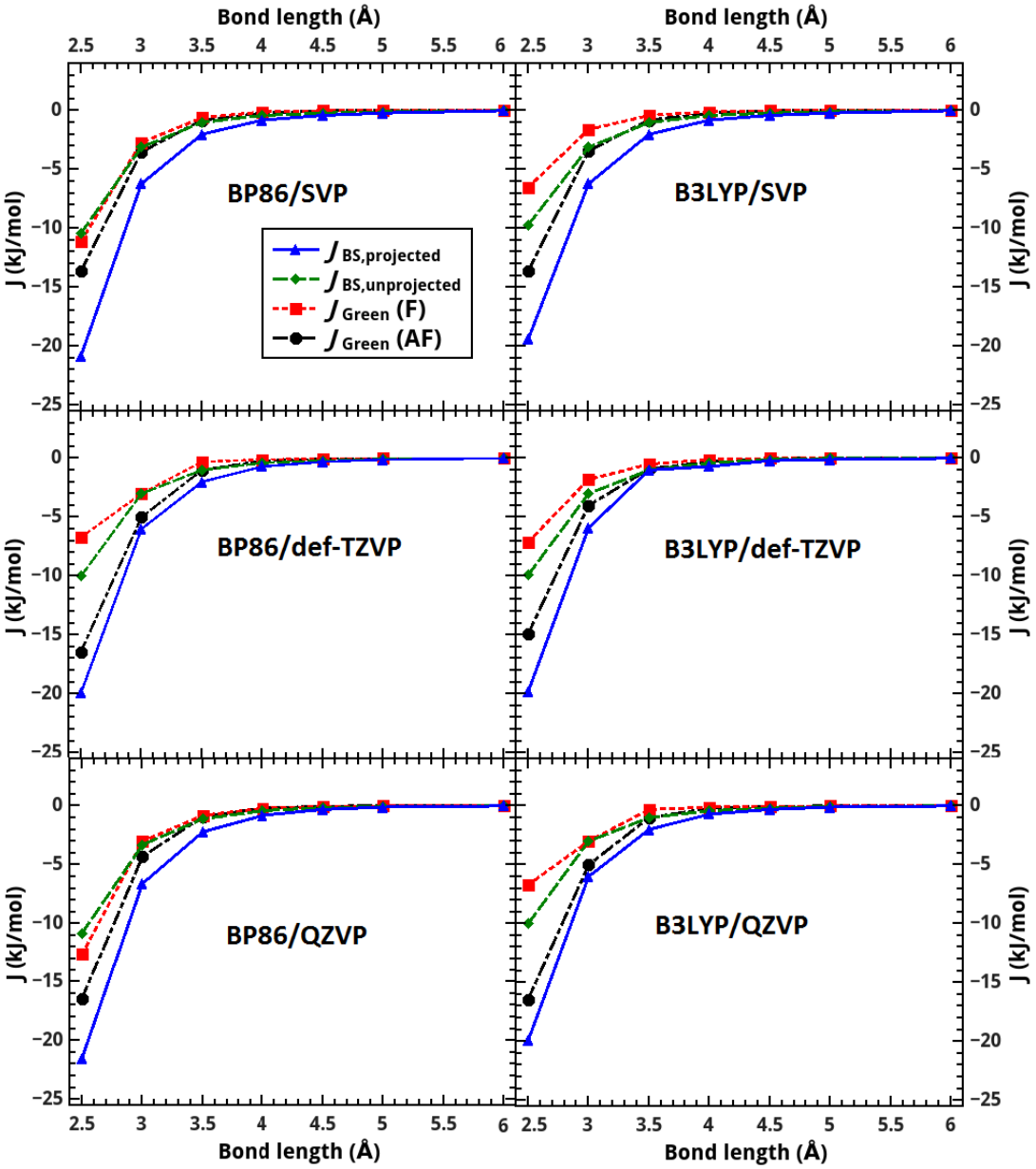

Figure 4.1: Magnetic coupling constants obtained from the Green's-function approach J_{Green} (F) / J_{Green} (AF) and the magnetic coupling constants calculated within the projected and unprojected BS formalism for the BP86 and the B3LYP functional and different basis sets for the dihydrogen molecule at different bond lengths.

J_{Green} (F) (red curve) is close to the $J_{\text{BS,unprojected}}$ expression (green curve), while the absolute J_{Green} (AF) values (black curve) are larger and in all cases in between the projected (blue curve) and the unprojected Noodleman expression. For B3LYP and for larger basis sets J_{Green} (AF) is closer to $J_{\text{BS,projected}}$ than

for BP86 and for smaller basis sets. For all of the parameters used, the same qualitative trends are found with a very similar order of the different J values, but quantitatively deviations up to a factor of 4 are found.

4.1.2 H−He−H Model System

In contrast to the direct spin interactions in the dihydrogen molecule, the H−He−H model system exhibits superexchange via a bridging closed-shell helium atom.

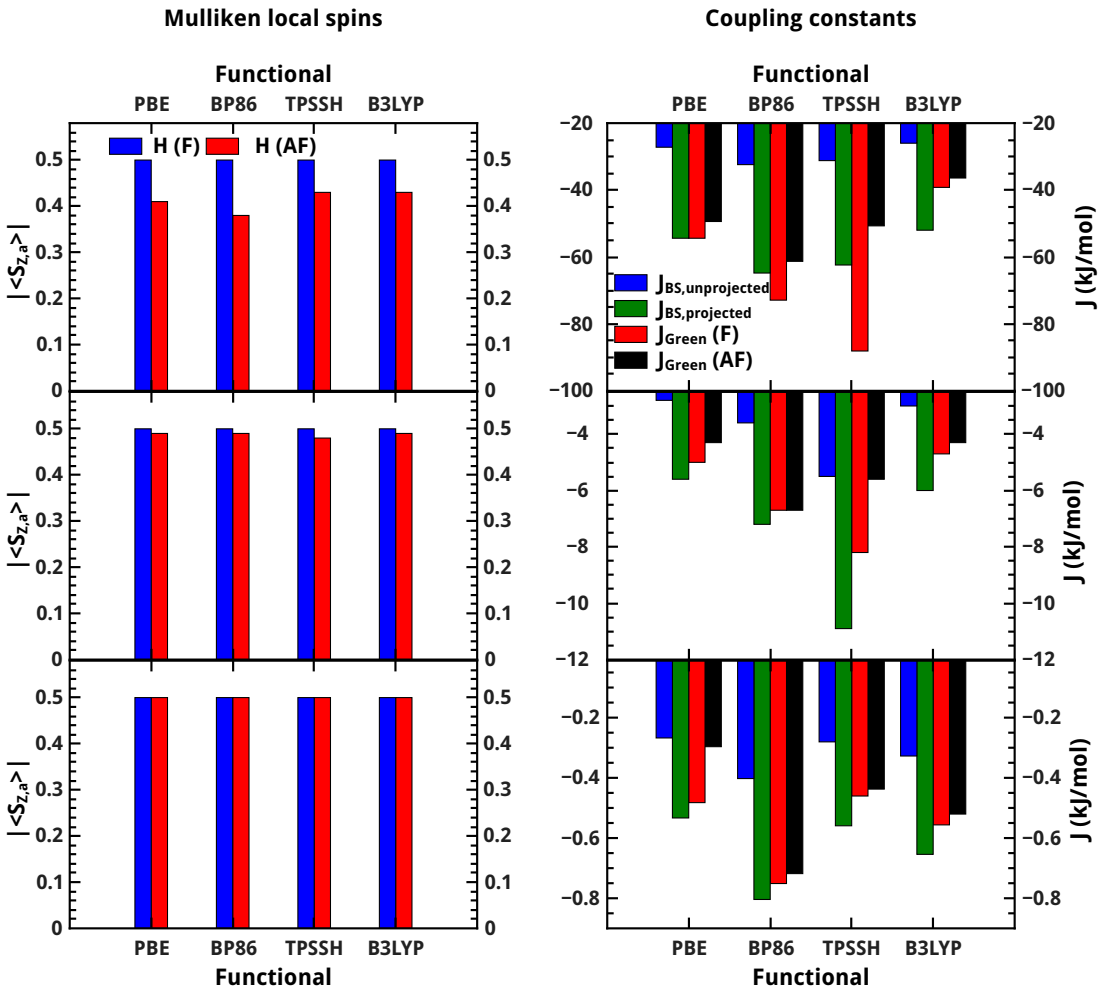

Figure 4.2: Local spins of the hydrogen atoms (left column), the magnetic exchange coupling constants (right column) calculated within the Green's-function approach J_{Green} (F)/J_{Green} (AF) and the magnetic coupling constants calculated within the projected and unprojected BS formalism for the BP86 and the B3LYP functional at three different H−He bond lengths, 1.25 Å (top), 1.625 Å (middle) and 2.0 Å (bottom).

As for the dihydrogen molecule a triplet high-spin state and an open-shell singlet state, approximated by a BS determinant, are obtained. To evaluate

the influence of the strength of the coupling on the performance of the Green's-function approach, three different H−He bond distances (1.25 Å, 1.625 Å and 2.0 Å) are considered. For these calculations two different basis sets (def-TZVP and QZVP) and four exchange-correlation functionals are applied, since the electronic structure (e.g. the local spins) is expected to show a larger dependence on the applied exchange-correlation functional compared with the dihydrogen molecule. The cosine behavior of the energy as a function of the angle θ between the two local spins is confirmed by non-collinear DFT calculations with the PBE functional (Section A.5 in the appendix). The changes in the magnetic exchange coupling constants according to an increase in the basis set size turn out to be very small, so that only the results obtained with def-TZVP are discussed here and the QZVP results are given in the appendix (Figure A.2 in Appendix A). In Figure 4.2 the local spins of the hydrogen atoms (left column) and the calculated magnetic exchange coupling constants (right column) obtained for the three different bond length are given. The local spins on the Helium bridge are not shown since they were zero for all distances.
The local spin analysis reveals that for the smallest bond length (1.25 Å) the magnitudes are about 0.1 a.u. smaller for the BS determinant than for the high-spin state, while the differences for the other two distances are rather small. This influences the calculated magnetic exchange coupling constants, since the Green's-function approach assumes a spin rotation without any changes in the spins' magnitudes. For a bond length of 1.25 Å the J_{Green} (F) (red bars) are higher than the $J_{\mathrm{BS,projected}}$ values (green bars) for all applied exchange–correlation functionals except for B3LYP, where J_{Green} (F) is found in between $J_{\mathrm{BS,projected}}$ and $J_{\mathrm{BS,unprojected}}$ (blue bars). In all cases, the J_{Green} (AF) values (black bars) are smaller than the J_{Green} (F) values. For the longer bond distances, where the spin remains the same, independent of the spin configuration, the J_{Green} (F) values are always between the values obtained from the unprojected and the projected formula. The J_{Green} (AF) values still remain the same relative to the BS values. Although in general a good qualitative agreement between both methods is found, no general scaling factor can be given here. Additionally, one should always keep in mind the sensitivity of the Green's-function approach to changes in the spins' magnitudes, violating the picture of rotating spins.

4.2 Larger Systems with Localized Spins

In this section, a number of dinuclear complexes with different electronic configurations is considered to see if the Green's-function approach is able to describe more complicated electronic structures. The complexes chosen for these studies are shown in Figure 4.3. The structures are optimized in their high-spin and low-spin states (approximated by BS solutions) and coupling constants are calculated for both spin-state structures. The para-bridged dimethylene radical is only optimized in the high-spin state and additionally the bond length between the methylene groups and the phenyl bridge is increased up to 1.8 Å to be able

to obtain an open-shell BS determinant.

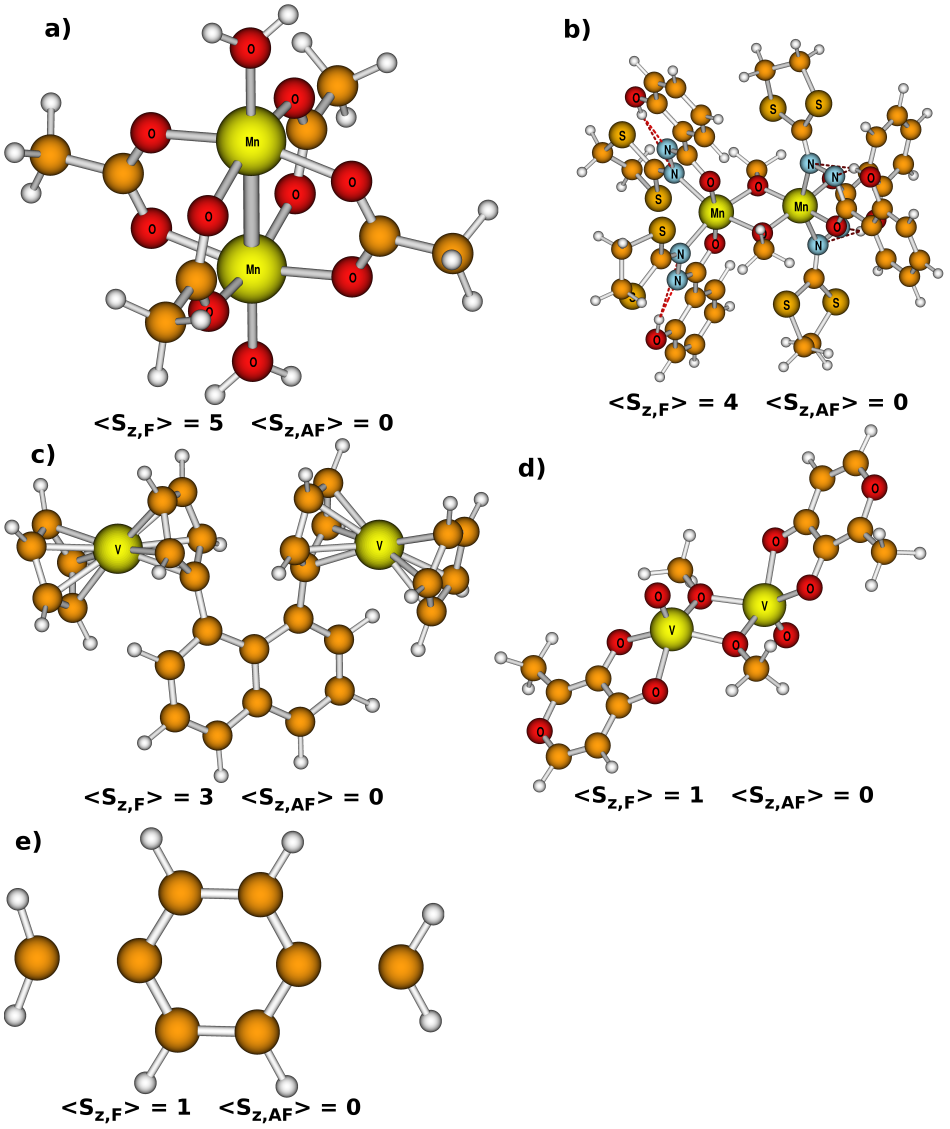

Figure 4.3: Structures and ideal $\hat{S}_z$ expectation values in both spin states for systems with localized spins optimized in the high-spin state (BP86/def-TZVP; c) optimized with Grimme's dispersion correction). a) $[Mn_2(Ac)_4(H_2O)_2]$, b) $[Mn_2(\mu-OMe)_2(HL)_4]$; H_2L=(2-salicyloyl-hydrazono-1,3-dithiolane), c) $\left[V_2\left(\eta^5-Cp\right)_2\left(\mu-\eta^5-1,8-DCN\right)\right]$ 1,8-DCN=1,8-dicyclopentadienylnaphthalene dianion; Cp=Cyclopentadienyl anion, d) $[V_2(\mu-O\text{-}Me)_2(O)_2(ma)_2]$; ma=maltato e) para-$C_8H_8$ (C−C bond length between benzene and methylene group was artificially elongated to 1.8 Å).

Again non-collinear DFT calculations with PBE (Figure A.5 in the appendix) on the high-spin structures give proof of a cosine behavior of the energy as a function of the angle θ between the two local spins for all systems studied in this section. Only for the para-C_8H_8 diradical small deviations are found around 90°. The coupling constant are in good agreement with those obtained

with GAUSSIAN09, which is an important prequisite for comparing the results (see Table A.2).

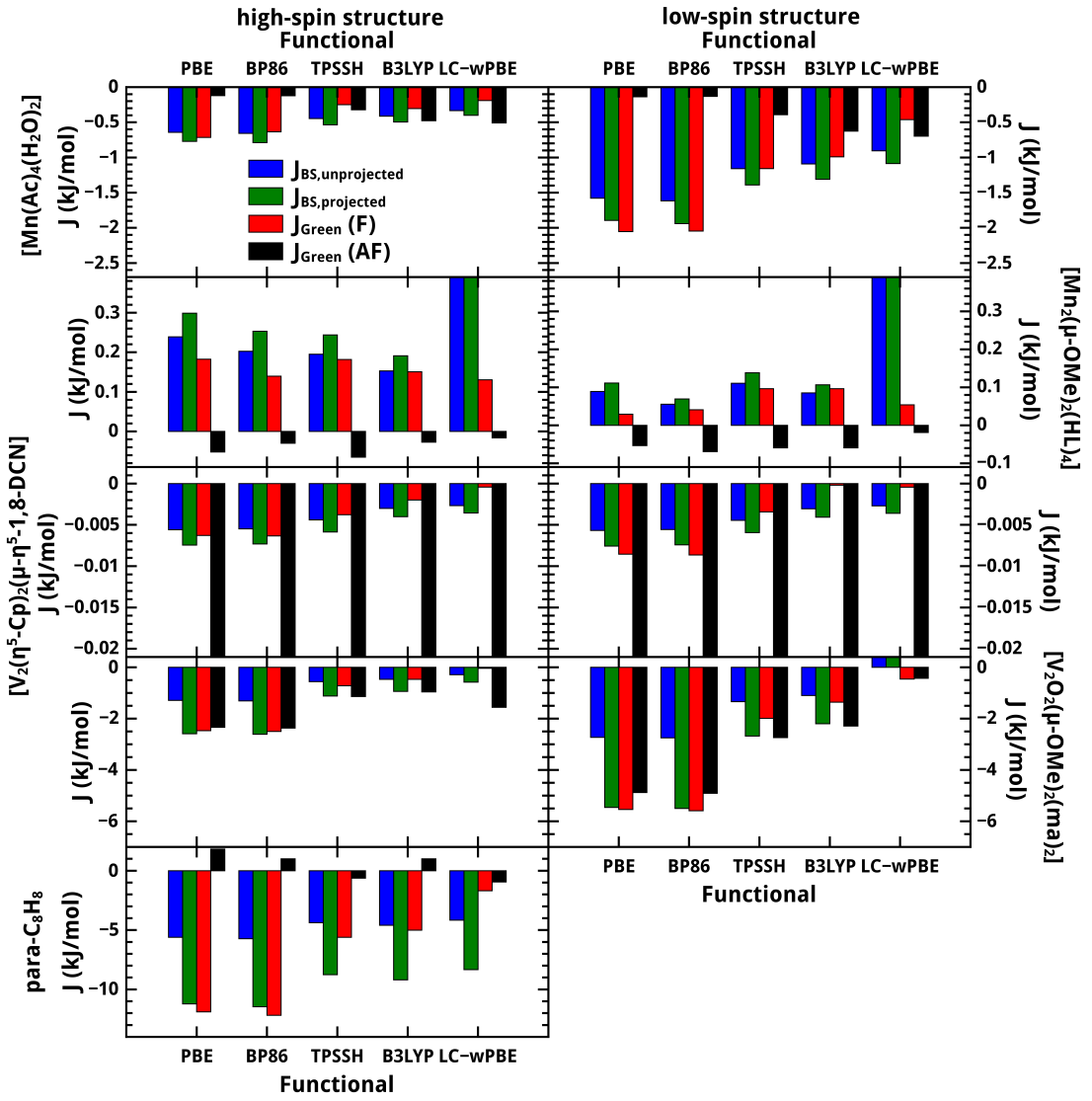

Figure 4.4: Magnetic exchange coupling constants obtained with different functionals for the compounds given in Figure 4.3 and different spin-state structures. LC-ωPBE BS values for $[Mn_2(\mu-OMe)_2(HL)_4]$ (high-spin and BS structure) and $[V_2(\mu-O\text{-}Me)_2(O)_2(ma)_2]$ (BS structure) are larger than the displayed range. Basis set: def-TZVP.

If single-point calculations for both spin states are performed on top of an optimized spin-state structure, this specific spin state is systematically stabilized against the other [153, 154]. The main purpose of this section lies again on the agreement between both methods, but also the effects of the underlying spin-state structure on the coupling constants was of interest. This is especially important for the Green's-function approach, since it is applied on one spin

state and therefore no structural relaxation effects can be taken into account.

Because the Green's-function approach needs the definition of the spin centers, a Mulliken local spin analysis is performed for each compound, to investigate if the spin remains on the spin centers or if it is reduced, meaning a higher degree of spin delocalization onto adjacent atoms, which could falsify the obtained magnetic coupling constants for the Green's-function approach. The local spin analysis reveals that the spins are very close to the ideal spins given in Figure 4.3 and are therefore not discussed explicitly but they are given in Figure A.3 in Appendix A.

The magnetic exchange coupling constants calculated with different exchange-correlation functionals are given in Figure 4.4 for the structures optimized in the ferromagnetically and in the antiferromagnetically coupled BS determinant. As expected, the structures with an antiferromagnetic ground state optimized for the BS spin configurations are coupled more strongly antiferromagnetic than the systems optimized in the high-spin state. Also the magnetic exchange coupling constants calculated for the ferromagnetically coupled $[Mn_2(\mu-OMe)_2(HL)_4]$ complex are stronger for the structure optimized in the high-spin state than for the BS structure. The coupling constants obtained within the BS approach with LC-ω-PBE for this system are strongly overestimated for both spin-state structures compared with the results produced by the other functionals. The same overestimation is also found for the single-point calculations performed on the BS structure of the $[V_2(\mu-O\text{-}Me)_2(O)_2(ma)_2]$ complex characterized by Sun and coworkers [155] and described with non-collinear DFT by Peralta and coworkers [123]. The J_{Green} (F) values are in the order of the other functionals, therefore the problem may arise from the BS-determinant in those cases.

The same qualitative trends are found for the BS formalism and for the Green's-function method applied to the high-spin state (J_{Green} (F), red). Only the results obtained from the Green's-function approach applied to the BS determinants (J_{Green} (AF), black) give magnetic exchange coupling constants which deviate in most cases quantitatively (e.g. for the bis-vanadocenyl complex , where the J_{Green} (AF) values are between -0.12 kJ/mol and -0.25 kJ/mol, which in combination with the very small J_{Green} (F) and J_{BS} values leads to a large relative deviation) or even qualitatively (e.g. for $[Mn_2(\mu-OMe)_2(HL)_4]$) from those obtained from the BS approach. It is interesting that for the $[V_2(\mu-O\text{-}Me)_2(O)_2(ma)_2]$ complex, which was studied by Peralta and coworkers [123], J_{Green} (F) and J_{Green} (AF) are in good agreement with each other. Because the non-collinear DFT calculations do not show any deviations from the cosine behavior for all complexes studied in this section, the problems might be related to the BS determinant itself.

For nearly all systems the coupling constants J_{Green} (F) for the pure functionals (BP86 and PBE) are rather comparable with the $J_{BS,projected}$ values (green bars), while the coupling constants obtained for the hybrid functionals as TPSSH and B3LYP are comparable to the unprojected values $J_{BS,unprojected}$. The same is true for the LC-ω-PBE functional for which the exchange coupling from the

Green's-function approach is always much weaker than the coupling predicted by the BS approach. A more detailed discussion of these relations is given at the end of the next section (Figure 4.9).

4.3 Larger systems with Delocalized Spins

In this part of the work, the focus lies on systems with a higher degree of spin delocalization. This is interesting, since it is questionable if the metal centers are still a good choice for the definition of the magnetic sites, if the spin is transferred to adjacent atoms.

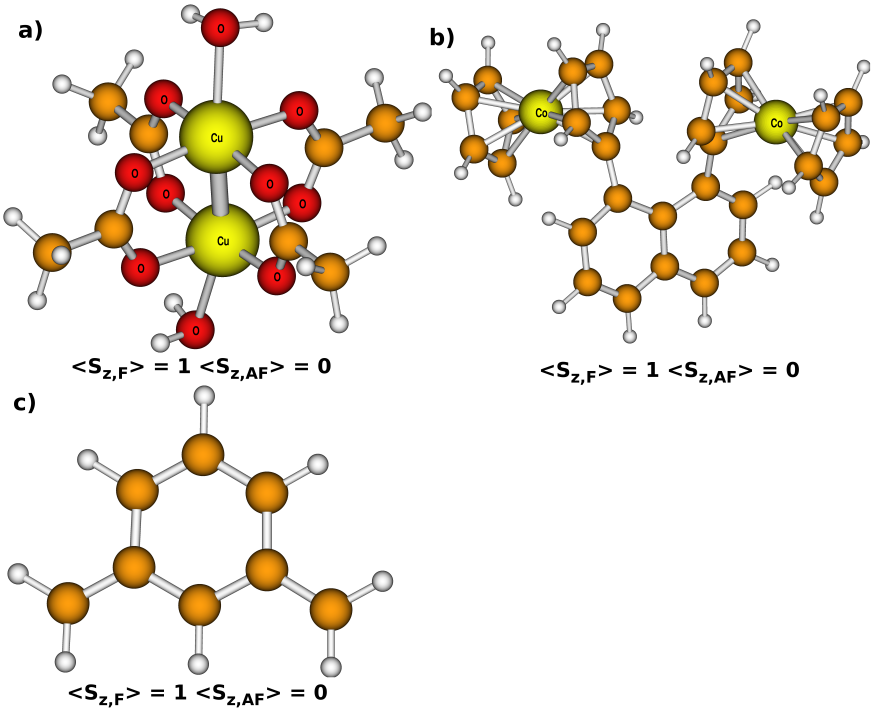

Figure 4.5: Structures and ideal $\hat{S}_z$ expectation values in both spin states for systems with delocalized spins optimized in the high-spin state (BP86/def-TZVP). a) Tetra-μ-acetato-diaqua-dicopper(II); $[Cu_2\,(Ac)_4\,(H_2O)_2]$ b) 1,8-Bis(cobaltocenyl)naphthalene; $\left[Co_2\left(\eta^5-Cp\right)_2\left(\mu-\eta^5-1,8-DCN\right)\right]$; 1,8-DCN=1,8-dicyclopentadienylnaphthalene dianion; Cp=Cyclopentadienyl anion, c) meta-dimethylenebenzene; meta-C_8H_8, d) para-dimethylenebenzene; meta-C_8H_8.

Therefore, two different complexes are chosen, a $[Cu_2\,(\mu-Ac)_4\,(H_2O)_2]$ complex and a $[Co_2\,(\eta^5-Cp)_2\,(\mu-\eta^5-1,8-DCN)]$ complex, both having formally one electron per metal center. Furthermore, a meta-substituted dimethylenebenzene diradical is investigated (see Figure 4.5) with a triplet high-spin and singlet low-spin state. All compounds are optimized in both spin states. For the high-spin structures non-collinear DFT calculations are performed, but due to convergence problems no data are obtained for the $[Cu_2\,(\mu-Ac)_4\,(H_2O)_2]$ complex. For the

$[Co_2(\eta^5-Cp)_2(\mu-\eta^5-1,8-DCN$ complex, the angular dependence shows a cosine shape, while for the meta-C_8H_8 the deviations are very strong (Figure A.6 in Section A).

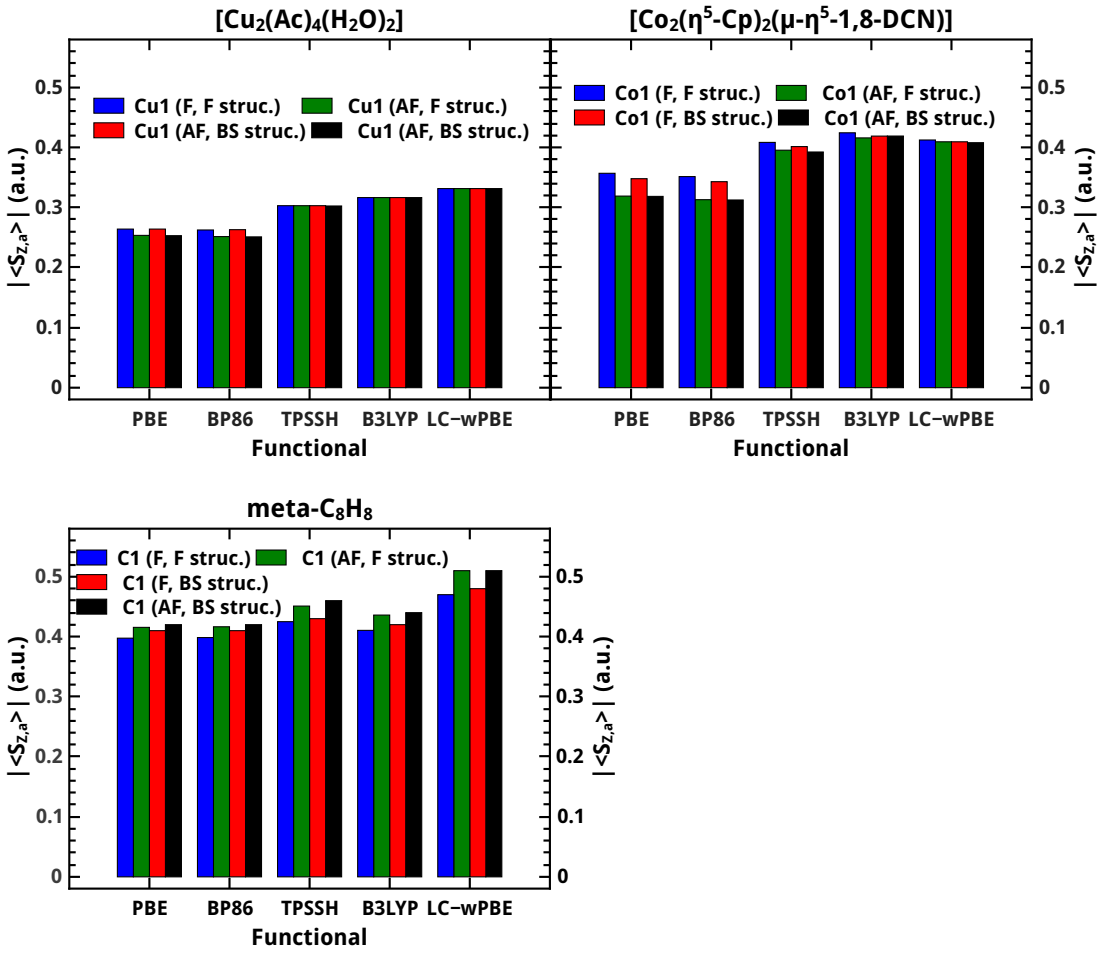

Figure 4.6: Mulliken local spins for the different compounds, spin states and spin-state structures given in Figure 4.5 for different functionals. In all cases only the spin of the main atom was taken into account. Basis set: def-TZVP.

Mulliken local spin analysis is performed to get information about the degree of spin delocalization in the molecules studied here. Since the deviations between the spin centers are small, the local spins in Figure 4.6 are given for one spin center only. It is found that the degree of spin delocalization increased from $[Co_2(\eta^5-Cp)_2(\mu-\eta^5-1,8-DCN)]$, where the spin on the Co(II) centers is roughly 0.4 a.u., to the $[Cu_2(Ac)_4(H_2O)_2]$ complex where the spin is only 0.3 a.u. on each copper atom. It can further be seen that the spin on the methylene carbon atoms in the meta-C_8H_8 diradical appears to be strongly localized, but there are significant negative and positive spin densities on the carbon atoms of the bridging benzene ring in the high-spin state, which are zero for the BS

solution (see Figure 4.7). For the other molecules in this section, the magnitude of the local spins remains nearly independent of the spin state. It can further be seen, that the spin on the metal centers is slightly lower for the BS determinants than for the high-spin states but for the hybrid functionals and LC-ωPBE the spins on the centers are very similar. The only exception is again meta-C_8H_8, where the local spin is slightly larger in the BS determinant.
The calculated magnetic coupling constants given in Figure 4.8 reveal that for the transition-metal complexes the coupling constants are in very good agreement with those obtained by the BS approach. For the dinuclear copper complex the same trends as for the transition-complexes, discussed in the previous section, are observed. As in the section before, all J_{Green} (F) values obtained for the 1,8-bis(cobaltocenyl)naphthalene complex with pure functionals are comparable with those obtained for the projected Noodleman expression, while a better agreement between J_{Green} (F) and the values of the unprojected formula is found when hybrid functionals are employed.

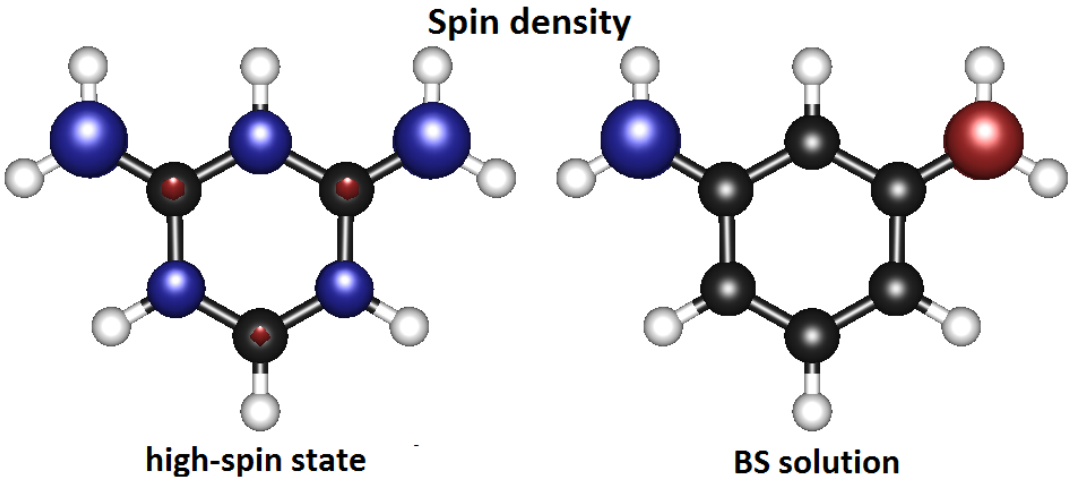

Figure 4.7: Spin density in the meta-C_8H_8 diradical for the high-spin state and the BS solution (BP86/def-TZVP). The single-point calculations are performed on top of the optimized high-spin structure.

For the 1,8-bis(cobaltocenyl)naphthalene complex qualitatively different coupling constants are obtained depending on the spin state, in which the structure is optimized. So ferromagnetic coupling is found for the high-spin structure, while antiferromagnetic coupling is found for the optimized structure of the BS solution. Even the coupling constants obtained from the BS approach by using the optimized spin-state structures (Appendix A, Table A.1) are ambiguous because the pure functionals, the B3LYP hybrid functional and LC-ωPBE give ferromagnetic coupling, while TPSSH predict antiferromagnetic coupling. Experimental studies on this system performed by Pagels and coworkers [136] agree with the TPSSH functional and reveals an antiferromagnetically coupled ground

state, which could be again related to problems with the description of the BS solution.

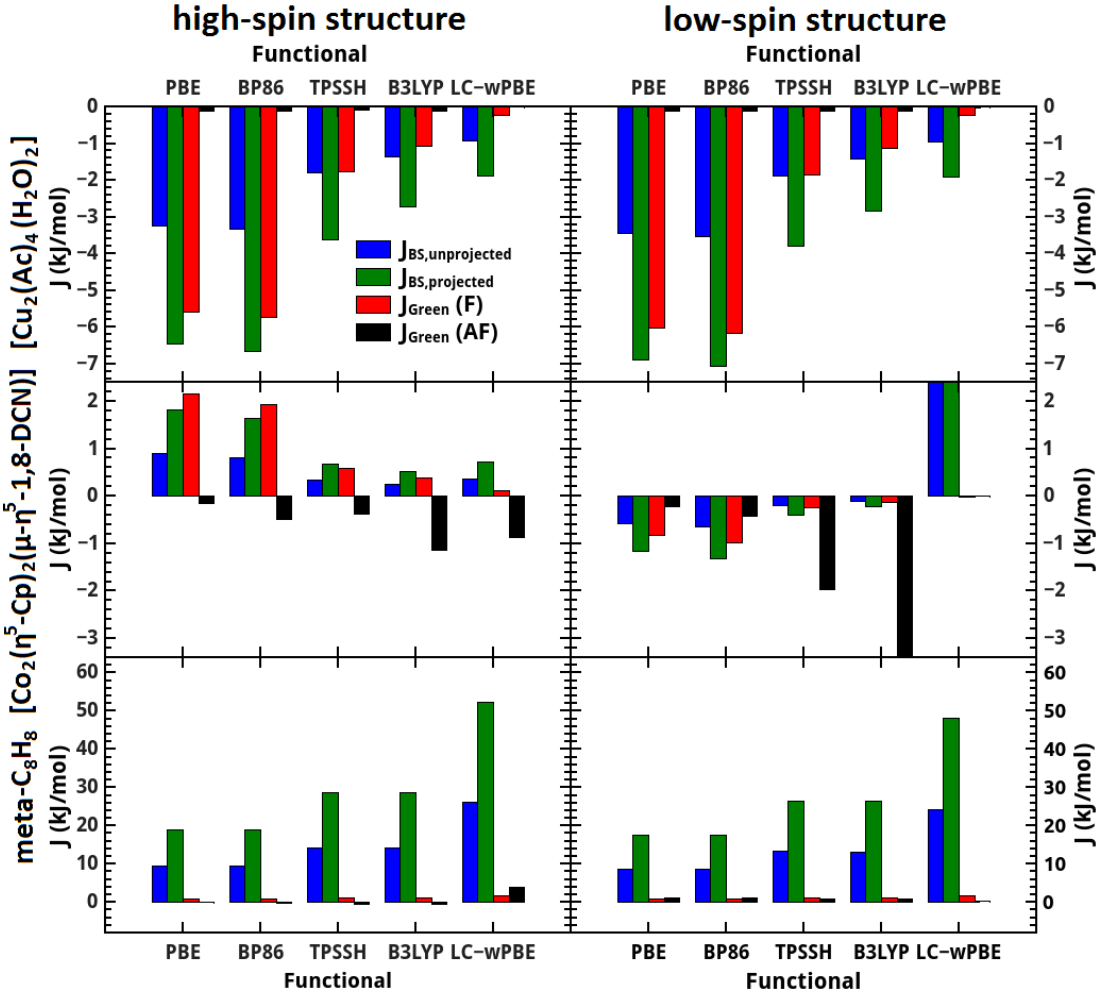

Figure 4.8: Magnetic coupling constants for the compounds given in Figure 4.5 for different spin-state structures and exchange-correlation functionals. For the low-spin structure of 1,8-bis(cobaltocene)naphthalene the LC-ωPBE BS values are larger than the displayed range. Basis set: def-TZVP.

To quantify the structural changes from one spin-state structure to the other several structural parameters for the 1,8-bis(cobaltocenyl)naphthalene complex and the 1,8-bis(vanadocenyl)naphthalene from the previous section are investigated, where the changes in the magnetic coupling constants are much smaller. Also the structural parameters in the $[Cu_2\,(Ac)_4\,(H_2O)_2]$ complex are investigated, where the coupling constants changes strongly. The structural parameters are not discussed explicitly here, but are given in Section A.6 of Appendix A for all structures from this and the previous section. However, this comparison reveals that the structural changes in the copper complex and the biscobaltocenyl complex are larger than in the vanadocenyl complex, where nearly all

parameters are constant independent of the spin-state structure. Consequently, the deviations in the magnetic exchange coupling constants correlate with the extent of the structural changes from one spin state to the other. This shows how crucial the effect of structural relaxation on the magnetic exchange coupling can be. It may be that molecules, for which different resonance structures can be written (for the 1,8-bis(cobaltocenyl)naphthalene complex, a closed-shell Lewis structure featuring two Co(I) centers can be formulated), are particularly susceptible to such effects, but this would have to be checked in future work.

For the structure optimized in the BS solution, it is observed for the LC-ωPBE functional, that the coupling constants obtained from the BS approach are strongly ferromagnetic which is not in agreement with all other functionals and the experimental measurements [136]. Such unreliable results were also found for the ferromagnetically coupled complex in the previous section. The J_{Green} (F) value is negative here but much too low, which could be again related to problems with the description of the BS solution.

For meta-C_8H_8 strong quantitative deviations from the BS approach are found, which might result from the strong spin delocalization onto the bridge. So it would be better to include the atoms on the benzene bridge, which is problematic because the magnetic sites share the same atoms on the bridge and therefore it is not possible to split them up properly.

Although there is no general scaling factor between the values obtained from the Green's-function approach and the BS formulas, it is interesting to see whether J_{Green} (F) values are generally closer to the values obtained from the spin projected or the unprojected BS approach ($J_{\text{BS,projected}}$ and $J_{\text{BS,unprojected}}$) for the different functionals employed. To quantify these observations the mean average percentage errors (MAPE) are calculated from all magnetic exchange coupling constants obtained for the compounds in this and the previous section,

$$\text{MAPE}\left(J_{\text{BS,projected}}\right) = \frac{100}{n}\sum_{t=1}^{n}\left|\frac{J_{\text{BS,projected}} - J_{\text{Green}}\ (\text{F})}{J_{\text{BS,projected}}}\right|, \tag{4.1}$$

$$\text{MAPE}\left(J_{\text{BS,unprojected}}\right) = \frac{100}{n}\sum_{t=1}^{n}\left|\frac{J_{\text{BS,unprojected}} - J_{\text{Green}}\ (\text{F})}{J_{\text{BS,unprojected}}}\right|. \tag{4.2}$$

MAPEs for J_{Green} (AF) are not calculated, since in most cases quantitative or even qualitative deviations between both approaches are found so that these values did not seem reliable at all. The MAPEs for J_{Green} (F) are given in Table 4.9. The meta-C_8H_8 diradical is not considered at all due to the problems with the definition of the magnetic sites. For LC-ωPBE, the results obtained for $[Mn_2\left(\mu-OMe\right)_2\left(HL\right)_4]$ (high-spin and BS structure), $[V_2\left(\mu-\text{O-Me}\right)_2\left(O\right)_2\left(ma\right)_2]$ (BS structure) and the $[Co_2\left(\eta^5-Cp\right)_2\left(\mu-\eta^5-1,8-DCN\right)]$ (BS structure) are not considered due to problems with the BS values.

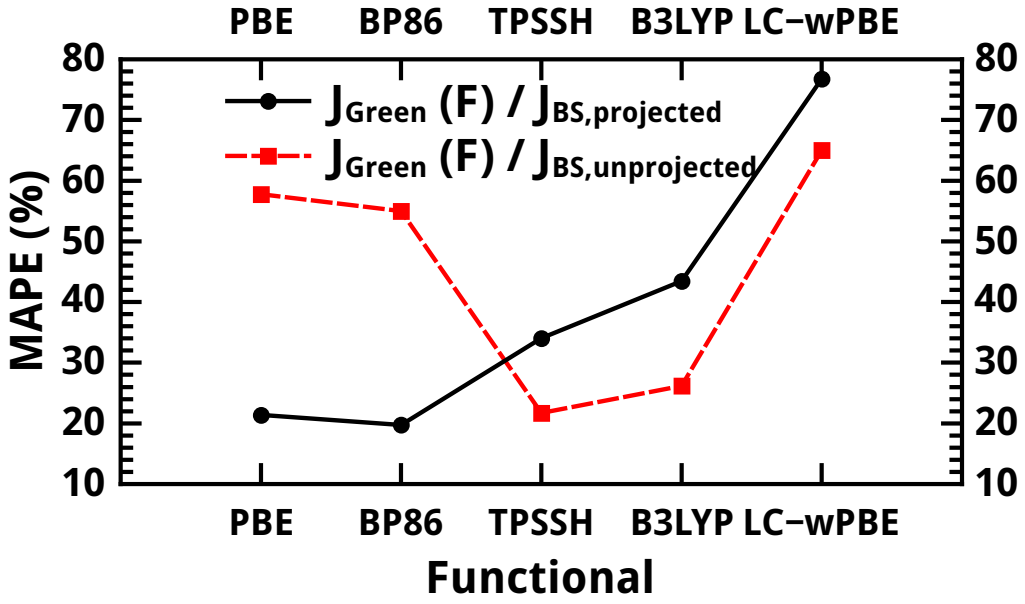

Figure 4.9: Mean absolute percentage errors (MAPEs) calculated according to Equations (4.1) and (4.2) for different exchange-correlation functionals considering all transition-metal complexes in this and the last chapter. Basis set: def-TZVP.

The MAPEs for the J_{Green} (F)/$J_{\text{BS,projected}}$ couple reveal that the values differ in only about 20% for the pure functionals as PBE and BP86, while MAPEs of roughly 35% for TPSSH, 43% for B3LYP and a MAPE of 77% for LC-ωPBE are found. For the J_{Green} (F)/$J_{\text{BS,unprojected}}$ couple the MAPEs are 58% and 55% for PBE and BP86, while the MAPEs for the hybrid functionals are about 20% (TPSSH: 21%; B3LYP: 26%) and 65% for LC-ωPBE. It can be seen that for pure functionals the J_{Green} (F) values approached those obtained with the projected formula, while the opposite is found for the hybrid and the LC-ωPBE functionals. These results suggest a systematic dependence on the applied exchange–correlation functional and possibly on the amount of exact Hartree–Fock exchange included (but further studies would be needed for a more solid statement). In general, the LC-ωPBE functional gives the largest deviations between the Green's-function and the BS approach compared with all other functionals, since the exchange coupling is underestimated for most of the systems considered here.

4.4 Bond-Angle Dependence of Exchange Coupling Constants in Systems with Delocalized Spins

The Green's-function method was able to reproduce the trends obtained for the H_2 and the H−He−H molecules by the BS approach well, and therefore it is interesting to see if such structural correlations are that well described in transition-

metal complexes. It is known from literature [95, 156–159] that the magnetic exchange coupling in ligand-bridged dinuclear complexes strongly depends on the metal–ligand–metal angles. Therefore, the dependence of the magnetic exchange coupling constants on the Cu−O−Cu angle θ in a $[Cu_2(\mu{-}OH)_2Cl_4]^{2-}$ complex is evaluated. This complex was already studied in further depth by Hoffmann and Hay [95] and increasing antiferromagnetic coupling with increasing Cu−O−Cu angle is observed. Angles between 80° and 110° are investigated by varying the angle in steps of 2° (single-point calculations for 82°, 88° and 94° did not converge). All other structural parameters are fixed to the values employed by Hoffmann and Hay [95] and are given in the methodology. The local spin analysis (see Section A.7 in Appendix A) reveals that the spin is highly delocalized onto the ligands, so that only local spins between 0.23 and 0.3 a.u. remain on the copper atoms depending on the angle and the applied functional. In general, the local spins on the copper(II) centers increase slightly with increasing angle and an increasing amount of Hartree-Fock exchange. The LC-ωPBE functional gives the strongest localization on the copper(II) centers.

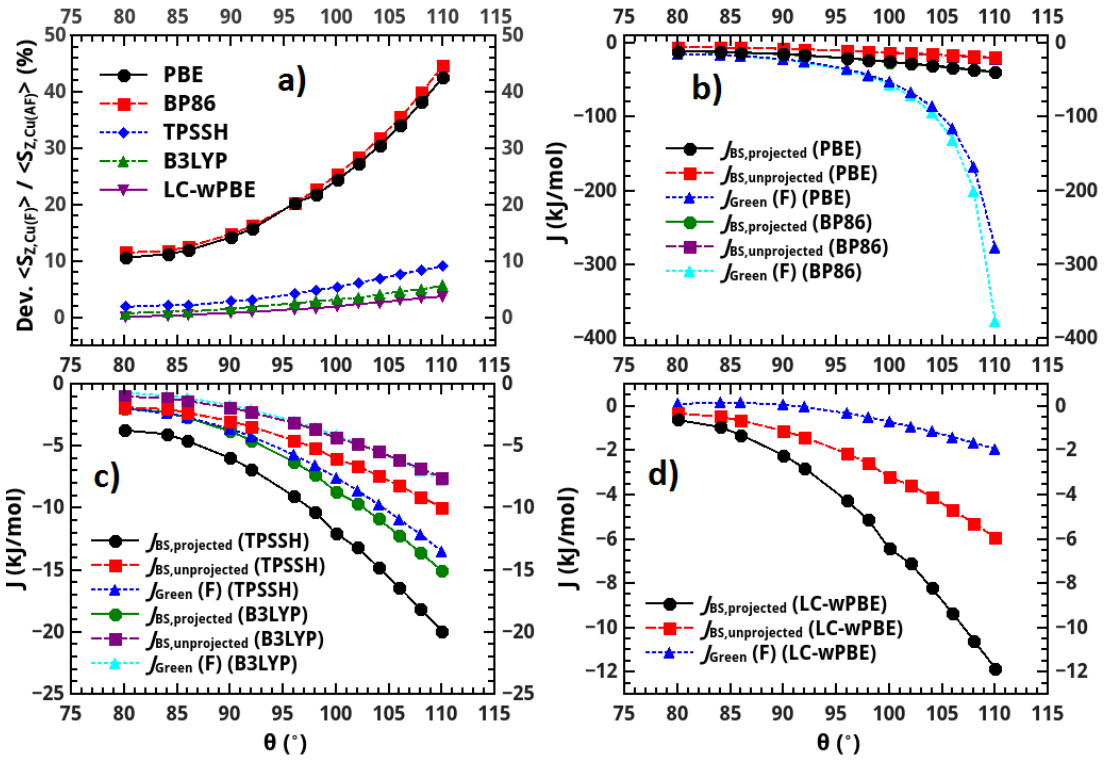

Figure 4.10: a) Deviations of the local spins on the copper(II) centers between the high-spin state and the BS solution. b)-d) Calculated magnetic exchange coupling constants obtained with different functionals as a function of Cu−O−Cu angle θ. Basis set: def-TZVP.

Following the HDvV Hamiltonian, only spin rotation is taken into account, therefore the deviations of the local spins' magnitudes on the copper atoms in

the high-spin state and the BS solution are given in percent (Figure 4.10). The deviations between both spin states are increased with increasing angle θ for the pure functionals as BP86 and PBE, while for TPSSH, B3LYP and LC-ωPBE the deviations are significantly smaller. These deviations in the local spins on the copper(II) centers have a drastic effect of the coupling constants calculated within the Green's-function approach, so that the antiferromagnetic exchange coupling is strongly overestimated by PBE and BP86 at higher Cu−O−Cu angles. For TPSSH and B3LYP the deviations between the local spins in both spin configurations are rather small, and the trends obtained by the BS approach are well reproduced by the Green's-function approach. Only the coupling constants calculated with LC-ωPBE are underestimated compared with the BS approach, which was observed for most complexes in this study.

4.5 Conclusions

In this chapter, an alternative method to the BS approach for the evaluation of magnetic exchange coupling constants was discussed which was based on Green's functions and which had been well established in the solid state community [49]. The advantage of this approach is that the coupling constant can be calculated from the high-spin state, circumventing the calculation of the BS determinant. In contrast to the conceptionally similar method of Peralta and coworkers [124], which solves the coupled-perturbed Kohn-Sham equations iteratively, the coupling constant in the Green's-function method can be obtained in one step, at the price of neglecting orbital relaxation. This approach was implemented in a post-processing tool JGreen for quantum chemistry program packages, and coupling constants were evaluated for several compounds and these values were compared to values obtained from spin-state energy differences within the BS approach.

For the simple model systems, the dihydrogen and the H−He−H molecules, it was found that the Green's-function approach gave the same qualitative trends as for the BS approach. While in the case of the dihydrogen molecule J_{Green} (F) is comparable with $J_{\mathrm{BS,unprojected}}$, and J_{Green} (AF) is comparable with $J_{\mathrm{BS,projected}}$; the opposite is found for H−He−H. Therefore no general scaling factor for comparing the BS and the Green's-function method could be given. The study on H−He−H further revealed that the Green's-function method is sensitive to changes in the magnitude of spins from one spin state to the other. In the BS approach the structures of both spin states can be optimized separately, while the Green's-function method is applied to one spin state only and no structural relaxation effects can be taken into account. Therefore several transition-metal complexes were investigated and the influence of the spin-state structures on the evaluated magnetic exchange coupling constants was discussed. For the coupling constants, the expected shift to stronger antiferromagnetic coupling was found, when the structures were optimized in the low-spin state approximated by the BS determinant. In the case of the 1,8–

bis(cobaltocene)naphthalene complex it was found that both methods gave a ferromagnetically coupled ground state for the high-spin structure and an antiferromagnetically coupled ground state for the BS structure. This demonstrates that in some cases structural relaxation effects are crucial to obtain qualitative agreement with the reference data and additionally reveals a potential pitfall of the Green's function approach. Except for some results obtained with the LC-ω-PBE functionals, where the coupling constants deviated strongly compared with all other functionals, a good qualitative agreement between J_{Green} (F) and the BS energy-difference formalism was found, while the J_{Green} (AF) values were in many cases in a qualitative disagreement with the BS approach. Non-collinear DFT calculations did not show any deviations from the cosine behavior of the HDvV Hamiltonian. Therefore, the problems seemed to be related to the BS determinant itself. From these observations, it can be concluded that the Green's function method should only be applied on the high-spin state and not on the BS determinant.

It could further be shown that the increasing delocalization of the spin density in those systems did not drastically affect the calculated magnetic exchange coupling constants, as long the local spins' magnitudes remained the same for both spin states. A problematic issue were molecules such as the meta-dimethylenebenzene, where two magnetic sites share atoms on the bridge, so that a proper spatial definition of the two magnetic sites was no longer possible. Additionally, non-collinear DFT calculations revealed strong deviations from a cosine behavior of the energy as a function of the angle between the two local spins. The mean average percentage errors (MAPEs) suggest that the Green's-function coupling constants obtained for the pure functionals (PBE and BP86) were rather comparable with the $J_{\mathrm{BS,projected}}$ values, while those obtained from the hybrid functionals (such as TPSSH and B3LYP) were rather comparable with the $J_{\mathrm{BS,projected}}$ values.

Also the bond-angle dependence of the magnetic exchange coupling constants in a dinuclear copper(II) complex was investigated, to see if the Green's function method is able to reproduce the structure–property correlations obtained from the BS approach. Although only half of the spin remained on the copper(II) centers, the trends predicted with the Green's function approach were in very good agreement with the BS approach for TPSSH and B3LYP. Strong deviations for BP86 and PBE due to the deviations in the local spins in the high-spin state and the BS solution were found, which violated the picture of local spins of fixed length assumed in the Heisenberg–Dirac–Van Vleck Hamiltonian.

The summarize, applied to the high-spin state, the Green's function method gives qualitative agreement with the results obtained with the BS approach and therefore constitutes a good alternative method with reduced computational cost. The drawbacks are that no orbital relaxation and structural relaxation effects are taken into account. For future work, it appears worthwhile to focus more on the problems concerning the description of magnetic exchange coupling constants in organic radicals. Since magnetic exchange coupling constants can

be decomposed into pairs of α- and β-spin orbitals within the Green's function method, it is also interesting to test its applicability as a tool for the analysis of exchange pathways [122, 160–162], which is done in Chapter 5. This may be relevant for the design of new molecular magnetic systems or materials.

5. Automated Exchange Pathway Analysis in Spin-Coupled Systems

In this chapter, the exchange pathways in two transition-metal complexes are discussed, which were previously analyzed in the literature based on visual inspection of the orbitals. The first system chosen is a $[Cu_2(OH)_2Cl_4]^{2-}$ model complex analyzed by Hay and coworkers [95] in order to evaluate the dependence of J on the Cu(II)–O–Cu(II) angle (compare Section 3.3). Further, a dinuclear Mn(III) complex, characterized by Brunhold and coworkers [122] by is considered.

5.1 A Model System with One Unpaired Electron per Spin Center: $[Cu_2(OH)_2Cl_4]^{2-}$

The exchange spin coupling in the $[Cu_2(OH)_2Cl_4]^{2-}$ complex is investigated as a function of the Cu–O–Cu angle θ (Figure 5.1), as analyzed by Hay *et al.* [95].

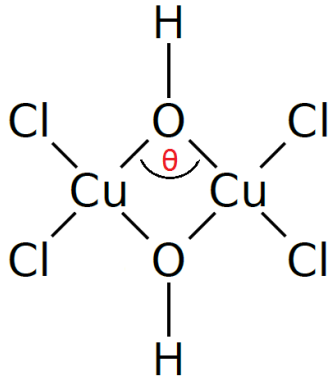

Figure 5.1: Lewis structure of the $[Cu_2(OH)_2Cl_4]^{2-}$ complex studied by Hay and coworkers [95]. θ denotes the angle varied in Figure 5.2.

The energy differences between the antibonding and bonding linear combinations of the magnetic orbitals, which are dominated by the copper $d_{x^2-y^2}$ orbitals, were calculated using the Hückel method, providing an analysis of the angular dependence of spin coupling in Ref. [95] (Equation (3.2)).
Here, this analysis is repeated with the Green's-function method (Equations (3.26) and (3.27)). The structural parameters are taken from Ref. [95], and single-point calculations with B3LYP/def-TZVP are carried out. This functional is

chosen, because in Chapter 4 a very good agreement between the BS approach and the Green's-function approach [163] was found, while BP86 showed larger deviations due to the decreasing spin density on the copper centers for the BS determinant.

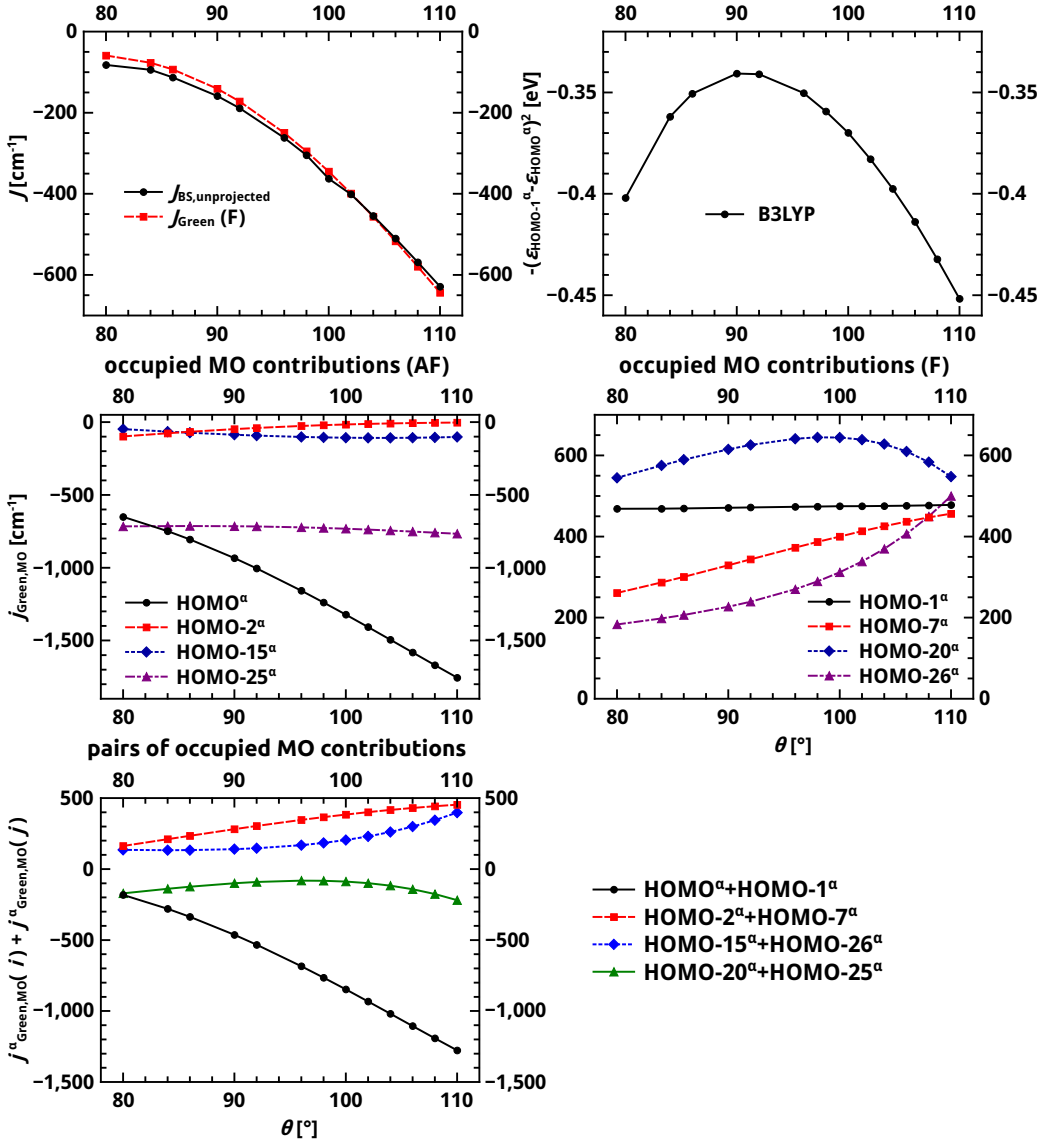

Figure 5.2: Exchange coupling constants obtained from the unprojected BS approach, $J_{\mathrm{BS,unprojected}}$, and from the Green's-function approach, J_{Green} (F) (top left), the negative square of the energy differences between the triplet HOMO-1$^{\alpha}$ and the HOMO$^{\alpha}$, being proportional to the antiferromagnetic contributions according to Equation (3.2) in the model of Hay and coworkers [95] (top right), and the ferromagnetic (middle left) and antiferromagnetic contributions (middle right) to the coupling constant evaluated from Equation (3.27). Furthermore, the sums over pairs from occupied-MO contributions are calculated (bottom-left). All calculations are performed with B3LYP/def-TZVP.

In Figure 5.2, the coupling constants obtained from the Green's-function approach, J_{Green} (F), and from the unprojected BS approach, $J_{\text{BS,unprojected}}$, (top left) are given as a function of the Cu−O−Cu angle θ. The coupling constants obtained from both approaches are in very good agreement, both are antiferromagnetic for all angles and increase in magnitude with increasing angle. Additionally, the negative square of the molecular orbital energy differences between the HOMO-1$^{\alpha}$ (bonding linear combination of magnetic orbitals) and the HOMO$^{\alpha}$ (antibonding linear combination) are given, which are proportional to the antiferromagnetic contributions to the coupling constant (top right in Figure 5.2).

The squared orbital splittings suggest a decrease in the antiferromagnetic contributions from 80° to 90°, and then increase again from 90° to 110° (Figure 5.2, top right). While the angular dependence observed between 90° and 110° is in agreement with the trend for the total exchange coupling constants, they deviate for the angles in the range between 80° to 90°.

The sum over all eight occupied α-orbital contributions, $j^{\alpha}_{\text{Green,MO}}(i)$, contributing more than 5% (Figure 5.2), is -141.9 cm^{-1} at an angle of θ=90°, which nearly perfectly matches the total value of the coupling constant of -140.9 cm^{-1} as obtained from the Green's-function approach. Both values are also in good qualitative agreement with the coupling constant of -158.8 cm^{-1}, obtained from the unprojected BS approach, which further validates an analysis of exchange spin coupling in terms of these eight contributions.

All of the eight MOs have $d_{x^2-y^2}$ contributions from the copper centers and p orbital character on the bridging oxygen atoms. However, it must be noted that the three highest-energy occupied orbitals have positive energies, indicating that the system is instable, which might be related to its model character. To illustrate that MOs energetically lying between the MOs shown in Figure 5.3 would not be chosen by visual inspection due to d orbitals involved, they are given in Appendix A. Half the MOs give rise to ferromagnetic contributions, and the other four MOs to antiferromagnetic contributions (Figure 5.2). The HOMO$^{\alpha}$ and the HOMO-1$^{\alpha}$ correspond to those discussed by Hay and coworkers [95]. In general, it can be seen that with increasing angles θ the antiferromagnetic contributions from the HOMO$^{\alpha}$ increase and dominate the spin coupling, while the contributions from the HOMO-1$^{\alpha}$ are ferromagnetic and do not change with increasing angle. However, at smaller angles, this may explain why the observed spin coupling deviates from the contributions calculated from the MO differences, the contributions from the HOMO$^{\alpha}$ are in the same order of magnitude as the antiferromagnetic and ferromagnetic contributions arising from lower lying MOs, which are not included in the model of Hoffmann.

To further analyze the different orbital contributions, it is worth looking explicitly at the main spin-flip excitations from α- to β-spin orbitals (Equation (3.26)) determining them (see Figure 5.3). All spin-flip excitations with a magnitude larger than 5% of the magnitude of the the occupied MO contributions are taken into account. The sum over these spin-flip excitations $j_{\text{Green}}(i,j)$ results

in a coupling constant of -142.0 cm^{-1} an angle of 90°, being again very close to the total coupling constant of -140.9 cm^{-1}.

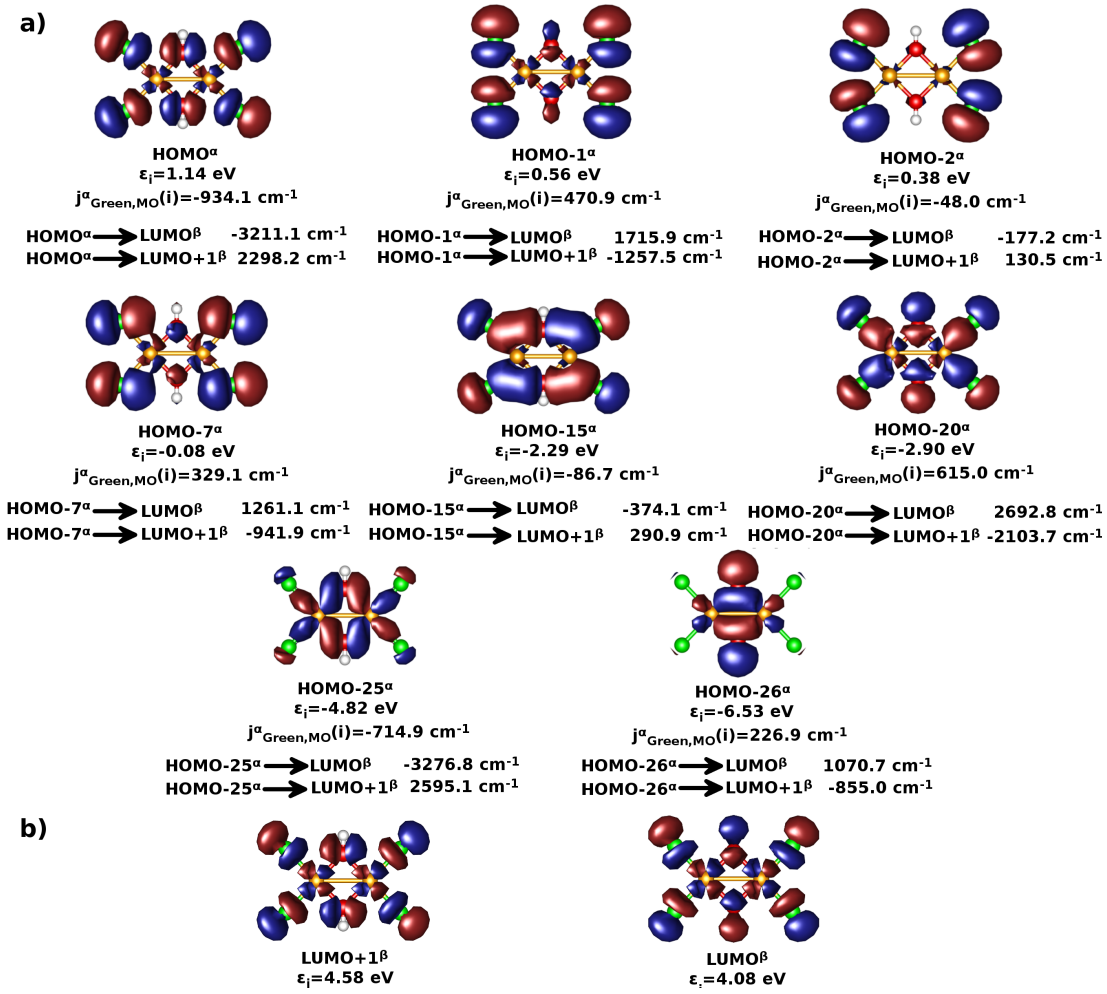

Figure 5.3: a) Occupied α spin orbitals giving the largest contributions $j^{\alpha}_{\mathrm{Green,MO}}(i)$ to the coupling constant for the high-spin state of the 90° structure of the $[Cu_2(OH)_2Cl_4]^{2-}$ complex calculated with B3LYP/def-TZVP. The largest spin-flip excitations $j_{\mathrm{Green}}(i,j)$ contributing to each are given below the MO plots, along with the energy difference between the two MOs. b) Main virtual β-spin orbitals involved in the spin-flip excitations.

All $j^{\alpha}_{\mathrm{Green,MO}}(i)$ values are mainly composed of spin-flip excitations from the occupied spin orbitals to the LUMO$^{\beta}$ and LUMO+1$^{\beta}$ (Figure 5.3). The LUMO$^{\beta}$ and the HOMO-1$^{\alpha}$ both feature bonding linear combinations of the metal d orbitals, while the LUMO+1$^{\beta}$ and HOMO$^{\alpha}$ show antibonding linear combinations. In all cases where the dominant pairs of molecular orbitals have the same type (antibonding or bonding combination of metal d orbitals), ferromagnetic contributions are obtained. The opposite is true if one of the spin orbitals involves a bonding and the other one an antibonding linear combination of the d orbitals. All contributions from an occupied spin orbital are dominated by

one ferromagnetic and one antiferromagnetic spin-flip excitation, which are in the same order of magnitude. The net contributions to the coupling constant appear to systematically correlate with the energetic gap between the occupied and the virtual orbital. This finding is in line with the findings for the dihydrogen molecule (Section 3.3).

From the analysis of the spin-flip excitations in the H_2 molecule (Section 3.4.3), it can be concluded that in order to obtain results comparable to the ansatz by Hay *et al.* [95], the sums of spin-flip excitations between pairs of bonding and antibonding linear combinations (one pair occupied and one pair virtual) must be taken into account. In this case, this is simply the sum over pairs of contributions arising from occupied MOs, which can be distinguished by the MO contours of the occupied MOs. For the eight MO contributions, four of such pairs could be formed for which the contributions to the coupling constants are summed up (Figure 5.2, middle). While the HOMO$^\alpha$/HOMO-1$^\alpha$ gives the leading (monotonically increasing) antiferromagnetic contributions, there is one weaker antiferromagnetic contribution from the HOMO-20$^\alpha$/HOMO-25$^\alpha$ pair, which give the same trend as observed for the Hoffmann model in this case, but however the agreement between the Hoffmann model is not given due to the importance of different pairs of MOs in this case.

5.2 A Model System with Multiple Unpaired Electrons per Spin Center: $[\mathbf{Mn_2O\,(O_2CH)_2}]^{2+}$

In this section, the exchange pathways in a $[Mn_2O\,(O_2CH)_2]^{2+}$ model system with four unpaired electrons per spin center is discussed, for which Brunhold et al. [122] analyzed the exchange pathways in terms of molecular orbitals, concluding that the weak antiferromagnetic exchange spin coupling results from a cancellation of ferromagnetic and antiferromagnetic contributions. To be able to directly compare the obtained results to those of Solomon, the same coordinates and coordinate frames as in the analysis in their work (Figure 5.4) are employed.

The coupling constants are obtained employing BP86/TZP on the structure given in Ref. [122]. These settings are equal to those of Solomon and coworkers, except that no C_{2v} symmetry and the frozen-core approximation is considered. The BS and Green's function coupling constants are in qualitative agreement with the results obtained in Ref. [122], and weak antiferromagnetic coupling is found in all cases (Table 5.1). Nevertheless, the values differ quantitatively. While $J_{\mathrm{BS,projected}}$ is found to be much lower than in Ref. [122], J_{Green} (F) is nearly three times larger than that value. This large percentage error is a consequence of the very small absolute values, and the difference between Ref. [122] and this work may be attributed to the all-electron basis set employed here, justifying an analysis of the exchange pathways in this system.

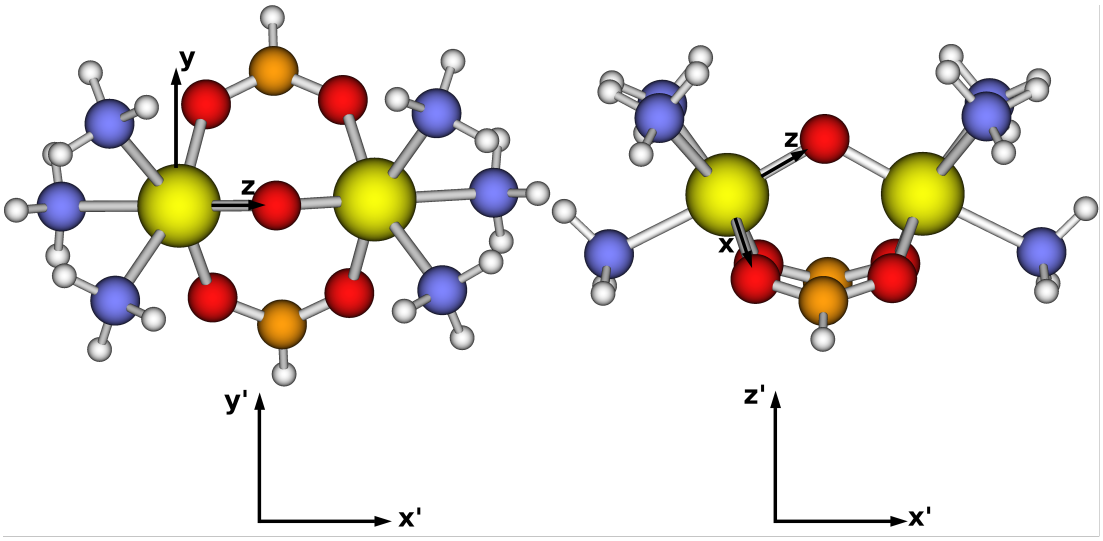

Figure 5.4: Local coordinate frames of the $[Mn_2O\,(O_2CH)_2]^{2+}$ complex for the MO analysis, following the work of Solomon and coworkers [122] in which x, y, and z refer to the Mn centers, and x',y', and z' refer to the bridging oxo-ligand.

In this analysis, only the molecular orbital contributions with a magnitude larger than or equal to 10 cm^{-1} are taken into account (see Figures 5.5 and 5.6). By summing up those contributions, a slightly ferromagnetic coupling constant is obtained (8.5 cm^{-1}), in disagreement with the total coupling constant, but still small enough to be considered reasonable. As in the previous section, all spin-flip excitations $j_{\mathrm{Green}}(i,j)$, needed to reproduce the $j^{\alpha}_{\mathrm{Green,MO}}(j)$ within an error range of 15%, are given in Figures 5.5 and 5.6 below the corresponding MO plots. Compared to the dinuclear copper(II) complex discussed in the previous section, there is a larger number of significant contributions to the coupling constant. This is to be expected since it possesses eight unpaired electrons instead of two as in the $[Cu_2(OH)_2Cl_4]^{2-}$ system.

Table 5.1: Heisenberg coupling constants obtained from single-point calculations on the structure provided by Solomon and coworkers [122] with BP86/TZP (our work: C_1 symmetry, all-electron; Brunhold: C_{2v}, effective core potential), employing the spin-projected BS approach, and the Green's-function approach applied to the high-spin state. The value obtained by Solomon [122] given for comparison, and the value J obtained as the sum over the largest occupied-orbital contributions as shown in Figures 5.5 and 5.6, $\tilde{J}_{\mathrm{Green}}$ (F), given for comparison.

Method	J
$J_{\mathrm{BS,proj}}$	-0.4 cm^{-1} (-0.005 kJ/mol)
J_{Green} (F)	-14.3 cm^{-1} (-0.17 kJ/mol)
J_{Solomon}	-5 cm^{-1} (-0.06 kJ/mol)
$\tilde{J}_{\mathrm{Green}}$ (F)	8.5 cm^{-1} (0.10 kJ/mol)

In order to study the exchange pathways in this compound within the Green's-

function approach, the contributions of spin-flip excitations between MOs and the d orbital contributions on the Mn(III) centers to these MOs of the high-spin states have been analyzed in order to identify the exchange pathways.

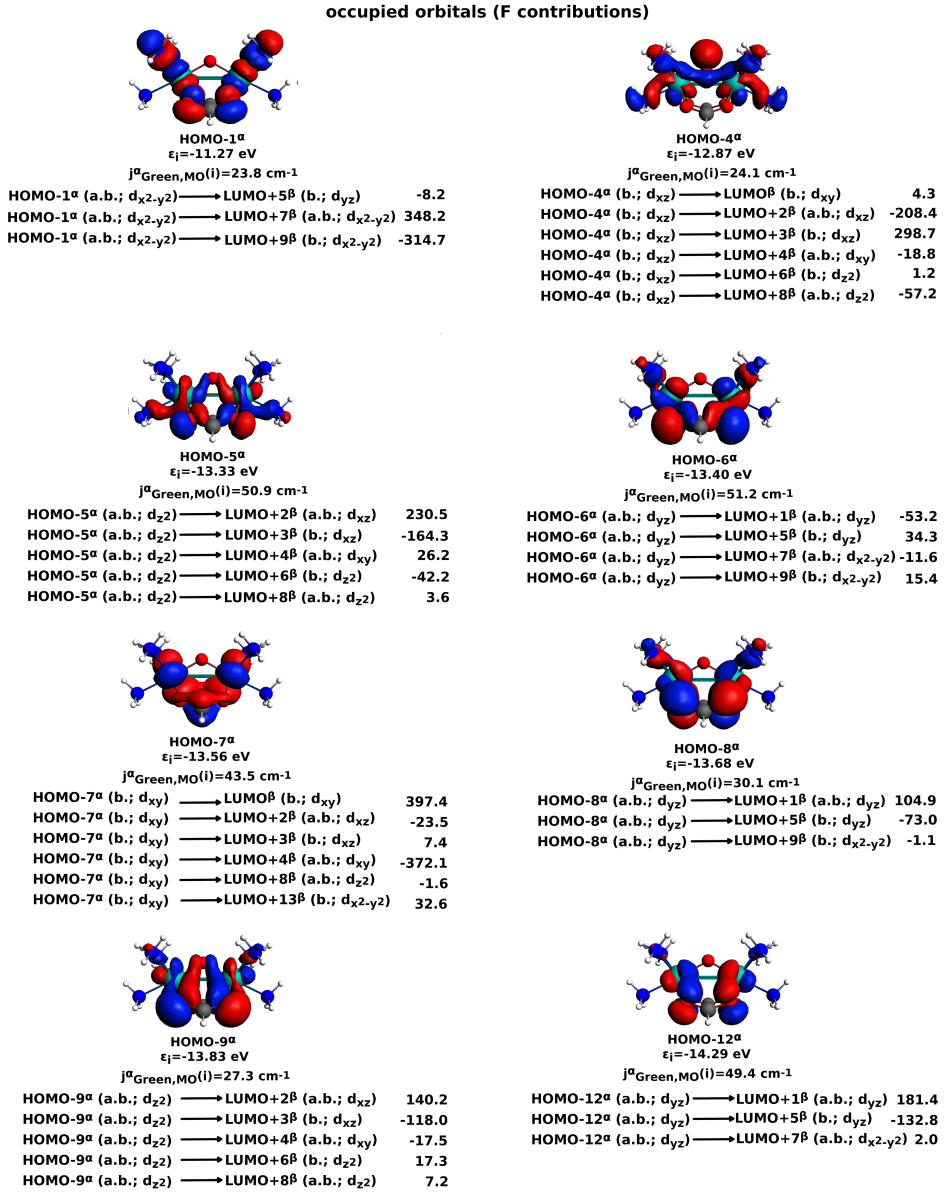

Figure 5.5: Occupied α spin orbitals giving the largest ferromagnetic contributions $j^{\alpha}_{\mathrm{Green,MO}}(i)$ to the coupling constant for the high-spin state of the $[\mathrm{Mn_2O\,(O_2CH)_2}]^{2+}$ complex calculated with BP86/TZP, contributions from occupied molecular orbitals to the coupling constant $j^{\alpha}_{\mathrm{Green,MO}}(i)$, and the largest spin-flip excitations corresponding to these contributions $j_{\mathrm{Green}}(i,j)$, both given in cm^{-1}. The corresponding β spin orbitals are given in Figure 5.7. The abbreviations b. and a.b. in parenthesis refer to the character, bonding and antibonding, respectively, and the d values refer to the kind of d orbital contributions on the Mn(III) center.

This is in the spirit of the argumentation by Brunhold et al., who analyzed the interactions between the α and β spin orbitals of the BS determinant.

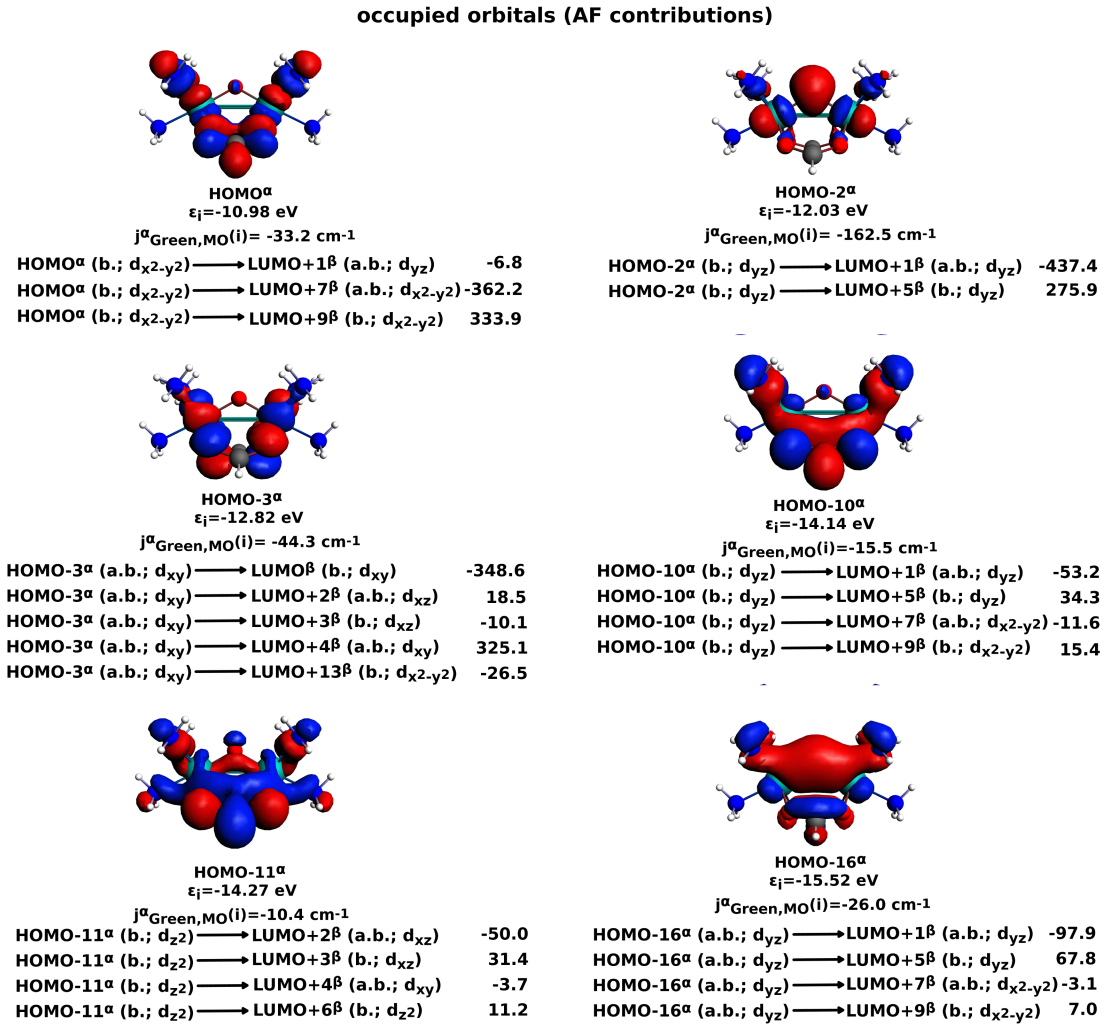

Figure 5.6: Occupied α spin orbitals giving the largest antiferromagnetic contributions $j^{\alpha}_{\mathrm{Green,MO}}(i)$ to the coupling constant for the high-spin state of the $[\mathrm{Mn_2O\,(O_2CH)_2}]^{2+}$ complex calculated with BP86/TZP, contributions from occupied molecular orbitals to the coupling constant $j^{\alpha}_{\mathrm{Green,MO}}(i)$, and the largest spin-flip excitations corresponding to these contributions $j_{\mathrm{Green}}(i,j)$, both given in cm^{-1}. The most important β spin orbitals are given in Figure 5.7. The abbreviations b. and a.b. in parenthesis refer to the character, bonding and antibonding, respectively, and the d values refer to kind of d orbital contributions on the Mn(III) center.

It should be noted that the BS orbitals approximately refer to the magnetic orbitals, while the high-spin orbitals discussed here are usually linear combinations of these orbitals.

In analogy to the Hoffmann system discussed in Section 5.1, the main spin-flip excitations occur between MOs involving the same d orbital contributions on the

Mn(III) centers, which differ in their sign and almost cancel (Figures 5.5 and 5.6). However, just simply summing up the contributions from occupied spin orbitals as for the H_2 and the dinuclear Cu(II) complex in the previous section is not possible because the spin-flip excitations involve virtual MOs with different d orbital contributions from the metal center and consequently the spin-flip excitations must be investigated separately. The dominating spin-flip excitation always originates from the pair of MOs being closer in energy. In addition, also spin-flip excitations between MOs with different kind of d orbital contributions are obtained. This new feature appears as a consequence of the larger number of formally singly occupied d orbitals in the system (eight unpaired electrons) compared to the dinuclear copper(II) complex.
The ferromagnetic contributions $j^{\alpha}_{\mathrm{Green,MO}}(i)$ from occupied MOs are comparable in size, and no leading contribution is found (Figure 5.5), while the antiferromagnetic contribution from the HOMO-2^{α} is significantly larger than all other antiferromagnetic contributions (Figure 5.6). The spin-flip excitations corresponding to the HOMO-2^{α} only include MOs with d_{yz} character on the Mn(III) center. This is in agreement with Ref. [122], where it is argued that the exchange pathway involving the two d_{yz} spin orbitals gives the largest contribution (which is antiferromagnetic).

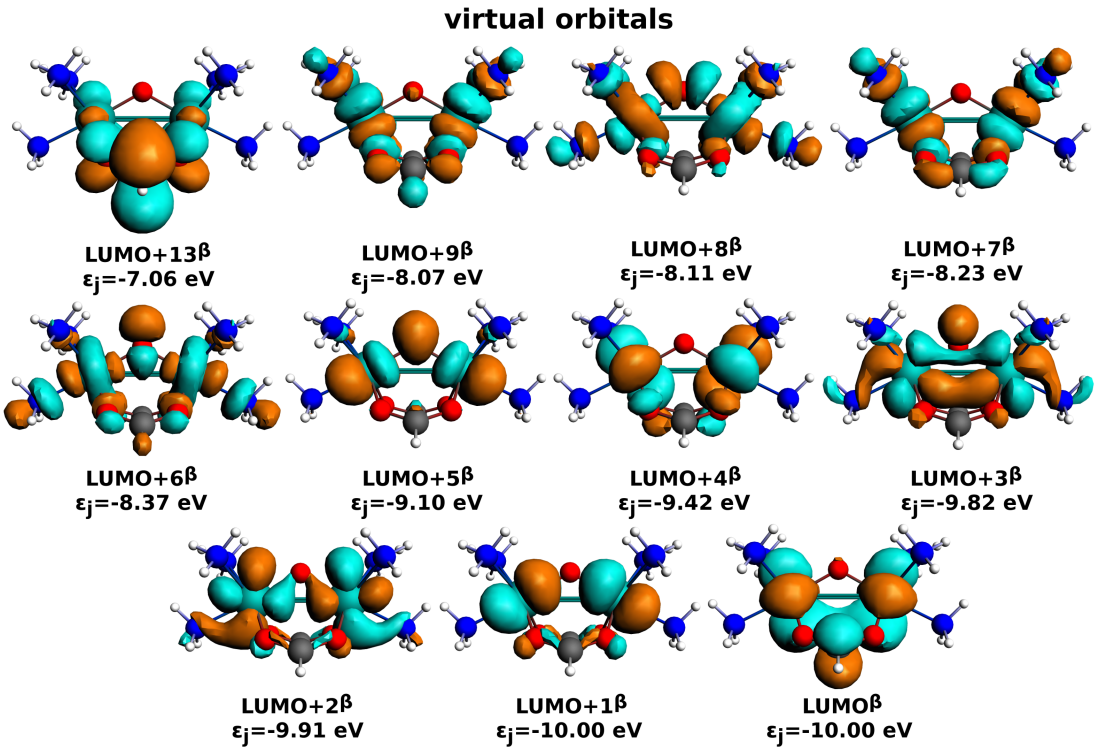

Figure 5.7: Virtual molecular orbitals for the the high-spin state of the $[Mn_2O\,(O_2CH)_2]^{2+}$ complex, involved in the largest spin-flip excitations (see Figures 5.5 and 5.6), calculated with BP86/TZP.

As concluded by Brunhold and coworkers [122], the symmetric d_{yz} orbital pathways (arising from spin-flip excitations between d_{yz} type orbitals) give the largest antiferromagnetic contribution. Also, the mixed ferromagnetic exchange pathway arising from spin-flip excitations between d_{z^2}- and d_{xz}-based MOs gives a ferromagnetic contribution to the coupling constant, as suggested in Ref. [122] (Table 5.2).

Table 5.2: Sums over the largest spin-flip excitations $j_{\mathrm{Green}}(i,j)$ classified according to the d orbital contributions on the manganese centers in the MOs. The values are given in cm^{-1}, and the electronic structure of the high-spin state is obtained with BP86/TZP. The postulated exchange pathways in Ref. [122] are given for comparison, where a "+" indicates a ferromagnetic contribution, a "−" indicates an antiferromagnetic contribution, and a "0" means that these exchange pathways were not considered by Brunhold et al..

spin-flip excitation type	$\sum_{type} j_{\mathrm{Green}}(i,j)$	Ref. [122]
$d_{x^2-y^2} \rightarrow d_{yz}$	1.1	0
$d_{x^2-y^2} \rightarrow d_{yz}$	−14.9	0
$d_{x^2-y^2} \rightarrow d_{x^2-y^2}$	5.3	0
$d_{yz} \rightarrow d_{yz}$	−71.2	−
$d_{xy} \rightarrow d_{xy}$	1.9	0
$d_{xy} \rightarrow d_{xz}$	−22.2	0
$d_{xy} \rightarrow d_{x^2-y^2}$	6.1	0
$d_{z^2} \rightarrow d_{xz}$	17.5	+
$d_{z^2} \rightarrow d_{z^2}$	−41.0	0
$d_{xz} \rightarrow d_{xz}$	90.4	−
$d_{xy} \rightarrow d_{z^2}$	48.3	0
$\sum$	11.3	−

Brunhold et al. further concluded that d_{xy}- and $d_{x^2-y^2}$-based MOs do not contribute due to their symmetry. This is indeed true for the symmetric spin-flip excitations between d_{xy}-based MOs, and for those between $d_{x^2-y^2}$-based MOs [122]. Nevertheless, there are significant contributions from spin-flip excitations involving $d_{x^2-y^2}$- or d_{xy}-based MOs and MOs including other d orbital contributions. However, the contributions from symmetric $d_{xz} \rightarrow d_{xz}$ spin-flip excitations, claimed as weakly antiferromagnetic by Brunhold and coworkers [122], are found to give the largest ferromagnetic contributions to the coupling constant. The antiferromagnetic contributions from symmetric exchange pathway involving spin-flip excitations between d_{z^2}-based MOs were also not mentioned in Ref. [122]. Despite these differences, our analysis confirms that the weak exchange-spin coupling in the dinuclear Mn(III) complex results from cancellations of different exchange pathways, and that the ferromagnetic contributions are determined by $d_{yz} \rightarrow d_{yz}$ interactions.

5.3 Conclusions

The aim of this chapter was to probe the Green's-function approach, derived by Lichtenstein and coworkers [32,49] and recently rederived based on the work by Ozaki and coworkers [127] employing local projection operators [163], as a method for the investigation of exchange pathways contributing to spin coupling in transition-metal complexes. Following Ref. [163], all analyses were carried out for the high-spin determinant.

It could be shown that the model derived by Hay and coworkers [95] is equivalent to the Green's-function approach, that the MO energy differences determine how large a contribution from a given occupied spin orbital is, and that the type of linear combinations of the metal d orbitals, bonding or antibonding, gives the sign of a contribution (as long as the unoccupied β MOs are higher in energy than the occupied α MOs). Two complexes were investigated, and the results were compared to findings from the literature. For the dinuclear copper(II) complex earlier studied by Hay *et al.* [95], the Green's-function method confirmed that the most significant contributions indeed arose from $d_{x^2-y^2}$-based molecular orbitals. Further, for small Cu−O−Cu angles the two-orbital model employed in Ref. [95] disagreed with the total exchange coupling constant, which probably originates from the lower lying MOs not considered in this model, which had the same order of magnitude as those of the HOMO$^\alpha$ and HOMO-1$^\alpha$. MO contributions were further decomposed into sums of occupied spin-up (α) MOs and unoccupied spin-down (β) MOs (spin-flip excitations). They were dominated by the pair of occupied and virtual orbitals that is closest in energy. Spin-flip excitations between bonding and antibonding linear combinations or vice versa always gave antiferromagnetic contributions, while spin-flip excitations between bonding and bonding, and between antibonding and antibonding linear combinations gave rise to ferromagnetic contributions. These "rules" were analyzed in more detail for a H_2 molecules in a minimal basis in Section 3.4.3.

Because the dinuclear manganese(III) complex studied by Brunhold and coworkers [122] includes four unpaired electrons on each spin center, the number of relevant contributions from occupied MOs was much higher than for the copper(II) complex. In addition to the spin-flip excitations between MOs involving the same type of d orbital contributions, also mixed exchange pathways were observed. It was demonstrated that the spin-flip excitations could be used to evaluate the contributions from different exchange pathways. Further, it was found that the results obtained in that way agreed with several of the conclusions by Brunhold and coworkers [122], based on visual inspection of the MOs from the BS determinant. The contributions obtained from the spin-flip excitations between d_{xz}-based MOs deviated qualitatively from the predicted values, and a strong ferromagnetic contribution was found, rather than the weak antiferromagnetic contribution mentioned by Brunhold et al. [122]. Additionally, considerable contributions from spin-flip excitations, not reported by the authors, were found (e.g. $d_{z^2} \rightarrow d_{z^2}$).

Overall, the results obtained from the Green's-function approach are considered to be in sufficiently good qualitative agreement with the results discussed in the literature, which suggests that it constitutes a useful method for the automated analysis of exchange pathways. In future studies, other interesting problems, as for example the description of the spin coupling in molecular chains on surfaces, will be addressed. Also the π-stacked bismetallocene complexes synthesized and characterized in the group of Jürgen Heck at the University of Hamburg, which are discussed in the next chapter, are interesting test cases for the Green's-function approach. There, it is used to determine the through-space and through-bond contributions by decomposition of the coupling constant into MO contributions.

6. Through–Space vs. Through–Bond Coupling in π-Stacked Bismetallocene Complexes

In this chapter, the spin coupling in π-stacked bismetallocene complexes differing in the bridge and the in metal centers (Figure 6.1) is investigated. In the following, the notation provided in Figure 6.1 is employed, which consists of the element symbols of the metals, and the following abbreviations for the bridges: NP=naphthalene, ANPA=acenaphthalene, and ANPY=acenaphthylene. These systems were synthesized and characterized by the Heck group [111,136,137,141] in the framework of the SFB 668 at the University of Hamburg and could potentially be applied as molecular analogues to atomic spin leads as used in the setup experimentally realized by Khajetoorians and coworkers [3]. These systems are also an interesting test case for the Green's-function approach because there are two potential contributions to spin coupling, through-space and through-bond mediated by the bridge. It was shown theoretically that such through-space interactions are most often antiferromagnetic, and ferromagnetic spin coupling only occurs when positive and negative regions of orbital overlap cancel each other [164–166]. Similar studies were also carried out to investigate the through-bond and through-space contributions to electron transfer biomolecules, where the through-space contributions were significant in cases of very long through-bond pathways [167–171]. Additionally, the influence of the topology of the bridge is taken into account here, with special emphasis on the transition from alternant to non-alternant hydrocarbons and the resulting competition of different exchange pathways. Also a naphthalene-bridged tetranuclear cobaltocene complex is taken into account to see if the Green's-function approach also works properly in the case of metallocene systems with more than two spin centers and if the results for the dinuclear complexes are transferable to larger spin chains potentially suitable for all-spin logic gates.

The structural and magnetic properties of the Co–NP–Co complex were already studied experimentally by Pagels and coworkers [136], and in complement to the magnetic measurements, also DFT calculations were carried out for the system with and without bridge. These calculations showed that the removal of the bridge leads to a decrease of the antiferromagnetic spin coupling by a factor of three [136]. Also the permethylated analogue of the Ni–NP–Ni system was the subject of DFT calculations and the removal of the bridge lead to a slight increase in the spin coupling [111]. However, this way to investigate the bridges' influence on the spin coupling has the disadvantage that it neglects the electronic influence of the bridge on the spin centers, which can be taken into

account by the Green's-function approach as presented in Section 3.4.

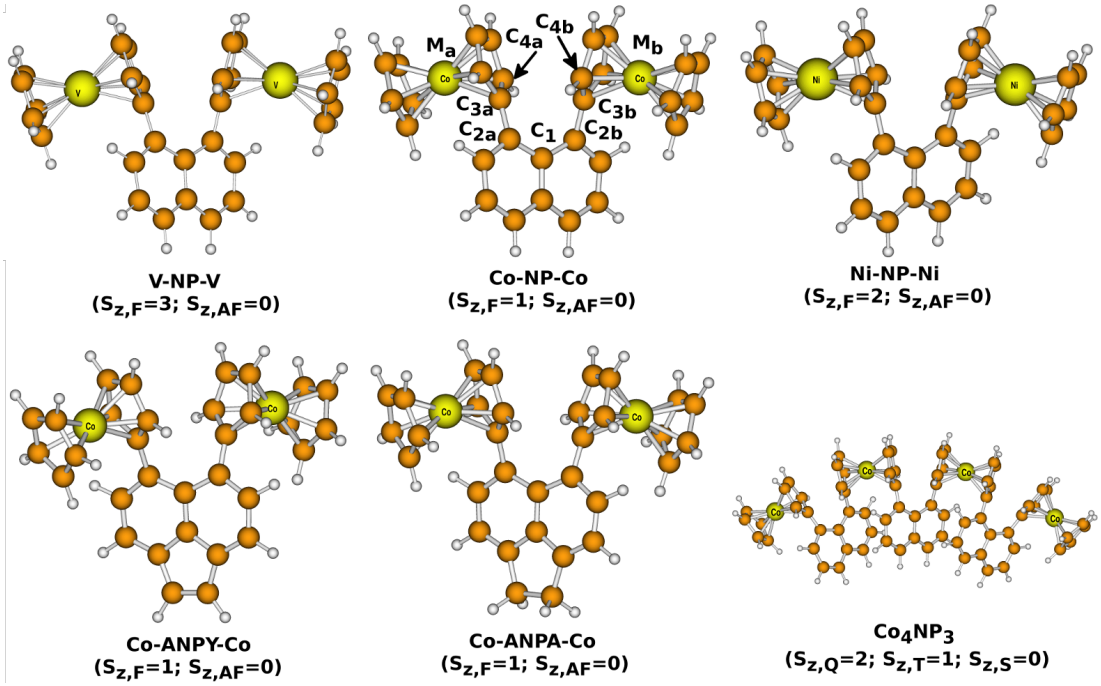

Figure 6.1: Structures of the metallocene complexes considered in this study optimized as BS determinants, using TPSSH /def2-TZVP, including the high-spin state ($\langle \hat{S}_{z,\mathrm{F}} \rangle$) and the antiferromagnetically coupled BS determinant ($\langle \hat{S}_{z,\mathrm{AF}} \rangle$). For the Co_4NP_3 system a quintet ($\langle \hat{S}_{z,\mathrm{Q}} \rangle = 2$) high-spin state, two BS determinants with $\langle \hat{S}_{z,\mathrm{T}} \rangle = 1$, and three BS determinants with $\langle \hat{S}_{z,\mathrm{S}} \rangle = 0$ are obtained.

Depending on the metal center, the number of unpaired electrons changes from one for Co(II) to two for Ni(II), and three for V(II). In the case of the Co_4NP_3 complex, six spin states must be considered differing in the local spin configurations and in the total $\hat{S}_z$ and $\hat{S}^2$ expectation values. One quintet spin configuration ($\uparrow\uparrow\uparrow\uparrow$), two BS determinants approximately referring to triplet states (spin configurations: $\downarrow\uparrow\uparrow\uparrow$ and $\uparrow\downarrow\uparrow\uparrow$), and three BS determinants approximating singlet states (spin configurations: $\uparrow\downarrow\uparrow\downarrow$, $\uparrow\uparrow\downarrow\downarrow$, and $\uparrow\downarrow\downarrow\uparrow$) are considered due to the symmetry of the system. Because structural relaxation effects cannot be taken into account in the Green's-function approach to evaluate exchange spin coupling constants introduced in Section 3.4, the low-spin molecular structures were employed, modelled by BS determinants, which experimentally constituted the ground state for all systems considered here [111, 136, 137, 141]. For the tetranuclear Co_4NP_3 complex, the structure is optimized for the $\uparrow\downarrow\uparrow\downarrow$ determinant, because for the analogous dinuclear Co–NP–Co, the nearest-neighbor interaction has been antiferromagnetic [136]. In all calculations the TPSSH hybrid functional has been employed, which has been shown to perform well in structure optimizations of mononuclear $3d$ transition-metal complexes [172–174]

and furthermore has been successfully used to predict spin-state energetics in mononuclear and dinuclear open-shell systems [175–178]. Only for Co_4NP_3, the structure optimizations are carried out with BP86 / def-TZVP using the RI approximation, and additional single-point calculations are performed with TPSSH / def2-TZVP on top of this structure. The structure optimizations are carried out with BP86 due to the size of this system, which would have made the optimizations with TPSSH much more demanding and time consuming. For the Green's-function approach, high-spin single-point calculations are carried out on top of the ↑↓↑↓ BS determinant. First, the dependence of the spin coupling on the bridge and on the metal center employed (Figure 6.1) is studied. Because the effectiveness of the through-space coupling should also depend on the torsional angle between the bridge and the metallocene moieties, the spin coupling is further analyzed as a function of these angles in Section 6.5.
First, the X-ray crystallographic structures of the complexes synthesized in the group of Jürgen Heck are compared to those obtained from structure optimizations (Section 6.1) to validate the computational methodology employed here. In Section 6.2, the coupling constants calculated by DFT are compared to the coupling constants obtained by experiment. In a next step, the local spin distributions from different fragments are analyzed in order to highlight the differences between the systems under study (Section 6.3). In Section 6.4, the largest contributions to the coupling constant are analyzed by the Green's-function approach, and the shapes of the corresponding occupied and virtual MOs are discussed to evaluate the relative importance of through-space vs. through-bond coupling. In Section 6.5, the influence of the torsional angles between the bridge and the cobaltocene moieties is discussed for Co–NP–Co and Co–ANPY–Co, since this is the structural parameter decisive for the relative importance of through-space and through-bond coupling.

6.1 Molecular Structures

In this section, selected structural parameters are discussed, defined according to Figure 6.1 and obtained from structure optimizations with TPSSH / def2-TZVP for the BS determinants. As far as possible, the calculated results are compared to the outcomes from X-ray structure analyses from the literature [111,136,137, 141] (Table 6.1).
In general, the optimized structures are in good agreement with the structures obtained from X-ray analysis. Only for Co–ANPA–Co, the torsional angles between the Cp ring and the bridge is underestimated by roughly 7°, which is larger than the deviations between the different chemical systems. While the distances between the Cp carbon atoms are very similar for all NP-bridged complexes, the distance between the metal atoms is found to decrease in the following order: V > Ni > Co. For the Co complexes involving different bridges (NP, ANPA, and ANPY), the distances vary only slightly, while the torsional angles are found to be the lowest for the ANPY-bridged complex. However,

the trend cannot be verified because no experimental values are available for that compound.

Table 6.1: Selected structural parameters (defined according to Figure 6.1) for the bismetallocene complexes under study obtained from X-ray structure analyses and from structure optimizations performed with TPSSH / def2-TZVP on the BS determinants. All values are given in Å or degrees, respectively.

	Experiment (X-ray structures)	
	V–NP–V [137]	Co–NP–Co [136]
M_a-M_b	7.1212	6.7392
$C_{3a}-C_{3b}$	2.9741	2.940
$C_1-C_{2a}-C_{3a}-C_{4a}$	42.516	40.280
$C_1-C_{2b}-C_{3b}-C_{4b}$	42.516	42.516
	Co–ANPA–Co [141]	–
M_a-M_b	6.7203	–
$C_{3a}-C_{3b}$	2.9947	–
$C_1-C_{2a}-C_{3a}-C_{4a}$	47.338	–
$C_1-C_{2b}-C_{3b}-C_{4b}$	47.870	–
	Theory	
	V–NP–V [137]	Co–NP–Co [136]
M_a-M_b	7.2018	6.8196
$C_{3a}-C_{3b}$	3.0361	3.0041
$C_1-C_{2a}-C_{3a}-C_{4a}$	41.676	39.947
C1b–C2b–C3b–C4b	41.674	39.948
	Ni–NP–Ni	Co–ANPY–Co
M_a-M_b	7.0160	6.8818
$C_{3a}-C_{3b}$	3.01648	3.1602
$C_1-C_{2a}-C_{3a}-C_{4a}$	39.394	35.246
$C_1-C_{2b}-C_{3b}-C_{4b}$	39.396	35.207
	Co–ANPA–Co [141]	–
M_a-M_b	6.8623	–
$C_{3a}-C_{3b}$	3.1260	–
$C_1-C_{2a}-C_{3a}-C_{4a}$	39.781	–
$C_1-C_{2b}-C_{3b}-C_{4b}$	40.209	–

6.2 Exchange Spin Coupling

Coupling constants are calculated for the dinuclear complexes optimized for the BS determinants with the unprojected BS method (see Section 2.3) and with the Green's-function approach applied to the electronic structures of the high-spin states, and the obtained values are compared whenever possible to the experimental coupling constants (Table 6.2). The unprojected BS method is

employed, because these coupling constants compare well with the one obtained from the Green's-function approach (see Chapter 4). In order to understand the influence of the bridges on the exchange spin coupling, the bridges are replaced by hydrogen atoms, and single point calculations are carried out for these arrangements of metallocenes.

Table 6.2: Coupling constants for the different dinuclear bridged bismetallocene complexes, in Figure 6.1 in cm^{-1} obtained from experiment and calculated with TPSSH / def2-TZVP on the low-spin structures optimized with the same functional using the unprojected BS approach ($J_{BS,unprojected}$) and the Green's-function approach (J_{Green} (F); on top of the electronic structure of high-spin state). Additionally, the coupling constants for the metallocene arrangments without bridge are given. For the Green's-function method, only the metal centers are included in the spin center definitions.

	with bridge			without bridge	
system	$J_{exp.}$	$J_{BS,unprojected}$	J_{Green} (F)	$J_{BS,unprojected}$	J_{Green} (F)
V–NP–V [137]	−2.1	−0.3	−0.4	−0.4	−0.2
Co–NP–Co [136]	−28.1	−15.7	−18.2	6.0	13.6
Ni–NP–Ni [111]	−31.5*	−21.3	−25.6	−22.2	−24.3
Co–ANPA–Co [141]	−42.3	−0.2	−3.3	–	–
Co–ANPY–Co [141]	−125.2	−120.7	−128.5	2.6	5.6

*Coupling constant for the permethylated nickelocene analogue [111].

For all systems in Table 6.2, the coupling constants calculated from both approaches are in good qualitative agreement with the experimental values. All are negative, indicating antiferromagnetic coupling. Only for the Co–ANPA–Co complex, the coupling constants are strongly underestimated, which could result from the deviations in the torsional angle between calculations and experiment. However, in the experimental studies of the crystal structure, a strong intermolecular interaction has been found [141], which also might be a problem in the determination of intramolecular coupling constants for this system. For evaluating intermolecular coupling constants, it would be necessary to use a larger number of molecules in the calculation, which is out of the scope of this work, but might be interesting for future studies. For the Ni–NP–Ni complex, the coupling constants are not directly comparable to the experiment because only the complex involving permethylated nickelocenes was experimentally accessible [111]. Attempts to synthesize the unmethylated analogue lead to the formation of mononuclear *ansa*-nickelocene compounds [179]. However, was shown for Co–NP–Co that a permethylation of the unsubstituted Cp ring leads to a reduction of the coupling strength [111]. The trends for the strength of the spin coupling (excluding the Co–ANPA–Co complex) from both theoretical approaches are in good agreement with the experiment, with the strength of the coupling increasing in the following order: V–NP–V < Co–NP–Co < Ni–NP–Ni < Co–ANPY–Co.

For all dinuclear Co systems, a removal of the bridge leads to slightly ferromagnetic coupling, while for Ni–NP–Ni and V–NP–V, the coupling constants are almost unaffected by the absence of the bridge. The Co–ANPA–Co system is not further considered because of the dramatic deviations between the theoretically obtained values and the experimental findings. The trend for the spin coupling in Co–NP–Co is in agreement with the DFT calculations by Pagels and coworkers [136], who showed that a removal of the bridge leads to a remarkable reduction of the spin coupling from moderate to very weak antiferromagnetic coupling. Our results give a slightly ferromagnetic coupling, which might be a consequence of the different parameters used in the calculations and of using the X-ray structure rather than carrying out structure optimizations. It should further be noted that the spin coupling is slightly increased in the Ni–NP–Ni systems for the values obtained from Noodleman's BS approch upon removal of the bridge, while it is slightly reduced in the case of the Green's-function approach. The former findings are in agreement with the calculations performed by Trtica and coworkers [111] on the permethylated analogues, which resulted in a larger antiferromagnetic coupling when the bridge was omitted. However, the changes in the spin coupling are so small (about 1 cm^{-1}) that this should not hinder a meaningful analysis by the Green's-function approach.

Table 6.3: Coupling constants for the Co_4NP_3 complex in Figure 6.1 in cm^{-1} calculated on the low-spin structures approximated by the ↑↓↑↓ BS determinant optimized with TPSSH / def2-TZVP using the equations provided in Section A.8. The Green's-function approach is applied to the electronic structure of the high-spin state of this structure (J_{Green} (F)). The x and y values refer to the cobaltocenes between which the interaction was calculated.

xy	$J_{\mathrm{BS},xy}$	$J'_{\mathrm{BS},xy}$	$J_{\mathrm{Green},xy}$ (F)
12	−100.0	−99.8	−80.5
23	−159.7	−159.1	−136.4
13	–	–	2.0

For evaluating spin coupling constants in the tetranuclear Co_4NP_3 system, the scheme proposed by Ruiz and coworkers [55] based on solving a set of linear equations spanned by all possible configurations of local spins in a given system is employed. In the derivation of the required equations, it is assumed that there is no interaction between the first and third, as well as between the first and fourth cobaltocenes ($J_{13} = J_{14} = 0$), and that $J_{12} = J_{34}$. Spin projection is neglected. Under these restrictions, the problem is overdetermined and two equations for J_{12} and J_{23} are obtained (given in Section A.8 in the appendix). Again, these coupling constants are compared with those obtained from the Green's-function approach (Table 6.3) to check if the Green's-function approach is also applicable to oligonuclear complexes involving more than two spin centers. No coupling constants are calculated for Co_4NP_3 without bridges, because the bridge influence is already covered in the analysis of the dinuclear Co–NP–

Co complex. The coupling constants calculated on the spin-state structure of the ↑↓↑↓ determinant of the tetranuclear Co_4NP_3 complex also corresponds to antiferromagnetic coupling between nearest neighbours. For the anaylsis presented by Ruiz and coworkers [55], it is reassuringly found that the two expressions referring to the same coupling constant always give nearly identical coupling constants. The coupling constants obtained from the Green's-function approach are in good agreement with those from Noodleman's BS method. To test if the assumption that the spin coupling between the first and third cobaltocene is zero, also $J_{\mathrm{Green},13}$ (F) is calculated, which is 2 cm^{-1}, and therefore underlines the correctness of this assumption. However, it should be kept in mind that the latter method requires all six spin states while the Green's-function method only requires the electronic structure of the high-spin state, which facilitates the description of these systems at low computational cost.

6.3 Local Spin Distributions

In this section, the local spins for the high-spin state of the bismetallocene complexes are given for the metal center of a given metallocene, both Cp rings belonging to these metallocenes, and the bridges in Figure 6.2. Also the local spins for the six different BS determinants in the Co_4NP_3 complex are discussed (Figure 6.3). The spin delocalization onto the Cp ligands is of interest because it effectively reduces the distance between the spins and therefore should lead to an increase of through-space interactions. Further, the degree of the spin delocalization onto the bridge should correlate with the through-bond contributions in the systems.

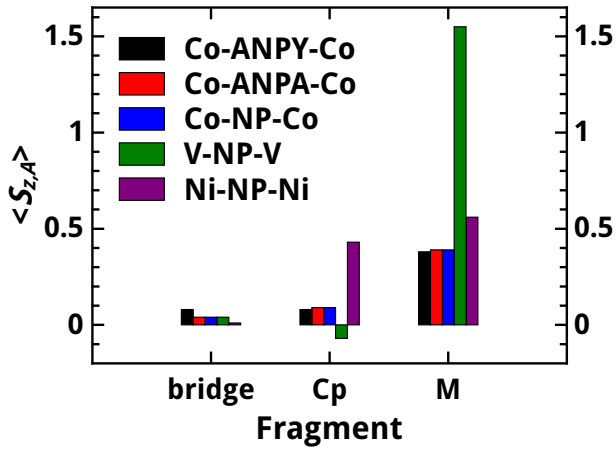

Figure 6.2: Local spins obtained from Mulliken partitioning (see Section 2.4) for the high-spin states of the different bismetallocene complexes under investigation, calculated with TPSSH / def2-TZVP on the structures optimized as BS determinants.

In almost all cases, the local spins on the Cp rings have the same sign as local

spins on the metal center itself. Only for V–NP–V, the spin on the metal center exceeds the ideal value of 1.5 a.u., which is compensated by a small net β spin density on the Cp ligands. This small degree of spin delocalization onto the Cp rings may be responsible for the weak through-space interactions in this system. Further, the degree of spin delocalization onto the Cp ring is the strongest for Ni–NP–Ni, in which roughly half of the spin is transferred to the Cp rings, while for the Co(II) systems 0.1 a.u. of the spin is transferred to the Cp ligands. The local spins on the bridge are largest for Co–ANPY–Co, for which the torsional angle is lowest and therefore the spin delocalization is expected to be larger than for the Co–NP–Co system. For Ni–NP–Ni, the spin contributions on the bridge are the lowest, which explains why the coupling does not change significantly upon removal of the bridge compared to the Co systems.

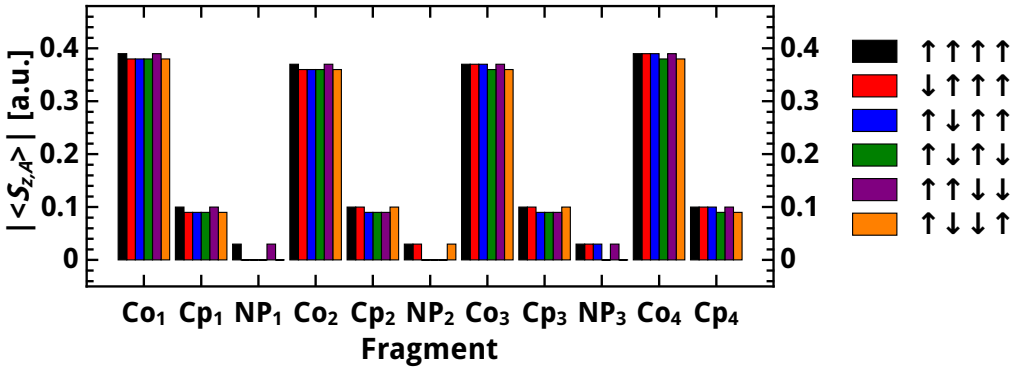

Figure 6.3: Absolute local spins obtained from Mulliken partitioning for the different spin configurations of the Co_4NP_3 complex calculated with TPSSH / def2-TZVP as single-point calculations on the optimized ↑↓↑↓ structure.

For Co_4NP_3, the local spins are about 0.4 a.u. for all Co centers. However, the local spins are smaller for the cobalt centers of the inner metallocenes. Furthermore, when the spins of two adjacent cobaltocenes are coupled antiferromagnetically, the spins' magnitudes on all fragments decrease compared to the cases in which the spins are ferromagnetically coupled. This could explain why the deviations observed between the coupling constants obtained with the Green's-function approach and Noodleman's BS approach are larger than for the dinuclear complexes. The local spin contributions on the bridges themselves reduce to zero if the spins on two adjacent cobaltocenes are coupled antiferromagnetically.

6.4 Understanding the Influence of the Bridge and the Metal Centers on the Spin Coupling by the Green's-Function Approach

In the following, the changes to spin coupling that occur upon introduction of the bridge are investigated by comparing the contributions from occupied α-spin orbitals and from spin-flip excitations corresponding to these contributions for the different systems in the presence and absence of the bridge. This is done in order to deepen our knowledge on the bridge effects on the exchange spin coupling. In Section 6.4.1, the Co systems with ANPY and NP bridges are studied, in which the bridge is found to heavily influence the spin coupling, followed in Section 6.4.2 by the V–NP–V and Ni–NP–Ni systems for which the presence of the bridge does not affect the spin coupling between the metallocenes. The Green's-function method might be in general more suitable for analyzing spin coupling than the removal of the bridge because the electronic effects of the bridge on the spin coupling are taken into account in the former method. In the following, first the contributions from occupied α spin orbitals are discussed to filter out the most significant ones, which are then further analyzed by taking into account the corresponding spin-flip excitations.

6.4.1 Biscobaltocene Complexes: Evaluating the Influence of the Bridge onto the Spin Coupling

To evaluate which occupied α spin orbitals are most important for the spin coupling, all contributions to the coupling constants with magnitudes larger than 5% of its total value (Table 6.2) from occupied α spin orbitals are calculated (Figure 6.4).
The contributions from the HOMO$^\alpha$ and HOMO-1$^\alpha$ are largest in magnitude for both systems regardless of whether the bridge is present or not. The HOMO$^\alpha$ is dominated by an antibonding linear combination of d_{xz} orbitals, while the HOMO-1$^\alpha$ is mainly a bonding linear combination of these orbitals. For the Co–NP–Co (Co–Co) system, also larger contributions from the HOMO-17$^\alpha$ (HOMO-14$^\alpha$) and HOMO-18$^\alpha$ (HOMO-15$^\alpha$) are found. However, the sums over the contributions from HOMO-17$^\alpha$ and HOMO-18$^\alpha$ for Co–NP–Co (and over the contributions from HOMO-14$^\alpha$ and HOMO-15$^\alpha$ for Co–Co) are close to zero (3.7 cm^{-1} for Co–NP–Co and 2.6 cm^{-1} for Co–Co) and are therefore neglected, so that only the spin-flip excitations of the HOMO$^\alpha$ and the HOMO-1$^\alpha$ are taken into account. For the same reason, the spin-flip excitations from the HOMO-17$^\alpha$ and HOMO-18$^\alpha$ are also neglected in the case of Co–ANPY–Co (and again from the HOMO-14$^\alpha$ and the HOMO-15$^\alpha$ for the corresponding Co–Co arrangement). The sums over the occupied orbital contributions from the HOMO$^\alpha$ and HOMO-1$^\alpha$ give approximate coupling constants of -28.7 cm^{-1} for Co–NP–Co and of 18.7 cm^{-1} for the corresponding Co–Co system, which were in good agreement with the total coupling constants of -28.5 cm^{-1} and 12.0 cm^{-1} obtained with

this method. Also for Co–ANPY–Co and for the corresponding Co–Co system, the coupling constant obtained as the sum over the HOMO$^{\alpha}$ and HOMO-1$^{\alpha}$ contributions (-151.7 cm^{-1} and 12.0 cm^{-1}) are in good agreement with the total coupling constants. From this analysis of the occupied MO contributions, it can be seen that the contributions of the HOMO$^{\alpha}$ and HOMO-1$^{\alpha}$ are sufficient to describe the spin coupling in both complexes. However, it must be noted that the energetic order of the bonding and antibonding linear combinations in the occupied MOs change from Co–ANPY–Co to Co–NP–Co.

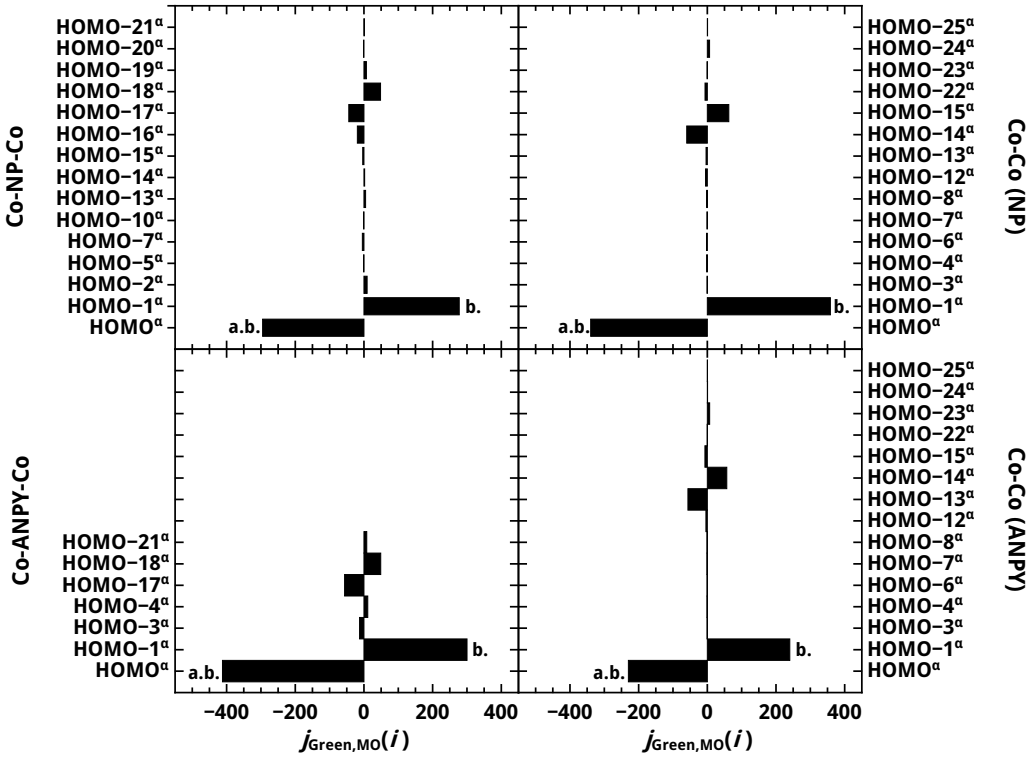

Figure 6.4: All orbital contributions to the coupling constants according to Equation (3.27) with magnitudes larger than 5% of its total value (see Table 6.2) from occupied α spin orbitals for Co–NP–Co (top row) and Co–ANPY–Co (bottom row) with (left column) and without bridge (right column), calculated with TPSSH / def2-TZVP based on high-spin single-point calculations on top of structures optimized as BS determinants. For the occupied-MO contributions considered in the analysis the bonding (b.) and (a.b.) antibonding characters are given next to the corresponding bars.

As a next step, the corresponding spin-flip excitations in the systems with and without bridge are taken into account in order to see if new contributions arise from bridge-centered MOs that are not found for the bridgeless systems. Therefore, the MOs of the Co–NP–Co and Co–ANPY–Co complexes are compared with those of the corresponding Co–Co systems in which the bridge is omitted.

The MOs for both Co(II)-substituted complexes are given in Figures 6.5 and 6.6.

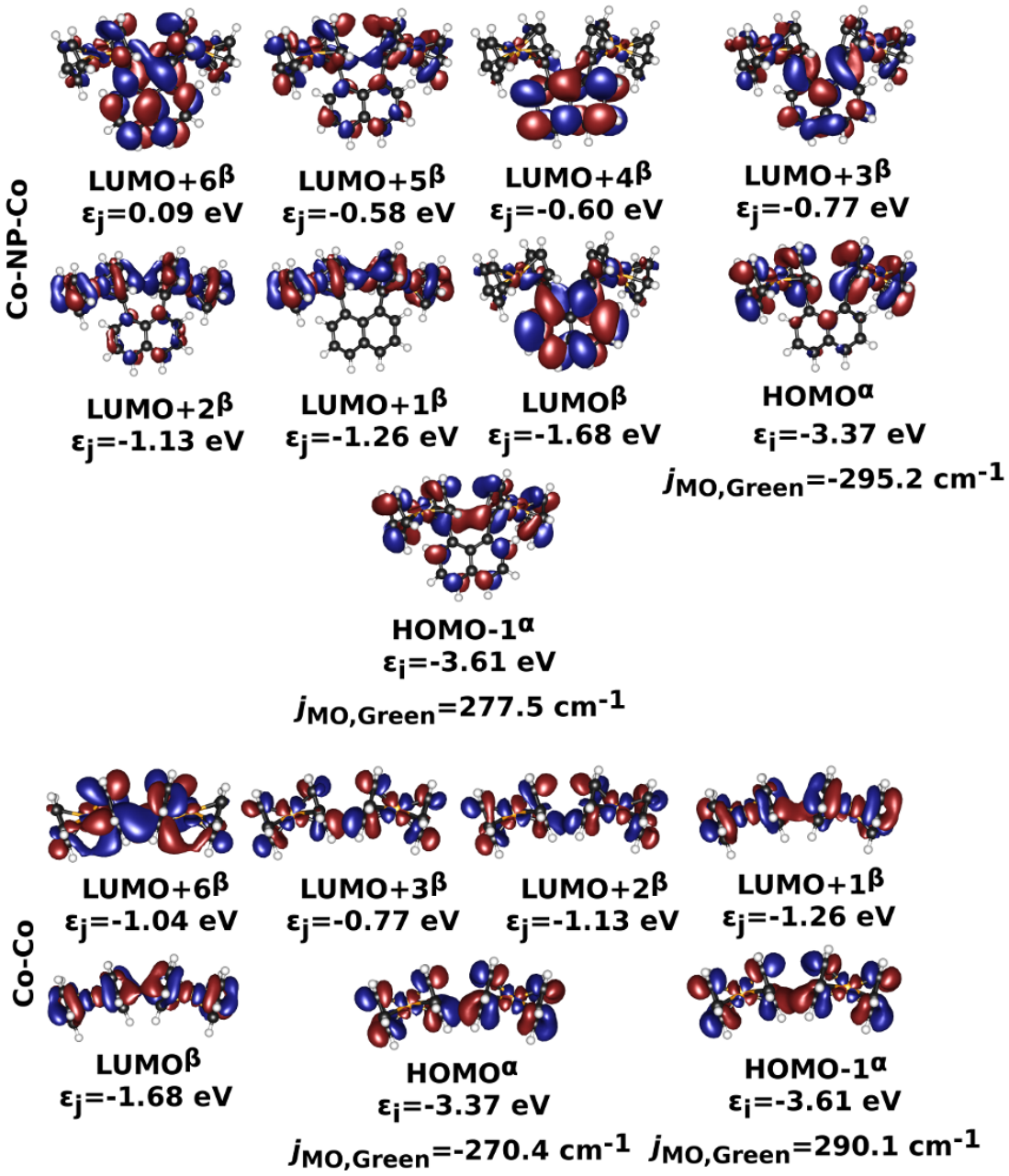

Figure 6.5: Contours and energies of the MOs calculated with TPSSH / def2-TZVP for Co–ANPY–Co and the corresponding cobaltocene arrangement excluding the bridges. Also the occupied MO contributions of the occupied α spin orbitals, $j^{\alpha}_{\mathrm{Green,MO}}(i)$, are given.

The MO contributions to the coupling constants to the cobaltocenes in Co–NP–Co and Co–ANPY–Co can be successfully mapped onto the contributions in the systems without bridges. However, it should be noted that in general the corresponding MOs in the systems with bridge have bridge contributions.

For both systems the energy gaps between the occupied α MOs and the virtual β MOs increase in the absence of the bridge.

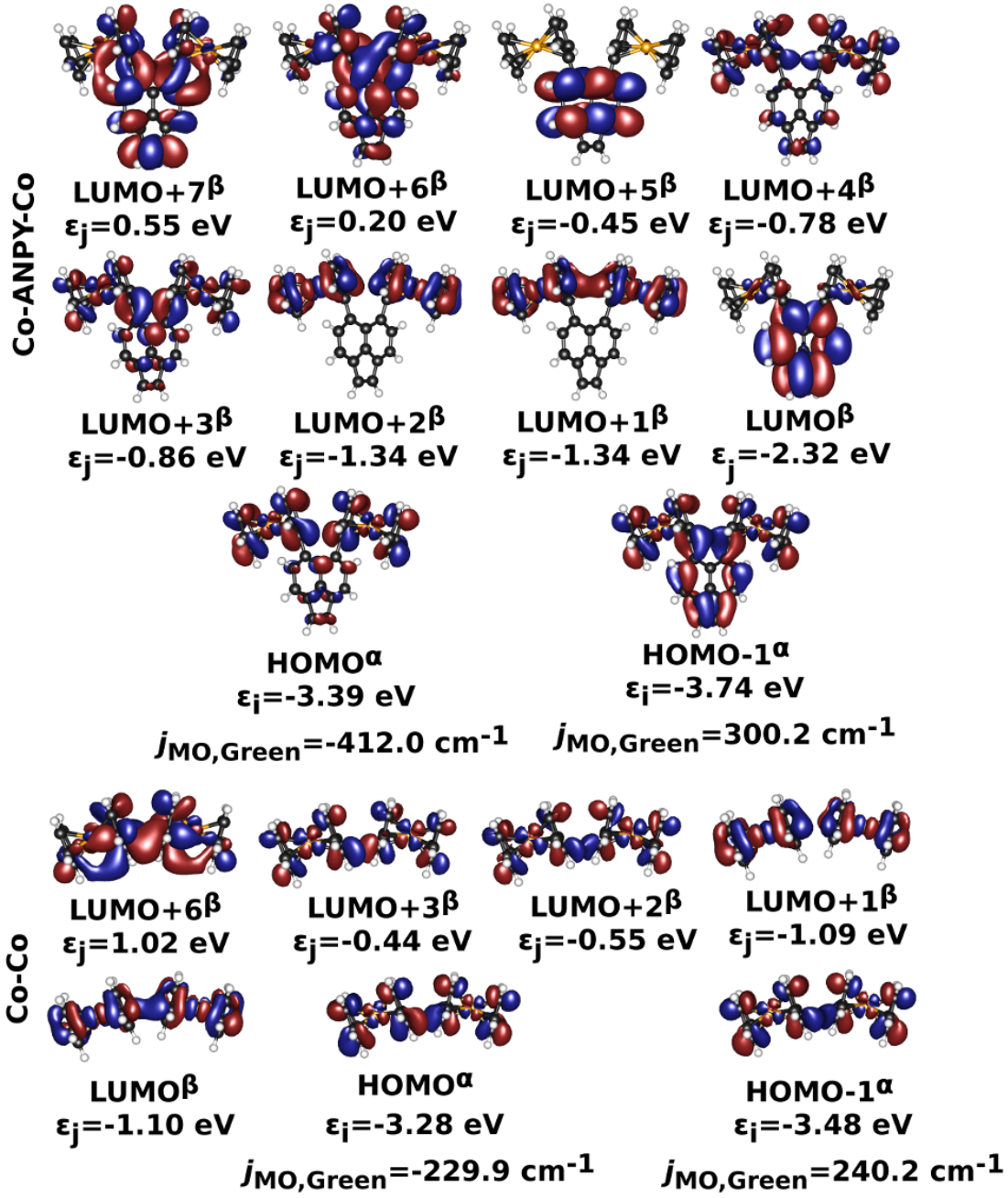

Figure 6.6: Contours and energies of the MOs calculated with TPSSH / def2-TZVP given for Co–NP–Co and the corresponding cobaltocene arrangement excluding the bridges. Also the occupied MO contributions of the occupied α spin orbitals, $j^{\alpha}_{\mathrm{Green,MO}}(i)$, are given.

Further, in both systems with a bridge, two bridge-centered MOs (LUMO$^{\beta}$ / LUMO+4$^{\beta}$ for Co–NP–Co, and LUMO$^{\beta}$ / LUMO+5$^{\beta}$ in Co–ANPY–Co; see

Figure 6.5) are found that have no correspondence to any MOs in the Co–Co (without bridge) systems. In all other cases, the virtual β MOs show d_{yz} and d_{xz} character on the cobalt centers.
As mentioned, the HOMO$^{\alpha}$ and HOMO-1$^{\alpha}$ constitute a pair of bonding and antibonding linear combinations of d_{xz} orbitals, but also the virtual β MOs as pairs of bonding and antibonding linear combinations are obtained. The sums over all four contributions arising from spin-flip excitations between the HOMO$^{\alpha}$ and HOMO-1$^{\alpha}$ and such pairs of virtual MOs orbitals are summed up and are given in addition to the spin-flip excitations (see $\sum_1$, $\sum_2$, ...) in Tables 6.4 and 6.5.

Table 6.4: Spin-flip excitations from the HOMO$^{\alpha}$ and HOMO-1$^{\alpha}$ to different pairs of bonding and antibonding virtual orbitals and their contributions ($j_{\mathrm{Green}}(i,j)$) in cm^{-1} for Co–NP–Co, and the corresponding spin-flip excitations in the systems without bridge by comparing the MO shapes for both systems in Figure 6.5, calculated with the Green's-function approach on the electronic structure of the high-spin state using the structures optimized for the BS determinants calculated with TPSSH /def2-TZVP.

with bridge		without bridge	
$i \rightarrow j$	$j_{\mathrm{Green}}(i,j)$	$i \rightarrow j$	$j_{\mathrm{Green}}(i,j)$
HOMO$^{\alpha}$ $\rightarrow$ LUMO$^{\beta}$	−633.4	−	−
HOMO$^{\alpha}$ $\rightarrow$ LUMO+4$^{\beta}$	349.4	−	−
HOMO-1$^{\alpha}$ $\rightarrow$ LUMO$^{\beta}$	596.9	−	−
HOMO-1$^{\alpha}$ $\rightarrow$ LUMO+4$^{\beta}$	−322.0	−	−
$\sum_1$	−9.2	−	−
HOMO$^{\alpha}$ $\rightarrow$ LUMO+1$^{\beta}$	79.9	HOMO$^{\alpha}$ $\rightarrow$ LUMO$^{\beta}$	108.5
HOMO$^{\alpha}$ $\rightarrow$ LUMO+2$^{\beta}$	−41.50	HOMO$^{\alpha}$ $\rightarrow$ LUMO+1$^{\beta}$	−161.4
HOMO-1$^{\alpha}$ $\rightarrow$ LUMO+1$^{\beta}$	−27.8	HOMO-1$^{\alpha}$ $\rightarrow$ LUMO$^{\beta}$	−46.7
HOMO-1$^{\alpha}$ $\rightarrow$ LUMO+2$^{\beta}$	9.8	HOMO-1$^{\alpha}$ $\rightarrow$ LUMO+1$^{\beta}$	243.9
$\sum_2$	20.4	$\sum_{2'}$	144.2
HOMO$^{\alpha}$ $\rightarrow$ LUMO+3$^{\beta}$	2206.2	HOMO$^{\alpha}$ $\rightarrow$ LUMO+3$^{\beta}$	4888.5
HOMO$^{\alpha}$ $\rightarrow$ LUMO+5$^{\beta}$	−2912.1	HOMO$^{\alpha}$ $\rightarrow$ LUMO+2$^{\beta}$	−5196.8
HOMO-1$^{\alpha}$ $\rightarrow$ LUMO+3$^{\beta}$	−2013.7	HOMO-1$^{\alpha}$ $\rightarrow$ LUMO+3$^{\beta}$	−4787.2
HOMO-1$^{\alpha}$ $\rightarrow$ LUMO+5$^{\beta}$	2650.2	HOMO-1$^{\alpha}$ $\rightarrow$ LUMO+2$^{\beta}$	4976.1
$\sum_3$	−69.4	$\sum_{3'}$	−119.3
HOMO-1$^{\alpha}$ $\rightarrow$ LUMO+6$^{\beta}$	682.0	HOMO-1$^{\alpha}$ $\rightarrow$ LUMO+6$^{\beta}$	49.3
HOMO$^{\alpha}$ $\rightarrow$ LUMO+6$^{\beta}$	−639.5	HOMO$^{\alpha}$ $\rightarrow$ LUMO+6$^{\beta}$	−56.6
$\sum_4$	42.6	$\sum_{4'}$	−7.3
$\sum_{\mathrm{tot}}$	−15.6	$\sum_{\mathrm{tot}'}$	17.5

The sums over these contributions are found to change quantitatively in some cases upon introduction of the bridge, as for example $\sum_3$ and $\sum_{3'}$ in Table 6.4, and in some cases they also qualitatively deviate from each other ($\sum_4$ and $\sum_{4'}$ in Table 6.4). For the Co–ANPY–Co system, it is also found that excluding

the sum over the spin-flip excitations to the bridge-centered MOs (denoted with $\sum_1$ in Tables 6.4 and 6.5), the resulting coupling is ferromagnetic in nature as observed for the corresponding Co(II)–Co(II) system, while for the NP-bridged complex, a weak antiferromagnetic coupling is obtained, which is in disagreement with the results obtained for the corresponding Co(II)–Co(II) system.

Table 6.5: Spin-flip excitations from the HOMO$^\alpha$ and HOMO-1$^\alpha$ to different pairs of bonding and antibonding virtual orbitals, and their contributions ($j_{\mathrm{Green}}(i,j)$) in cm^{-1} for Co–ANPY–Co, and the corresponding spin-flip excitations in the systems without bridge obtained by comparing the MO shapes in both systems in Figure 6.6 calculated with the Green's-function approach on the electronic structure of the high-spin state using the structures optimized for the BS determinants calculated with TPSSH /def2-TZVP.

with bridge		without bridge	
$i \rightarrow j$	$j_{\mathrm{Green}}(i,j)$	$i \rightarrow j$	$j_{\mathrm{Green}}(i,j)$
HOMO$^\alpha \rightarrow$ LUMO$^\beta$	-552.8	–	–
HOMO-1$^\alpha \rightarrow$ LUMO$^\beta$	409.7	–	–
$\sum_1$	-143.1	–	–
HOMO$^\alpha \rightarrow$ LUMO+2$^\beta$	61.3	HOMO$^\alpha \rightarrow$ LUMO+1$^\beta$	73.8
–	–	HOMO$^\alpha \rightarrow$ LUMO$^\beta$	-64.4
HOMO-1$^\alpha \rightarrow$ LUMO+2$^\beta$	-22.7	HOMO$^\alpha \rightarrow$ LUMO+1$^\beta$	-37.2
HOMO-1$^\alpha \rightarrow$ LUMO+1$^\beta$	11.3	HOMO-1$^\alpha \rightarrow$ LUMO$^\beta$	103.6
$\sum_2$	49.9	$\sum_{2'}$	75.8
HOMO$^\alpha \rightarrow$ LUMO+3$^\beta$	2676.6	HOMO$^\alpha \rightarrow$ LUMO+3$^\beta$	4893.4
HOMO$^\alpha \rightarrow$ LUMO+4$^\beta$	-2884.0	HOMO$^\alpha \rightarrow$ LUMO+2$^\beta$	-5222.7
HOMO-1$^\alpha \rightarrow$ LUMO+3$^\beta$	-2256.1	HOMO-1$^\alpha \rightarrow$ LUMO+3$^\beta$	-4804.2
HOMO-1$^\alpha \rightarrow$ LUMO+4$^\beta$	2406.6	HOMO-1$^\alpha \rightarrow$ LUMO+2$^\beta$	5077.3
$\sum_3$	-56.9	$\sum_{3'}$	-56.2
HOMO$^\alpha \rightarrow$ LUMO+6$^\beta$	335.8	HOMO$^\alpha \rightarrow$ LUMO+6$^\beta$	-63.5
HOMO$^\alpha \rightarrow$ LUMO+7$^\beta$	41.4	–	–
HOMO-1$^\alpha \rightarrow$ LUMO+6$^\beta$	-289.7	HOMO-1$^\alpha \rightarrow$ LUMO+6$^\beta$	56.2
HOMO-1$^\alpha \rightarrow$ LUMO+7$^\beta$	36.3	–	–
$\sum_4$	41.1	$\sum_{4'}$	-7.3
$\sum_{\mathrm{tot}}$	-108.9	$\sum_{\mathrm{tot}'}$	12.3

In this context it is also worth mentioning that while for the Co(II)–NP–Co(II) system two bridge-centered virtual β spin orbitals are involved in the largest spin-flip excitations (see spin-flip excitations contributing to $\sum_1$ in Table 6.4 and the corresponding MOs in Figure 6.5, top), only one of the bridge-centered MOs is involved (LUMO$^\beta$ in Table 6.5), while the bridge-centered LUMO+5$^\beta$ does not play a role in the spin coupling. This might occur due to this orbital missing coefficients on the acetylene part in the acenaphthylene bridge. This MO has the same shape as the LUMO+4$^\beta$ for the Co–NP–Co system, for which the contributions from the spin-flip excitations involving this MO are found to

give ferromagnetic contributions. This "ferromagnetic" pathway is inactive for Co–ANPY–Co, which results in much larger antiferromagnetic contributions from the bridge-centered virtual MOs.

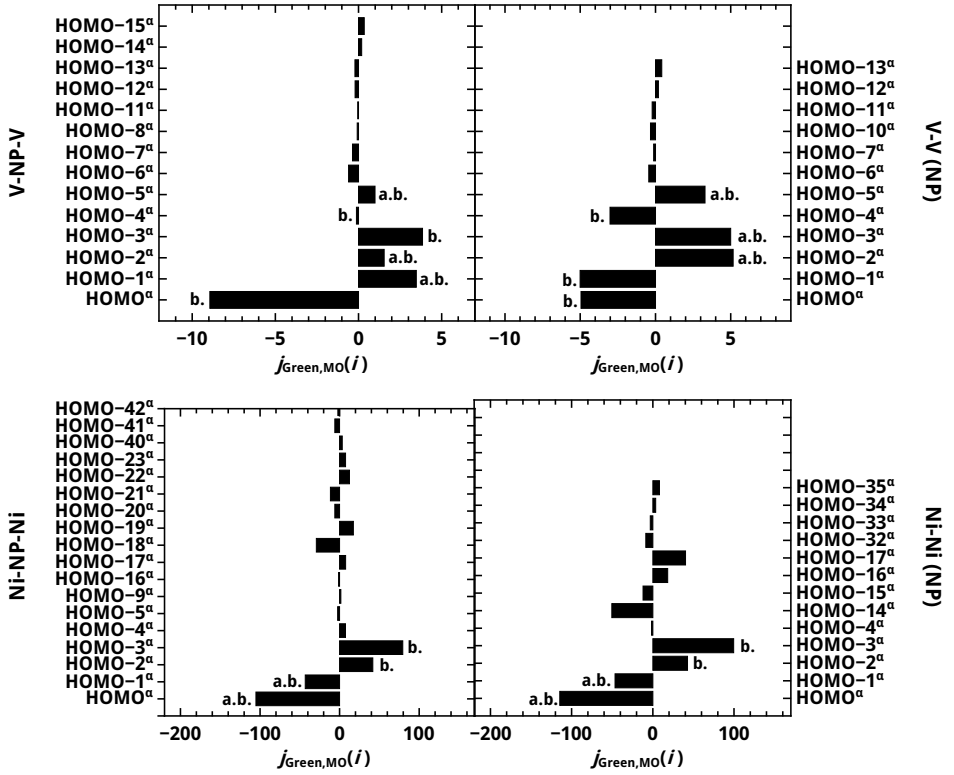

Figure 6.7: All contributions to the coupling constants with magnitudes larger than 5% of it (Table 6.2) from occupied α spin orbitals for Ni–NP–Ni (top row) and V–NP–V (bottom row) for the systems with (left column) and without bridge (right column) calculated with TPSSH / def2-TZVP for the electronic structure of the high-spin states obtained from single-point calculations on the structures of the BS determinants. For the occupied-MO contributions considered in the analysis the bonding (b.) and (a.b.) antibonding characters are given next to the corresponding bars.

From these findings it can be concluded that the estimated through-bond contributions resulting from spin-flip excitations to bridge-centered MOs are antiferromagnetic in both systems under study here, while the through–space contributions are very weak, which highlights the crucial influence of the bridge on the spin coupling. However, it needs to be noted that these are only qualitative estimations because some of the other MOs also show bridge contributions that are neglected here, and further spin-flip excitations from other occupied α spin orbitals to these bridge-centered virtual β spin orbitals are neglected as well. These other bridge contributions are expected to give smaller contributions to the through-bond contributions and it would further need some implementations to take these contributions into account, which would be interesting for future studies, but is out of the scope of this work.

6.4.2 Bisvanadocene and Bisnickelocene Complexes

As for the bis(cobaltocene) complexes in the previous section, all contributions from occupied α spin orbitals larger than 5% of the total coupling constant are calculated for V–NP–V and Ni–NP–Ni (Figure 6.7).

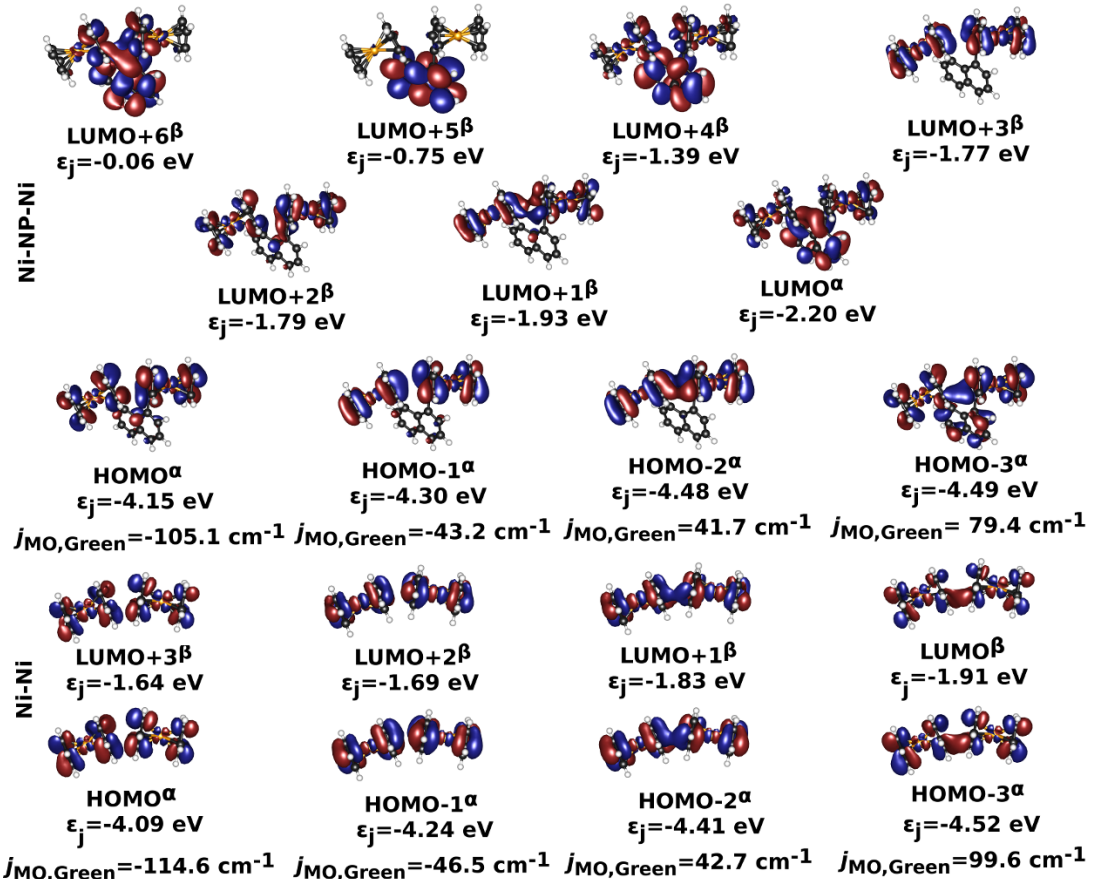

Figure 6.8: Contours and energies of the MOs calculated with TPSSH / def2-TZVP given for Ni(II)–NP–Ni(II) and the corresponding nickelocene arrangement omitting the bridges. Also the occupied MO contributions of the occupied α spin orbitals, $j^{\alpha}_{\mathrm{Green,MO}}(i)$, are given.

The contributions are much larger for Ni–NP–Ni than for V–NP–V. As for the cobaltocene complexes, the contributions arising from the singly occupied MOs in the Ni–NP–Ni complex give a coupling constant of -28.2 cm^{-1}, while the deviations between these contributions and the total coupling constants are larger for the Ni–Ni system without bridge, where the coupling constant of -19.2 cm^{-1} is roughly 5 cm^{-1} lower than the total coupling constant in Table 6.2 if only highest four occupied α MOs are included. Because only qualitative trends are of interest, these deviations are acceptable. The MO contours of the MOs involved in the largest spin-flip excitations for the Ni–NP–Ni system and the bridgeless Ni–Ni analogue are given in Figure 6.8. As in the previous section, the MOs of Ni–NP–Ni are compared to the ones of

the Ni–Ni system to compare the spin-flip excitations in both systems and thus to identify potentially arising contributions from spin-flip excitations involving bridge-centered MOs (Tables 6.6 and 6.7).

Table 6.6: Spin-flip excitations from the HOMO-3$^{\alpha}$ and HOMO$^{\alpha}$ to different pairs of bonding and antibonding virtual orbitals and their contributions ($j_{\mathrm{Green}}(i,j)$) in cm^{-1} for Ni–NP–Ni and the corresponding spin-flip excitations in the systems without bridge calculated with the Green's-function approach on the electronic structure of the high-spin state for the structures optimized for the BS determinants calculated with TPSSH /def2-TZVP.

with bridge		without bridge	
$i \rightarrow j$	$j_{\mathrm{Green}}(i,j)$	$i \rightarrow j$	$j_{\mathrm{Green}}(i,j)$
HOMO$^{\alpha}$ $\rightarrow$ LUMO$^{\beta}$	−504.0	HOMO$^{\alpha}$ $\rightarrow$ LUMO$^{\beta}$	−666.5
HOMO$^{\alpha}$ $\rightarrow$ LUMO+2$^{\beta}$	489.9	HOMO$^{\alpha}$ $\rightarrow$ LUMO+3$^{\beta}$	563.7
HOMO-3$^{\alpha}$ $\rightarrow$ LUMO$^{\beta}$	400.5	HOMO-3$^{\alpha}$ $\rightarrow$ LUMO$^{\beta}$	641.6
HOMO-3$^{\alpha}$ $\rightarrow$ LUMO+2$^{\beta}$	−455.8	HOMO-3$^{\alpha}$ $\rightarrow$ LUMO+3$^{\beta}$	−539.7
$\sum_1$	−69.3	$\sum_1'$	−0.8
HOMO$^{\alpha}$ $\rightarrow$ LUMO+1$^{\beta}$	37.5	HOMO$^{\alpha}$ $\rightarrow$ LUMO+1$^{\beta}$	–
HOMO$^{\alpha}$ $\rightarrow$ LUMO+3$^{\beta}$	−22.3	HOMO$^{\alpha}$ $\rightarrow$ LUMO+2$^{\beta}$	−10.4
HOMO-3$^{\alpha}$ $\rightarrow$ LUMO+1$^{\beta}$	−6.8	HOMO-3$^{\alpha}$ $\rightarrow$ LUMO+1$^{\beta}$	−4.8
HOMO-3$^{\alpha}$ $\rightarrow$ LUMO+3$^{\beta}$	54.3	HOMO-3$^{\alpha}$ $\rightarrow$ LUMO+2$^{\beta}$	1.2
$\sum_2$	62.8	$\sum_{2'}$	−13.9
HOMO$^{\alpha}$ $\rightarrow$ LUMO+4$^{\beta}$	−117.1	–	–
HOMO$^{\alpha}$ $\rightarrow$ LUMO+6$^{\beta}$	11.9	–	–
HOMO-3$^{\alpha}$ $\rightarrow$ LUMO+4$^{\beta}$	95.9	–	–
HOMO-3$^{\alpha}$ $\rightarrow$ LUMO+6$^{\beta}$	−9.6	–	–
$\sum_3$	−18.9	–	–
$\sum_{\mathrm{tot}}$	−25.5	$\sum_{\mathrm{tot}'}$	−14.7

It can be seen by comparing the MOs for the nickelocene systems (Figure 6.8) that the LUMO+4$^{\beta}$, the LUMO+5$^{\beta}$, and the LUMO+6$^{\beta}$ in the Ni–NP–Ni complex have no analogues in the Ni–Ni structure where the bridge is omitted. However, while only the LUMO+5$^{\beta}$ is fully bridge-centered, it gives no contributions to the coupling constants.

The analysis of the spin-flip excitations reveals that although new bridge-centered virtual β spin orbitals are found, the most significant occupied α MO contribution do not involve any spin-flip excitations to these MOs, as for example observed for the Co systems in the previous section. This however shows that the bridge is not as strongly involved in the spin coupling as for the Co systems.

Table 6.7: Spin-flip excitations from the HOMO-2$^\alpha$ and HOMO-1$^\alpha$ to different pairs of bonding and antibonding virtual orbitals and their contributions ($j_{\mathrm{Green}}(i,j)$) in cm^{-1} for Ni–NP–Ni and the corresponding spin-flip excitations in the systems without bridge calculated with the Green's-function approach on the electronic structure of the high-spin state on the structure optimized in the BS determinant calculated with TPSSH / def2-TZVP.

with bridge		without bridge	
$i \rightarrow j$	$j_{\mathrm{Green}}(i,j)$	$i \rightarrow j$	$j_{\mathrm{Green}}(i,j)$
HOMO-1$^\alpha$ $\rightarrow$ LUMO$^\beta$	25.1	HOMO-1$^\alpha$ $\rightarrow$ LUMO$^\beta$	–
HOMO-1$^\alpha$ $\rightarrow$ LUMO+2$^\beta$	−35.0	HOMO-1$^\alpha$ $\rightarrow$ LUMO+3$^\beta$	−5.8
HOMO-2$^\alpha$ $\rightarrow$ LUMO$^\beta$	−11.3	HOMO-2$^\alpha$ $\rightarrow$ LUMO$^\beta$	−10.0
HOMO-2$^\alpha$ $\rightarrow$ LUMO+2$^\beta$	55.9	HOMO-2$^\alpha$ $\rightarrow$ LUMO+3$^\beta$	–
$\sum_4$	34.6	$\sum_{4'}$	−15.8
HOMO-1$^\alpha$ $\rightarrow$ LUMO+1$^\beta$	−601.3	HOMO-1$^\alpha$ $\rightarrow$ LUMO+1$^\beta$	−654.5
HOMO-1$^\alpha$ $\rightarrow$ LUMO+3$^\beta$	563.5	HOMO-1$^\alpha$ $\rightarrow$ LUMO+2$^\beta$	615.7
HOMO-2$^\alpha$ $\rightarrow$ LUMO+1$^\beta$	572.1	HOMO-2$^\alpha$ $\rightarrow$ LUMO+1$^\beta$	633.7
HOMO-2$^\alpha$ $\rightarrow$ LUMO+3$^\beta$	−574.0	HOMO-2$^\alpha$ $\rightarrow$ LUMO+2$^\beta$	−583.6
$\sum_5$	−56.9	$\sum_{5'}$	11.3
HOMO-1$^\alpha$ $\rightarrow$ LUMO+4$^\beta$	9.7	–	–
HOMO-1$^\alpha$ $\rightarrow$ LUMO+6$^\beta$	−3.1	–	–
HOMO-2$^\alpha$ $\rightarrow$ LUMO+4$^\beta$	−5.3	–	–
HOMO-2$^\alpha$ $\rightarrow$ LUMO+6$^\beta$	2.2	–	–
$\sum_6$	3.5	–	–
$\sum_{\mathrm{tot}}$	−1.5	$\sum_{\mathrm{tot}'}$	−4.5

6.4.3 Virtual Bridge-Centered Molecular Orbitals: The Key to the Through-Space and Through-Bond Contributions?

The knowledge about the virtual β spin MOs with mainly bridge character provides the opportunity to automatically evaluate the through-bond contributions by summing up the contributions arising from all occupied α spin orbitals to these virtual bridge-centered β spin MOs ($j^{\beta}_{\mathrm{Green,MO(virt)}}(j)$), defined according to Equation (3.28). Summing up these values for all important bridge-centered virtual β MOs then results in the estimated through-bond contributions. The through-space contributions are then estimated as the differences between the total coupling constants and the estimated through-bond contributions. However, it must be noted again that this way of estimating the different contributions neglects the fact that some other MOs also have bridge contributions. In all cases, only contributions larger than 5% of the total coupling constant are considered. This is also important for systems as the Ni–NP–Ni and V–NP–V complexes with more than one unpaired electron on each spin center, which makes an analysis by hand quite tedious due to the larger number of contributions. The highest occupied α and the lowest unoccupied β spin orbitals for V–NP–V are

given in Figure A.8 in the Appendix. The thus-obtained through-bond and through-space contributions are given in Table 6.8.

Table 6.8: Estimated through-bond contributions obtained from the Green's-function approach by adding up the contributions from the virtual bridge-centered β spin orbitals and trough-space contributions calculated as the difference between total coupling constant and the estimated through-bond contributions. The calculations are performed on the electronic structures of the high-spin states obtained with TPSSH / def2-TZVP on the molecular structures optimized as BS determinants.

system	bridge MOs	through-space	through-bond
V–NP–V	LUMO$^{\beta}$	−1.1	0.6
Ni–NP–Ni	LUMO+5$^{\beta}$*	−25.6	0.0
Co–NP–Co	LUMO$^{\beta}$, LUMO+4$^{\beta}$	−5.4	−12.8
Co–ANPY–Co	LUMO$^{\beta}$, LUMO+5$^{\beta}$*	27.6	−156.2

* Contributions from the LUMO+5$^{\beta}$ are smaller than 5% of the coupling constant and are not shown in the analysis.

The estimated through-bond and through-space contributions are very similar to those obtained by visual inspection of the largest spin-flip excitations. While for V–NP–V and Ni–NP–Ni only insignificant contributions from the bridge are found, the contributions from the bridge-centered MOs in the Co–NP–Co and Co–ANPY–Co complexes are much larger than the corresponding contributions from the direct through-space interaction, which was already explained in the previous section by the low-lying bridge-centered MOs in the Co(II) systems. However, the through-space interactions in the Co–ANPY–Co system are ferromagnetic, while the contributions from the Co–NP–Co are slightly antiferromagnetic, which is a consequence of the ferromagnetic contributions from the LUMO+4$^{\beta}$ in the latter system, while the corresponding MO (LUMO+5$^{\beta}$) in the former system does not give any significant contributions. However, the contributions for the bridgeless systems are slightly ferromagnetic in both systems, which shows that the electronic effects due to the presence of the bridge indeed appear to modify the through-space contributions compared to the through-space contributions obtained by removing the bridge. This analysis shows that the contributions from bridge-centered virtual β MOs are a good qualitative measure for the through-bond contributions in the systems under study here.

6.5 Angular Dependence of Spin Coupling in Biscobaltocene Complexes

In a last step, the spin coupling in the Co–NP–Co and Co–ANPY–Co complexes is analyzed as a function of the torsional angles θ between the Cp planes and the

plane spanned by the bridge (Figure 6.9) to see how far the through-space and through-bond contributions are affected by changes in θ. Therefore, the torsional angles are fixed to certain values, and constrained structure optimizations are carried out for the BS determinants using TPSSH / def2-TZVP.

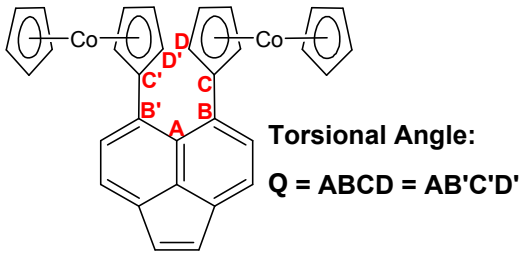

Figure 6.9: Definition of the θ angles which are systematically varied in this section to study their effect on the spin coupling in the Co–NP–Co and Co–ANPY–Co complexes.

In the following, the coupling constants obtained from the BS–high-spin energy differences are first compared to those from the Green's-function approach (Section 6.5.1). In Section 6.5.2, the angular dependence of the local spins on the different fragments in both systems is studied. In Section 6.5.3, finally the through-bond contributions arising from virtual bridge-centered β spin orbitals are analyzed to obtain estimated values for the through-bond and indirectly also for the through-space contributions.

6.5.1 Spin Coupling Constants

Coupling constants are calculated from the energy-difference between the unprojected BS determinants and the high-spin determinants on the one hand and from the Green's-function approach employing the electronic structure of the high-spin state on the other hand (Figure 6.10) and compared to each other.

The trends for the coupling constants are in good qualitative agreement with each other for both methods, although at lower θ values the coupling constants from the BS approach deviate in an unsystematic manner from the Green's-function approach for Co–NP–Co. It should also be noted that the coupling constants from the Green's-function approach are always more strongly antiferromagnetic than the BS values. For both bridges, opposite trends were observed for the dependence of J on the torsional angle, giving a decreasing antiferromagnetic spin coupling for Co–ANPY–Co, and an increasing antiferromagnetic spin coupling for Co–NP–Co with increasing angle, until both curves meet at 80° regardless of the method used. These results support the validity of a further investigation of the spin coupling by the Green's-function approach.

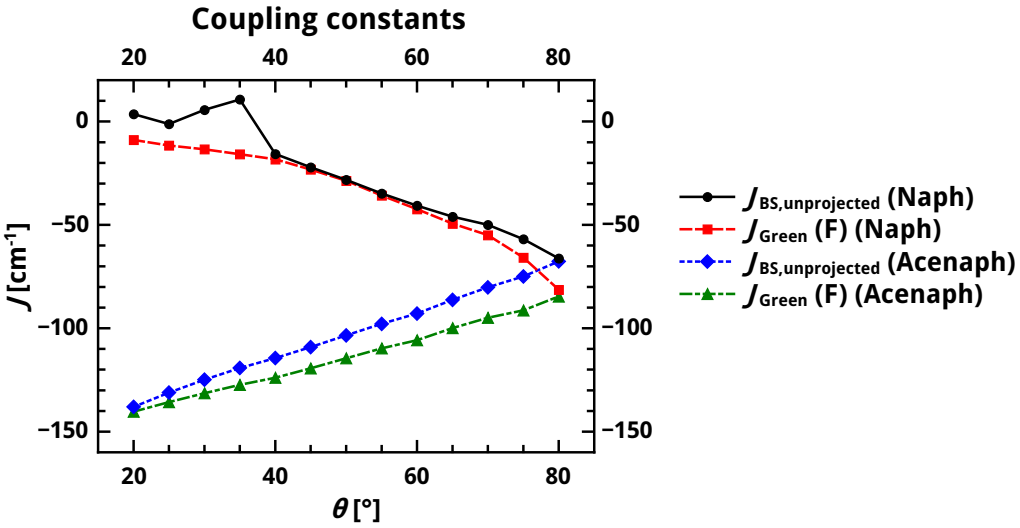

Figure 6.10: Coupling constants calculated with the unprojected BS approach and with the Green's-function approach applied to the electronic structure of the high-spin state employing the BS constrained-optimized structures and TPSSH / def2-TZVP.

6.5.2 Local Spins

The π conjugation between the Cp rings and the bridge might change with respect to the torsional angles in both complexes, which might also affect the spin transfer onto the bridge. Therefore, the local spins for the cobalt(II) ions, the Cp rings, and the bridges are studied for Co–NP–Co and Co–ANPY–Co in the high-spin and low-spin state approximated by a BS determinant (Figure 6.11) as a function of the torsional angles θ.

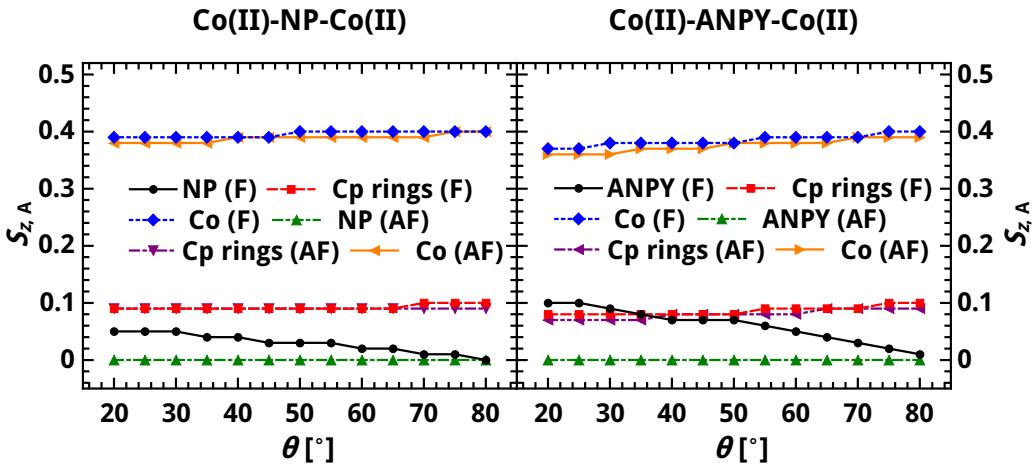

Figure 6.11: Mulliken local spins calculated for the high-spin state and BS determinants of Co(II)–NP–Co(II) and Co(II)–ANPY–Co(II) as a function of the torsional angle θ calculated with TPSSH / def2-TZVP on the molecular structures optimized as BS determinants.

In the high-spin state, the local spins on the bridges decrease for both complexes with increasing angle θ, while for the low-spin states approximated by the BS determinants, the spin contributions from the bridge are zero. However, the local spins for the ANPY-bridged complex are always larger than those of the NP-bridged complex. For the Co(II) ions and the Cp rings, the local spins increase with the torsional angle, which is in agreement with the expectations of a smaller spin transfer onto the bridge with larger twisting.

6.5.3 Exchange Pathways from the Green's-Function Approach

The scheme successfully employed in Section 6.4.3 is here used to see how far the brigde contributions to spin coupling change with increasing angle θ. Therefore, the virtual-orbital contributions from the bridge-centered MOs are summed up (the same virtual β MOs as in the previous section are considered), and the differences to the coupling constants are evaluated to obtain estimated values for the through-space contributions (Figure 6.12).

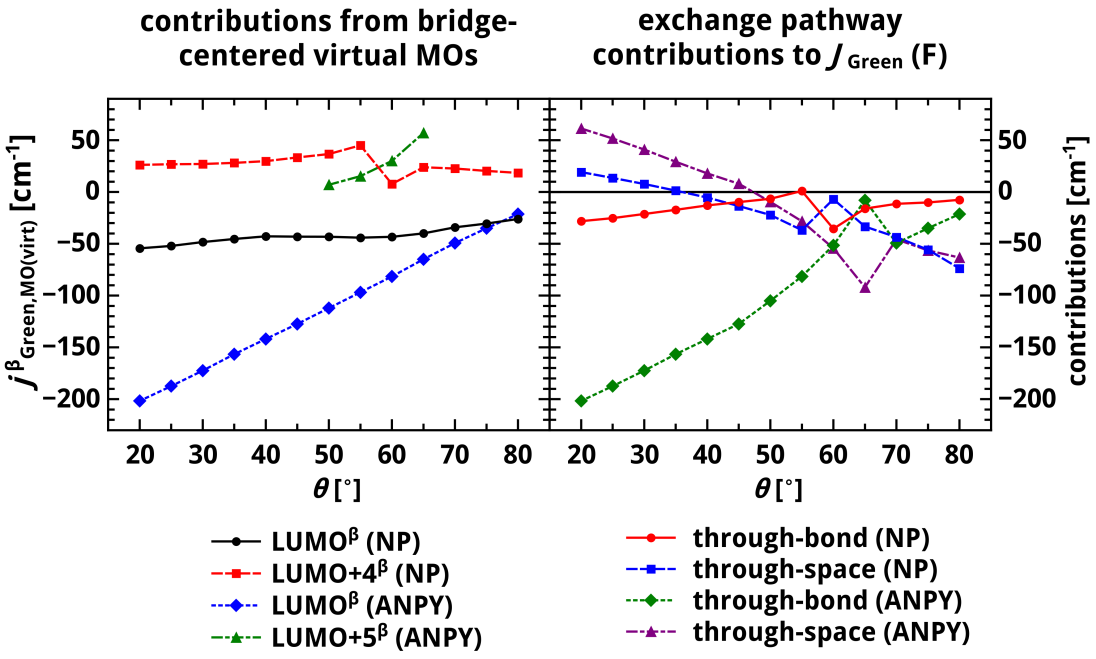

Figure 6.12: Virtual β spin orbital contributions, $j^{\beta}_{\mathrm{Green,MO(virt)}}$ according to Equation (3.28), for the Co–NP–Co and Co–ANPY–Co complexes calculated by the Green's-function approach on the electronic high-spin state structures calculated with TPSSH / def2-TZVP (left), calculated through-bond contributions obtained by adding up the values on the left, and through-bond contributions resulting from the energy difference between the total coupling constants and the through-bond contributions.

For the NP bridge, the $j^{\beta}_{\mathrm{Green,MO(virt)}}$ values of the LUMO$^{\beta}$ and the LUMO+4$^{\beta}$ must be taken into account, while for the ANPY bridge only the LUMO$^{\beta}$

gives significant contributions at all angles considered. Only for angles between 50° and 65° the LUMO+5^{β} gives contributions larger than 5% of the coupling constant, while these contributions were lower at all other angles. The contributions from the LUMO$^{\beta}$ are antiferromagnetic and decrease in strength upon an increase in θ. Nevertheless, these contributions are in general much weaker for the NP than for the ANPY bridge, and the changes are the contributions are in general larger for the latter bridge. This correlates with the spin density contributions on the bridge studied in the previous section, which have been much lower for the NP bridge than for the ANPY bridge and change less strongly with increasing angle.
However, the contributions in the NP-bridged system from the the LUMO+4^{β} are ferromagnetic and increase in strength up to an θ value of 55°, then pass a minimum at 60°, increase and then decrease again. This trend might result from neglecting the bridge contributions in the not fully bridge-centered MOs, or it could indeed by a real feature in the angular dependence of the spin coupling. By calculating the sums over these contributions from both systems, the through-bond contributions to the coupling constants are estimated. It is found that up to an angle of 55° the contributions from the bridge are antiferromagnetic and decrease in strength with increasing angle, while the estimated through-space contributions show a trend towards antiferromagnetic coupling. At higher angles however, unsystematic deviations are found as a result of the features in the contributions obtained from the spin-flip excitations. Although some unsystematic deviations from the expected trend for the through-space and through-bond contributions are observed, it is found that the through-bond contributions approach zero at larger angles, which is physically reasonable since the π conjugation between Cp rings and bridge is not possible anymore at 90°.

6.6 Conclusions

In this chapter, different π-stacked bismetallocene complexes were investigated and the effect of employing different bridges and metal centeres was investigated. For these systems, two different potential contributions exist, through-space and through-bond respectively. To investigate the role of both mechanisms the Green's-function approach was used to investigate the contributions of these two pathways. In addition, the topology of the bridge was taken into account and especially the effect of going from alternant to non-alternant hydrocarbon bridges was taken into account. Also a tetranuclear cobaltocene complex was considered here, to see if the Green's-function approach is applicable to metallocene systems with more than two spin centers.
The DFT structural parameters were in good agreement with the experiment. Only in the case of Co–ANPA–Co, the torsional angles between the Cp rings and the bridge were underestimated by 7°. Also, the calculated coupling constants obtained from the BS energy-difference approach and from the Green's-

function approach were both in good agreement with the experimental values; only for the Co–ANPA–Co system the antiferromagnetic coupling was strongly underestimated, which could be related to the underestimation of the torsional angle. For the tetranuclear cobaltocene complex, the nearest-neighbor interaction was antiferromagnetic for the coupling between the outer cobaltocenes with the inner ones, and between the inner cobaltocenes, regardless whether the Green's-function method or the BS-energy-difference method was employed. This shows that the Green's-function approach can also be applied to metallocene complexes with more than two centers, where only the high-spin state must be taken into account and not all six spin orientations as in the BS approach. In all cases antiferromagnetic coupling was observed. For Ni–NP–Ni and V–NP–V, the omittance of the bridge did not influence the spin coupling much, while in Co–NP–Co and Co–ANPY–Co the spin coupling was slightly ferromagnetic if the bridge was omitted, in contrast to the antiferromagnetic behavior when the bridge was present.

To understand these findings, the largest contributions from spin-flip excitations arising from the singly occupied α spin orbitals for the Ni–NP–Ni, Co–ANPY–Co, and Co–NP–Co complexes were investigated and found to reproduce the coupling constants well. Comparing these spin-flip excitations to the ones for the systems without bridge gave us the opportunity to highlight the changes that result from the introduction of the bridge. For Co–ANPY–Co, the LUMO$^{\beta}$ was identified as a bridge-localized MO producing large antiferromagnetic contributions, while the through-space interactions were ferromagnetic as for the systems without bridge. By going from the ANPY to the NP bridge, although two bridge-centered MOs were found among the virtual β spin orbitals lowest in energy, only the one with coefficients on the acetylene part produced large antiferromagnetic contributions, while the other one was not involved in the spin coupling. For the naphthalene bridge, the second bridge-centered virtual MO gave ferromagnetic contributions leading to a smaller antiferromagnetic net contribution. For the Ni–NP–Ni complex, these bridge-centered MOs were much higher in energy than for the Co systems and were not involved in the largest contributions from the spin-flip excitations.

By calculating the sums over spin-flip excitations to bridge-centered virtual β spin orbitals, the through-bond and through-space contributions to the coupling constant could be successfully reproduced compared to an MO analysis by hand. For the V–NP–V system, also the LUMO$^{\beta}$ was the only bridge-centered MO and gave very weak ferromagnetic contributions (smaller than 1 cm^{-1}).

Finally, the angular dependence of the spin coupling and the contributions to the spin coupling from both potential pathways on the torsional angle between the bridge and the Cp rings was studied. The coupling constants calculated with the Green's-function approach were in good agreement with those obtained from the unprojected BS approach. Only at very low angles, unsystematic deviations for the coupling constants calculated with the BS approach compared from the expected trends were observed, which were not found for the Green's-function

approach.
The local spins showed that the spin delocalization onto the bridge decreased with increasing torsional angle irrespective of the bridge, but were always larger for the ANPY bridge than for the NP bridge. By analyzing the contributions to the coupling constant from bridge-centered virtual β spin orbitals, it was shown that the through-space interactions indeed shifted to antiferromagnetic coupling with increasing angle, while the bridge contributions approached zero. This shows that the choice of the metal center has a crucial influence on the degree of spin delocalization onto the Cp ligands and the bridge and therefore indirectly determines whether the bridge affects the spin coupling at all. If it does, also the dependence on the structural parameters, as for example the torsional angles, can be very drastic as for the Co–NP–Co and Co–ANPY–Co systems.

7. Analyzing Spin Coupling Pathways: Conclusions

In this part, a Green's-function approach, orginally derived by Lichtenstein and coworkers [32] in the context of solid-state physics (and rederived by the author [180] employing local projection operators following Ozaki and coworkers), was tested intensively as a method for the prediction and understanding of spin coupling by decomposing it into contributions from molecular orbitals.

In Chapter 4, coupling constants were calculated for a large number of spin-coupled systems by employing this Green's-function approach, and the values were compared to Noodleman's BS approach usually used in the literature. The results of both approaches were in reasonable agreement, as long as the former was applied to the high-spin state, and as long as structural relaxation effects from one spin state to another had a small influence. Strong changes in the spins' magnitudes also lead to strong deviations for the Green's-function approach compared with the BS approach [163].

These encouraging results suggested to employ the Green's-function approach as a method for the automated evaluation of exchange pathways in transition–metal complexes. In Chapter 5, two dinuclear complexes known from the literature were analyzed to see if this approach is able to recover the literature findings to a large extent by taking into account the contributions from spin-flip excitations between occupied α and virtual β spin orbitals. It could be concluded that the Green's-function approach is a reliable tool for the discussion of exchange pathways.

In Chapter 6, the spin coupling and the corresponding exchange pathways were investigated in a series of π-stacked bismetallocene complexes, differing in the bridges as well as in the metal center employed. These systems are interesting due to the two potential exchange pathways, involving a through-space and a through-bond contribution. The Green's-function should have an advantage over the omittance of the bridge, because it covers the electronic effects of the bridge on the the spin coupling, while these contributions are missing in the latter approach. For the bisnickelocene and bisvanadocene complexes, the Green's-function approach showed that although there were low-lying bridge-centered MOs, the contributions from these MOs were insignificant in both contributions. This is also in agreement with the coupling constants for the bridgless systems, which were found to only slightly change compared to the systems with a bridge. However, in the biscobaltocene complexes, the contributions from bridge-centered MOs were large and antiferromagnetic. For Co–ANPY–

Co, the resulting through-space contributions were more strongly ferromagnetic than the coupling constants obtained for system without bridge. However, for the Co–NP–Co system, the through-space contributions were slightly antiferromagnetic which was in contrast to the slightly ferromagnetic coupling constants for the bridgeless analogue. This underlined the crucial influence of the bridge on the spin coupling. By studying the dependence of the spin coupling on the torsional angles between the bridge and the Cp rings, it could be observed that at low angles the through-space contributions were ferromagnetic and the bridge contributions are antiferromagnetic, but with increasing angle the former contributions were shifted to antiferromagnetic coupling until the contributions from both pathways changed their sign. However, in this chapter only the contributions from fully bridge-centered MOs were considered for the through-bond contributions, while the bridge contributions to other MOs were neglected. In future work, it is therefore reasonable to calculate the contributions for all occupied and virtual MOs, the contributions from the MO coefficients on the bridge for these MOs, and then decompose the contributions to the coupling constants arising from these MOs by multiplying the contributions by the MO contributions from bridge and spin centers.

After showing that a reliable prediction and understanding of spin coupling is feasible, it is interesting to see how spin coupling could be potentially controlled by light. In the next chapter, the switching behavior and the spin coupling of a series of metallocene-substituted photochromic DTE switches is investigated with the aim to obtain spin-coupled cobaltocene switches in which the spin coupling can potentially be switched by light of an appropriate wavelength.

Part II: Controlling Magnetic Properties by Photoswitchable Bridges

Molecular photochromic switches are able to undergo reversible transformations between isomeric forms with different optical, physical and chemical properties and are therefore interesting for various photonic devices [181–184]. Different types of photochromic switches involving for example azo bridges [185–187] and spiropyranes [188–190] were reported. However, these switches are often hardly of interest for applications because of thermal instability or irreversibility of the photoreaction. One class of photochromic switches fulfilling both prequisites are dithienylethene (DTE) switches [182, 191] (Figure 7.1). This class of switches consists of two aromatic thiophene systems connected via ethene or cycloalkene bridges. The open form is cross-conjugated, and the thiophene π systems are isolated. Irradiation with ultraviolet (UV) light initiates a reaction to the closed form, which is now fully π-conjugated. The reverse ring-opening reaction can be initiated by irradiation with visible light. The theoretical basics of the photoswitching are discussed in further depth in Chapter 8. In principle, these structural changes can be used to switch different properties, as for example fluorescence [192–196], catalytic activity [197–201], non-linear optical activity [202–207], or conductance [208–212].

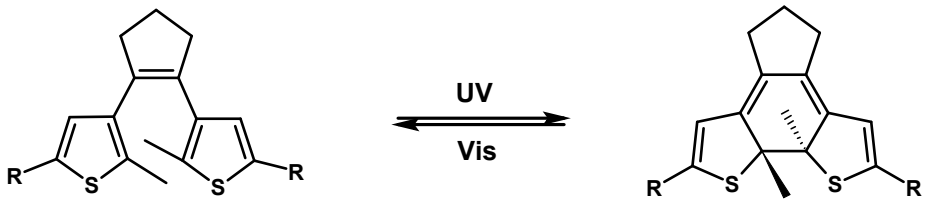

Figure 7.1: Isomeric forms of the DTE switch, and the wavelength of light initiating the interconversion between both forms.

Another interesting application is the switching of exchange spin coupling in magnetic systems employing photochromic switches to bridge two moieties carrying unpaired electrons. By using the spin coupling as an output, they could be used as information processing units, controlled by light [25]. Matsuda and coworkers [25, 210] demonstrated this by synthesizing a photochromic DTE switch bridging two nitronyl nitroxide (NNO) radical moieties. They found that

due to the cross-conjugation in the open form, the unpaired electrons on the NNO moieties only weakly interact with each other. Because the nature of the photochromic bridge changes from cross-conjugated to fully conjugated upon photocyclization, the spin coupling is strongly increased in the closed form.
In addition to the experimental studies carried out, a large number of different photochromic switches have been characterized theoretically [207, 213–216]. For example, Irie systematically investigated the effect of the bridge and of different aromatic groups on the switching behavior of photochromic diarylethene switches by means of semi-empirical calculations [182]. Because of their outstanding properties, the 1,2-bis(2-methylthien-3-yl)cyclopentene switches were targets of many further theoretical investigations involving DFT [217] and multi-reference approaches such as the complete active space self-consistent field (CASSCF) method [218]. Also DTE switches with platinum(I)- [219] and ruthenium(II)-based organometallic groups [220] were successfully described by quantum chemical methods.
Escribano and coworkers [221] synthesized a series of metallocene-substituted DTE switches with the aim of obtaining metal-organic counterparts to the NNO-substituted system described by Matsuda and coworkers [25, 210]. The eventual goal was to obtain metallocene-based systems with photoswitchable spin coupling. Furthermore, a route towards chirally substituted DTE-based photoswitches should be opened. Therefore, two photochromic cores were synthesized, differing in the size of the bridging cycloalkene ring, a five-membered cyclopentene and, for the first time, a six-membered cyclohexene ring. In contrast to the former, the latter allows for chiral chemical substitution. These photochromic cores were decorated with different substituents, and their structural and optical properties were characterized. As a complement to the experimental studies, and to explain the observed switching behavior, DFT and TDDFT calculations are discussed in this part.
In Chapter 9, two "bare" chlorine-substituted DTE switches, differing in the size of the cycloalkene ring, are compared to each other. This is a good starting point, since they showed a very good switching behavior [180], and therefore are taken as a reference to evaluate the influence of the metallocene substituents on the switching.
In Chapter 10, diamagnetic ferrocene-substituted switches are investigated, which is the next step in terms of complexity before going to open-shell moieties [222]. These switches were compared to an ethynyl-spaced DTE analogue synthesized by Guirado and coworkers [223], and to the chlorine-substituted switches discussed in Chapter 9.
In Chapter 11, the complexity of the systems is increased even further, and the switching properties of two cobaltocene-based switches are compared. In the first system, the photochromic unit is linked via a sp^3 hybridized carbon atom to the metallocene, preventing π conjugation with the photochromic bridge. In the second, the connecting carbon atom of the Cp ring is sp^2 hybridized, and the Cp ligand is therefore in conjugation to the π system of the photochromic

switch.
One of the goals by comparing these different switches is to elucidate if and how the metallocenes affect the DTE switching behavior. Both diamagnetic and paramagnetic metallocene centers are studied.
Besides the switching behavior, it is checked if DFT is able to describe the spin coupling in these systems correctly. Matsuda pointed out [25] that for the closed form of the NNO system, two resonance structures can be drawn (see also Figure 12.1 in Chapter 12), referring to an open-shell and a closed-shell singlet state. Similar resonance structures can also be drawn for the cobaltocene-substituted switch. Although EPR measurements revealed an open-shell ground state for the NNO system of Matsuda and coworkers [25] in the closed form, this must not necessarily be the case for the cobaltocene system. It is checked if DFT is able to give an unambiguous description of the bis(cobaltocene) complexes by comparing them to the synthesized NNO system. Furthermore, the influence of different photochromic bridges on the properties, and the effect of perfluoration of the cycloalkene ring are taken into account. Different exchange–correlation functionals with different amounts of Hartree–Fock exchange are employed, in order to evaluate the influence on the structural parameters, the diradical characters, the spin coupling, and the aromaticity in these systems. The amount of Hartree–Fock exchange is taken into account, because it was shown earlier that is has a strong influence on the spin-state energetics in transition-metal complexes [224]. The aromaticity is studied because Sun and coworkers [37] found that open-shell character in polycyclic aromatic hydrocarbons increases with increasing aromaticity in diradicals possessing a singlet ground state. It is checked if similar correlations exist for for the magnetic DTE switches investigated here. Because the π system of the bridge is found to play an important role for the exchange coupling, it is also checked how far the coupling constants from the Green's-function method depend on the definition of the magnetic centers by excluding and including the bridge in the definition. It should be pointed out that since to date no X-ray crystallographic and magnetic data could be obtained experimentally for the magnetic switches under study here, these theoretical calculations constitute the only source of knowledge on these properties so far, to be compared with experimental findings at a later point.

8. Theoretical Basics of Dithienyl Ethene Photoswitching

In this chapter, the different aspects of the photoreactions in DTE switches are discussed. First the Woodward–Hoffmann rules are revised, which provide a connection between the MO symmetry and stereospecificity of electrocyclic ring-opening and ring-closure reactions (Section 8.1), from which the reactivity of photochromic switches can be understood. Afterwards, the different kinds of photoreactions are discussed (Section 8.2). In Section 8.3, a notation used for the different photochromic switches in Chapters 9-11 is introduced.

8.1 Woodward–Hoffmann Rules for Pericyclic Reactions

As mentioned in the introduction, the open and closed isomer show a remarkable stability in the ground state, hindering thermally activated cyclization and cycloreversion.

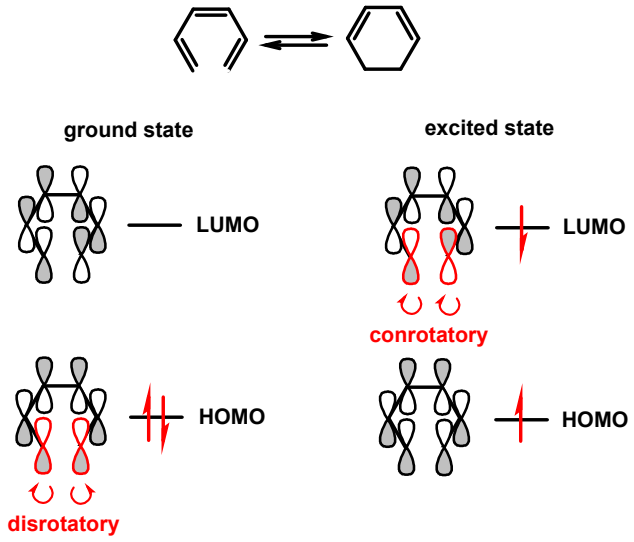

Figure 8.1: Frontier orbitals of the 1,3,5-hexatriene involved in the pericyclic ring closure reaction in the ground and the lowest excited state.

This can be understood by the Woodward–Hoffmann rules [225–228], which explain the stereospecificity of electrocyclic ring-opening and ring-closure reactions

in the ground state (by thermal activation), and in excited states (by irradiation with light) for systems with $4n$ and $(4n + 2)$ π electrons. The DTE switches (Figure 7.1) refer to the latter systems, for which the most simple example is the 1,3,5-hexatriene, which is used to illustrate the Woodward-Hoffmann rules (Figure 8.1).

In the ground state only the HOMO of the hexatriene molecule is occupied, in which the p orbitals on the terminal carbon atoms have the same phase and the p orbitals need to be rotated in a disrotatory fashion to form a σ bond, present in the closed form. However, if an electron is excited to the LUMO, in which the the p orbitals on the terminal carbon atoms show the opposite phase, forming a σ bond only by a conrotatory rotation of the p orbitals. However, these symmetry relations also imply that the conrotatory in the ground state and the disrotatory ring closure in the excited states are symmetry forbidden, and consequently these types of reactions show large activation barriers.

However when going from 1,3,5-hexatriene to DTE switches, the situation becomes a little more complicated because two different relative orientations of the thiophene subunits are found, antiparallel and parallel respectively (Figure 8.2). For the parallel orientation, the Woodward–Hoffmann rules allow for a conrotatory ring closure reaction in the ground state, while a disrotatory ring closure reaction is expected to occur for the antiparallel orientation. However, the calculations by Nakamura *et al.* [229] pointed out the energy differences between the open forms and closed forms are too large for both orientations, making a ring closure reaction unlikely in both orientations. In the excited state however, only the antiparallel orientation of the thiophene rings results in the formation of the closed form, while the parallel orientation cannot be switched.

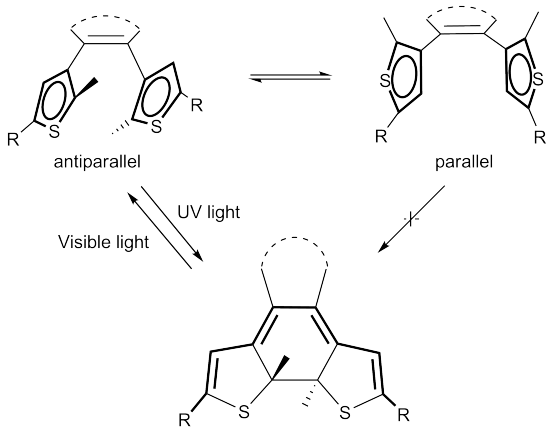

Figure 8.2: Scheme of the antiparallel and parallel orientation of the open forms and reactivity in the ring closure reaction (Figure is taken from Ref. [180]).

8.2 Types of Photoreactions

In this section, the different types of photoreactions are covered that can be potentially observed. The first type of photoreactions are the adiabatic reactions, in which the molecules are excited from the ground state to a higher electronic state, and then relax to the energy minimum of the excited state, which coincides with a minimum on the potential energy surface (PES) of the ground state (top-left panel in Figure 8.3). For this type of photoreaction it is theoretically possible that all reactants are transformed to the product.

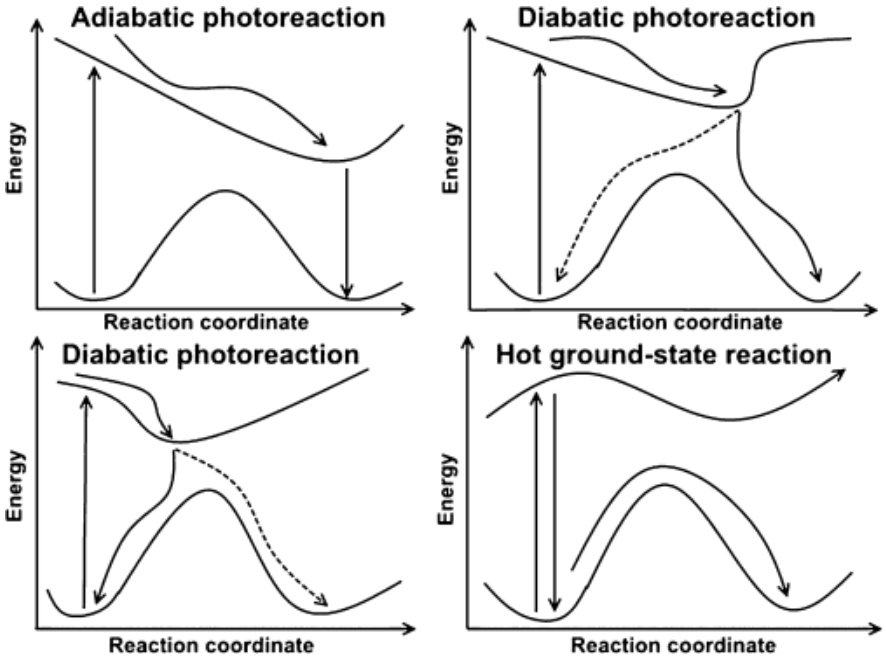

Figure 8.3: Different types of photoreactions (after Refs. [217] and [230]).

The second type of photoreactions are diabatic photoreactions , where the energy minimum of the excited state nearly coincides with the transition state (TS) of the ground-state PES (top-right and bottom-left panel in Figure 8.3). This leads to a radiationless transition from the energy minimum of the excited state's PES to the TS of the ground state, from which the switch reacts to the product or to the reactant minimum. The quantum yields strongly depend on the exact location of the minimum on the PES of the excited state. If it is shifted to the right of the ground-state TS (top-right panel in Figure 8.3), more molecules will be transformed to the product, while more molecules will be transformed back to the starting material when the minimum is shifted to the left of the TS (bottom-left panel in Figure 8.3). The last type of photoreaction is the hot ground-state reaction (bottom-right panel in Figure 8.3), which gains the energy to overcome the TS in the ground state by a radiationless relaxation from the excited state to the ground state [217, 230].

8.3 Notations for the Systems Under Investigation

In this section, a notation for the different photochromic switches studied in Chapters 9-11 is introduced. The switches in these chapters differ by the substituents and by the size of the bridging cycloalkene ring (six-membered vs. five-membered) of the DTE switch. Therefore, the DTE switches bridged by a five-membered cyclopentene ring will be noted as "5DTE", and those with a six-membered cyclohexene ring as "6DTE". The halogen substituents are denoted by their element symbols (Cl and I), while in the case of the metallocenes the element symbol of the metal center is considered (e.g. Fe(II) for ferrocene). The notations themselves, are composed of the abbreviations of the bridge and the substituents, in example the cyclopentene-bridged, ferrocene-substituted switch is denoted as Fe(II)–5DTE–Fe(II).

9. Bare Switches: Chlorine-Substituted Dithienylethenes

The aim of this chapter is to compare the photoswitching behavior of halogen-substituted cyclohexene and -pentene based DTE molecules (Figure 9.1). The cyclohexene-structures were not synthesized before, but would allow for access to chirally substituted photoswitches.

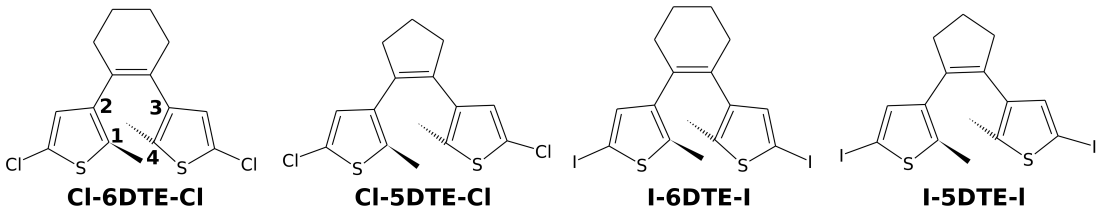

Figure 9.1: Molecular switches under study. The numbered carbon atoms are used to define the torsional angle employed in Table 9.1.

Therefore, 1,2-bis(5-chloro-2-methyl-thien-3-yl)cyclohexene was synthesized by Alejandra Escribano [180, 221] in the group of Jürgen Heck at the University of Hamburg and its behavior during the irradiation with light of different wavelengths was investigated. To obtain deeper insight into the photoswitching properties, KS-DFT calculations of this molecule and of the analogous 1,2-bis(5-chloro-2-methylthien-3-yl)cyclopentene are performed. They are compared with the respective iodo-substituted forms, the newly synthesized 1,2-bis(5-iodo-2-methylthien-3-yl)cyclohexene and the 1,2-bis(5-iodo-2-methylthien-3-yl)cyclopentene [180]. In the following not the full names of the compound are used, but the notation in Section 8.3 is employed.
Based on KS-DFT calculations, the following questions are tried to be answered: 1) How does inserting an additional methylene group in the cyclopentene affect the relative stability of the open and closed forms of the diarylethene switches, in particular through a difference in ring strain? 2) How does the enlarged ring size of the dithienylethene affect the efficiency of photoswitching by modifying shapes and energies of molecular orbitals? For this purpose, molecular structure optimizations and time-dependent DFT (TDDFT) calculations of UV/Vis spectra and orbital contributions to electronic transitions are performed, using the BP86 [41, 231]and the B3LYP [232, 233]exchange–correlation functionals in combination with Ahlrich's def-TZVP [234, 235] basis set. For question (2),

molecular orbital (MO) contributions to the most intense peaks in the calculated UV/Vis spectra are analyzed. The contributing MO transitions are classified according to whether they support ring opening/closure or not, based on whether the MOs to and from which the transition is made have a bonding or an antibonding pattern on the two carbon atoms, where bonds are formed and broken in the process.

9.1 Molecular Structures and Relative Energies

Table 9.1: C1−C4 (C−C) distances between the reactive carbon atoms of the thiophene subunits and torsional angles (as indicated in Figure 9.1) for the open-form isomers of the chloro and iodo variants of the cyclopentenyl switch and their cyclohexenyl congeners optimized using different density functionals (D = dispersion correction of Grimme). Basis set: def-TZVP.

	Cl-5DTE-Cl	
Method	C−C distance [pm]	Torsional angle [°]*
exp.	–	–
BP86	363.0	92.5
BP86-D	325.3	79.3
B3LYP	367.4	82.7
B3LYP-D	331.2	80.9
	Cl-6DTE-Cl	
exp.	350.9(2)	77.5(1)
BP86	362.9	74.3
BP86-D	336.5	73.5
B3LYP	367.4	75.2
B3LYP-D	340.9	74.6
	I-5DTE-I	
exp.	345.79(53)	84.81(29)
BP86	362.8	92.0
BP86-D	324.9	79.9
B3LYP	373.1	94.3
B3LYP-D	331.3	81.2
	I-6DTE-I	
exp.	–	–
BP86	362.9	80.7
BP86-D	336.3	73.9
B3LYP	367.1	82.7
B3LYP-D	339.9	74.8

* Torsional angle (C1−C2−C3−C4, Figure 1)

Structure optimizations with BP86 and B3LYP, with and without including the second generation of the dispersion correction by Grimme [236] (-D), are carried out. For Cl-5DTE-Cl and I-6DTE-I, structural data obtained from a X-ray structure analysis [180, 221] were available, to which the results are compared. Table 9.1 shows the theoretical torsional angles between two planes defined by the thiophene rings and the bond lengths for the open-form isomers of the four switches under study.
Compared to the experimental data, the optimized structures obtained with the BP86 and B3LYP functionals both overestimate the distance between the reactive carbon atoms and the torsional angles. When including Grimmes dispersion correction, the obtained interatomic distances and the torsional angles are underestimated. Nonetheless, the B3LYP-D functional in both cases is in best agreement with the experimental data. While such comparisons are common practice, these conclusions should be interpreted with caution because packing effects in the crystal could play an important role. As expected, the bond lengths, the interatomic distances, and the torsional angles are not influenced by the halogen substituents. For both substituents, using dispersion-corrected functionals result in shorter C–C distances for the 6-ring than for the 5-ring structures, while without this correction, the opposite is true. The torsional angles are always larger for the 6-ring structures. Another difference is found for the central cycloalkene itself (cyclopentenyl and cyclohexenyl derivatives): while the cyclopentene ring is almost planar, the cyclohexene ring shows a half-chair conformation.

Table 9.2: Calculated energy differences between the closed and the open form isomers for the four structures under study (Figure 9.1), optimized with different density functionals (D=dispersion correction of Grimme). All values are given in kJ/mol. Basis set: def-TZVP.

	$E_{(\text{closed})} - E_{(\text{open})}$	
	chloro-substituted switches	
Functional	5DTE	6DTE
BP86	27.1	23.7
BP86-D	15.7	11.9
B3LYP	44.1	42.0
B3LYP-D	30.1	27.0
	iodo-substituted switches	
BP86	32.2	29.0
BP86-D	20.8	17.6
B3LYP	50.1	48.0
B3LYP-D	36.1	33.5

Although the maximal distance between the reactive carbon atoms allowing a ring closure is unknown, Kobatake and coworkers [237] mentioned that the cyclization is able to occur in the crystalline state up to a distance of 420 pm

in the antiparallel conformation. The switching in the parallel conformation however is symmetry forbidden (Section 8.1). The distances between the reactive carbon atoms are in the same range for both types of cycloalkene rings and are always shorter than the limit given by Irie, so that the ring closure is not hindered in that way.
It can be seen from Table 9.2, that the open form is always considerably more stable than the closed form, with energy differences ranging from about 15 kJ/mol to about 50 kJ/mol. The energy differences $E_{(\text{closed})} - E_{(\text{open})}$ are slightly larger for the iodine-substituted compounds than for the chlorine-substituted ones, and slightly larger for the for the 5DTE switches than for the 6DTE ones.

9.2 Comparison of the Photoswitching Behavior of the Chloro-Substituted Switches

To investigate the photoswitching behavior, the experimental UV/Vis spectra [180, 221] recorded in *n*-hexane are compared to the spectra calculated with TDDFT. Because *n*-hexane is non-polar, it is not expected to influence the results drastically and solvent effects are therefore neglected in all calculations. Additionally, the potential energy surfaces of the ground states and the first excited states are scanned as a function of the distance $R\,(\mathrm{C}-\mathrm{C})$ between the two reactive carbon atoms participating in the ring-closure and ring-opening reactions, to get a more detailed picture of the reaction mechanism. Since the halogen substituent is expected to have only a small effect on the switching behavior, only the chlorine-substituted switches are studied in the following. The structures optimized with B3LYP-D and BP86, which are in best and second-best agreement with the X-ray structures, are used. The UV/Vis spectra are calculated with TDDFT using the same exchange–correlation functionals as for the structure optimizations. For the calculations of the excitation energies it is not possible to include dispersion correction.

9.2.1 UV/Vis Spectra

The measured absorption bands are roughly the same for both switches (see Figure 9.2, left vs. right upper panel). In the spectrum of the open-form isomers, one absorption band appears at 233 nm for Cl−6DTE−Cl and 238 nm for Cl−5DTE−Cl (Table 9.3). But there is also a clue for another band appearing below 200 nm for both structures. The spectra calculated with TDDFT give similar results: a transition at 218 nm (240 nm) for Cl-6DTE-Cl and at 229 nm (237 nm) for Cl-5DTE-Cl calculated with B3LYP (BP86) (middle and lower panel of Figure 9.2) is found. In the measured spectra of the closed isomers, these absorption bands still appear at the same position in the spectrum. In addition, a shoulder appears at about 310 nm for both switches and new absorption bands arise at 455 nm for Cl−6DTE−Cl, and at 448 nm for Cl−5DTE−Cl. The same is found for the calculated spectra, where new shoulders are formed at 300 nm

(340 nm) for both switches, and new transitions appear at 493 nm (564 nm) for Cl−6DTE−Cl, and at 478 nm (547 nm) for Cl−5DTE−Cl when using the B3LYP (BP86) functional. The intensity of the lower-energy band at 240 nm decreases less strongly for the measured spectra than for the calculated ones. The reason for this may be that under experimental conditions not all molecules could be converted to the closed-form isomer.

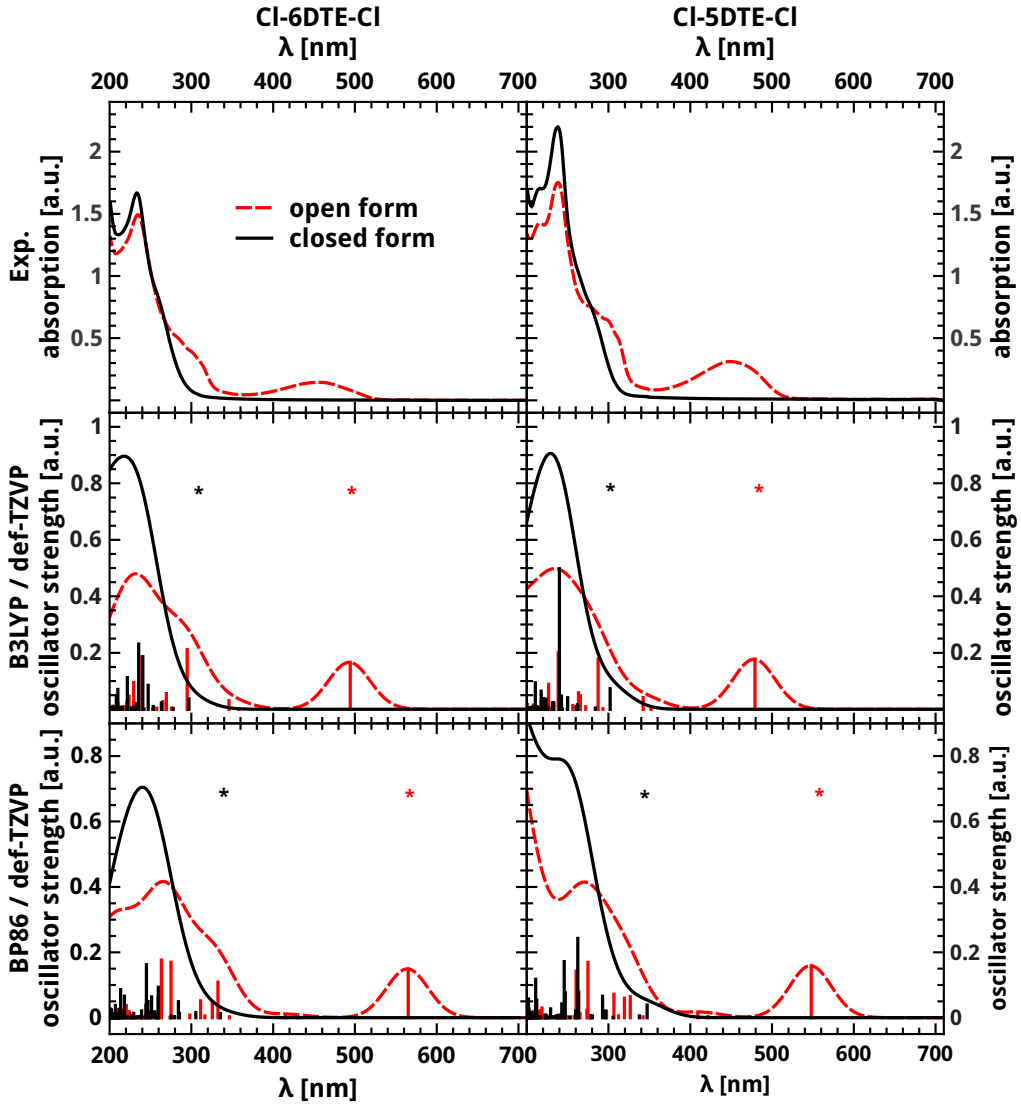

Figure 9.2: Experimental spectra in *n*-hexane and calculated UV/Vis spectra (Gaussian broadening with a half-width of 60 nm for the theoretical spectra) of both isomeric forms of Cl-6DTE-Cl and Cl-5DTE-Cl. The spectra are calculated with BP86/def-TZVP and B3LYP/def-TZVP using TDDFT and the structures optimized with BP86/def-TZVP and B3LYP-D/def-TZVP (The stars denote the positions of the HOMO–LUMO transitions).

According to Feringa and co-workers [238], the band found at 240 nm represents the HOMO–LUMO transition, which must correspond to the lowest energy

transition found in the spectrum. However, in Figure 9.2 the absorption which constitutes the HOMO–LUMO transition Cl−6DTE−Cl is found at 297 nm for the open-form isomer calculated with the B3LYP functional (and for BP86 at 347 nm, not shown) as a small transition with low intensity. This observation is in agreement with theoretical studies in the literature [217,218], which reported low-intensity HOMO–LUMO transitions for different dithienylethene analogues. For Cl−5DTE−Cl, the HOMO–LUMO excitation is found for the open form at 302 nm (347 nm) for B3LYP (BP86), which is only very slightly red-shifted compared to Cl−6DTE−Cl. Since the calculated intensities are small for the HOMO–LUMO transition [217], it is reasonable to assume that the large band at 240 nm is a superimposition of the HOMO–LUMO and other transitions which are split in two different transitions in the calculated spectra [217] (see the discussion of orbital contributions below).

Table 9.3: Position of the absorption bands of the experimental (in *n*-hexane) and calculated UV/Vis spectra in nm. Values from the literature [223] are obtained with the B3LYP functional, the DZVp basis set and the Stevens–Basch–Krauss–Jasien–Cundari effective core potential (SBKJC-ECP). In all other calculations, the basis set was def-TZVP, and no ECPs are used.

	Cl−6DTE−Cl	
method	open form	closed form
exp.	233	235, ∼310 (sh), 455
BP86	240	265, ∼310 (sh), 564
B3LYP	218	232, ∼300 (sh), 493
	Cl−5DTE−Cl	
exp.	238	238, ∼310 (sh), 448
BP86	237	270, ∼340 (sh), 547
B3LYP	229	234, ∼300 (sh), 478
SBKJC-ECP/DZVp/B3LYP [223]	256	423

TDDFT calculations on Cl−5DTE−Cl were already performed by Guirado *et al.* [223] using the B3LYP functional in combination with the double-zeta DZVp basis set and an effective core potential (ECP) for the inner shells. In contrast, in this work a triple-zeta basis set without any ECPs is used, which should give improved results. This is true for the open form of Cl−5DTE−Cl, while the agreement between the experimental spectrum and the calculated spectra of the closed-form isomer is better for the results obtained by Guirado *et al.* [223]. This might be due to error compensation arising from the ECP and the smaller basis set, or from the neglection of solvent effects in the calculations. By comparing these two sets of calculations, no systematic dependence on the basis set size can be extracted with respect to the over- or underestimation of the excitation wavelengths.

Although in all spectra the most intense excitations are located at about 250 nm,

it can be seen from Figure 9.3 for the example of the cyclohexene switch that the MOs contributing to these transitions do not have a shape that leads to ring closure. In some cases the MOs have suitable phases on the thiophene carbon atoms where the double bond is located in the open form, as for example in the HOMO-1, but a σ bond between the cyclopentene carbon atoms. For the HOMO-2, the important coefficients on the thiophene rings are missing. The only MOs shown in Figure 9.3 which have coefficients and phases leading to ring closure are the HOMO and the LUMO. The equivalent orbitals for the closed form of the 6DTE switch are given in Figure 9.4.

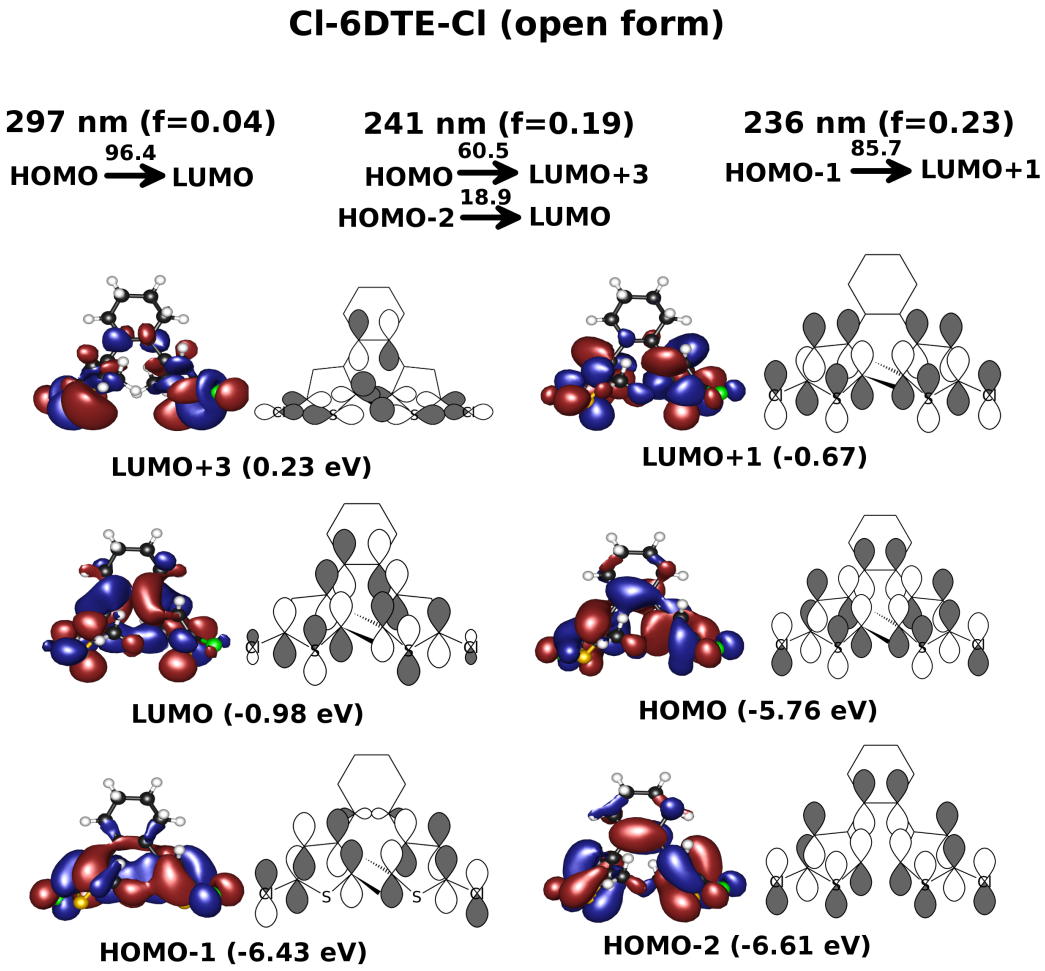

Figure 9.3: Molecular orbital excitations with their weights (given on the arrows), oscillator strengths f and molecular orbital energies [eV] corresponding to the most intense peaks in the UV/Vis spectrum of the open form of Cl−6DTE−Cl calculated with B3LYP/def-TZVP using TDDFT on the structure optimized with B3LYP-D/def-TZVP.

The importance of the HOMO–LUMO transition for the ring-opening and ring-closure reaction was also confirmed by Staykov and co-workers [217] for the

perfluorinated Cl–5DTE–Cl switch. As a consequence, only the shapes of the HOMOs and LUMOs are analyzed for all calculated structures. The MOs for both isomeric forms of both switches calculated with B3LYP-D (top) and BP86 (bottom) are shown in Figure 9.5 (the MOs on the top-left are the same as in Figure 9.3 and Figure 9.4 and are shown again for better comparison).

The HOMO–LUMO transitions for the cyclopentenyl- and the cyclohexenyl-bridged switches are very similar. Also the MOs calculated for the structures optimized with B3LYP-D have the same relative coefficients on the carbon atoms participating in the ring-opening and ring-closure reactions as the BP86 ones.

To get a more detailed picture of the probabilities for these MO transitions initiating ring closure (and ring opening), the transition dipole moments for the HOMO–LUMO-dominated excitations for both isomeric forms of the switches are studied, $d_{01,\text{open}}$ and $d_{01,\text{closed}}$ (see Table 9.4).

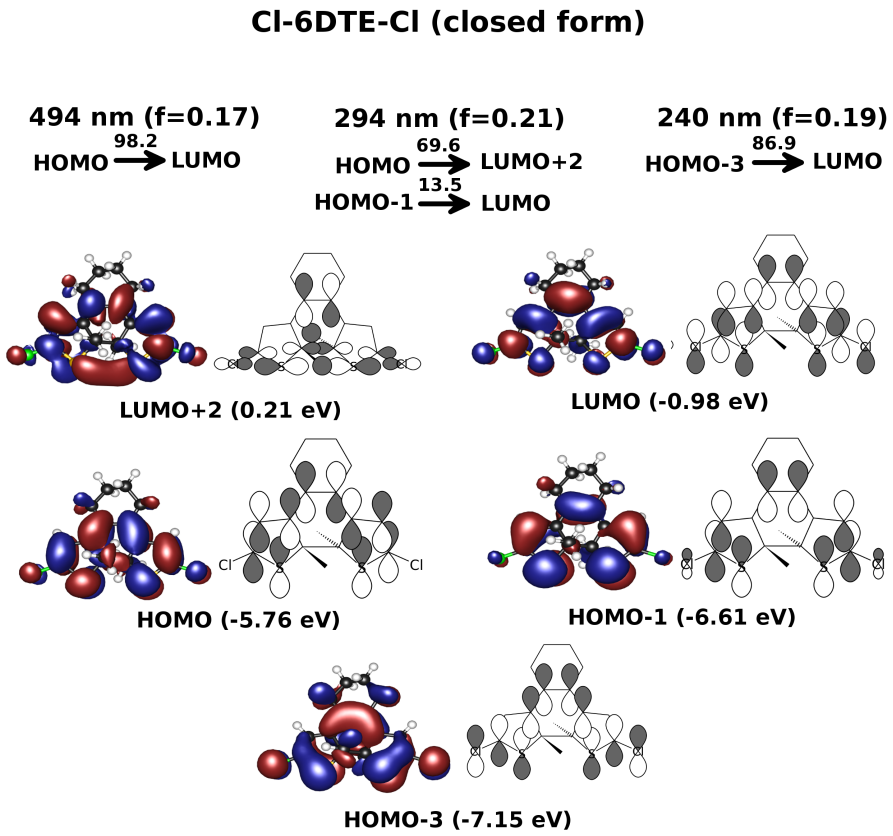

Figure 9.4: Molecular orbital excitations with their weights (given on the arrows), oscillator strengths f and molecular orbital energies [eV] corresponding to the most intense peaks in the UV/Vis spectrum of the closed form of Cl–6DTE–Cl calculated with B3LYP/def-TZVP using TDDFT on the structure optimized with B3LYP-D/def-TZVP.

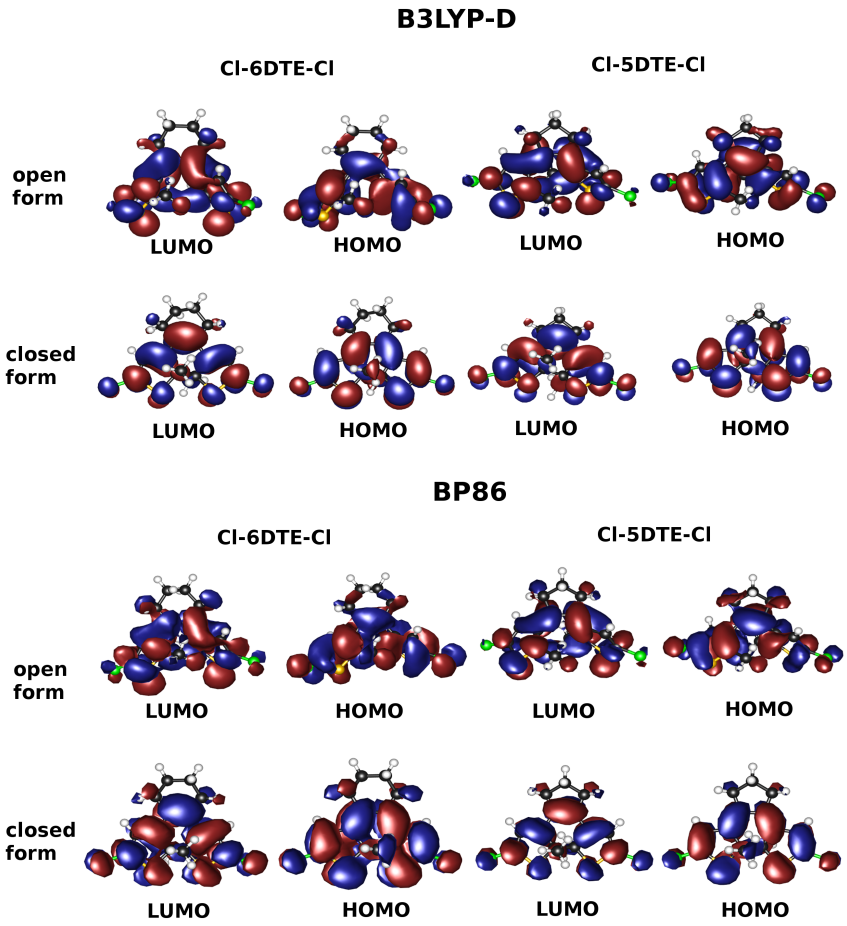

Figure 9.5: HOMOs and LUMOs for both switches and both isomeric forms calculated with B3LYP-D/def-TZVP (top) and BP86/def-TZVP (bottom).

Since the square of the transition dipole moment is equal to the probability of the excitation (and proportional to the oscillator strengths reported in Figure 9.3 and Figure 9.4), it can be seen as a characteristic quantity for the efficiency of the excitations.

Table 9.4: Transition dipole moments for the HOMO–LUMO transition of the optimized structures of both isomers of Cl–6DTE–Cl and Cl–5DTE–Cl. Basis set: def-TZVP.

switch	functional	$d_{01,\text{open}}$ (Debye)	$d_{01,\text{closed}}$ (Debye)
Cl–6DTE–Cl	B3LYP	1.50	4.08
Cl–5DTE–Cl	B3LYP	2.12	4.14
Cl–6DTE–Cl	BP86	0.95	4.13
Cl–5DTE–Cl	BP86	1.66	4.19

For both molecular switches, the transition dipole moments of the HOMO–LUMO excitations are much larger for the closed forms than for the open forms, and their values do not depend strongly on the functional. For the open form, the transition probability calculated with B3LYP (BP86) is 41% (75%) higher for Cl–5DTE–Cl than for Cl–6DTE–Cl. This results in much higher intensities for the HOMO–LUMO excitation for Cl–5DTE–Cl because the intensity is proportional to the square of the transition dipole moment. Note that this still leads to similar absorption spectra for six- and five-membered ring species because the absolute intensities of the HOMO–LUMO transitions are small in the open forms.

9.2.2 Potential Energy Surface Scans

Although the transition dipole moments at the energetic minimum structures of the open and closed forms are important in the context of the efficiency of the transition itself, they do not provide full information about the reactivity of the switches.

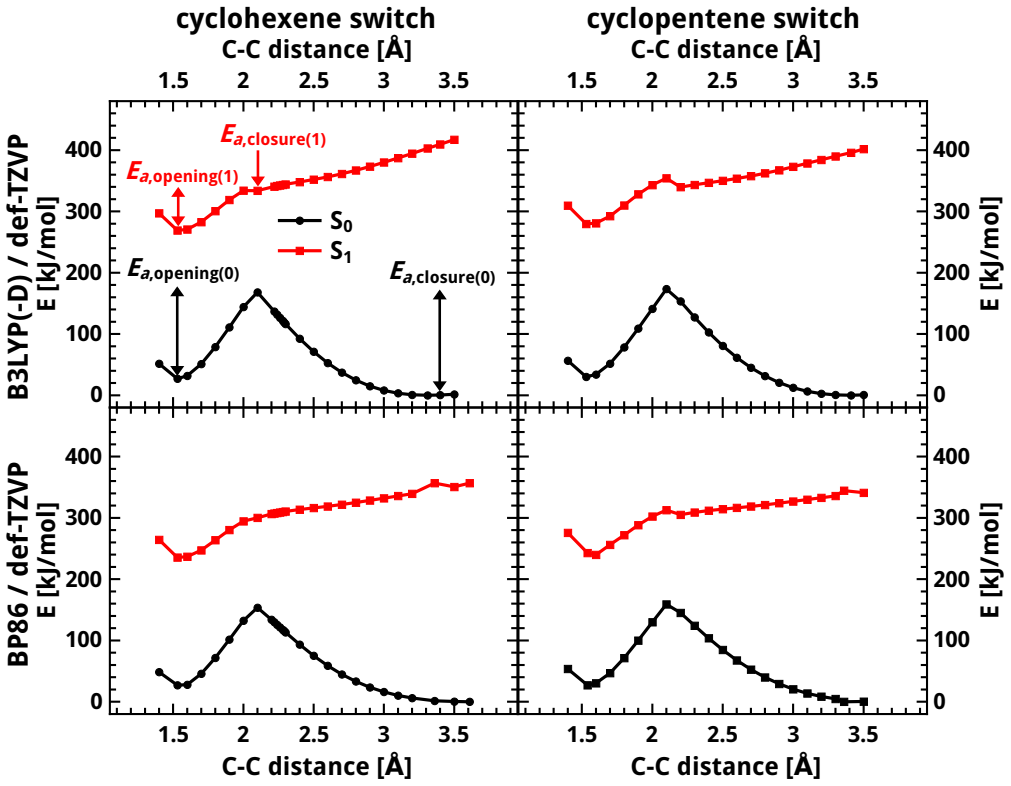

Figure 9.6: Potential energy surface for Cl–6DTE–Cl (left column), and Cl–5DTE–Cl (right column) for B3LYP(-D)/def-TZVP (upper row) and BP86/def-TZVP (lower row) of the ground state and the first excited singlet state as function of the C–C distance of the carbon atoms participating in cyclization and cycloreversion. For each fixed C–C distance, all other atomic coordinates are relaxed.

The discussion of the molecular orbital shapes corresponding to the excitation energies for Cl–6DTE–Cl and Cl–5DTE–Cl in both isomeric forms revealed that only the HOMO–LUMO excitation is important for the switching mechanism (see Figures 9.3 and 9.4). Therefore, an analysis of the PES of the ground state (S_0) and the first excited state (S_1) is performed as a function of the distance between the reactive carbon atoms participating in ring opening and ring closure. First, constrained structure optimizations in the electronic ground state are carried out with the B3LYP-D and BP86 functionals and the def-TZVP basis set for several points on the PES keeping the distance between the reactive carbon atoms of the thiophene rings R(C−C) fixed. Then, TDDFT is used to calculate the energies, transition dipole moments, and molecular orbital contributions for the 30 lowest singlet excitations for each optimized ground-state structure, where the same exchange–correlation functionals as used in the structure optimizations are employed (B3LYP and BP86). Note that for a full picture of the mechanism, a more sophisticated PES scan is required [218], which is beyond the scope of this comparative study. Furthermore, there is evidence of conical intersections in such systems [237], which may be a problem for standard TDDFT. Therefore multireference wave function methods such as CASSCF/CASPT2 may need to be employed to describe these crossing points between two PESs.
The obtained PESs are given in Figure 9.6. For both switches and for both exchange-correlation functionals, there is a large activation barrier between the two isomeric forms in the ground state. The reaction barriers for cyclization and cycloreversion in the ground state are only slightly larger for Cl–5DTE–Cl than for Cl–6DTE–Cl, independent of the applied exchange–correlation functional (see Table 9.5, second and third column). Due to the height of the activation barriers, which reflect that the reaction is symmetry forbidden (see Section 8.1), both switches are expected to be thermally stable and no hot ground-state reaction can take place.

Table 9.5: Ground-state (first excited singlet-state) activation barriers for the ring-opening $E_{\mathrm{a,opening(0)}}$ ($E_{\mathrm{a,opening(1)}}$), and ring-closure $E_{\mathrm{a,closure(0)}}$ ($E_{\mathrm{a,closure(1)}}$) reactions. The values are given in kJ/mol. Basis set: def-TZVP.

B3LYP-D / B3LYP				
switch	$E_{\mathrm{a,closure(0)}}$	$E_{\mathrm{a,opening(1)}}$	$E_{\mathrm{a,closure(1)}}$	$E_{\mathrm{a,opening(1)}}$
Cl–6DTE–Cl	168.1	141.1	0.1	64.9
Cl–5DTE–Cl	173.4	143.3	14.5	74.4
BP86				
Cl–6DTE–Cl	153.6	126.5	no minimum	no minimum
Cl–5DTE–Cl	159.1	128.8	7.5	40.9

The PES of the first excited singlet state shows a global minimum, which

coincides with the minimum of the closed form in the ground state, and a shallow local minimum at a C–C distance of around 2.3 Å (except for the cyclohexenyl switch calculated with BP86), which cannot be clearly distinguished from a numerical error. In the work of Guillaumont and co-workers [218], the PES for the first excited state of the ethynyl-bridged switch obtained with CASSCF/CASPT2 shows a similar shallow minimum, so it appears to be a consistent feature of the excited-state PES.

The activation energy of the cyclization (cycloreversion) reaction in the ground state $E_{\mathrm{a,closure(0)}}$ ($E_{\mathrm{a,opening(0)}}$) is calculated as the difference between the energies of the optimized open form (closed form) isomer and the TS on the ground-state PES (see Table 9.5, column 4). The reaction barriers in the first excited state for the cyclization $E_{\mathrm{a,closure(1)}}$ are calculated as the energy differences between the TS between the two minima and the shallow minimum on the PES. This appears to be reasonable, since after excitation of the closed-form isomer to the first excited state, the energy monotonically decreases until the local minimum is reached, and then the system has only to overcome this small barrier ending up in the global minimum of S_1, and then relaxes back to the ground state (adiabatic reaction). Similar results are also obtained by Staykov and co-workers [217] with TDDFT for the perfluorinated analogue of the cyclopentenyl switch.

The activation barrier for the cycloreversion reaction in the first excited state $E_{\mathrm{a,opening(1)}}$ is calculated as the energy difference between the TS and the lower-energy local minimum on the first-excited-state PES (see Table 9.5, column 5). Following the argumentation of Asano [239], the molecule relaxes to the ground state at the local minimum of the first excited state (diabatic reaction), because the amount of energy needed to further follow the PES of the first excited state, which constantly increases in energy as the distances between the reactive carbon atoms increase, makes the adiabatic reaction unlikely.

For the PES of the first excited state of Cl–6DTE–Cl calculated with BP86, no local minimum is found and the activation barrier for ring closure $E_{\mathrm{a,closing(1)}}$ calculated with B3LYP(-D) is only 0.1 kJ/mol. Since the energy barrier $E_{\mathrm{a,opening(1)}}$ is much larger than $E_{\mathrm{a,closing(1)}}$, the quantum yield of the cycloreversion reaction should be lower than for the cyclization reaction. This is in agreement with the experiment [239] and also with a CASSCF(10/10) study on a model system [218]. Guillaumont and coworkers further mentioned that the second and third excited state have the same shape as the first excited state, but reduced energetic barriers for the cycloreversion reaction. Those higher excited states are accessible via a stepwise multiphoton process and the quantum yield can be increased by irradiation with high-intensity picosecond laser pulses [218].

Overall, the reaction barriers for cyclization and cycloreversion in the first excited state are much smaller compared to those in the ground state and, as already observed for the ground state, the barriers are slightly larger for Cl–5DTE–Cl than for Cl–6DTE–Cl.

9.3 Conclusions

In this chapter, the structural and optical properties, as well as the ring closure reaction of chloro- (and iodo-) substituted [180, 221] dithienylethene switches were studied. The goal was to check whether replacing the five-membered ring by a six-membered one would change the photoswitching behavior of these compounds. Molecular structure optimizations were carried out with Kohn–Sham density functional theory using the BP86 and B3LYP exchange–correlation functionals with and without the empirical dispersion correction by Grimme (-D) [236]. It was found that the best agreement with experimental structures from X-ray crystallography was obtained with B3LYP-D, followed by BP86. The ring size does not affect the molecular structural parameters strongly. While the angle between the thiophene rings in the open form is somewhat larger for the six-membered-ring derivatives than for the five-membered ones, no clear trend with respect to the ring size is found for the distance between the reactive carbon atoms. The UV/Vis spectra calculated with TDDFT for the open form using the BP86 and the B3LYP functional were in good agreement with the experiment, while those for the closed-form isomer were somewhat different. These differences may indicate that not all open-form isomers are transformed to the closed form. The calculations reveal that only the HOMO–LUMO transition, which is of low intensity, contributes to ring closure. The same was found for the cycloreversion reaction, but the HOMO–LUMO transition is of considerably higher intensity here. The transition dipole moments for the closed-form isomer are similar for both switches, while those for the open-form isomers are significantly larger for the cyclopentene than for Cl–6DTE–Cl, resulting in a higher efficiency of this excitation for Cl–5DTE–Cl (which still results in similar UV/Vis spectra because of the small contribution of this transition). From a scan of the potential energy surfaces of the ground state and the first excited singlet state, it could be seen that there are no significant differences between both switches, although the reaction barriers in both states are slightly lower for Cl–6DTE–Cl. In the ground state, the activation barriers for cyclization and cycloreversion are considerably larger than in the first excited state, so that both isomers are thermally stable at room temperature. The open form is always more stable than the closed form, with a slightly larger energy difference to the closed form for Cl–5DTE–Cl than for Cl–6DTE–Cl. In the first excited state, the reaction barriers are strongly reduced and the activation barrier for the cycloreversion is much higher than for the cyclization. Overall, it could be shown that going from the well-studied cyclopentene photoswitch to its cyclohexene analogue, the switching properties get slightly worse, but do not change significantly. This opens those types of photochromic switches for chiral substitution and lay a solid foundation for the study of metallocene-substituted switches in the following chapters.

10. Adding Metallocenes: Ferrocene-Substituted Dithienylethenes

In this chapter, closed-shell ferrocene-substituted DTE switches, again differing in the size of the cycloalkene ring, are discussed (see Figure 10.1).

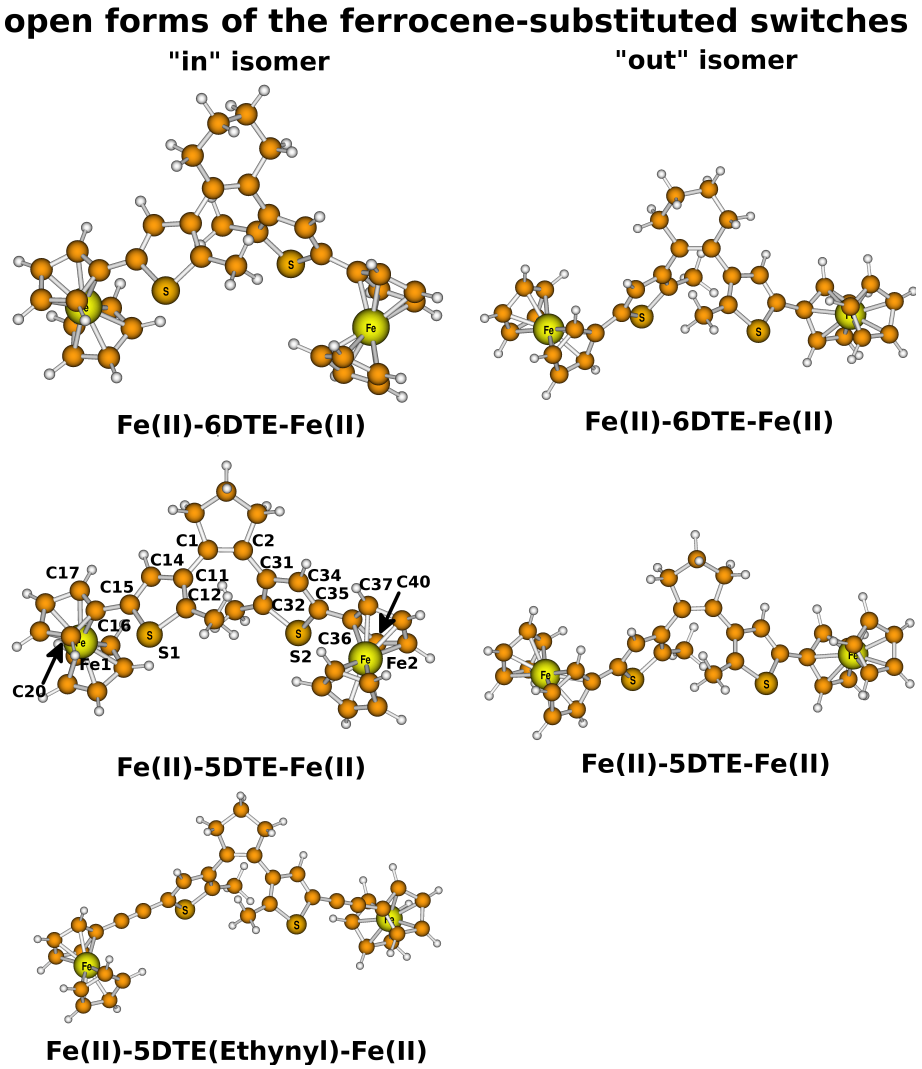

Figure 10.1: Molecular structures for the different ferrocene-substituted switches under study, optimized with BP86 / def-TZVP. The numbering scheme is used in Table 10.1 for the definition of the structural parameters.

In analogy to the chlorine-substituted switches, molecular structure optimizations with the BP86 functional are carried out, and the results are compared to the experimental structures obtained from a X-ray structure analysis by Escribano [221, 222] (Section 10.1). Again, the system notations from Section 8.3 are employed. On top of the optimized structures, TDDFT calculations are carried out in order to calculate the optical properties for the systems synthesized, and an ethynyl-bridged analogue synthesized by Guirado and coworkers [223], for which no TDDFT calculations had been carried out (Section 10.2.1). It was observed experimentally that the switching reaction was not as efficient as in the case of the organic derivatives [180, 221]. To understand the different behavior, the potential energy surfaces of the ground and excited states are studied in Section 10.2.2 as a function of the distance between the methylated carbon atoms, forming the single bond in the closed isomer for the cyclopentene-bridged, ferrocene-substituted switch with DFT and TDDFT. The results are compared to those obtained for the chlorine-substituted congener.

10.1 Molecular Structures and Relative Energies

The structural parameters of Fe(II)–6DTE–Fe(II) and Fe(II)–5DTE–Fe(II) from the X-ray structure analysis of Escribano are given in Table 10.1 (more information about the X-ray crystal structure analysis can be found in Refs. [221,222]). The experimental data are compared to the structures obtained from molecular structure optimizations with the pure BP86 functional, by using Ahlrich's triple-zeta basis set with polarization functions on all atoms, def-TZVP. The BP86 functional without any dispersion correction is chosen, as it gave the second best result in the previous chapter (and Ref. [163]) for the chlorine-substituted congeners, thanks to density fitting at a computationally reduced cost relative to the best choice (the hybrid functional B3LYP in combination with Grimme's empirical dispersion correction). In the optimizations, two closed-form isomers and two open-form isomers are taken into account, differing in the relative orientation of the ferrocene moieties with respect to the bridging photochromic core. In one structure, the ferrocene substituents point away from the photochromic core (referred to as "out" in Figure 10.1), and in the other they point towards it (referred to as "in" in Figure 10.1). Both relative orientations are considered, because they can be obtained from each other by simple rotation, which implies that both may be relevant for the optical properties in solution. In the crystal structure, only the "in" form is present [221,222]. The distance between the reactive, methylated carbon atoms is experimentally 17 pm longer for Fe(II)–5DTE–Fe(II) than for Fe(II)–6DTE–Fe(II). For the cyclopentene structure optimized with the BP86 functional, this non-bonding distance is in very good agreement with the experiment, whereas it is strongly overestimated for Fe(II)–6DTE–Fe(II). Therefore, the DFT calculations give the opposite trend as found in experiment. This discrepancy might result from packing effects in the crystal structure of Fe(II)–6DTE–Fe(II), which cannot be considered in the

DFT optimizations, from an artefact of BP86, or from the lack of dispersion effects in the calculations (compare with the chlorine-substituted switches in the previous chapter).

Table 10.1: Selected parameters for Fe(II)–6DTE–Fe(II) and Fe(II)–5DTE–Fe(II) obtained from the x-ray structure analysis [221, 222], and the structure optimizations with BP86 / def-TZVP. The planes of the estimated angles are defined as ϕ=C12–C11–C31–C32, θ_1=C14–C15–C16–C17, and θ_2=S1–C15–C16–C20 [°] (see Figure 10.1). For the experimental θ angles, θ_1 equals θ_3 and θ_2 equals θ_4, whereas they differ by 1–2° in the calculated structures (all calculated θ values are given in Table 10.1 in Appendix B). The "in" orientations with torsional angles of 0° are taken as reference. The structure optimizations are performed with the BP86 functional. Basis set: def-TZVP.

Fe(II)–5DTE–Fe(II)				
Method	C1–C2	C12–C32	C15–C16	C35–C36
exp. ("in")	134.62	361.48	145.84	145.84
BP86 ("in")	136.35	360.59	145.31	145.31
BP86 ("out")	136.20	362.82	145.32	145.34
Method	Fe–Fe	ϕ	θ_1 / θ_2	–
exp. ("in")	1165.42	81.209	113.592 / 9.637	–
BP86 ("in")	1199.83	77.112	14.002 / 14.563	–
BP86 ("out")	1356.23	81.881	168.166 / 170.256	–
Fe(II)–5DTE–Fe(II)				
Method	C1–C2	C12–C32	C15–C16	C35–C36
exp. ("in")	134.02	344.42	146.04	145.79
BP86 ("in")	135.91	365.88	145.35	145.35
BP86 ("out")	135.99	367.39	145.32	145.30
Method	Fe–Fe	ϕ	θ_1 / θ_2	–
exp. ("in")	1073.81	82.844	21.745 / 20.056	–
BP86 ("in")	1039.47	94.748	19.334 / 20.620	–
BP86 ("out")	1286.07	96.209	19.334 / 20.620	–

The torsional angles between the thiophene planes defined according to Figure 10.1 are in good agreement with the experiment for the cyclopentene complex, while they are overestimated by 10 to 15° for the cyclohexene complex. The average torsional angles between the thiophene and the cyclopentadienyl rings attached to the photochromic core θ (defined as: θ_1: C14–C15–C16–C17, θ_2: S1–C15–C16–C20, θ_3: C34–C35–C36–C37, θ_4: S2–C35–C36–C40; see Figure 10.1) indicate that the ferrocenes are slightly tilted by approximately 15° with respect to the thiophene planes irrespective of the isomeric open or closed form (Table B.1). For comparison, the θ angles for the perfectly coplanar "in" orientation would be zero.

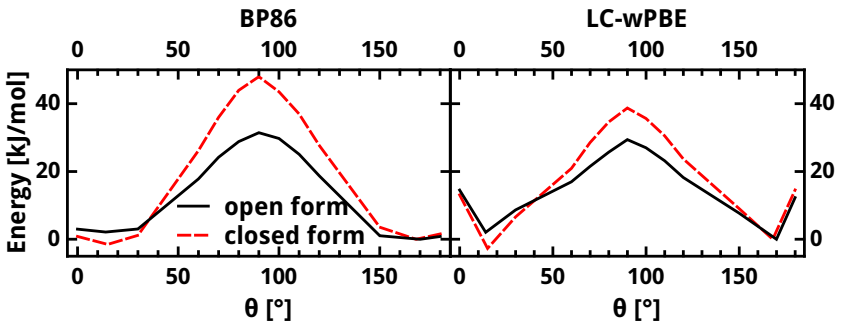

Figure 10.2: Calculated potential energy scans as a function of the $\theta = \theta_1 = \theta_2 = \theta_3 = \theta_4$ torsional angles (all other parameters are relaxed) for Fe(II)–5DTE–Fe(II). The structure optimizations are carried out with BP86 for both plots, combined with LC-ωPBE single point calculations for the right-hand side plot. Basis set: def-TZVP.

An additional scan of these torsional angles (Figure 10.2) for Fe(II)–5DTE–Fe(II) was performed by fixing $\theta = \theta_1 = \theta_2 = \theta_3 = \theta_4$ to specific values and performing constrained molecular structure optimizations. This scan revealed that the perfectly coplanar orientations (θ=0°) are energetically destabilized for all structures calculated with respect to the optimized structures, but a larger destabilization is found for LC-ωPBE than for BP86. The rotation barriers for the open isomers are about 30 kJ/mol regardless of the employed functional. For the closed isomer, they are roughly 10 kJ/mol higher than for the other open form if LC-ωPBE is employed and 20 kJ/mol higher for BP86, with energy maxima at 90°, at which the π systems are orthogonal to each other. According to the literature [240], atropisomers are considered to be stable if the energy barrier between them is at least 93.3 kJ/mol (which corresponds to a half life of 1000 s at room temperature). Although the minimal requirements for NMR spectroscopy are less strict (half lives between 10^{-2} and 10^{-1} s), only one set of signals was found at −60°C in the variable-temperature NMR spectroscopy measurements for the cyclopentene complex [221, 222], which indicates that the energy barrier for rotation is smaller than 20 kJ/mol [241]. Therefore, the LC-ωPBE and BP86 functionals strongly overestimate the energy barriers by at least 50%, which is in the same order of magnitude as the errors found in the literature for torsional barriers in organic systems [242, 243]. For Fe(II)–5DTE(Ethynyl)–Fe(II) complex (Figure 10.1), however, the rotation barriers might be smaller because the steric interactions are reduced by the ethynyl spacers.

For the structure of the cyclohexene complex the X-ray structure analysis [221, 222] and the structure optimization with DFT both gave a half-chair configuration, while the cyclopentene ring is planar.

As in the previous study on the chlorine-substituted switches, only the switchable, antiparallel conformations are taken into account (see Section 8.1).

According to the energy order calculated for the different isomeric forms of

the cyclopentene and cyclohexene complexes (see Appendix B.1), it becomes clear that the open forms are more stable by 25 to 30 kJ/mol than the closed-form ones, just as for the halogen-terminated switches discussed in the previous chapter [180]. This is in harmony with the findings of Nakamura and Irie, who argued that this stabilization of the open isomer with respect to the closed isomer correlates with its higher aromaticity [182].

10.2 Photoswitching Behavior

In this section, the photoswitching behavior of the different ferrocene-substituted switches is studied. Therefore, the UV/Vis spectra measured in *n*-hexane [221, 222] are compared to the spectra calculated by TDDFT (Section 10.2.1). Further, a PES scan for Fe(II)–5DTE–Fe(II) is performed and the results are compared to Cl–5DTE–Cl, described in the previous chapter (Section 10.2.2).

10.2.1 UV/Vis Spectra

UV/Vis spectra for the ferrocene-substituted cyclopentene and cyclohexene complexes were recorded by Alejandra Escribano [221, 222] in *n*-hexane. The measured spectra, together with those calculated with the range-separated LC-ωPBE functional on top of the BP86 optimized structures, are given in Figure 10.3. In addition, the polarizable continuum model (PCM) with parameters for *n*-hexane was employed. Although BP86 had given reliable results for the chlorine-substituted structures in the previous section [180], the range-separated LC-ωPBE functional was employed here, because it showed the correct asymptotic 1/r behavior for the exchange-correlation functional for large electron–electron distances [244,245] and, therefore, should be suitable to describe possible metal-to-ligand charge-transfer (MLCT) excitations. In the calculated spectra, the open and closed forms of the "in" and "out" conformers are considered. Because the optical data for the "out" and "in" conformers showed similar optical behavior, only the spectra for the in conformers are given in Figure 10.3. Moreover, the ethynyl-linked 1,2-bis-(5'-ethynylferrocene-2'-methylthien-3'-yl)cyclopentene of Guirado is considered [223] to investigate the influence of the conjugation length on the optical properties. Although the solutions became light pink upon irradiation with a light source of 366 nm, no significant changes are observed in the experimental spectra. For Fe(II)–6DTE–Fe(II), small changes are observed in the visible region of the spectrum, in which the intensity increases over the entire range, but no new absorption band appeared. This result suggests that almost no switching within the open and closed forms occurred [222]. The two intense excitations below λ=300 nm in the calculated spectra of the open forms of Fe(II)–5DTE/6DTE–Fe(II) are too close to each other relative to the distance of these bands in the experimental spectra, so that they appear as one intense shoulder in the calculated spectra.

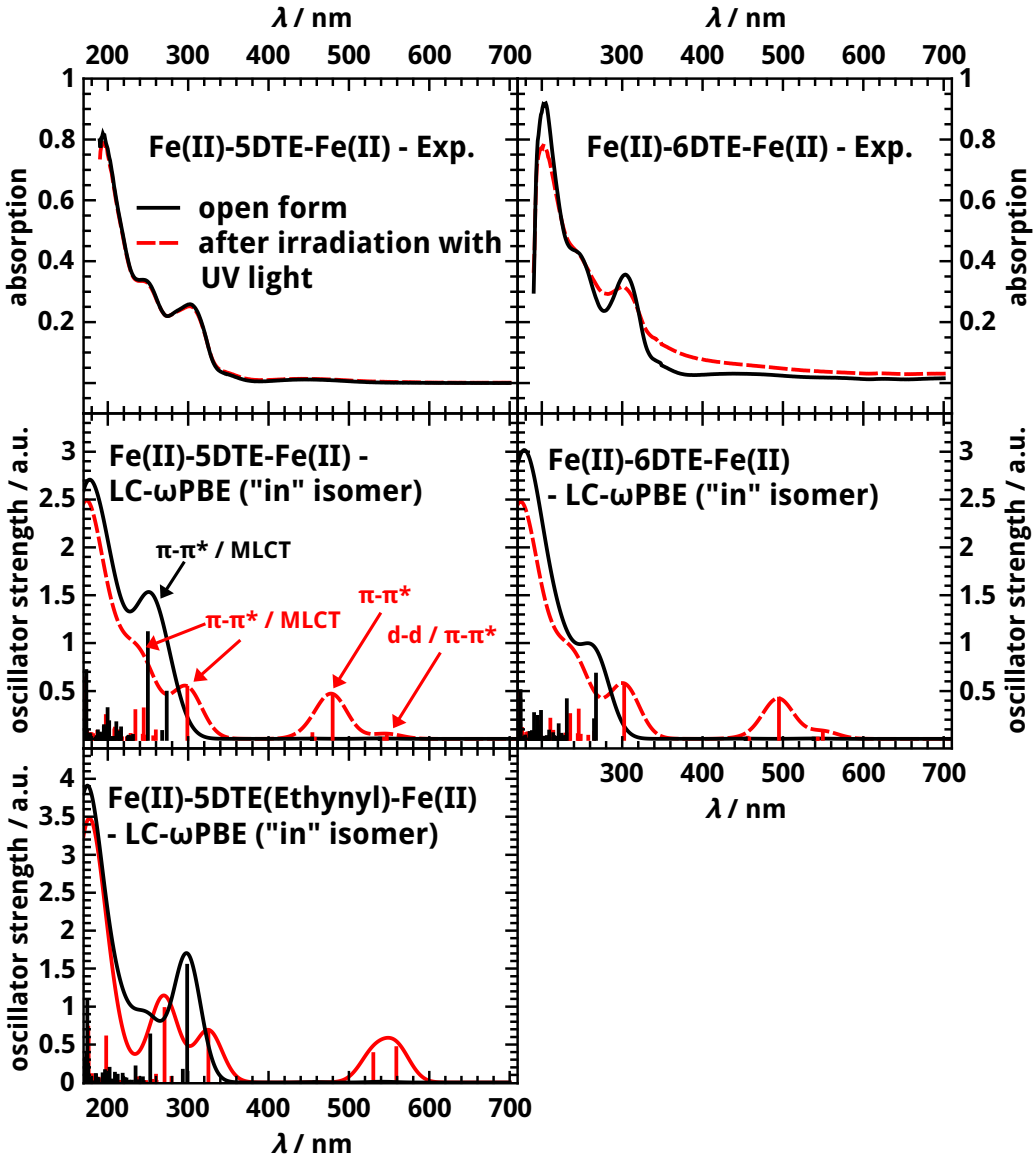

Figure 10.3: UV/Vis spectra obtained from experiment (A. Escribano [221,222]) for the different isomers of Fe(II)–5DTE–Fe(II) [concentration 6.85x10^{-5} M, path length(d) = 1 cm] and Fe(II)–6DTE–Fe(II) (7.47x10^{-5} M, d = 1 cm) in n-hexane (top; absorption given in arbitrary units), compared with TDDFT results by using LC-ωPBE on top of BP86-optimized structures (middle). Basis set: def-TZVP. Calculated spectra are broadened with Gaussian functions employing a half width of 40 nm. The UV/Vis spectrum for Fe(II)–5DTE(Ethynyl)–Fe(II) characterized experimentally by Guirado and coworkers [223] is calculated for comparison (bottom). For Fe(II)–5DTE–Fe(II), the measured initial spectrum and the spectrum after 47 min under irradiation with a light source of l = 366 nm are given, and for the cyclohexene switch the initial spectrum and the spectrum after 219 min under irradiation with the same light source.

Only for ethynyl-linked switch (Figure 10.1), as synthesized by Guirado [223], does the open isomer show an absorption at λ=434 nm (Table 10.2); this is

also obtained for the theoretical spectra at λ=457 nm, but it is of very low intensity.

Table 10.2: UV/Vis absorption spectroscopic data for Fe(II)–5DTE–Fe(II) and Fe(II)–6DTE–Fe(II) in *n*-hexane and for Fe(II)–5DTE(Ethynyl)–Fe(II) synthesized by Guirado [223] in acetonitrile obtained from measurements [221, 222] and the corresponding data obtained from TDDFT calculations with LC-ωPBE in combination with the PCM model on the structures optimized with BP86[a].

Bridge	Method	Open Isomer[b]	Closed isomer
	exp.	352 (sh, 2740)	449 (1185***)
Fe(II)–5DTE–Fe(II) ("in")	LC-ωPBE	178 (2.71), 251 (sh, 1.53*)	174 (2.49), 238 (sh, 0.96), 296 (sh, 0.56), 478 (0.47), 540 (sh, 0.06)
Fe(II)–5DTE–Fe(II) ("out")	LC-ωPBE	175 (2.72), 249 (1.81*)	173 (2.51), 238 (sh, 0.96), 301 (sh, 0.58), 484 (0.48), 545 (sh, 0.09)
Fe(II)–6DTE–Fe(II)	exp.	354 (sh, 3383)	450 (1555***)
Fe(II)–6DTE–Fe(II) ("in")	LC-ωPBE	178 (3.02), 257 (1.00)	174 (2.48), 238 (sh, 1.00), 301 (sh, 0.60), 500 (0.42), 554 (sh, 0.12)
Fe(II)–6DTE–Fe(II) ("out")	LC-ωPBE	176 (2.89), 228 (sh, 1.50), 265 (sh, 1.17)	173 (2.49), 238 (sh, 1.00), 301 (sh, 0.60), 500 (0.42), 554 (sh, 0.12)
Fe(II)–5DTE(Ethynyl)–Fe(II)	exp.	434**	438, 560
Fe(II)–5DTE(Ethynyl)–Fe(II) ("in")	LC-ωPBE	175 (3.91), 298 (1.70), 457 (0.01), 542 (0.01)	177 (3.48), 270 (1.15), 325 (0.69), 463 (0.00), 548 (0.59)

[a] The wavelengths λ are given in nm, the molecular extinction coefficients ϵ in the experimental spectra is given in parenthesis, and for the theoretical data the oscillator strengths are given in parenthesis; basis set: def-TZVP; [b] sh = shoulder; * overlap of two intense excitations; ** in Ref. [223] the UV region is not included (<400 nm); ***spectrum shows absorption in the visible region in the initial state but this might be due to some molecules already being in the closed form.

For the closed switch, a spectrum similar to that of the open one is experimentally and theoretically observed, but a new absorption band appears in the

visible region of the spectrum for the closed isomer. The UV region in the calculated spectra of the open isomers is in good agreement with the experimental spectra. For all open forms, an intense absorption in the UV region is found, whereas there is no significant absorption in the visible region.

To further characterize the absorption bands, the molecular orbital (MO) transitions of the most intense excitations (Table B.2; see also the Appendix B.1.2 for the MO plots of Fe(II)–5DTE–Fe(II) and Fe(II)–6DTE–Fe(II)) are analyzed and compared with the chlorine- substituted analogues. The optical properties of Fe(II)–5DTE–Fe(II) are also compared with those of Fe(II)–5DTE(Ethynyl)–Fe(II) by Guirado [223] featuring an ethynyl spacer. Also the results of the "out" conformer are given in Appendix B.1.2. The study on the chloro-substituted switches in Chapter 9 and in the literature [180,217,239], revealed that the first excited singlet state caused by excitation from the HOMO to the LUMO is the crucial excitation involved in the ring-closing and ring-opening reactions. To be able to compare the results with the Cl–5DTE/6DTE–Cl switches from the previous chapter, single-point calculations are performed with the LC-ωPBE functional and the so-obtained results are in good agreement with the findings obtained in the previous chapter. For the "in" orientation of Fe(II)–5DTE–Fe(II) and Fe(II)–6DTE–Fe(II), the contours of the HOMOs and LUMOs refer to those of the chlorine-substituted switches (Appendix B.1.2), which were identified as responsible for the switching reaction. However, for the Fe(II)–5DTE–Fe(II) the HOMO–LUMO excitation dominates the 13th excited singlet state (S_{13}), while the HOMO–LUMO-dominated excitation is identified as the first excited state. The excitation energies for the HOMO−LUMO-dominated transitions of Fe(II)–5DTE–Fe(II) and Fe(II)–6DTE–Fe(II) (λ=273 nm for 5DTE and λ=267 nm for 6DTE) are bathochromically shifted relative to those of the chlorine-substituted reference switches (λ=256 nm for Cl–5DTE–Cl and λ=240 nm for Cl–6DTE–Cl). This might result from participation of ferrocene in the π system of the photochromic switch through their cyclopentadienyl ligands, which are nearly perfectly coplanar to the plane spanned by the thiophene ring in the solid state. The introduction of the organometallic substituents can be seen to increase the oscillator strength of the HOMO–LUMO transition, which makes this excitation more probable. The 15th excited singlet state S_{15} in the spectra of the open form of Fe(II)–5DTE–Fe(II), which is very close in energy to the 13th, are dominated by $\pi - \pi^*$ transitions, whereas pure MLCT transitions play only a minor role (Table B.2). For Fe(II)–5DTE(Ethynyl)–Fe(II) synthesized by Guirado *et al.* [223], the excitations show no new features relative to without spacer, and therefore, the switching behavior should also not significantly differ from the switches presented herein. However, as already mentioned above, a general comparison with the spectra obtained by Guirado is not possible because the UV region is excluded in those measurements [223].

In the closed form of Fe(II)–5DTE–Fe(II), the S_5 (oscillator strength f=0.45 a.u.) excitation is the origin of the larger absorption band in the visible region and is dominated by the HOMO–LUMO transition (Table B.2). For the smaller

shoulders arising from the first singlet excitation appearing on the right of the larger absorption bands in the visible region, the largest contributions arise from d–d excitations on the ferrocene moieties (Table B.2). The UV part of the spectrum contains $\pi - \pi^*$ transitions but also a significant amount of MLCT excitations from the ferrocene group onto the photochromic bridge.

10.2.2 Potential Energy Surface Scans

To gain a better understanding of the underlying mechanism initiated by irradiation of UV light, a scan of the potential energy surfaces (PESs) of the ground state and the first 20 excited singlet states is performed for the "in" conformer of Fe(II)–5DTE–Fe(II) (Figure 10.4).

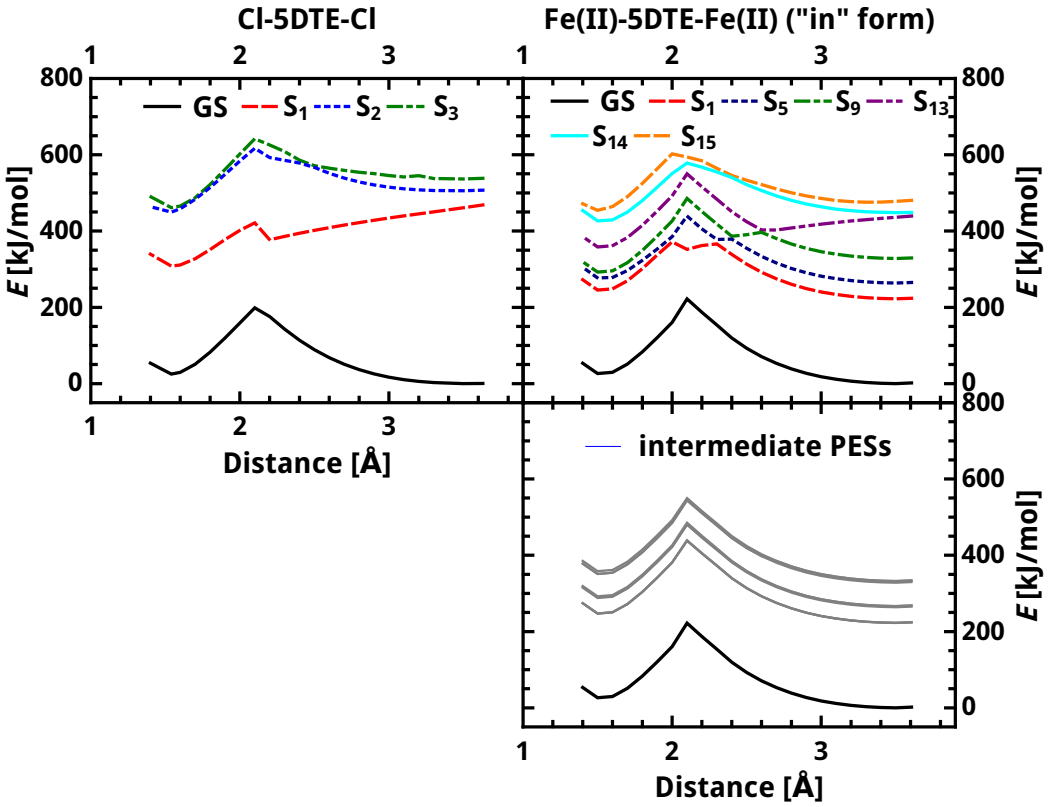

Figure 10.4: Potential energy surface scans for Cl–5DTE–Cl (left) and the "in" conformer of Fe(II)–5DTE–Fe(II) (right) and intermediate PES not involved in the switching reaction of the latter compound (bottom). All structures are optimized with BP86 and the def-TZVP basis set at fixed distances between the two reactive carbon atoms. On the optimized structures single-point energy calculations and TDDFT calculations are performed with the LC-ωPBE functional by employing the PCM model (n-hexane) and the same basis set.

The LC-ωPBE functional is used to perform single-point energy calculations and TDDFT calculations on structures optimized with the BP86 functional for

fixed distances between the reactive carbon atoms forming the single bond in the closed isomer. For comparison, additional LC-ωPBE single-point calculations (including the first eight excited states) are performed for Cl–5DTE–Cl by using the BP86-optimized structures from the scan for the chlorine-substituted switches in Chapter 9 (which could not be directly compared with the results obtained here, because the spectra in this chapter are calculated with a different functional).
For Fe(II)–5DTE–Fe(II), the different excited-state PESs are much closer in energy than those of the chlorine-substituted switch, which can be explained by the mixing of the ferrocene orbitals with those of the π system of the photochromic core. From the PES scan, the thermal activation barriers for cyclization in the excited states are estimated by subtracting the energy maxima on the excited-state PESs and the energy of the local minima on the right-hand side of the energy barriers. For the cycloreversion, the energies of the global minimum referring to the closed form and the maxima are taken to obtain estimated values (Table 10.3). The ground-state PES of Cl–5DTE–Cl, as well as that of Fe(II)–5DTE–Fe(II) show significant energy barriers of 198.7 and 222.1 kJ/mol, respectively, for cyclization (reflecting, as for Cl–5DTE–Cl, that the cyclization is thermally forbidden according to the Woodward–Hoffmann rules [217]), which makes a ground-state reaction thermally impossible. Whereas for the chlorine-substituted reference switch the reaction mainly takes place on the S_1 potential energy surface, the situation is more complicated for Fe(II)–5DTE–Fe(II) (Figure 10.4). Notably, the activation barrier in the ground state (first excited singlet state S_1) is 198.7 kJ/mol (44.1 kJ/mol) for the chlorine-substituted switch, which is higher than the activation barrier of 168.1 kJ/mol (14.5 kJ/mol) as obtained in our previous study [180] with BP86. This might be a consequence of employing the BP86 functional for the structure optimizations and the LC-ωPBE functional for the TDDFT calculations.

Table 10.3: Estimated activation barriers for the cyclization and cycloreversion in the chlorine-substituted reference switch and the ferrocenyl-substituted cyclopentene-bridged switch. The results are obtained from single-point and TDDFT calculations with LC–ωPBE and def-TZVP on structures optimized with BP86 and the same basis set.

chloro-substituted cyclopentene switch		
State	$E_{\mathrm{a,closure}}$ [kJ/mol]	$E_{\mathrm{a,opening}}$ [kJ/mol]
S_0 (GS)	198.7	173.6
S_1	44.3	113.3
ferrocene-substituted cyclopentene switch		
S_0 (GS)	222.1	195.6
S_1	19.7	126.3
S_5	61.5	162.3
S_9	99.2	193.2
S_{13}	147.4	191.8

For Fe(II)–5DTE–Fe(II) in the open form, the excitation predominantly takes place between the ground state and the 15th (oscillator strength f=1.11 a.u.) and 13th (f=0.48 a.u.) excited singlet states. As already discussed earlier, the 13th excited state for the open isomer of the cyclopentene switch shows the same MO excitations as the first excited singlet state in the chlorine-substituted reference switch. However, whereas for Cl–5DTE–Cl the reaction can take place on the S_1 surface in an adiabatic process, the activation barrier on the S_{13} PES is much higher with 147.4 kJ/mol. Therefore, a multistep process with the involvement of many PESs is more likely than a strict adiabatic process. The HOMO–LUMO-dominated excitations form a path along the reaction coordinate involving the S_{13}, S_9, S_5, and S_1 potential energy surfaces (analysis of these excitations is given in Appendix B.1.2). However, the suggested pathway is strongly disturbed by many d–d- and MLCT-dominated PESs lying in between the HOMO–LUMO-dominated pathway. They have shapes similar to the PES of the ground state with high activation barriers for cyclization. If a molecule reaches these PESs, radiationless relaxation to the open-form isomer is more probable than overcoming the energy barrier towards the closed form (see bottom of Figure 10.4). Therefore, these states might be the reason why the switching behavior of the ferrocene-substituted switches is much poorer than that of the chlorine-substituted switches. However, these explanations are qualitative in nature and should be interpreted with a grain of salt, because transition probabilities between the different excited states are not calculated, and therefore, it is not known whether a transition between two PESs is likely to happen.
Additionally, only the non-bonding C–C distance is taken into account, whereas the torsional angles between the thiophene planes constituting a second reaction coordinate are not included in the scan [239]. Further, the description with DFT/TDDFT does generally not allow for reliable treatment of conical intersections due to their multireference character [246,247] which plays an important role in the relaxation process of the chlorine-substituted switch [239]. Nonetheless, the calculations are very likely reliable enough to offer a compelling qualitative explanation for the mechanism behind the reduced switching ability of the ferrocene-substituted switch.

10.3 Conclusions

In this chapter, the effect of ferrocenyl substituents on the switching behavior of the photochromic DTE cores was studied. Again, the influence of the size of the bridging cycloalkene ring (five-membered vs. six-membered ring) was taken into account. The optimized structures of the open forms obtained with BP86 were in good qualitative agreement with the experimental structures for Fe(II)–5DTE–Fe(II), while for Fe(II)–6DTE–Fe(II), larger deviations between theory and experiment were found. The DFT energy barriers for rotation of the ferrocene moieties between the “in” and “out” orientations were between 30

and 40 kJ/mol. However, the variable-temperature NMR measurements carried out for the cyclopentene-bridged complex gave only one set of signals at −60 C° [221,222], so that the rotational barrier must be below 20 kJ/mol. The deviations between experiment and theory are however reasonable if taking into account typical error margins of DFT. This however means that the rotation between the "in" and "out" orientation in solution is expected to occur. The spectra obtained by performing TDDFT calculations with the range-separated LC-ωPBE functional were in good agreement with the measured ones. By comparing the experimental and theoretical optical data, it was further concluded that only a very small amount of the open isomer was transformed into the closed isomer upon irradiation.

The Fe(II)–5DTE(Ethynyl)–Fe(II) published by Guirado and co-workers [223] has spectral features similar to those of Fe(II)–5DTE–Fe(II), so that the switching behavior is not expected to strongly differ from the systems under investigation considered here, but a detailed experimental comparison was impossible due to the different wavelength ranges here and in Ref. [223].

To understand the poor switching behavior of the ferrocene substituted switches, a scan of the potential energy surface (PES) of the ferrocene-substituted cyclopentene switch as a function of the distance between the reactive thiophene carbon atoms was performed, and the results were compared with the PESs of the chlorine-substituted reference switch. In contrast to the chlorine-substituted switch (for which the cyclization is mainly determined by the S_1 state as discussed in Chapter 9), there were many energetically nearly degenerate excited-state PESs showing energy barriers higher than those of the chlorine-substituted switch. Therefore, transitions between different excited states might be more likely than the adiabatic reaction on one of the PESs. A reaction pathway determined by the HOMO–LUMO-dominated excitations was identified, but it is presumably strongly perturbed by intermediate *d–d* and charge-transfer excitations from the ferrocene moieties to the photochromic core and *vice versa*. This could result in the low conversation rate between open and closed isomers, which would generate only a small fraction of the switches in the closed form, whereas most of the molecules relax back to the open form.

11. Adding Metallocene Spin Centers: Cobaltocene-Substituted Dithienylethenes

As a final step towards photoswitchable spin-coupled metallocene compounds, the structural parameters, the spin densities, and the photoswitching behavior of different diamagnetic and open-shell cobaltocene switches are calculated by means of DFT and TDDFT (Figure 11.1 in this chapter), and compared to the experimental findings of Alejandra Escribano [221] from the group of Jürgen Heck, University of Hamburg. Further, the results are compared to the findings for the chloro-substituted switch in Chapter 9. In the following, the notations in Section 8.3 for the systems in this chapter are used.

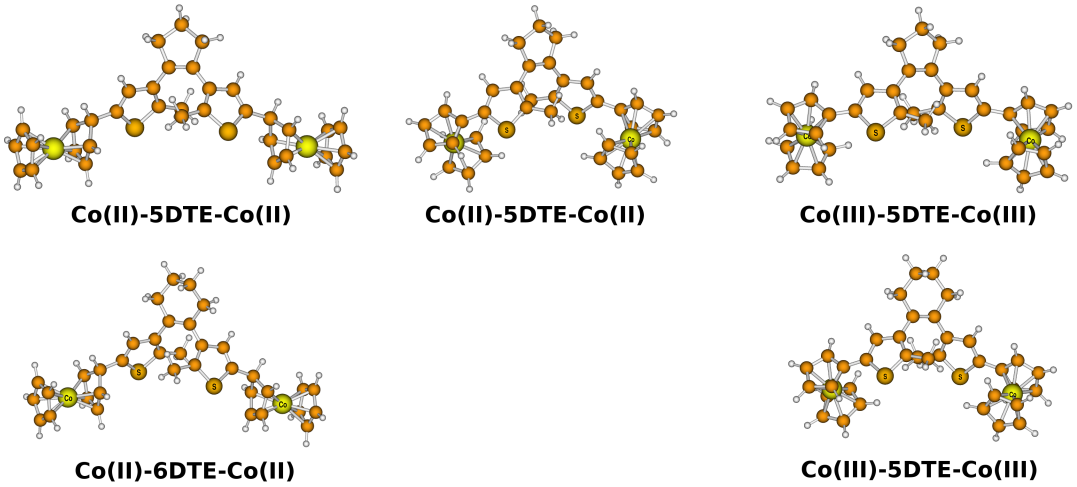

Figure 11.1: Molecular structures of the open form of the cobaltocene-based switches under study, optimized with B3LYP-D3 / def-TZVP. For the magnetic Co(II) systems the BS structure is shown.

The Co(I) substituents are linked to the photochromic core via a sp^3-hybridized carbon atom, while the Co(II) and the positively charged Co(III) substituents, are in π conjugation with the photochromic core. Therefore, in the Co(I) systems, the switching behavior should not be as strongly affected by the substituent as for example for the Co(II) systems. It is explored to what extent this is true, and if this influences the switching properties. If the Co(II) systems were switchable reasonably well, this would allow for switching on and off magnetic interactions.
In Chapter 10, two possible rotamers were reported ("in" and "out"). However,

in the crystal structures only the "in" isomer was found. The rotational barriers are low enough to allow for rotation between both orientations in solution at room temperature. However, the structural and optical properties were very similar for those compounds, and therefore only the "in" orientations are reported for the cobaltocene-based systems under study here.

11.1 Molecular Structures in the Open Form

The most important structural parameters, obtained from the X-ray structure analysis (for more information see [221]) and the DFT structure optimizations, are discussed for the Co(I) and Co(III) cyclopentene and cyclohexene switches in their open forms (Table 11.1). No structural data for the Co(II) complexes and for the closed forms of all compounds are reported due to the lack of experimental data.
For the structure optimizations, the B3LYP hybrid functional in combination with the dispersion correction of Grimme in its third generation [248] is used, combined with Ahlrich's def-TZVP basis set. These parameters are chosen because they gave the best results for the chloro-substituted photochromic switches (Chapter 9), and allow for a direct comparison to those results.

Table 11.1: Selected distances (pm) and torsional angles (°) in the Co(I) cyclohexene and cyclopentene switches, as well as the Co(III) cyclopentene and cyclohexene switches obtained from the X-ray structure analysis [221] and from structure optimizations carried out with B3LYP-D3 / def-TZVP.

	Experiment (X-ray analysis)			
Method	Co(I)-5DTE-Co(I)	Co(I)-6DTE-Co(I)	Co(III)-5DTE-Co(III)	Co(III)-6DTE-Co(III)
C12−C32	344.92	330.60	349.36	349.25
C12−C11−C31−C32	74.89	74.65	74.977	94.743
	Molecular structure optimizations (DFT)			
C12−C32	346.92	339.66	354.43	333.16
C12−C11−C31−C32	77.184	82.080	72.923	80.788

For the Co(I)-5DTE/6DTE-Co(I) systems the bond distances between the reactive thiophene carbon atoms and the torsional angles obtained from the structure optimizations, are in good qualitative agreement with the parameters obtained from the X-ray structure analysis. For Co(III)-5DTE-Co(III), the parameters are also in good agreement, but for the corresponding cyclohexene switch larger deviations are found. This might be explained by packing effects in the crystal structure, or simply the failure of the employed exchange–correlation functional.

11.2 Spin Density Distribution in the Open Form

To check whether the DFT calculations are able to reproduce the spin density in the open form Co(II)–6DTE–Co(II) switch correctly and to see if spin polarization takes place (Section 3.2), the spin density for the high-spin state of the open isomer is calculated and compared to the expected spin densities obtained from the chemical shifts δ, from ^{13}C nuclear magnetic resonance spectroscopy (Table 11.3; see also Ref. [221] for more details on the experiments). However, it must be noted that the energy difference between the BS determinant and the high-spin state is nearly zero in the open form ($E_{\mathrm{F}} - E_{\mathrm{AF}} = -0.95$ cm^{-1}), so that both spin-states are expected to be populated at room temperature which is expected to influence the chemical shifts obtained. However, for the DFT calculations the high-spin state is taken into account because even in an open-shell singlet no spin density should be present in the molecule. It must be noted however, that only seven of the twelve signals could have been reliably assigned (the other five signals are given in italics in Table 11.3) [221, 249].

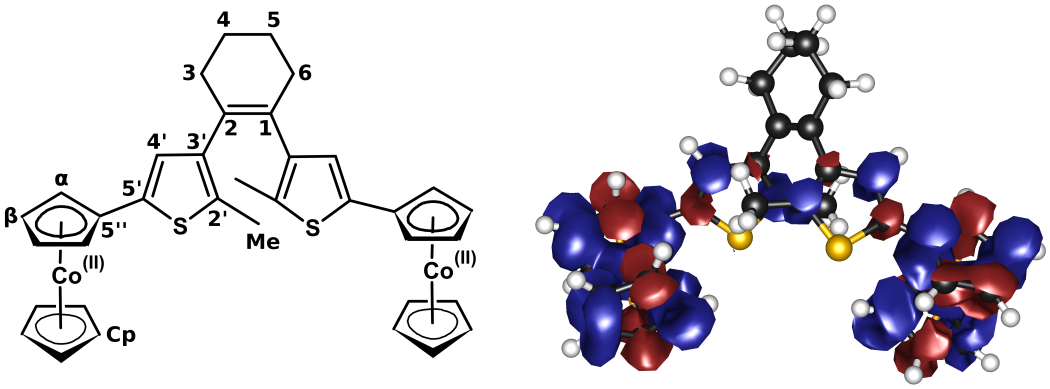

Figure 11.2: Numbering scheme used for the NMR signals in Table 11.3 (left), and spin density plot for the high-spin state of Co(II)–6DTE–Co(II) in the open form calculated with B3LYP-D3 / def-TZVP (right; see Table 11.2).

These findings are compared to the spin densities obtained from DFT calculations for the high-spin state of the complex (Figure 11.2). To be able to evaluate the influence of spin density on the chemical shifts δ in experiment, the Co(II)–6DTE–Co(II) complex is compared to the diamagnetic Co(III)–6DTE–Co(III) system [221], for which the shifts are much smaller ($\nu \leq \delta \leq 14$ ppm). In the following, a positive chemical shift refers to a shift to higher frequencies (or lower field), and corresponds to a positive spin density on the atom. On the other hand negative chemical shifts result from a negative spin density on the corresponding atom, which is the convention normally used in literature.

Table 11.2: Local spins in a.u. for the high-spin state for Co(II)–6DTE–Co(II) calculated with B3LYP-D3 / def-TZVP.

carbon atom	$\langle \hat{S}_{z,A} \rangle$	carbon atom	$\langle \hat{S}_{z,A} \rangle$
Me	−0.00(2)	5”	+0.03
1/2	−0.00(1)	α	−0.03
4/5	0.00	β	+0.03
3/6	0.00	2’	+0.01
3’	−0.01	5’	−0.01
4’	+0.02	–	–
Cp*	+0.03	–	–

* The sum over all Cp carbon atoms is calculated.

Table 11.3: ^{13}C-NMR signal shifts δ [ppm] for Co(II)–6DTE–Co(II) at room temperature in toluene-d_8 (400 MHz) (see Figure 11.2)*.

carbon atom	δ	carbon atom	δ
Me	−22.87-(−26.31)**	*5”*	*604.69*
1/2	132.90	α/β	*390.57*
4/5	18.87	α/β	*272.18*
3/6	23.30	*2’*	*30.98*
3’	18.23	*5’*	*−214.62*
4’	353.29	–	–
Cp	589.89	–	–

*The signals which could not be securely identified are given in cursive.
** A range is given because the methyl (Me) carbon atoms gave a quartet resulting from the coupling with the three protons.

The signal at 604.69 ppm probably refers to carbon atom 5” (Figure 11.2, Table 11.2 and 11.3), which, according to the shift, carries positive spin density. This is confirmed by the spin density obtained for the high-spin state (+0.03 a.u.).
According to the literature [250], the spin density of the carbon atom of the bridge (atom 5’ here), attached to an atom of the Cp ring normally shows a spin inversion with respect to that carbon atom, so that a negative spin density should be found, which is indeed confirmed by the signal at −214.62 ppm and the spin density of −0.01 a.u. obtained from the DFT calculations.
According to the spin polarization mechanism (see Section 3.2), carbon atom 4’ possesses positive spin density, which is confirmed by theory and experiment

(δ=353.29 ppm), and is in agreement with the work of Köhler and coworkers [250, 251].
For the signal of carbon atom 3', a chemical shift of 18.23 ppm is obtained. Although the value is positive, it is shifted to smaller ppm values compared to the diamagnetic Co(III)–6DTE–Co(III) compound (δ=132.97 ppm [221]). This implies a shift towards negative spin density, which is indeed confirmed by the small amounts of negative spin density in the DFT calculations. This smaller shift is in agreement with the lower spin density on 3' compared to that on 5' as obtained from DFT.
The signals of the carbon atoms of the methyl groups show a shift to higher fields (negative chemical shifts), which is again in agreement with the calculated spin density (-0.002).
The signals for the carbon atoms of the unsubstituted Cp ring are shifted downfield, indicating α-spin density. According to the DFT results however, both, α, and β spin densities are found on the different carbon atoms on the Cp ring. However, the net spin density is positive (0.03 a.u. in Figure 11.2), and the unsubstituted Cp rings are expected to rotate, which leads to an average signal for the unsubstituted Cp ligand in Table 11.3.
However, for the substituted Cp ring experimentally positive spin density is found on the α and β position of the ring, while in disagreement with experiment negative spin density is found for the carbon atom in β position of the ring, although the chemical shift suggests a positive spin density. This could be a consequence of an erroneous description of the spin density on the substituted Cp ligand.

11.3 Photoswitching behavior of the Cobaltocene-substituted Switches

As for the chloro- and ferrocene-substituted photochromic switches (Chapters 9 and 10), the aim is to understand the switching properties in terms of the optical properties (Section 11.3.1) by means of TDDFT, and the results are compared to the experimental findings by A. Escribano [221]. Furthermore, the ground-state and excited-state PESs of the Co(I)–5DTE–Co(I) and the Co(II)–5DTE–Co(II) switches are studied as a function of the reactive thiophene carbon atoms forming the single bond in the closed form, in order to illustrate the differences in the switching behavior (Section 11.3.2).

11.3.1 UV/Vis Spectra

Therefore, the UV/Vis spectra are calculated by means of TDDFT employing the B3LYP functional. For the Co(II)–5DTE–Co(II) system, structure optimizations are carried out in both spin states (S=1 and S=0, the latter modeled by a Broken-Symmetry determinant). For both isomers, the BS determinant constitutes the ground state. However, it should be noted that in the open form

the BS determinant is only slightly stabilized ($E_F - E_{AF} = -0.95$ cm^{-1}) against the high-spin state, while for the closed form isomer a much larger stabilization is found ($E_F - E_{AF} = -144.77$ cm^{-1}). This increase of the ground-state stabilization from the open to the closed form is expected, because of the change from cross conjugation in the open form to full π conjugation in the closed form.

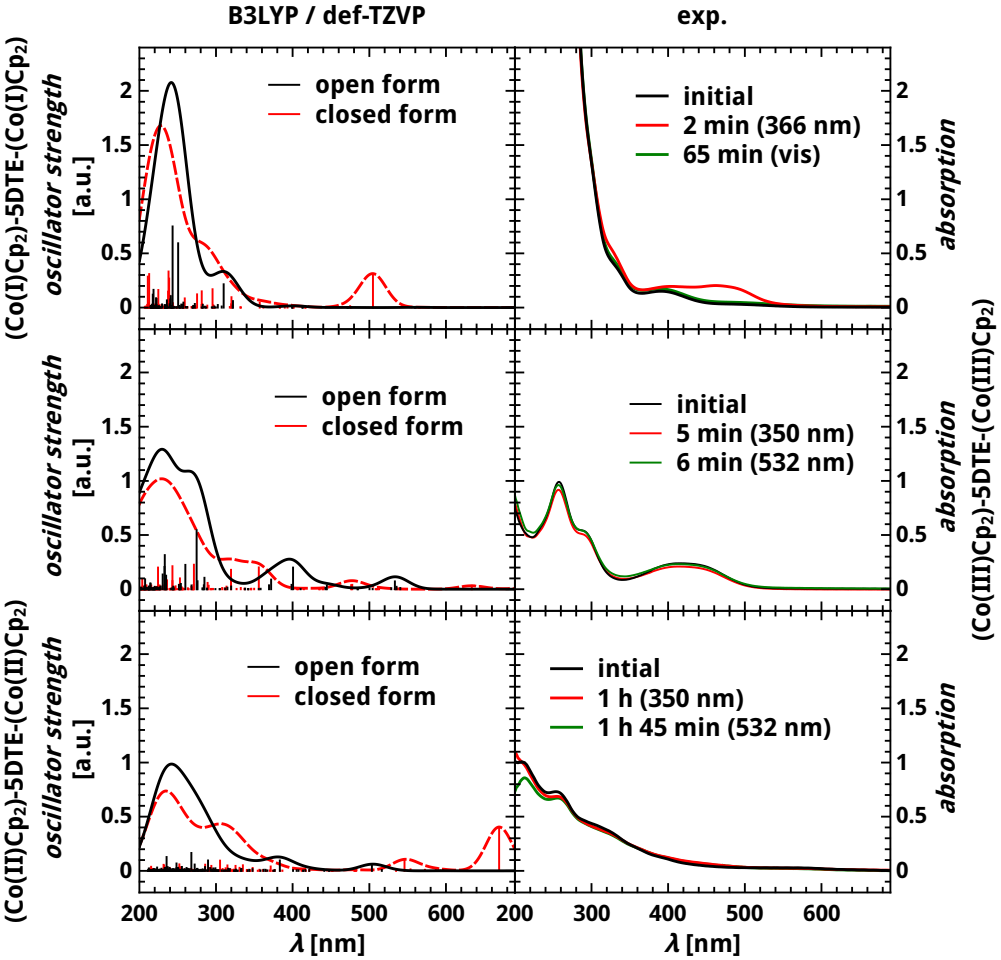

Figure 11.3: UV/Vis spectra obtained from TDDFT calculations with B3LYP / def-TZVP without any solvent effects (left column), and experimentally measured spectra [221] (right column) for the Co(I)–5DTE–Co(I) (top row; exp.: *n*-hexane, $9.43 \cdot 10^{-5}$ M, $d = 1$), the Co(III)–5DTE–Co(III) (middle row; exp.: acetonitrile, $d = 1$) , and the Co(II)–5DTE–Co(II) systems (bottom row; exp.: *n*-pentane, $1.89 \cdot 10^{-6}$ M, $d = 1$). The wavelengths of the employed light sources are given in the figure, and all measurements were carried out at room temperature.

The calculated spectra are given with the experimental ones in Figure 11.3. In the experiment, the Co(II)–5DTE–Co(II), and Co(I)–5DTE–Co(I) switches were measured in non-polar solvents (*n*-pentane, and *n*-hexane), which are expected to only weakly influence the spectra. Therefore, in the TDDFT calculations no

solvent effects are taken into account (for consistency also not for the Co(III)–5DTE–Co(III) switch).
For the Co(I)–5DTE–Co(I) system (top row in Figure 10.3; Table 11.4), the experimental and the theoretical spectra are in good agreement with each other, although the new appearing absorption band in the open form is located at 504 nm and therefore red-shifted compared to the experimental band at 468 nm. Experimentally, four switching cycles could have been realized for the Co(I)–5DTE–Co(I) system by employing wavelengths of 350 nm and 532 nm.

Table 11.4: Experimental UV-vis spectroscopic data for the Co(I)–5DTE–Co(I) in *n*-hexane and DFT values employing B3LYP / def-TZVP.

Experimental data: λ, nm (ϵ, cm^{-1})	
Open Isomer	Closed Isomer (2 min irradiation UV light)
220; 250; 334 (sh, 3477); 390 (1697)	220; 250; 329 (sh, 5302); 400 (2015); 468 (2121)
Theoretical data: λ, nm (oscillator strength, a.u.)	
Open Isomer	Closed Isomer
242 (2.08); 309 (sh, 0.33); 400 (0.02)	227 (1.68); 241 (2.08); 309 (sh, 0.33); 400 (0.02), 504 (0.31)

In contrast to the Co(I)–5DTE–Co(I) complex, the Co(III)–5DTE–Co(III) and Co(II)–5DTE–Co(II) switches are η^5-coordinated, and therefore the metal centers might influence the switching properties more strongly.
For the diamagnetic Co(III)–5DTE–Co(III) complexes, the best switching behavior was observed in acetonitrile, but even in this solvent the changes in the spectrum were small compared to the Co(I)–5DTE–Co(I) system [221]. The calculated spectrum of the open form is in very good agreement with the experimental spectrum. The poor switching behavior becomes visible by comparing it to the spectrum of the closed form, calculated with B3LYP / def-TZVP. In the spectrum of the closed form the excitation initiating the ring-opening reaction is found at 771 nm (outside of the displayed range in the spectra in Figure 11.3), and can therefore not be observed in the experimental spectrum. Nevertheless, the absorption band at about 430 nm, appearing in the experimental and theoretical spectra of the open form should completely vanish in the closed form, which can be seen from the theoretical spectrum of the closed form. In the experimental spectrum, this expected decrease is indeed observed, but is only very small, underlining the poor switching behavior.
Also the switching behavior of the Co(II)–5DTE–Co(II) switch was very poor, which can be easily seen from the fact that no increase in the visual part of the spectrum is observed (bottom-right panel in Figure 11.3). The calculated spectrum of the Co(II)–5DTE–Co(II) switch in the open form shows the same

features as found in the experimental spectrum. As for the Co(III)–5DTE–Co(III) complex, a new absorption band at 660 nm appears in the closed form, which is absent in the experimental spectrum after irradiation with the UV light source.

11.3.2 Potential Energy Surface Scans

To understand why Co(I)–5DTE–Co(I) demonstrates a much better switching behavior than Co(II)–5DTE–Co(II), a scan along the distance between the reactive carbon atoms are performed and the potential energy surfaces (PES) of the ground states and the excited states are analyzed to gain deeper insight in the switching mechanisms.

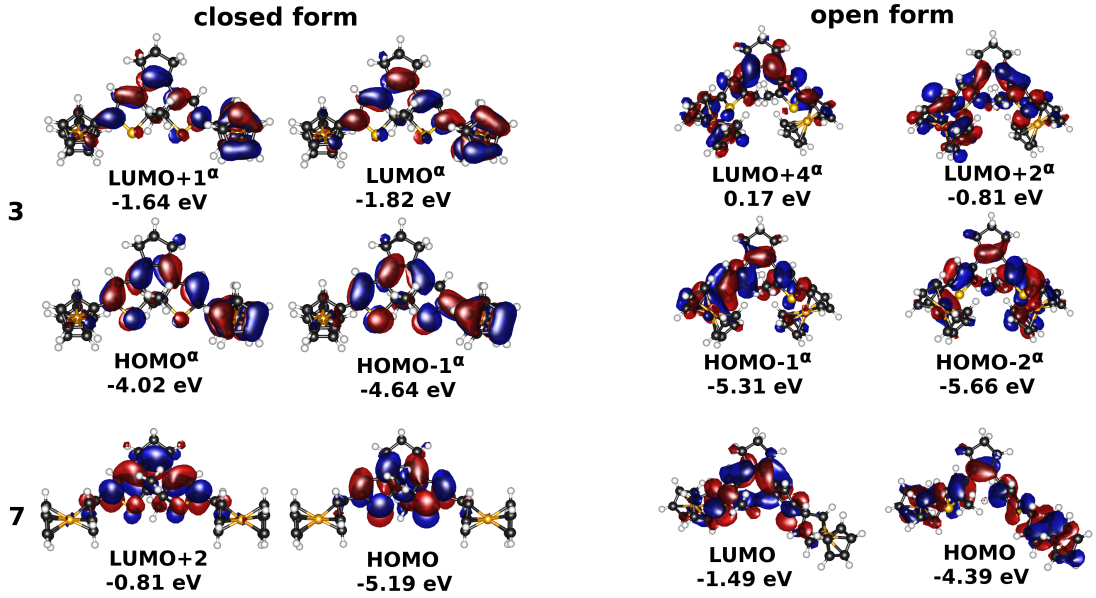

Figure 11.4: Molecular orbitals supporting the ring-opening and ring-closure reaction in the open and closed forms of Co(I)–5DTE–Co(I) and Co(II)–5DTE–Co(II) calculated with B3LYP-D3 / def-TZVP.

As in the previous two chapters, the other structural parameters are allowed to relax for each C−C distance. It should be noted that for reasons of computational efficiency, the second parameter, the torsional angle between the thiophene planes, is not considered explicitly, [239] and that a reliable treatment of conical intersections in DFT may also be problematic [246,247]. Further, for the Co(II)–5DTE–Co(II) only the singlet ground state (modeled by a BS determinant) is taken into account in the calculations, while the triplet state is excluded from the analysis. While these limitations of this approach should be pointed out clearly, it is considered reliable enough to provide a qualitative picture allowing for a comparison between the two switches. In the following,

the singlet states are referred to as S_x, with index 0 standing for the ground state and larger x for the excited states.

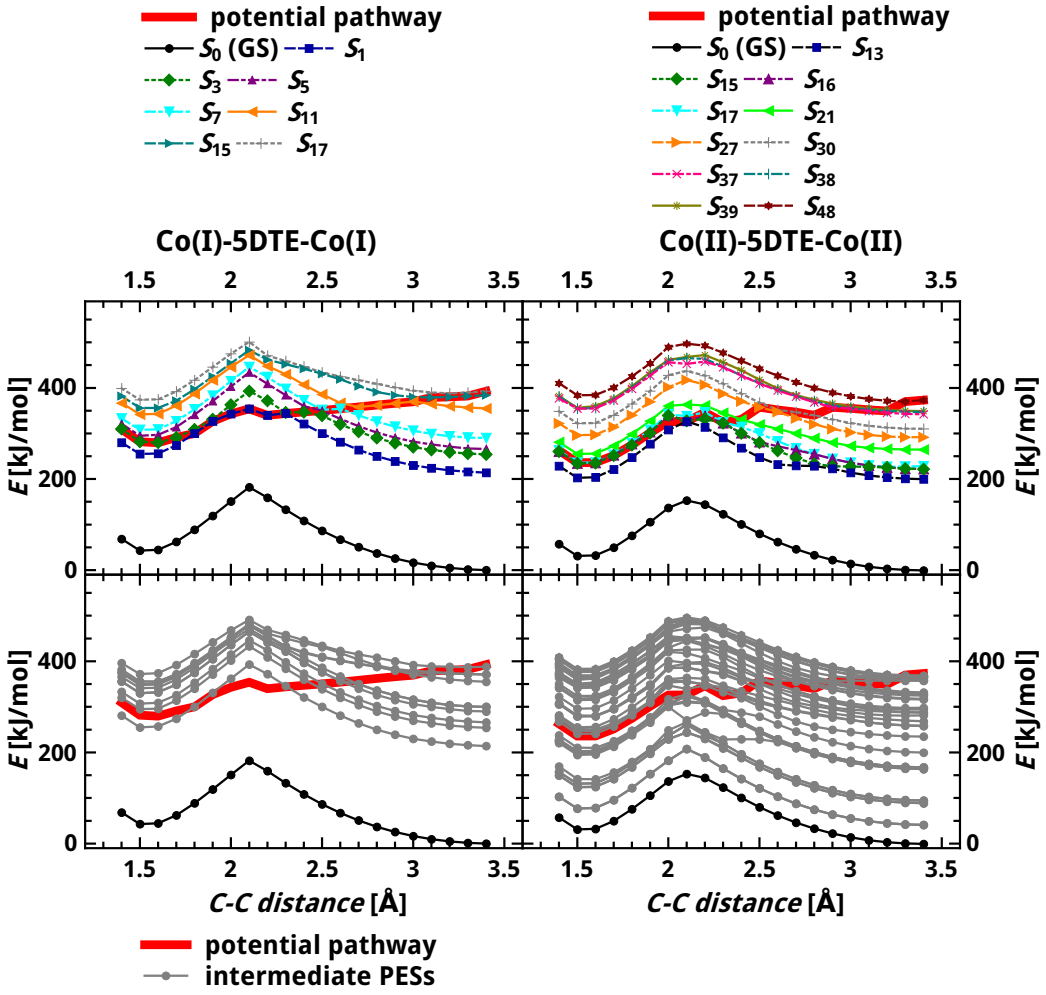

Figure 11.5: Reaction pathways (see also Table B.3 for exact composition) and potential energy surfaces referring to them, as a function of the distance between the reactive thiophene carbon atoms, forming the single bond in the closed form, for Co(I)–5DTE–Co(I) and Co(II)–5DTE–Co(II) switches. Intermediate PESs, not involved in the reaction pathways, and the reaction pathways for both systems (bottom). In all calculations B3LYP-D3 in combination with the def-TZVP basis set was employed.

First, the MOs having the correct shape to support the ring-closure reaction have been identified in the closed and open isomers (Figure 11.4). While for Co(I)–5DTE–Co(I), only one occupied and one virtual orbital have the correct shape to support the photoreaction, two occupied and virtual orbitals are obtained for Co(II)–5DTE–Co(II). Further, although similar in shape, the energetic order of these MOs is different for a given system when going from the open form to the closed form, which complicates an analysis of the excited-state PESs.
For both cobaltocene-based switches the excited states are studied for excitations

involving mainly transitions between the MOs having the contours as shown in Figure 11.4. From this analysis, it is possible to identify one potential reaction pathway for each compound. This is surprising because of the larger numbers of MOs in Figure 11.4, which are expected to support ring opening and ring closure for Co(II)–5DTE–Co(II). However, the MO shapes change strongly with decreasing C–C distance, so that only one reliable reaction pathway is found. The reaction pathways for both switches (bold red lines), together with the excited states involved in these, are given in Figure 11.5. A more detailed list of these excitations is given in Table B.3 in the appendix. However, there are PESs lying energetically between the PESs forming the reaction pathway, which potentially hinders the ring closure (Figure 11.5, bottom).

The ground-state energy barrier for cyclization for Co(I)–5DTE-Co(I) is 182 kJ/mol, which is larger than that for Co(II)–5DTE–Co(II) (153 kJ/mol). However, for all cases the ground-state reaction is unlikely to happen. By looking at the PESs of the excited states, it can be seen that the potential reaction pathways for both switches have a very similar shape as the first excited-state PES for the chloro-substituted switch (Figure 9.6). Nevertheless, as also observed for the ferrocene switch in Chapter 10, the reaction pathway does not involve one excited state, but different states very close in energy. As pointed out before, this is a consequence of the mixing of MO contributions from the bridge with those of the metallocenes.

To initiate the photocyclization reaction in Co(I)–5DTE–Co(I), the system must be excited in the S_{17} state, in which the contribution from the HOMO→LUMO+2 transition is 65.9% of the total excitation (Table B.3). The MOs involved, have the shapes initiating the ring closure reaction (see MOs in Figure 11.4). The oscillator strength for this transition is equal to 0.03 a.u. (λ=305 nm) for a bond length of 3.4 Å. For Co(II)–5DTE–Co(II), the excitation needs to take place to the S_{48} state, which includes contributions of 44.3% from the HOMO-$1^{\alpha/\beta}$ →LUMO+2α/β, initiating the ring closure reaction. However, this excitation only possesses an oscillator strength of 0.01 a.u. (λ=317 nm), which is only one-third of the intensity of the corresponding excitation in the Co(I)–5DTE–Co(I) system, meaning the latter excitation is less likely to happen. This trend is maintained for all C−C distances (see Table B.3).

Further, it must be mentioned that the number of excited-state PESs involved in ring closure is much higher for Co(II)–5DTE–Co(II) than for Co(I)–5DTE–Co(I), and also the number of PESs being close in energy to the relevant transitions but not playing a role for the switching reactions, is higher. This further supports the experimental observations, and underlines the poorer switching behavior of Co(II)–5DTE–Co(II) compared with Co(I)–5DTE–Co(I).

At least, also the activation barriers of both reaction pathways must be considered. For Co(I)–5DTE–Co(I), the energetic barrier for cyclization, calculated by taking the energy difference between the maximum at 2.1 Å (S_1) and the minimum at 2.2 Å (S_1), is 14 kJ/mol, which is relatively low. For (Co(II)Cp_2)-5DTE-(Co(II)Cp_2), three very small activation barriers must be considered, because

three minima, and maxima ($\Delta_1 = E\left(S_{38}, 3.2\ \text{Å}\right) - E\left(S_{37}, 2.9\ \text{Å}\right) = 8$ kJ/mol; $\Delta_2 = E\left(S_{27}, 2.5\ \text{Å}\right) - E\left(S_{30}, 2.8\ \text{Å}\right) = 18$ kJ/mol; $\Delta_3 = E\left(S_{15}, 2.2\ \text{Å}\right) - E\left(S_{21}, 2.4\ \text{Å}\right) = 7$ kJ/mol) are found. All reaction barriers are very small, and should be no hindrance for the cyclization.

11.4 Conclusions

In this chapter, the switching behavior of different cobaltocene-based photochromic switches was investigated (Figure 11.1). The structural parameters of the open forms obtained from DFT were in good agreement for all switches, except for Co(III)–6DTE–Co(III), for which deviations of roughly 14° were obtained compared with the X-ray crystallographic structure. The spin densities for the Co(II)–6DTE–Co(II) system were compared to the results from NMR spectroscopy, and were in overall agreement. Only the spin densities on the carbon atoms of the unsubstituted Cp ring calculated with DFT showed different spin densities for different atoms, which is in disagreement with experiment (where only positive spin density was found on the Cp carbon atoms), but presumably resulted from a rotation of the Cp rings. Moreover, the spin density on the β carbon atom of the substituted Cp ring deviated from the spin density expected from the chemical shifts, which most likely corresponds to an artificial description of the spin density by DFT in that case.
From the UV/Vis measurements, it became obvious that only Co(I)–5DTE/6DTE–Co(I) switches (Figure 11.1) were able to perform up to four cycles, while the changes in the spectra for Co(III)–5DTE–Co(III) were rather small, and for the Co(II)–5DTE–Co(II) no changes could be observed. The spectra calculated for the cyclopentene switches with TDDFT were in good agreement with the measured ones.
In order to explain these large differences in the switching behavior between Co(I)–5DTE–Co(I) and Co(II)–5DTE–Co(II), PES scans of the ground states and the excited states with respect to the distance between the reactive thiophene carbon atoms, forming the single bond in the closed form, were performed. The contributions from the cobaltocene-based substituent to the MOs, being responsible for the switching, were larger for Co(II)–5DTE–Co(II) than for Co(I)–5DTE–Co(I) (especially at lower distances). The perturbance of the switching reaction also manifested in the contributions of the MO transitions supporting ring closure, which were always larger for Co(I)–5DTE–Co(I). Furthermore, the number of PESs, which were close in energy to the reaction pathways is much larger for Co(II)–5DTE–Co(II) than for Co(I)–5DTE–Co(I), and even larger than for the ferrocene-substituted system studied in Chapter 10 (although one must interpret this with caution because the functional differed from the one used in this part). These theoretical findings were able to explain the large differences in the switching behavior between Co(I)–5DTE–Co(I) and Co(II)–5DTE–Co(II).

12. Is There a Correlation between Aromaticity and Open-Shell Character in Dithienylethene Switches?

In this chapter, magneto-structural correlations are studied for a series of spin-coupled photochromic switches closely related to the closed form of the dithienylethenes studied in the previous chapters (Figure 12.1, bottom), with two different resonance structures, one referring to a closed-shell singlet and a second referring to an open-shell singlet state (Figure 12.1, top).

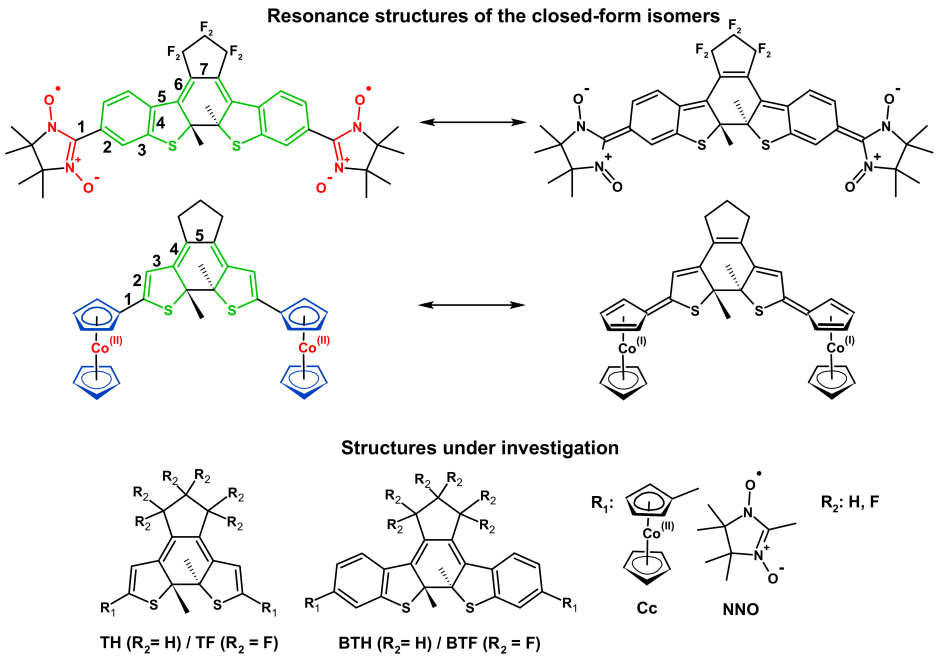

Figure 12.1: Resonance structures of the closed-form isomer of the switch synthesized by Matsuda [25] and cobaltocene-substituted switch as synthesized by Escribano and coworkers [221, 249] (top). The colors are used for the definitions of the spin centers employed in the Green's-function approach in Figure 12.2, and to highlight the bonds included in the calculation of the "harmonic oscillator model of electron density" (HOMHED) values (Figure 12.5). The numbers refer to the bonds, which are used in the bond length analysis in Figure 12.6. Note that the term "resonance structures" may be debatable here, as for the pairs of structures depicted on the left and right of the resonance arrow, not only the electronic properties, but also bond lengths and angles would be expected to differ when each was allowed to relax structurally. Lewis structures and abbreviations of the different bridges and magnetic moieties used to build up the systems under investigation (bottom).

One of the central problems in theory concerning such kind of systems is that in some cases an unambiguous prediction of the dominant resonance structures (Figure 12.1, top) is not possible with DFT, and consequently also the prediction of bond lengths and other properties becomes difficult or even impossible. Therefore, one goal pursued in this chapter is to investigate when these problems occur. Furthermore, these kind of switches may be of interest in the context of logic applications, as for example in information processing units controlled by light [209].
Two different photochromic bridges are taken into account (bottom of Figure 12.1), a thiophene and a benzothiophene bridge, both differing in the length of the π system. These bridges are combined with two different kind of radical moieties involving cobaltocene (Cc) and NNO groups. Additionally, the effect of the perfluoration of the cyclopentene ring is considered.
In Section 12.1, the magnetic properties of the closed form are studied, and in Section 12.2 the aromaticity in the systems to see, if correlations between the open-shell character and the aromaticity in these systems exist, so that trends for one property can be transferred to each other. Especially for the Cc systems, these correlations are interesting, because the π system of the substituted Cp ligands is intact in the open-shell resonance structure, while it is destroyed in the closed-shell one (top in Figure 12.1) and it has recently been shown by Sun and coworkers [37] that such correlations exist for polyhydrocarbons.
Another aim is to understand how the spin center definition in the Green's-function approach affects the calculated coupling constants compared to the BS approach, especially if atoms of the photochromic bridge are taken into account.

12.1 Magnetic Properties

In Section 12.1.1, first the spin coupling constants calculated with the BS approach and the Green's-function approach for all compounds are compared, since this provides an especially challenging test case. In Section 12.1.2, then the open-shell character is investigated by the $\langle \hat{S}^2 \rangle$ values for the low-spin states, and additionally the diradical characters y calculated from the natural orbital occupations are discussed.

12.1.1 Exchange Coupling Constants

The spin coupling constants of all photochromic switches obtained from the BS approach and the Green's-function approach are given in Figure 12.2 for different bridges, substituents and exchange–correlation functionals. To check to what extend the obtained coupling constants depend on the exact choice of the spin centers, different definitions are employed. For the Cc systems, the coupling constants have been calculated using the cobalt atoms as the spin center ($J_{\mathrm{Green,Co}}$ (F); red fragments in Figure 12.1), including additionally the carbon atoms of the cyclopentadienyl rings ($J_{\mathrm{Green,Cc}}$ (F); blue and red fragments in

Figure 12.1), and also including half of the bridge into the spin-center definition ($J_{\mathrm{Green,Cc+bridge}}$ (F); green, blue, and red fragments in Figure 12.1).

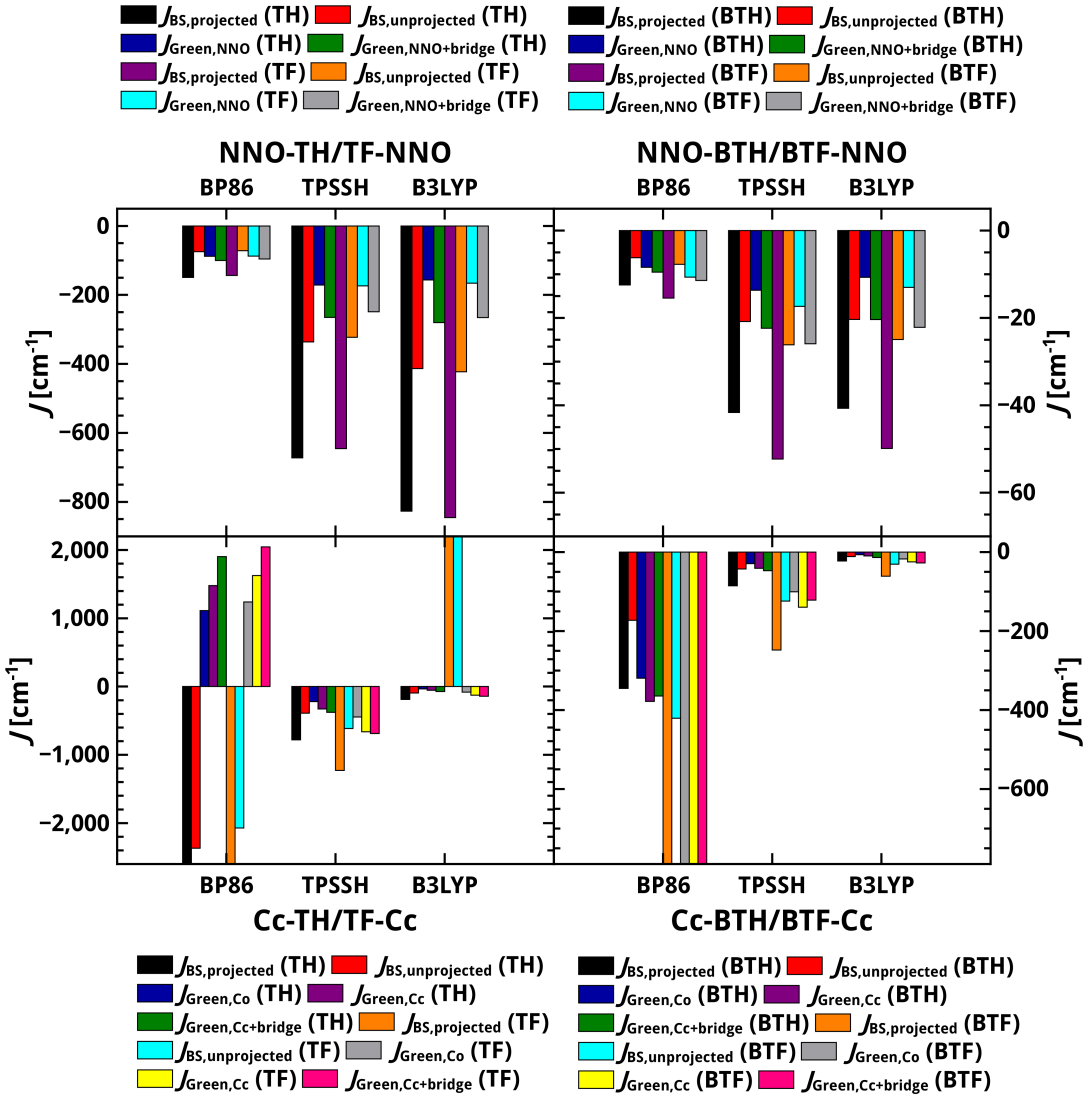

Figure 12.2: Exchange-spin coupling constants J calculated for different bridges and substituents (bottom in Figure 12.1) from the unprojected, and projected BS approach, and the Green's-function approach using three different functionals and the def-TZVP basis set. For the Cc systems, the coupling constants have been calculated using the cobalt atoms as the spin center $J_{\mathrm{Green,Co}}$ (F) (red fragments in Figure 12.1), including additionally the carbon atoms of the cyclopentadienyl rings $J_{\mathrm{Green,Cc}}$ (F) (red and blue fragments in Figure 12.1), and also including half of the bridge into the spin-center definition $J_{\mathrm{Green,Cc+bridge}}$ (F) (green, blue, and red fragments in Figure 12.1). In analogy for the NNO systems, the NNO groups ($J_{\mathrm{Green,NNO}}$ (F); red fragment in Figure 12.1), and the NNO substituents including the bridge ($J_{\mathrm{Green,NNO+bridge}}$ (F); green and red fragments in Figure 12.1).

For the NNO systems, the NNO groups ($J_{\mathrm{Green,NNO}}$ (F); red fragments in Figure 12.1), and the NNO substituents and the bridge ($J_{\mathrm{Green,NNO+bridge}}$ (F);

green+red fragments in Figure 12.1) are considered.
For all systems an antiferromagnetically coupled ground state is obtained with the BS approach. Although in general in good agreement, the Green's-function approach gives large qualitative deviations for the Cc–TH–Cc, and Cc-TF–Cc systems (bottom-left in Figure 12.2), employing the BP86 functional. But also the BS approach fails for Cc–TF–Cc system, for which the predicted exchange coupling is ferromagnetic, which qualitatively disagrees with all other values obtained for this system. In general, it can be seen that the definition of the spin center within the Green's-function approach indeed has a remarkable influence on the calculated coupling constants for the systems under study, and that the values improve compared to the BS values when the bridge is included. This proves that the Green's-function approach can also be used in cases with strongly delocalized spin density as long as the spin centers can be properly defined, which is not possible when the bridge possesses atoms that are shared by both magnetic sites (meta-dimethylenebenzene).

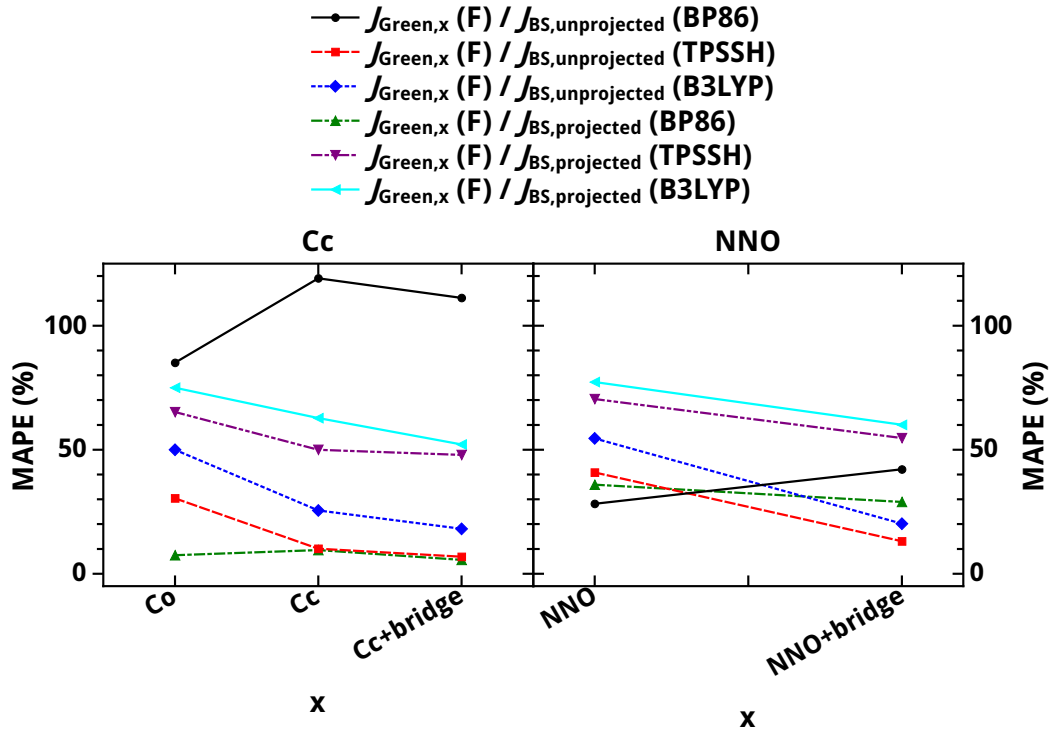

Figure 12.3: Mean average percentage errors (MAPEs) in percent calculated for the Cc-substituted (left) and the NNO-substituted systems (right) in percent for different exchange–correlation functionals in combination with def-TZVP. For BP86, only the coupling constants for the Cc–BTH–Cc are taken into account and all other Cc systems are neglected due to the large deviations between both approaches for this functional. For the NNO substituent, all coupling constants are considered.

The strength of the coupling decreases with increasing amount of Hartree–Fock

(HF) exchange for all Cc systems, and for the NNO–TH/TF–NNO systems. For the NNO–BTH/BTF–NNO systems however, the strength of the coupling increases from BP86 to TPSSH, and then decreases again for B3LYP.
The perfluoration of the bridging cyclopentene ring leads to different trends depending on the length of the bridge. While for the BTH/BTF pair the coupling strength increases upon perfluoration (much stronger for Cc than for NNO), it slightly decreases for the TH/TF pair, irrespective of the employed exchange–correlation functional. The extension of the switches' π systems lead in all cases to a decrease in the coupling strength.
To quantify the influence of the spin center definition in the Green's-function approach, the mean average percentage errors between the different coupling constants calculated from the Green's-function approach and those calculated from the projected and unprojected BS approach (Figure 12.3) are evaluated according to Equations (4.1) and (4.2) (Section 4.3). The BS values are taken as the reference in all cases. For B3LYP, the coupling constants for the Cc–TF–Cc are neglected due to the strong deviations of the BS approach. For BP86, only the coupling constants for the Cc–BTH–Cc are taken into account and all other Cc systems are neglected due to the large deviations between both approaches for this functional. For the NNO substituent, all coupling constants are considered.
It can be easily seen that like for the complexes discussed in Chapter 4, the coupling constants calculated with BP86 from the Green's-function approach, regardless which substituent is employed, are rather comparable to those obtained from the projected BS approach (green curves in Figure 12.3). However, for the coupling constants calculated with TPSSH and B3LYP are rather comparable to the value obtained from the unprojected BS approach (red and blue curves in Figure 12.3). The MAPEs between the coupling constants calculated with the Green's-function approach and the projected BS approach for the Cc systems using the BP86 functional (green curve in the left panel in Figure 12.3) slightly enlarge by inclusion of the Cp ligands into the spin center definition, but reaches the overall lowest MAPE for this combination if also the bridge is included. In all other cases the MAPEs between the coupling constants from the unprojected BS approach and the Green's-function approach continuously decrease by extension of the spin center definition for BP86. The same is true for the MAPEs between the values from the unprojected BS approach and Green's-function approach employing the hybrid functionals. This illustrates that the extension of the spin center definition in the Green's-function approach indeed improves the predicted coupling constants.

12.1.2 Diradical Characters and $\hat{S}^2$ Expectation Values

The diradical characters y strongly differ for the Cc systems with respect to bridge and the chosen exchange–correlation functional (top-left panel in Figure 12.4), while those calculated for the NNO system are always one (top-right

in Figure 12.4). For the Cc–TH–Cc and Cc–TF–Cc systems, a closed-shell singlet ground state is found (diradical character of zero), which explains the strong deviations of the Green's-function method from the BS approach. With increasing amount of employed HF exchange, the diradical characters for the Cc systems increase. This is in correlation with the decreasing coupling constants, which might be a consequence of the stronger localization of the spins on the magnetic sites, as displayed by the trend for y. Perfluoration of the cyclopentene ring leads to a decrease in y for the Cc systems, which results in a larger spin coupling, following the same argumentation as used for the influence of the HF exchange. The diradical characters further increase upon elongation of the photochromic bridge, which again correlates with the decrease of the coupling strength. Two different effects could contribute to this trend. On the one hand the distance between the spin centers increases, on the other hand the potentially higher aromaticity of the BTH and BTF bridges could further play a role, as recently found for polyhydrocarbons [37].

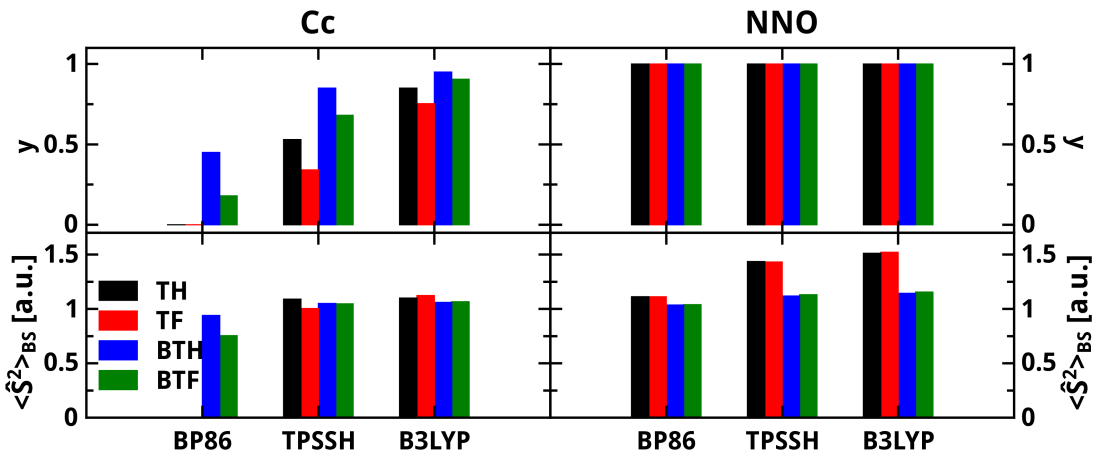

Figure 12.4: Diradical characters y calculated from the occupation numbers of the natural orbital according to Equations (2.16) and (2.17), and the $\hat{S}^2$ expectation values of the BS determinant, $\langle \hat{S}^2 \rangle_{\mathrm{BS}}$, calculated with three different exchange–correlation functionals and the def-TZVP basis set.

The $\hat{S}^2$ expectation values show that for the NNO–TH–NNO and NNO–TF–NNO systems the spin contamination in the BS solution exceeds a value of one for the hybrid functionals. For all other systems, the $\langle \hat{S}^2 \rangle_{\mathrm{BS}}$ values are very close to, or even below one. This could imply a potential pitfall for the Green's-function method, which assumes a local spin rotation when transitioning from the ferromagnetically coupled to the low-spin state, but is known to fail when strong changes in the spins' magnitudes occur. Nevertheless, it could be seen that the MAPEs are not significantly larger for the NNO systems than for the Cc systems (see Figure 12.3).

12.2 Aromaticity

To evaluate potential correlations between the open-shell character and the aromaticity of a given system, in Section 12.2.1, the HOMHED model (see Section 2.5.1) is used to gain information about the aromaticity from structural parameters, by comparing the bond lengths of the structures under study to "ideal" bond lengths of aromatic systems. This is of high relevance, especially for the substituted Cp rings of the Cc substituents having an aromatic π system in the open-shell resonance structure that is destroyed in the closed-shell resonance structure (top of Figure 12.1). It is also worth looking at the bond lengths of the photochromic core, which are the exact opposite of each other in both resonance structures (top of Figure 12.1). In Section 12.2.2, the HOMO-LUMO gaps are discussed as an electronic measure for the stability of the compounds.

12.2.1 Structural Measures for Aromaticity

In order to study the aromaticity in these compounds the HOMHED values have been calculated by the using the parameterization given in Ref. [79] (see "Computational Methodology" chapter). It can be seen that the total HOMHED values increase in most cases from BP86 to TPSSH, and then decrease again for B3LYP. This trend does not correlate with the trends found for the diradical characters and coupling constants. However, the trend is dominated by the strong changes in the HOMHED values for the bridge part. For the Cc systems, it has been found that with increasing Hartree–Fock exchange the HOMHED values for the Cp ligands (declared as radical moieties) of the cobaltocenes monotonically increase which is in agreement with the trends observed for the diradical characters. Considering the resonance structures (top in Figure 12.1), it can be easily seen that the aromatic system of the Cp rings is destroyed in the closed-shell resonance structure. In agreement with Sun and coworkers [37], the driving force behind favoring the open-shell character could be the aromatic stabilization of the π systems of the Cp rings. Also, an elongation of the π system leads to an increase of the total HOMHED values, being again related to a larger aromaticity in the BTH and BTF bridges, involving a condensed, aromatic benzene ring.
In order to understand the trends for the HOMHED values of the bridge, the bond length alternation patterns in the photochromic switches, including bond lengths of several bonds (defined in top of Figure 12.1), are calculated for the low-spin state (Figure 12.6). This is helpful to identify at first glance which resonance structures is dominant for a given compound because the alternation of single and double bonds in the photochromic core in the closed-shell and open-shell resonance structures is the exact opposite (top in Figure 12.1). Further the hydrogen-substituted bridges (noted as TH/TF and BTH/BTF) are considered in order to investigate the influence of the substituents on the bond lengths of the photochromic core.

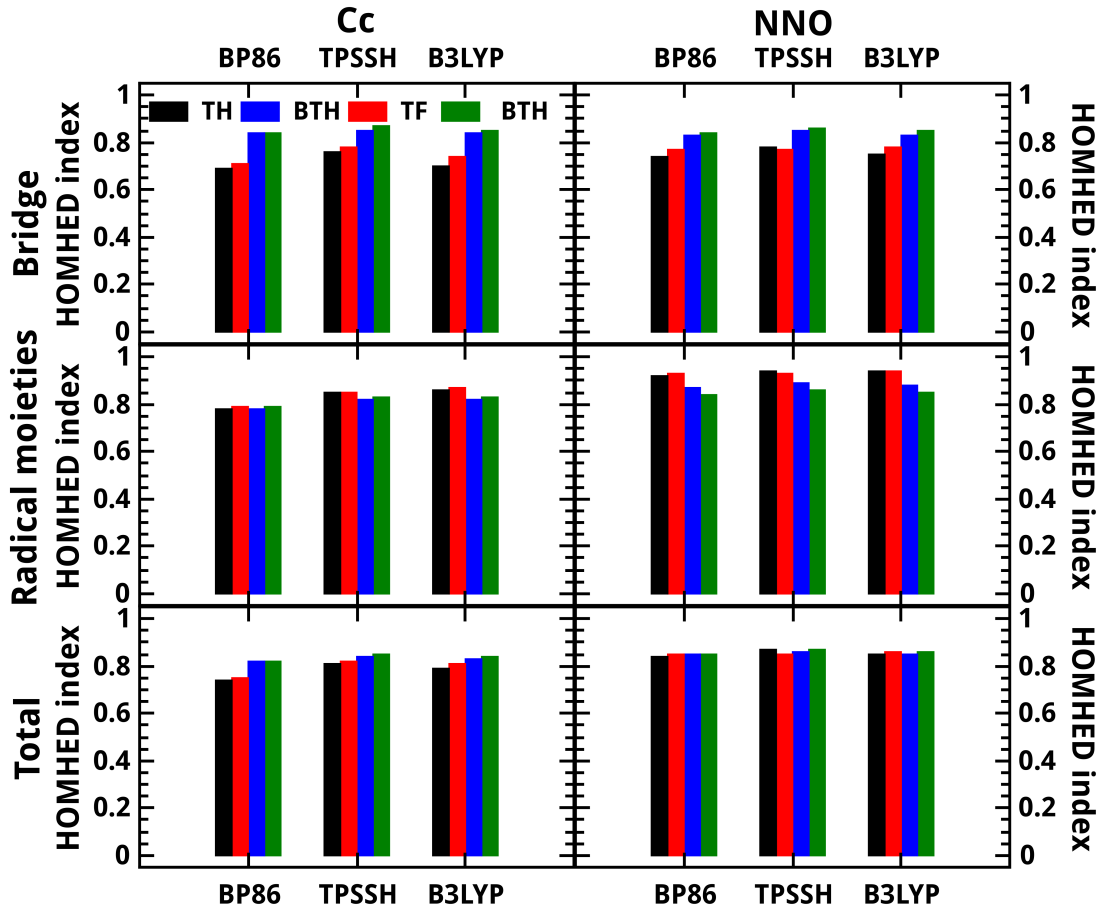

Figure 12.5: HOMHED values (according to the definition in Section 2.5.1) for the bridge (top row; bonds considered are given in green in Figure 12.1, excluding the single bonds to the methylated carbon atom, and including the bond between the substituents and the bridge), the radical moieties (middle row; bonds are given in blue for the Cc system; only the Cp ring attached to the photochromic core is considered); red for the NNO moieties in Figure 12.1) and for the sum of both fragments. Basis set: def-TZVP.

While for the BTH and BTF bridges, the Cc and NNO substituents appear to have nearly no influence on the bond lengths on the thiophene fragment (the benzene part is affected more strongly; right column in Figure 12.6), the bond lengths for the TH and TF bridges are smaller than for the unsubstituted switches (left column in Figure 12.6). Furthermore, the effect of perfluoration only slightly influences the bond lengths in favor of a bond length equalization, as also found for the HOMHED values (see Figure 12.5). For the BS structures of the Cc–TH–Cc and Cc–TF–Cc systems the bond length alternation pattern refers to the closed-shell resonance structure in Figure 12.1, while for all other combinations the bond length alternation pattern of the open-shell resonance structure is obtained. This is in agreement with the diradical characters of zero for both systems. When going from BP86 to the TPSSH, and the B3LYP functional the bond length alternation pattern changes in favor of the open-shell

resonance structure in Figure 12.1.

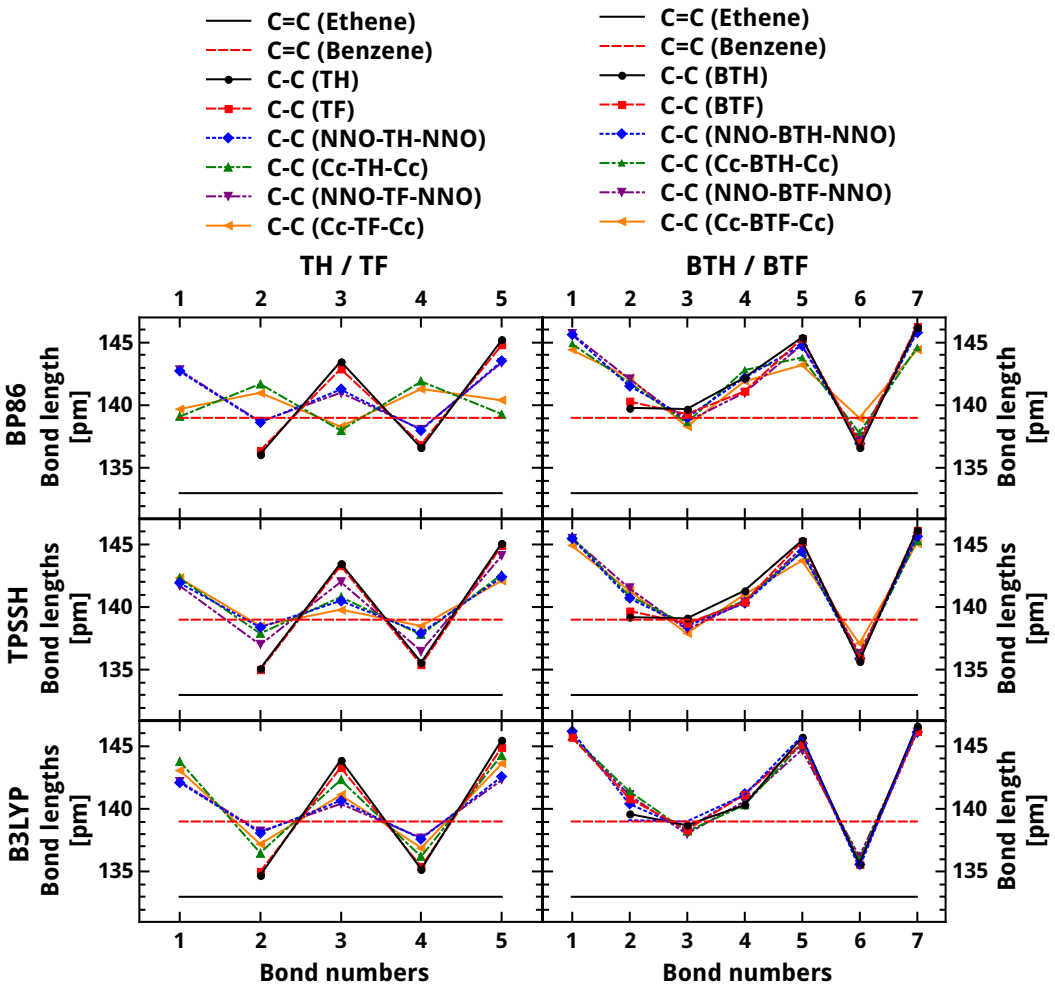

Figure 12.6: Bond lengths of chosen bonds defined according to Figure 12.1, which are expected to change from one resonance structure to the other, calculated with different exchange–correlation functionals for the BS determinants of all systems under investigation (bottom in Figure 12.1). The bond lengths for the hydrogen-substituted bridges TH, TF, BTH, and BTF and the lengths of the double bonds C=C are given for ethene and benzene for comparison. Basis set: def-TZVP.

This also explains the maximum in the HOMHED values for TPSSH, which results from the fact that TPSSH is close to the "crossover" point between both patterns.

12.2.2 HOMO-LUMO Gaps

The HOMO–LUMO gaps are a measure for the electronic stability towards nucleophilic and electrophilic substitution [80] (see also Section 2.5.2). The

frontier MOs are given in Figure 12.7 for all compounds and exchange–correlation functionals.

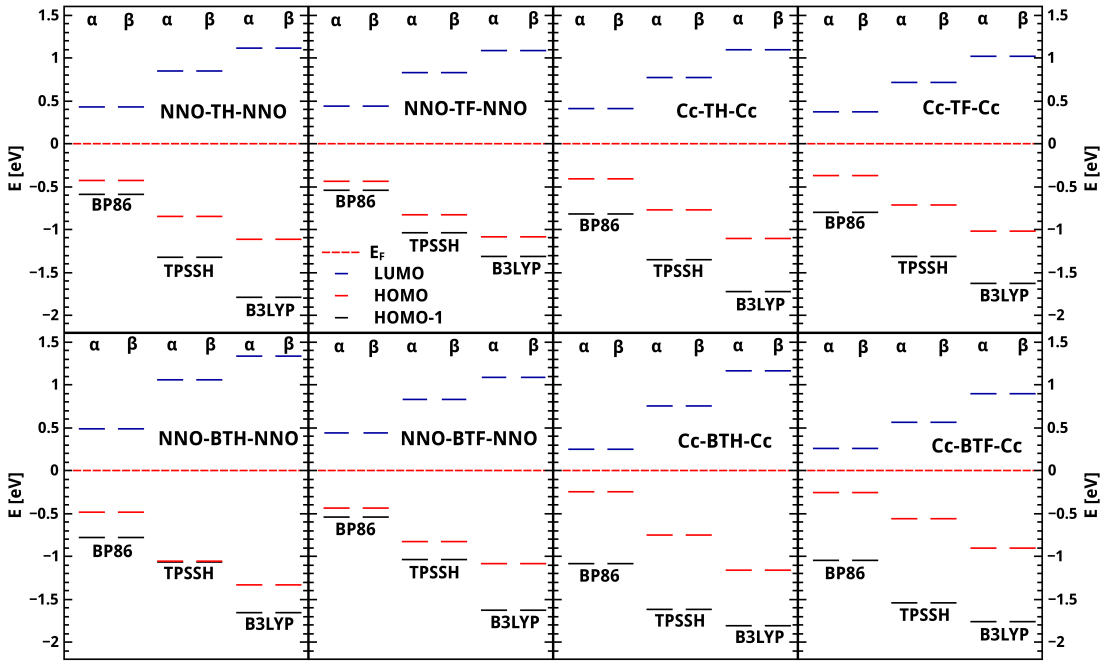

Figure 12.7: Frontier spin orbital energies obtained for the BS determinant of different magnetic photochromic switches obtained with the def-TZVP basis set and different exchange–correlation functionals.

For the BS solution, the spin orbitals are energetically degenerate, although they differ in their space parts, and therefore the HOMO–LUMO gaps are always the same for α and β spin orbitals. The HOMO–LUMO gaps for a given compound increase with the amount of HF exchange employed in the functional, which correlates with the increase in the diradical characters y for the Cc systems, and further with the HOMHED values for the Cp rings of the Cc groups.

12.3 Conclusions

In this chapter, the closed-form isomers of different photochromic switches decorated with two open-shell substituents were investigated in more detail. These systems are interesting because a closed-shell and an open-shell resonance structure can be formulated for them. The correct prediction of the structural parameters, as well as the magnetic properties is challenging within the framework in DFT due to the choice of the exchange–correlation functional and in particular to the amount of Hartree–Fock exchange used in the functional. But also the choice of the substituents and the photoswitchable itself is assumed to play a role. The aim was therefore to investigate how far the open-shell character and

the exchange spin coupling are influenced by the amount of Hartree–Fock exchange in the functional, the perfluoration of the cyclopentene ring, the length of the photochromic bridge, and the choice of the open-shell moieties. Furthermore, the molecules in this chapter were used to test the Green's-function approach. For the first time it was also checked how the definition of the spin centers in the Green's-function approach influences the calculated coupling constants, compared to those obtained from the BS approach. Since Sun and coworkers [37] showed that there is a correlation between the open-shell character and the aromaticity it was also checked if similar correlations also hold for the DTE switches under investigation.

The coupling constants calculated with the BS and the Green's-function approach were consistently antiferromagnetic in most cases. Only in three cases deviations between both methods were observed. Moreover, it was found that an inclusion of the bridge into the spin center definitions for the Green's-function approach in all cases improves the the calculated coupling constants compared to the BS approach. Again, the coupling constants obtained with BP86 should be compared to the projected BS expression, while the values obtained with TPSSH and B3LYP should rather be compared with the unprojected formula. The coupling strength was found to decrease upon bridge elongation, with increasing Hartree–Fock exchange (in most of the cases), and increased upon perfluoration of the cycloalkene ring. All these trends correlated with the diradical characters for the Cc systems, which increase upon bridge elongation, and with the amount of Hartree–Fock exchange employed, and decrease upon perfluoration. For the NNO systems, the diradical characters are always one, which underlines how crucial the influence of the radical substituent is. For the NNO diradicals (especially for NNO–TH/TF–NNO systems) the spin contamination in the BS determinant was abnormally high (up to values of 1.5 a.u.). Nevertheless, this did not lead to larger deviations for the Green's-function compared to the BS approach, which could be seen from the calculated mean average percentage errors. This is interesting because a reduction of the spins' magnitudes from one spin-state to another could be seen to lead to large deviations between both methods.

The aromaticity was described by the Harmonic oscillator model of hetereocyclic electron density (HOMHED) model which calculates the aromaticity by comparing the bond lengths of ideally aromatic compounds to the bond lengths of the systems under investigation. According to the HOMHED values, the aromaticity of the Cp rings monotonically increases with increasing Hartree–Fock exchange, which could be the driving force behind the increasing open-shell character in the Cc systems with TH and TF bridges. For the BTH and BTF bridges however the HOMHED values increase from BP86 to TPSSH and decrease again for B3LYP. But it must be noted however, that in these cases the pure distance and the aromaticity of the bridge is in general higher, which might become more important than the aromaticity of the Cp ring. The HOMHED values for the bridge dominated the HOMHED trends, but showed an increase

from BP86 to TPSSH, and decreased to B3LYP again. To understand this trend, the bond length alternation patterns were investigated, which are the exact opposite of each other for both resonance structures. They revealed that with increasing amount of Hartree–Fock exchange the open-shell form of the closed photochromic switch is more strongly favored, and the TPSSH structure is close to the "crossover" point between both resonance structures, and therefore shows the largest degree of bond equalization. The HOMO–LUMO gaps were not sensitive to the the kind of open-shell moieties employed, but were monotonically increasing with increasing Hartree–Fock exchange, which was also found for the diradical characters.

13. Controlling Magnetic Properties by Photoswitchable Bridges: Conclusions

In this part, a series of metallocene-substituted dithienylethene switches, synthesized by A. Escribano [221] in the framework of the SFB 668, were theoretically investigated to create spin-coupled systems which can be controlled by light. In the experiment, a route towards chirally substituted switches was opened by replacing the cyclopentene ring in the DTE switch, for the first time, by a cyclohexene ring.

The first goal was to rationalize the photoswitching behavior of these compounds in comparison with experiment by means of DFT and TDDFT calculations. Therefore, first "bare" chlorine-substituted switches were investigated with special emphasis on the comparison between the cyclohexene ("6DTE") and cyclopentene ("5DTE") switch (Chapter 9). These systems are a good starting point because the cyclopentene switch is known to show good switching behavior and is highly resistant to fatigue [238]. The structural and optical properties calculated with DFT and TDDFT were in good agreement with the experimental findings, and a PES scan as a function of the distance between the reactive thiophene carbon atoms revealed that the ring closure reactions are adiabatic processes only involving the first excited singlet state. According to the calculated transition dipole moments and the reaction barriers, the cyclopentene switch should perform slightly better than the cyclohexene switch, but no significant differences appeared.

The switching behavior of the DTE switches drastically worsened upon introduction of diamagnetic ferrocene moieties (Chapter 10), and only slight changes in the experimental UV/Vis spectra were observed upon irradiation with UV light. As for the chlorine-substituted switches, the structural and optical properties for the cyclopentene and cyclohexene switches differed only slightly. Again, a PES scan along the distance between the reactive thiophene carbon atoms was performed to understand why the switching behavior was so poor compared to the "bare" DTE molecules. It was found that the transitions supporting ring closure (and ring opening) were not adiabatic anymore, but included different excited states along the reaction coordinate referring to a diabatic reaction pathway with transitions between different excited-state PESs. However, there were also excited-state PESs very close in energy to the reaction pathway, mostly referring to $d-d$ transitions, which showed larger activation barriers and thus did not support ring closure, therefore potentially hinder cyclization when transitions to them occur.

In Chapter 11, DTE switches with both magnetic and non-magnetic cobaltocene-based substituents were investigated. Special emphasis was put on the comparison between the paramagnetic Co(II)–5DTE–Co(II) switch, which showed no switching at all, and the diamagnetic Co(I)–5DTE–Co(I) complex, which showed the best switching behavior of all metallocene-substituted switches investigated here. In the case of the former system, the carbon atom of the Cp ring attached to the DTE core is sp^2-hybridized and in conjugation with the π system of the DTE part, while for the latter the Cp carbon atom is sp^3-hybridized and therefore not in conjugation with the π system. Again, the theoretical findings for the structural properties were in good agreement with the experiment. Only for the Co(II)–6DTE–Co(II) complex, the deviations for the structural parameters were comparatively large. However, because the switching behavior was very similar for both cycloalkene rings, the cyclohexene DTE switches were not considered in the analysis of the switching behavior. For Co(II)–5DTE–Co(II), it was found that in both isomeric forms the open-shell singlet state is the ground state, which was nearly degenerate with the high-spin state in the open form and much stronger stabilized in the closed form. As in the two previous chapters, PES scans were performed for Co(I)–5DTE–Co(I) and Co(II)–5DTE–Co(II). As for the ferrocene-substituted switches, a diabatic reaction for the cyclization had to be taken into account for both switches. However, the number of excited states close in energy to the reaction pathways but not supporting it was the largest for Co(II)–5DTE–Co(II) among all systems, while the Co(I)–5DTE–Co(I) showed the lowest number of these "hindering" states. This however might be a consequence of the prohibition of interactions between the π system of the Cp ring with that of the photochromic bridge in the latter system. This was also underlined by the MOs supporting the photoreaction in the closed form, which possessed no contributions from the substituents in Co(I)–5DTE–Co(I), but larger contributions in Co(II)–5DTE–Co(II).

From these studies it is concluded that the introduction of the metallocenes to photochromic switches reduces the switching ability strongly due to the interaction between the metallocenes and the photochromic core by π conjugation, causing many transitions which are close in energy to the transitions leading to ring opening and ring closure, but actually not supporting these reactions. However, if there is no π conjugation between the DTE switch and the metallocenes, as for example for Co(I)–5DTE–Co(I), fewer of these states were found and the switching behavior improved compared to the other metallocene-substituted switches (although it is still worse than for the chlorine-substituted switch).

Our second goal was to investigate the magneto-structural correlations in the closed form of different magnetic photochromic switches. This is potentially a challenge for DFT, because two different resonance structures can be drawn, one being an open-shell and the second one being closed-shell singlet [25] (Chapter 12). Therefore, two different bridges were taken into account, differing in the length of the π system, two different spin-polarized moieties (NNO and cobal-

tocene). Further emphasis was on the effect of perfluoration of the bridging cyclopentene and on the choice of the exchange–correlation functional and on the open-shell character in these systems. Further, potential correlations between the open-shell character and the aromaticity in these systems were checked, which had been recently shown by Sun and coworkers [37] for polyhydrocarbons. Finally, the influence of the spin center definition in the Green's-function approach on the calculated coupling constants was evaluated in comparison to the BS approach.

The spin coupling in these systems was antiferromagnetic in all cases. In most cases, the coupling constants from the BS approach were in good agreement with the Green's-function approach, and large deviations were only found in cases in which the BS determinant converged to a closed-shell singlet (and in one case were the BS approach gave an unrealistically strong antiferromagnetic coupling). It could be shown that the inclusion of the bridge in the spin center definition of the Green's-function approach indeed improved the obtained values with respect to the BS approach. It was found that regardless of the parameters employed, the NNO-substituted systems always showed diradical characters of one, while they varied considerably for the cobaltocene systems. For example, an elongation of the bridge and an increase of the amount of Hartree–Fock exchange lead to an increase in the diradical character for the cobaltocene systems. The perfluoration of the cyclopentene ring in the cobaltocene systems, however, lead to a reduction of the diradical character. The HOMHED values, which estimate the aromaticity by comparing the bond lengths of the structure to ideal values for aromatic systems, showed for the cobaltocene systems that the aromaticity of the Cp ring increased with the amount of HF exchange, which correlated with an increase in the diradical characters. This indicated that maintaining the aromaticity in the Cp ring indeed appeared to be the driving force behind the open-shell character in these systems. For the BTH and BTF bridges this correlation was not found, which might result from the lower influence of the Cc groups on the bond lengths of the bonds participating in ring-opening and ring-closure reactions, due to the presence of the condensed aromatic ring in the benzothiophene bridge and it perfluorated analogue, which could be observed from the smaller changes in the bond lengths in the photochromic core compared with the unsubstituted reference switches.

Controlling spin coupling is an important aspect for spintronic devices, but also the energetic stabilization of the ground state against excited spin states is an important criterion to be able to operate systems at sufficiently high temperatures. One way of increasing the stability is the introduction of radical bridges, which could further stabilize the ground state by additional spin–spin interactions with the bridge. Therefore, the next chapter is devoted to the influence of radical bridges on the spin coupling in donor–acceptor diradicals, which was started in the author's Bachelor's thesis and for which a substantial amount of new data was generated during this thesis [35].

Part III: Increasing Spin Coupling by Radical Bridges

Controlling the relative orientation of local electron spins in the ground state is an important goal in molecular magnetism [252] and molecular spintronics [253]. This relative orientation is often dominated by exchange coupling and/or spin polarization [254], which leads to either ferromagnetic (parallel) or antiferromagnetic (antiparallel) alignment of the spins in the ground state, and which can be mediated over quite long distances via closed-shell subunits (superexchange) [252, 254–257]. In addition to the local spin arrangement in the ground state, the energetic separation from other relative spin orientations is important for designing molecule-based magnets and spintronic devices or materials.

For certain lanthanide complexes, it was found that while they exhibit remarkable single-ion magnetic anisotropy, coupling of multiple magnetic centers by typical closed-shell bridging ligands is weak. Long and coworkers solved this problem by introducing a spin-polarized bridge [258–261] which couples antiferromagnetically to each lanthanide center, resulting in a parallel alignment of the (larger) lanthanide magnetic moments and a considerably larger total magnetic moment. Related complexes were synthesized and characterized using organic radical bridging ligands [262–264] and 3*d*-transition-metal centers [265].

Radical bridges are also interesting for other cases in which closed-shell linkers only weakly couple spins, such as magnetic metal-organic frameworks (MOFs) [266, 267], where spin-polarized transition-metal centers are bridged by organic linkers. The length of these organic linkers is known to play a decisive role for tuning the pore size [268, 269]. With increasing length of the linkers, the interactions between the spin centers decrease (often, but not necessarily exponentially [254–257]). This problem may be solved by employing radical linkers, which could mediate the exchange-spin coupling between the magnetic subunits and stabilize the ground state against the remaining spin states [270]. A first example for a porous material based on a covalent organic framework of Nickel porphyrins with post-synthetically functionalized radical linkers was given in 2015, but the focus was on electrochemical energy storage and not on magnetic properties [271]. Otherwise, several MOFs with radical linkers have been synthesized, but so far a combination of magnetic properties with suitable permanent porosity was difficult to realize.

Radical bridging ligands were studied with respect to their influence on the electronic structure of Ruthenium mixed-valence complexes [272, 273] and on the charge-recombination dynamics in electron-donor–bridge–electron acceptor

systems, for which the effects of introducing different spin densities on the bridge were studied using tert-butylphenylnitroxide radical groups centrally attached to meta-linked phenyl bridges [274,275]. Spin-bearing mixed-valence semiquinone–Co(III)(pyridine)$_2$-catecholates linking nitronyl nitroxide radicals have also been investigated as model systems for exchange interactions between localized spins and the spins of itinerant electrons [276].

While the idea of using radical linkers or bridges for increasing interactions between spin centers has been widely accepted and applied, there exists a dearth of systematic studies on the relation between the chemical structure of the radical bridge and (a) the spin arrangement in the ground state and (b) its stabilization with respect to spin excitations. The goal is to assess by how much spin-polarized bridging ligands can stabilize the relative local spin orientation in the ground spin state, measured as the energy between the ground state and the first excited spin state (obtained by inverting the spin orientation on one spin center), using Kohn-Sham density functional theory (KS-DFT) calculations. Since spin state energetics are known to depend strongly on the approximate exchange–correlation functional, in particular on the amount of exact-exchange admixture [277, 278], a range of functionals with different amounts of exact exchange were compared, including the double hybrid B2PLYP, in which apart from replacing part of the exchange functional by a Hartree–Fock expression, a perturbation-theory-based part is mixed into the correlation functional [236]. Additionally, the influence of Grimme's empirical dispersion correction [248] is tested.

In the author's bachelor's thesis [35] a set of organic di- and triradicals were chosen in which a nitronyl nitroxide (NNO) and a semiquinone (SQ) radical with one unpaired electron each are connected by a benzene bridge, to which the radical units were attached via ethynyl spacers in the meta position relative to NNO and SQ (see Figure 14.1). In the meta position to these two radicals, a third substituent, X, was attached that may be a radical or a closed-shell group. These structures are abbreviated as NNO–X(Spacer)–SQ. The choice of spin centers was inspired by systems studied experimentally by two of the authors and their coworkers, modeling the charge-separated state of electron-donor–bridge–acceptor systems [255]. The model substituents directly attached to the benzene rings are either small radicals, X=CH_2·, X=NH·, and X=O·, or the corresponding closed-shell groups obtained by adding a hydrogen atom, X=CH_3, X=NH_2, and X=OH. The ethynyl spacers were chosen to prevent unfavorable steric interactions between the individual components of the system, ensuring that purely electronic effects are studied.

The bridges under investigation here are identical to those studied theoretically in our group with respect to their "spin filtering" properties [279]. In that context, significant differences were found between the three radical substituents. As a relationship between electron transport/transfer and exchange spin coupling has been noted since the 1950s [99,106,107,255,280,281], it will be interesting to determine whether the three radical substituents also lead to quite different

behavior when affecting spin coupling in organic radicals.
The "X" radical substituents are not stable under experimental conditions. Therefore in this work, additionally a complex in which the benzene ring of the bridge is functionalized by a stable nitroxyl radical substituent (abbreviated as NO) or its closed-shell counterpart (NOH) is considered, in which the semiquinone moiety is protected by a zinc complex as employed in previous work [255], and where the synthetically demanding ethynyl linkers are eliminated (resulting in the structure NNO–NO–SQ(Zn), see Figure 14.1). The results are compared to the results obtained for the model systems in the author's bachelor's thesis [35]. To bridge the gap to the model systems, this structure is also compared with NNO–NH–SQ(Zn), NNO–NH–SQ, and the corresponding closed-shell-bridge diradicals. This comparison will allow to judge the transferability of these calculations on model systems to the synthetically accessible ones.
This part is organized as follows: In Section 14.1.1 the dependence of spin state energy splittings on radical versus closed shell bridges and on the choice of the exchange–correlation functional is discussed, and then these findings are illustrated with plots of magnetic orbitals obtained in the author's Bachelor thesis [35]. In Section 14.1.2, the trends in local spin distributions of these model systems are discussed. In Section 14.2, new results of the influence of the ethynyl spacers and the stabilizing zinc complex on the spin-state energetics and local spins are discussed, and the potentially synthesizable NNO-NOH/NO-SQ(Zn) di- and triradical pair is investigated. In Section 14.3, the coupling constants obtained from the BS approach are compared to those obtained from the Green's-function approach applied to the electronic structure of the high-spin state to see if these systems are well described by the latter approach.

14. Results and Discussion

The Lewis structures of the triradicals employed in this study (as described in the introduction) are shown in Figure 14.1. The orientation of local spins on the NNO, the bridge, and the semiquinone radical units are designated as "up" (u) or "down" (d) (where "up" by convention refers to majority or α spins, and "down" to minority or β spins). For example, "uud" refers to a state in which the NNO and the radical substituent on the bridge couple ferromagnetically, and the spins on the bridge and on the semiquinone unit couple antiferromagnetically.

14.1 Model systems

14.1.1 Relative spin-state energies and magnetic orbitals

The spin-state energies of the diradicals shown in Figure 14.1 reveal that the meta-connected diradicals with closed-shell bridges have an antiferromagnetically coupled ground state ("ud") for all functionals except for the B2PLYP functional (where strong ferromagnetic coupling is found). Experimental findings for very similar systems suggest that the coupling in the ground state is antiferromagnetic which is in agreement with our findings (excluding B2PLYP) [255].
When using radical bridges for the meta-connected systems, the "duu" state becomes the ground state, still showing antiparallel alignment between NNO and SQ, while the spin of the "X" radical substituent spin was oriented parallel to the spin of the SQ subunit. This is true for all three radical substituents and for all functionals. The only exception was again the B2PLYP functional which qualitatively deviates from all other functionals in all cases. Therefore these results are not further considered in the discussion about the increase in the ground state stabilization. The preference for ferromagnetic coupling between X and SQ can be rationalized by the magnetic molecular orbitals (MOs) [282] located on these parts of the structure: The contours of these MOs can be used to estimate the exchange integral, which contributes to ferromagnetic coupling [95]. Magnetic MOs roughly corresponded to the singly occupied MOs in the Broken-Symmetry determinant modeling the antiferromagnetically coupled state. The coupling between X and SQ can therefore be attributed to the HOMO$^{\beta}$ and HOMO-1$^{\alpha}$ in the first three rows of Figure C.7 having coefficients on shared atoms, which should lead to a non-zero exchange integral [95]. The antiferromagnetic coupling between NNO and X was not obvious from similar MO arguments, as both HOMO$^{\alpha}$ (located on NNO) and HOMO$^{\beta}$ (located mainly

on the bridge) for X=NH· and X=O· share common atoms.

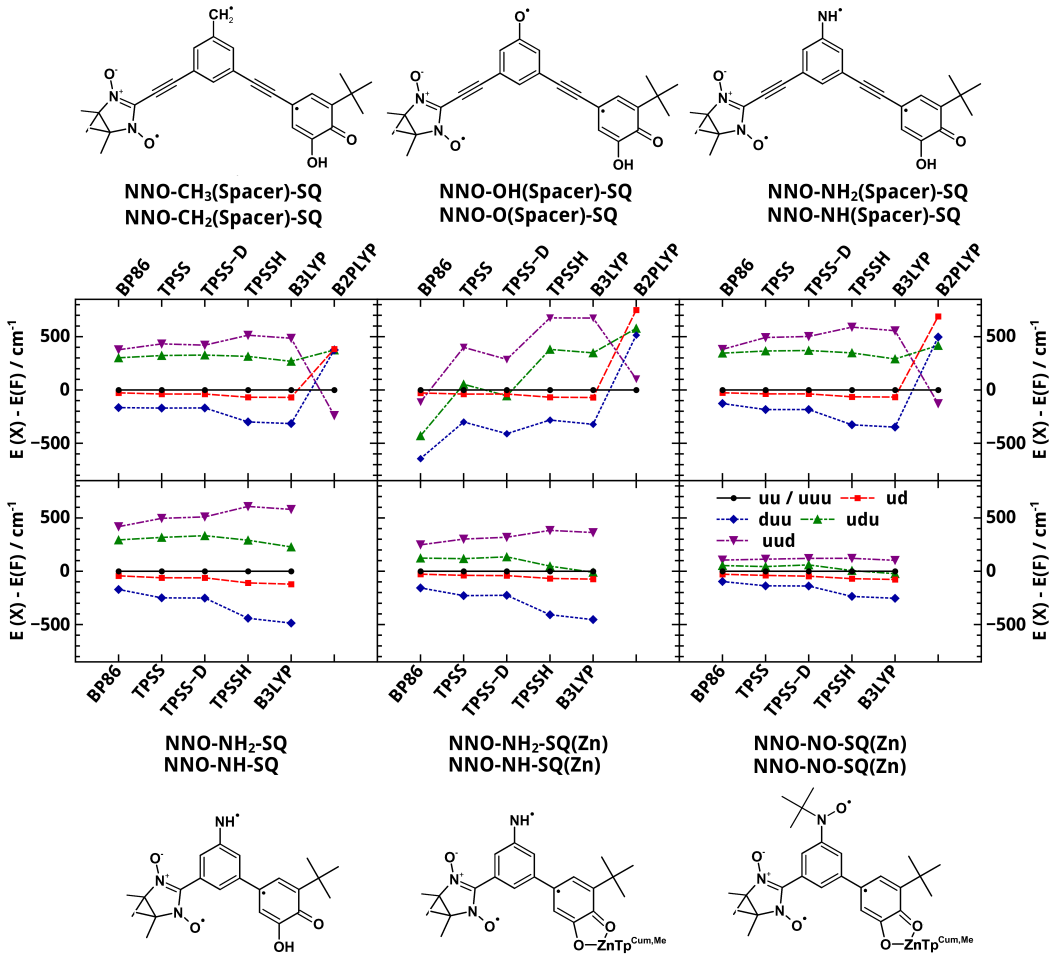

Figure 14.1: Relative spin-state energies of meta-connected ethynyl-bridged model radicals NNO–X(spacer)–SQ for X=CH_2·/CH_3 (left), X=NH·/NH_2 (middle) and X=O·/OH (right) obtained in the author's Bachelor's thesis [35] given in the upper row for different exchange–correlation functionals. In the lower row the results for three other diradical / triradical systems including a realistic NNO–NO–SQ(Zn) system studied in Section 14.2 are shown. All energies are given relative to the ferromagnetically coupled (F) state, which is "uu" for systems with a closed-shell and "uuu" for systems with an open-shell bridge.

For X=CH_2· the two MOs are spatially separate suggesting small spin coupling. This tendency in one of the MOs to localize may partially explain the different behavior of the NNO–X coupling compared with the X–SQ coupling. It may also explain why for X=CH_2· and X=NH·, it is energetically more favorable to flip the spin on NNO rather than on SQ, leading to the "uuu" spin state. The next-highest-energy spin state for these two substituents was the all-antiferromagnetic one which can be obtained from the "duu" ground state

by flipping the spin on the SQ, "udu", and the overall least favorable is the one where NNO and X couple ferromagnetically and X and SQ antiferromagnetically ("uud"). Again, this is consistent between all functionals for those two substituents. The absolute values of spin-state energy splittings are surprisingly independent of X for X=CH_2· and X=NH·.

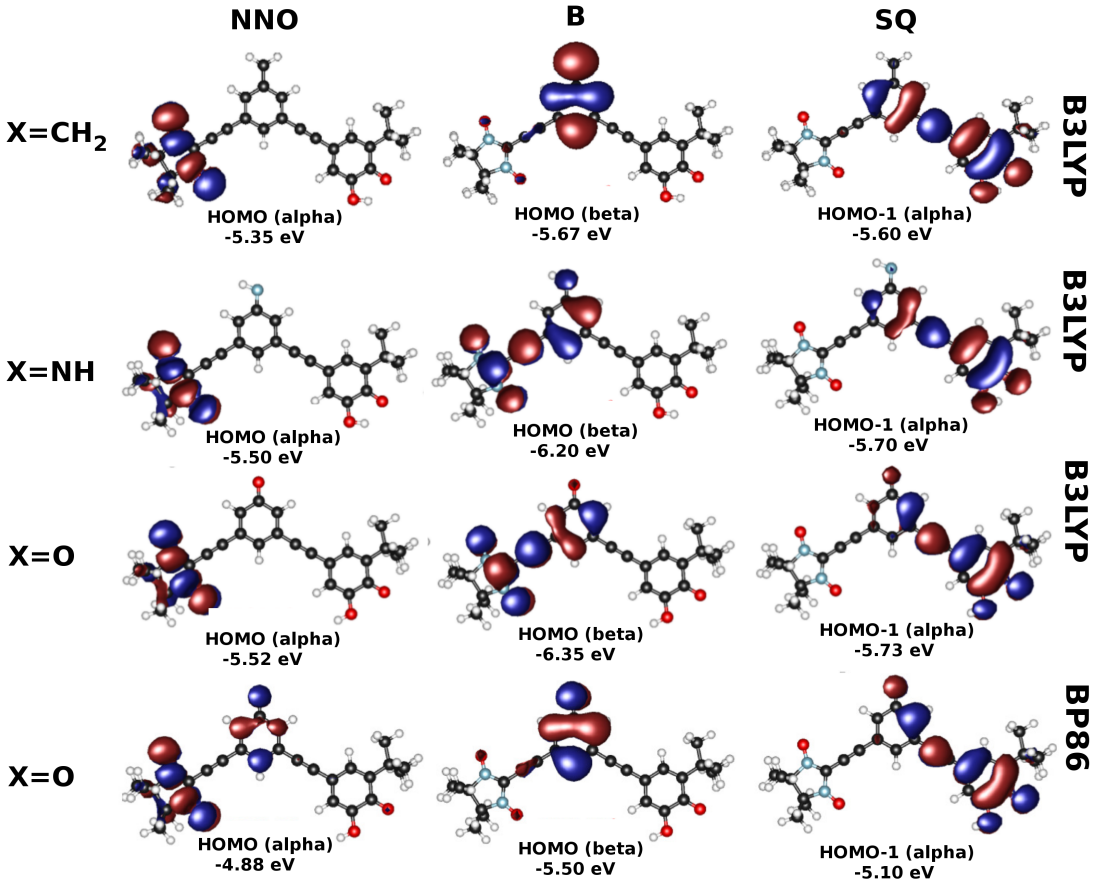

Figure 14.2: Top three rows: Effectively singly occupied MOs for the meta-connected triradicals for the X=CH_2/NH/O radical substituents on the bridge and ethynyl spacer obtained in the author's Bachelor thesis [35]. "udu" determinant, B3LYP/def-TZVP. Bottom row: The same for X=O using BP86/def-TZVP. The abbreviations at the top indicate whether the orbital is mainly located on the NNO unit, the bridge (B) or on the semiquinone (SQ). The molecular orbitals of the udu determinant are chosen because they roughly correspond to (localized) magnetic orbitals and thus can help in qualitatively understanding exchange coupling in these systems.

For X=O·, the situation was somewhat less clear: While the "duu" state is always the ground state as before, the energetic order of the remaining states depends on the exchange–correlation functional. This can be rationalized to some extent by the dependence of the nature of the magnetic MOs on the exchange–correlation functional. For X=O·, the B3LYP $HOMO^{\beta}$ shown in the

third row of Figure C.7 was delocalized onto NNO, while the BP86 HOMO$^{\beta}$ shown in the bottom row of Figure C.7 is localized on the bridge. The MOs obtained with pure functionals were similar in shape to the BP86 ones, and the ones obtained with hybrid functionals similar to the B3LYP MOs. In contrast, for the other two substituents the contours of the magnetic MOs are relatively independent of the functional[1].
Comparing the ground-state spin configurations of the diradicals and the triradicals, the coupling between the NNO and SQ units is not changed qualitatively by the presence of the radical substituent on the bridge. However, the energy differences between the ground state (du or duu) and the next-highest state (the all-ferromagnetically coupled uu or uuu) increased significantly in most cases. For example, considering the NNO–CH_3(Spacer)–SQ and NNO–CH_2·(Spacer)–SQ, the splitting between the all-ferromagnetically coupled state and the ground state was 4.4 (TPSS, TPSS-D and TPSSH) to 6.2 (BP86) times larger for the radical bridge compared with the closed-shell bridge. For NNO-NH_2(Spacer)-SQ and NNO-NH·(Spacer)-SQ, the increase in ground-state stabilization due to introducing a radical bridge is by factor of 4.9 (BP86) to 5.2 (B3LYP) (more details are given in Section C.3 of Appendix C). Interestingly, the more hybrid character in the functional, the larger the spin state splittings (the functionals in Figure 14.1 were ordered from left to right according to increasing hybrid character). This is in contrast to reports of larger exact exchange admixtures favoring the high-spin state in mononuclear transition metal complexes [277, 278]. Exceptions from this "rule" are the "udu" states, and all BP86 spin state energies for the O(Spacer) bridge when compared with TPSS. Adding an empirical dispersion correction minimally influences spin-state energetics, as can be seen by comparing the TPSS and TPSS-D results, except for a slight down shift of energies relative to the "uuu" state for the O(Spacer) bridge upon adding the correction term.

14.1.2 Local spins

Local spins summed up over the relevant parts of the structures in the author's Bachelor's thesis [35] (NNO radical unit, bridge B, SQ radical unit) are a valuable tool for quantifying changes in molecular electronic structure. In Figure 14.3, these sums over local spins calculated from the Mulliken partitioning scheme (see Equation (2.11)) are reported for all structures, spin states and functionals under study. A (summed-up) local spin of 0.5 a.u. corresponds to one unpaired electron located on a specific fragment of the molecular structure. The bridges were defined to include the C≡C spacers. A part of the SQ's spin is delocalized onto the bridge. This portion decreases from about 0.07 to 0 with increasing exact exchange in the functional for all systems under study. This corresponded to the well-known trend of more pronounced spin localization for larger exact

[1]For B2PLYP, HOMO$^{\alpha}$ and HOMO$^{\alpha}$-1 are exchanged with respect to their energetic order compared with the other hybrid functionals for all X(Spacer) structures.

exchange admixture (compare, e.g., Ref. [58]).

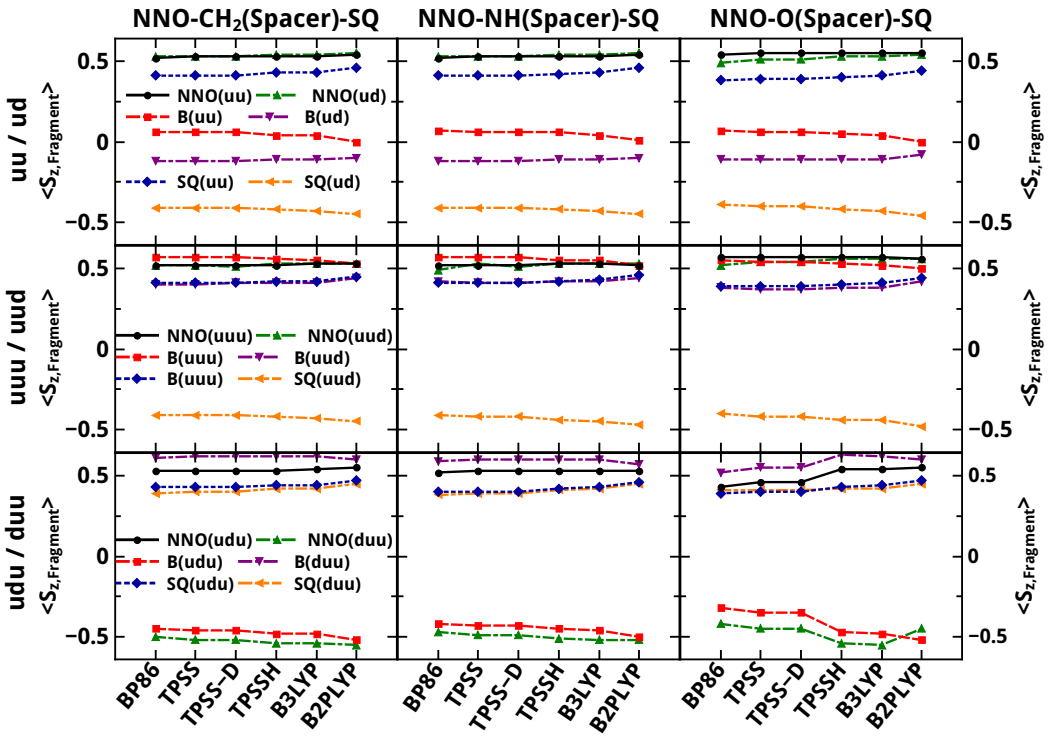

Figure 14.3: Mulliken local spins for the NNO, SQ and the bridge fragments calculated with different exchange-correlation functionals as obtained in the author's Bachelor's thesis [35]. Basis set: def-TZVP.

Also for all other systems, there is a clear trend toward more spin localization on the NNO and SQ radical units with increasing exact exchange admixture, while the spin on the bridge increases or decreases depending on the relative spin orientation compared to the NNO and SQ units. In most cases, the variation of the subsystems' local spins does not exceed 0.07. The main exception are the two X=O systems, for which the most pronounced variations with respect to the functional had already been found in the spin state energetics and the nature of the MOs.

14.2 Comparison with a realistic molecular system

The model systems discussed above feature chemically instable spin centers on the bridge. Another concern is the semiquinone unit, which needs to be stabilized, *e.g.* by a coordinated zinc complex ion as in the experimentally studied systems [255]. Also, introducing ethynyl spacers may prove to be a synthetical challenge. To test how far these findings for the model systems obtained in the author's Bachelor's thesis [35] can be transferred to structures that are likely

accessible by chemical synthesis, these results are compared to the triradical NNO-NO-SQ(Zn), where "NO" is a stable nitroxyl-based radical substituent (Figure 14.1) and its analogous closed-shell-bridge diradical NNO-NOH-SQ(Zn) are obtained by adding a hydrogen. The results were "interpolated" between the model systems and the realistic one by changing in a stepwise fashion the three features that distinguish them. Thus, the following four structures are compared: NNO–NH(spacer)–SQ, NNO–NH–SQ, NNO–NH–SQ(Zn), NNO–NO–SQ(Zn). The B2PLYP functional has not been considered here because it has always displayed qualitative deviations from the other functionals in the previous section.

The nature of the ground state does not change when going from a model system to a realistic one: for all four structures under discussion in this section, the energetically most stable spin orientation is du for the diradicals and duu for the spinpolarized-bridge triradicals (see Figure 14.1 bottom row; for coupling constants see Section C.7 in Appendix C and the next section). The coupling constants for the potentially synthesizable system are between -14.2 cm^{-1} (BP86) and -38.5 cm^{-1} (B3LYP). This is the same order of magnitude as the coupling constant experimentally determined for an analogous meta-phenylene bridged diradical (without NOH substituent) as synthesized by Kirk and coworkers [283], has been -31.8 cm^{-1}. As above, spin state energy splittings are generally increased with increasing exact exchange admixture in the exchange–correlation functional. The energetic ordering of the different spin states is also quite unaffected by the details of the structure and the functional, except for a crossover between the udu and uuu orientations at higher exact exchange for the Zn-containing structures. For the closed-shell-bridge diradicals, introducing ethynyl spacers decreases spin-state energy splittings as expected. Binding the Zn(II) ion to the semiquinone radical has the same effect, which appeared to be related to the larger torsional angle between the SQ(Zn) moiety and the bridge originating from the sterically demanding zinc complex (Section C.4 in Appendix C). This possibly leads to weaker communication when compared with the NNO-NH-SQ complex. For the triradicals, this decrease is surprisingly less pronounced. However, replacing the model radical substituent NH by the more realistic sterically protected nitroxyl radical leads to significantly reduced absolute spin-state energy splittings for the triradicals. From a qualitative point of view, in the realistic NNO–NO–SQ(Zn) system, the stabilization of the ground state with respect to the next-highest spin state ranged from 3.0 for TPSS-D and B3LYP to 3.5 for TPSS, while they are about twice as large in the NNO–NH–SQ(Zn) model system, where the stabilization is between 5.5 for TPSS-D and 6.0 for TPSSH and B3LYP. This is found to correlate with the much lower degree of spin delocalization onto the phenyl ring for the NO-substituted bridge: For the NH system, 40-47% of the total spin is found on the phenyl ring (depending on the spin state and the functional), while in the case of the NO triradical the spin contributions on the phenyl ring are between 6% and 24% (see also Table C.3 in Appendix C). The effect of this substitution

is less pronounced for the diradicals. Still, the overall conclusions that can be drawn from the model systems were highly transferable to a system which may be synthetically achievable.

14.3 Coupling constants from the Green's-function approach

In this section, the coupling constants for the NNO–NOH–SQ(Zn) di- and NNO–NO–SQ(Zn) triradicals are studied by the Green's-function approach and compared to the results obtained from the BS approach in order to see if the spin coupling can be properly described by the former approach which turned out to be problematic in the case of the meta-dimethylenebenzene diradical possessing the same substitution pattern (Section 4.3). The NNO spin center has been defined by the sp^2 hybridized oxygen, nitrogen and carbon atoms while the sp^3 hybridized backbone has been omitted. The spin center definition for the SQ(Zn) substituent included the carbon and the oxygen atoms of the SQ ring, while the complex fragment has been omitted because it did not carry any significant spin density. The NO spin center is defined by the nitrogen and oxygen atoms themselves and the carbon atoms of the phenyl ring.

Table 14.1: Coupling constants calculated with different functionals and the def-TZVP basis set, using the BS approach (using the Equations in Section C.7), and the Green's-function method applied to the electronic structure of the high-spin state on the optimized structure of the "duu" determinant.

	NNO–NOH–SQ(Zn)					
Functional	$J_{\mathrm{BS,unproj}}$			J_{Green} (F)		
BP86	−21.8			0.2		
TPSS	−18.0			−0.3		
TPSSH	−32.2			−1.4		
B3LYP	−34.7			−1.7		
	NNO–NO–SQ(Zn)					
Functional	$J_{\mathrm{BS},13}$	$J_{\mathrm{BS},12}$	$J_{\mathrm{BS},23}$	$J_{\mathrm{Green},13}$ (F)	$J_{\mathrm{Green},12}$ (F)	$J_{\mathrm{Green},23}$ (F)
BP86	−10.1	−32.3	61.2	−0.5	−102.3	165.2
TPSS	−16.6	−52.1	77.6	−0.8	−113.4	176.4
TPSSH	−29.4	−90.7	95.9	−2.1	−162.6	205.1
B3LYP	−31.8	−96.9	89.4	−2.4	−147.2	194.2

The coupling constants between the NNO and SQ(Zn) groups obtained from the Green's-function approach are crucially underestimated in the diradicals compared to those obtained by the unprojected BS approach. By introducing a spin center of the bridge one can see that while the coupling constants between the radical moieties are still underestimated, the new coupling constants between the bridge and the radical moieties are heavily overestimated. These problems

have been expected and can be easily rationalized by the spin transfer of the SQ(Zn) onto the bridge (from SQ(Zn) to NO) and the spin delocalization from the bridge onto the NNO part (see Figure C.1 in Appendix C). The bridge cannot be splitted up symmetrically into three parts belonging to two magnetic sites because of the carbon atom of the phenyl ring that must be involved in both spin center definitions which would lead to an artificial interaction of the spin density with itself.

15. Increasing Spin Coupling by Radical Bridges: Conclusions

In this part, the stabilization of the ground state with respect to spin flips that derive from introducing a spin on the bridge for a range of meta-connected benzene-ring-based bridges connecting a nitronyl nitroxide and a semiquinone radical unit was theoretically studied. As already noted in the author's bachelor's thesis, replacing a closed-shell substituent on the bridge by a radical substituent X=CH_2· or X=NH· increased this stabilization by a factor of about 3 to 6. However, it should be noted that for all systems the B2PLYP functional qualitatively deviated from all other functionals. This suggests that radical bridges are an effective means of stabilizing the ground-state spin configurations. Systems possessing an X=O· substituent were much more sensitive to the choice of exchange–correlation functional than both their closed-shell analogs and the equivalent triradicals with X=CH_2· or X=NH·. The X=O model systems may serve as a starting point for simplified small model systems that can be treated by accurate correlated electronic structure methods. If they showed the same erratic dependence on the functional as the X=O systems that were studied here, they may serve as sensitive test cases for evaluating and constructing more reliable exchange correlation functionals for spin-state energetics.
In this work, comparing the model systems with a potentially synthesizable meta-bridged structure revealed a good qualitative agreement in terms of spin-state energetics. The potentially realizable complex discussed in this work shows a maximal stabilization of the ground state up to a factor of 3.5 compared with the diradical, while for the model systems and complexes constructed as interpolations between the two, the stabilization may be up to twice as large (e.g. a factor of 6). Furthermore, the absolute spin-state energy splittings were smaller in the potentially stable complex. This difference was mainly attributed to the change of the radical substituent from a simple NH group in the model to a sterically protected nitroxyl group in the realistic system. This was in line with the decreasing delocalization of spin density from the radical substituent onto the phenyl ring, underlining the crucial influence of the bridge. To obtain an optimal stabilization of the ground state, further effort must be expended in the study of different radical bridges and how they affect spin-state energetics. These considerations will be addressed in future work.
The different di- and triradicals were also used as test cases for the Green's-function approach. Therefore, the coupling constants obtained with this approach were compared to those obtained with Noodleman's BS approach. The

spin coupling constants obtained from the Green's-function were strongly underestimated compared with Noodleman's BS method because the spin densities of the different spin centers were delocalized onto the bridge. Consequently, the spin center definitions would need to take into account all these bridge atoms, which is problematic because it would include an artificial self-interaction of the spin densities on these shared atoms. This problem could be tackled by employing a localized MO basis in the SCF calculations which would allow for a MO-based assignment scheme to the magnetic sites, as an alternative to the basis-function based assignment used here. One code for performing SCF calculations in such a localized MO basis was used in the work of Hahn and coworkers [284].

Conclusion and Perspective

Spintronics could be the answer for some of the problems modern computer architectures are facing, because information transfer limits the power efficiency and the speed of computation [6]. One solution could be the integration of logic elements into the memory that can itself perform simple logic operations, which would also reduce the information transfer between memory and CPUs. To make this information transfer more power-efficient, purely spin-based elements are promising. Khajetoorians and coworkers recently realized a nanoscale all-spin based logic gate formed by two spin coupled leads, built up from spin-polarized iron atoms, where input spins are switched via two cobalt clusters connected to the chains, and where the output is read by a spin-polarized STM tip. [3]. Molecular chains have certain advantages over atomic spins. First of all, molecules are in general able to self-assemble on surfaces, while atoms must be placed atom by atom, which makes them hardly applicable in commercial applications. The second advantage is that the spin coupling in molecular chains is mediated by superexchange, which may be stronger than the pure RKKY-mediated spin coupling between atoms on metal surfaces. It is therefore an important task to understand to which extent the spin coupling is mediated via superexchange and which contributions arise from RKKY interactions. Besides experimental studies, theory could give valuable insights in the spin coupling in these systems. Besides such understanding, also the control of spin coupling by external stimuli is an important task. A large stabilization of the ground state is another important prequisite for a spin-based molecular device.

15.1 Summary

One goal of this work was to check if DFT is able to provide a reliable description of spin coupling in molecules that are potentially interesting for spintronic devices. In most cases, the trends produced for the coupling constants by different exchange–correlation functionals were consistent; only for the cobaltocene-substituted dithienyl ethene derivatives studied in Chapter 12 for example the diradical character ranged from fully closed-shell to larger open-shell characters. Also the trends obtained for the switching behavior of different dithienylethene derivatives was in qualitative agreement with experiment.
Further, the Green's-function approach to spin coupling was shown to perform well for molecular systems, as long as the Heisenberg picture is not violated as for example by reduction in the spins' magnitudes when going from one spin

state to another, and as long as structural relaxation effects are not important. Even for systems possessing more than two spin centers, the coupling constants were in good agreement with the BS method. Taking into account the bridge in the spin center definition of the Green's-function method, the calculated coupling constants systematically improved compared to their BS reference values. Moreover, a newly developed automated exchange pathway analysis with the Green's-function method gave results, which were consistent with those reported earlier in the literature. Thus, this method was successfully applied to understand the role of the bridge in different π-stacked bismetallocens.
All systems in this thesis were of the form A–bridge–B, varying in the bridge and in the substituents A and B. Only for the donor–acceptor di- and triradicals investigated in part III, A differed from B, while in all other cases both substituents were equal. The choice of the substituents for a given bridge heavily influenced the obtained properties in several cases. For example, by substituting the chlorine substituents by metallocenes, it was shown that the switching ability strongly worsened. Also for the π-stacked bismetallocene complexes, the choice of the metal center affected the total coupling constants, as well as the contributions from through-space and through-bond contributions to these coupling constants. On the other hand, for the donor–acceptor di- and triradicals the trends did not change qualitatively as a function of the exact composure of the SQ group representing substituent B.
The choice of the bridge was shown to have a large effect on the spin coupling for a given pair of radical moieties. For example, for the π-stacked biscobaltocenes the antiferromagnetic spin coupling increased for the biscobaltocene complexes by a factor of four when going from the naphthalene to the acenaphthylene bridge. The same was found for the spin coupling in the closed form of the cobaltocene-substituted dithienyl ethene derivatives under study, where the benzothiophene bridges lead to an increase in the open-shell character and to a reduction of spin coupling.

15.2 Outlook

Although this work provided valuable insights in the spin coupling in many relevant molecular systems, additional methodological developments as well as answers to the open questions that remain in this work are needed. Furthermore, larger and in particular more complicated systems might be interesting for future studies. The most important open issues are the following:

- The Green's-function approach gave large deviations from the values obtained with the BS approach when employed to the electronic structure of the BS determinant. An important task is therefore to analyze the MO contributions to identify the origin of these deviations.

- The rederivation of the Green's-function approach allows for using different partitioning schemes besides the Löwdin one used in this thesis. In general,

it might be interesting how the choice of the local partitioning scheme influences the obtained coupling constants compared to the BS method.

- One future goal will be the description of atomic and molecular spins on metallic and magnetic surfaces by using the Green's-function approach in order to separate the RKKY contributions from the superexchange contributions to spin coupling.

- Most of the metallocene-substituted dithienylethene derivatives showed a very poor switching behavior, which could be rationalized by the PES scans. While studying the spin coupling in the cobaltocenes, it could be observed that there is a correlation between the changes in the bond lengths between the carbon atoms participating in cyclization and cycloreversion reactions with the observed diradical character. Therefore, it might be interesting to see how these two parameters influence the switching reactions.

- The magnetic switches in Chapter 12 further revealed that one needs to find a reliable strategy to obtain accurate diradical characters from DFT, because especially for the cobaltocene systems the diradical characters changed from closed-shell to open-shell with increasing amount of HF exchange.

- For the donor–acceptor di- and triradicals in part III, the spin coupling constants were ambiguous because a proper definition of the spin centers is hardly possible when spin orbitals are strongly delocalized and include contributions from different fragments. One could potentially solve these problems by using the Green's-function approach in combination with DFT performed by using localized Fermi orbitals as recently published by Hahn and coworkers [284].

- Further, the study on the donor–acceptor di- and triradicals revealed that the degree of spin delocalization from the formally spin-bearing atoms onto the remainder of the radical bridges correlates with the strength of the observed spin coupling, which could be the key to obtain molecules with very large coupling constants and should therefore be studied in further depth.

These tasks will be tackled in our laboratory in the near future. The focus will be on the conceptional improvement of the Green's-function approach to solve the problems with its present form.

16. Acknowledgements

First of all I want to thank Prof. Dr. Carmen Herrmann for being such an outstanding supervisor. She gave me the possibility to work on this very interesting topic which covered quantum chemistry but also aspects from theoretical physics. She provided a very good education in the field of molecular spintronics, but also in quantum chemistry in general. She was always there to discuss urgent questions and problems arising from my research. I also want to thank her for the hours of critical proof reading of my manuscripts and this thesis. Besides that, she also gave me the possibility to extend and deepen my knowledge by participating in numerous conferences and two summerschools, including a summerschool in Sostrup (Denmark) on electronic structure theory and a summerschool on magnetism in Cluj-Napoca (Romania).

I would also like to thank M.Sc. Alexander Voigt, M.Sc. Martin Zöllner, B.Sc. Konrad Stork, and M.Sc. Philipp Bahlke for being such a great company in the office and for fruitful discussions of problems that arose from my work and the exchange of ideas in general. A. Voigt and K. Stork also supported my research by two internships in our group. Further, I would like to thank M.Sc. Youssef Akil and M.Sc. Philip Saul for critical proofreading of different parts of my work. In this context, I would also like to thank M.Sc. Mariana Hildebrand (Imperial College London) for continuous information exchange on different parts of theoretical material science.

Furthermore, I would like to thank our collaborators. I want to acknowledge in particular Prof. Dr. Alexander I. Lichtenstein (University of Hamburg) and Jos Tasche (Durham University) for the helpful discussions on the Green's-function method and the preliminary work of J. Tasche on this method. Further, I acknowledge our experimental collaborators from Hamburg, Prof. Dr. Jürgen Heck, and his doctoral student Dipl. Chem. Sarah Puhl and postdoctoral research fellow Dr. Alejandra Escribano for the very fruitful collaborations on the photochromic switches and the π-stacked bismetallocene complexes. Last but not least, I would like to thank Prof. Dr. David Shultz (North Carolina State University) and Prof. Dr. Martin Kirk (University of New Mexico) for their suggestions for a potentially synthesizable triradical, and for the critical proofreading of the manuscript we have handed in. I am also thankful to Prof. Dr. Gabriel Bester from the University of Hamburg for accepting to be the co-examiner of this thesis, and Prof. Dr. Tobias Schwabe and Prof. Dr. Jürgen Heck for agreeing to be part of the defense committee.

Financial support by the collaborative research center SFB 668 "Magnetism–

from single atoms to nanostructures" and a "Hamburg Global" scholarship for the Sostrup summerschool in 2014 is acknowledged. I would also like to thank Prof. Dr. Roland Wiesendanger (University of Hamburg) for giving me the chance to organize annual workshops for doctoral students in the framework of the SFB 668, and his secretary, Andrea Beese, who took over the financial transactions. I would also like to thank the IT service in the Chemistry department for hard- and software support, and the RRZ and the HLRN for computational resources, and in particular Hinnerk Stüben and Thomas Orgis, who were always helpful when there were problems with the computational infrastructure or different programs. Also Misses Beate Susemihl is acknowledged for always being helpful regarding the administrative issues in our institute.
Finally, I am deeply indebted to my family for their continuous psychological support during my studies. Especially my parents, Meike and Rolf Steenbock and my sister Inken Steenbock always were there for me. Furthermore, I would like to thank M.Sc. Philip Saul, M.Sc. Thomas Rutkowski, M.Sc. Mariana Hildebrand, M.Sc. Youssef Akil, Daniel Johannes, Klaudia Jankowska (also for taking care of my cats during conferences), and all my other friends that cheered me up or helped me relaxing during the partially stressful process of writing.

A. Additional Information for Part I

A.1 Dihydrogen Molecule

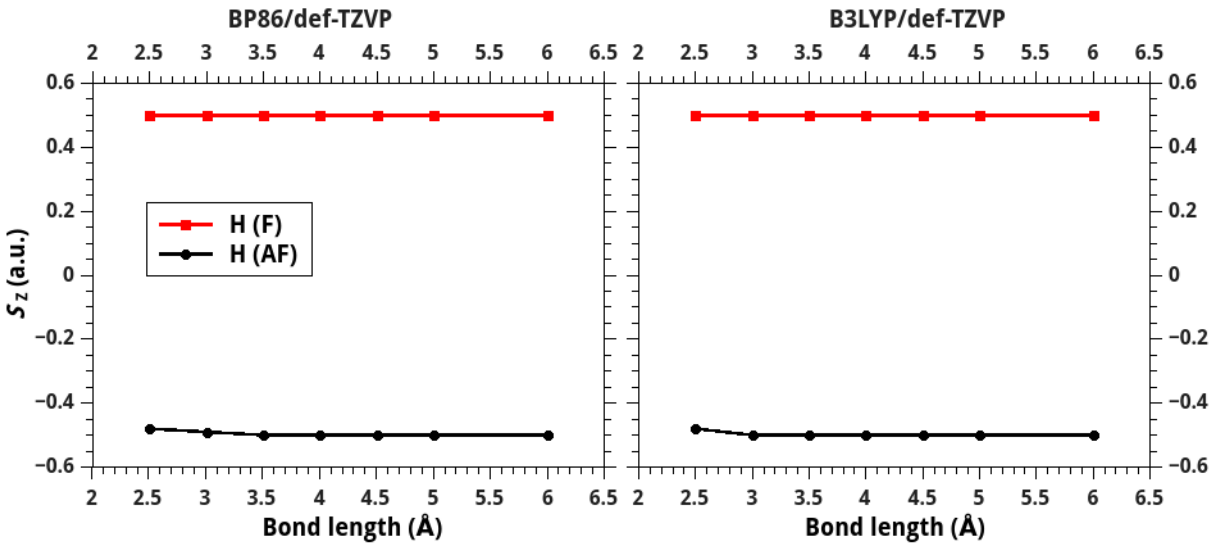

Figure A.1: Local spins for the dihydrogen molecule obtained by a Mulliken population analysis using BP86 (left-hand site) and B3LYP (right-hand site). Basis set: def-TZVP.

A.2 H−He−H Model System

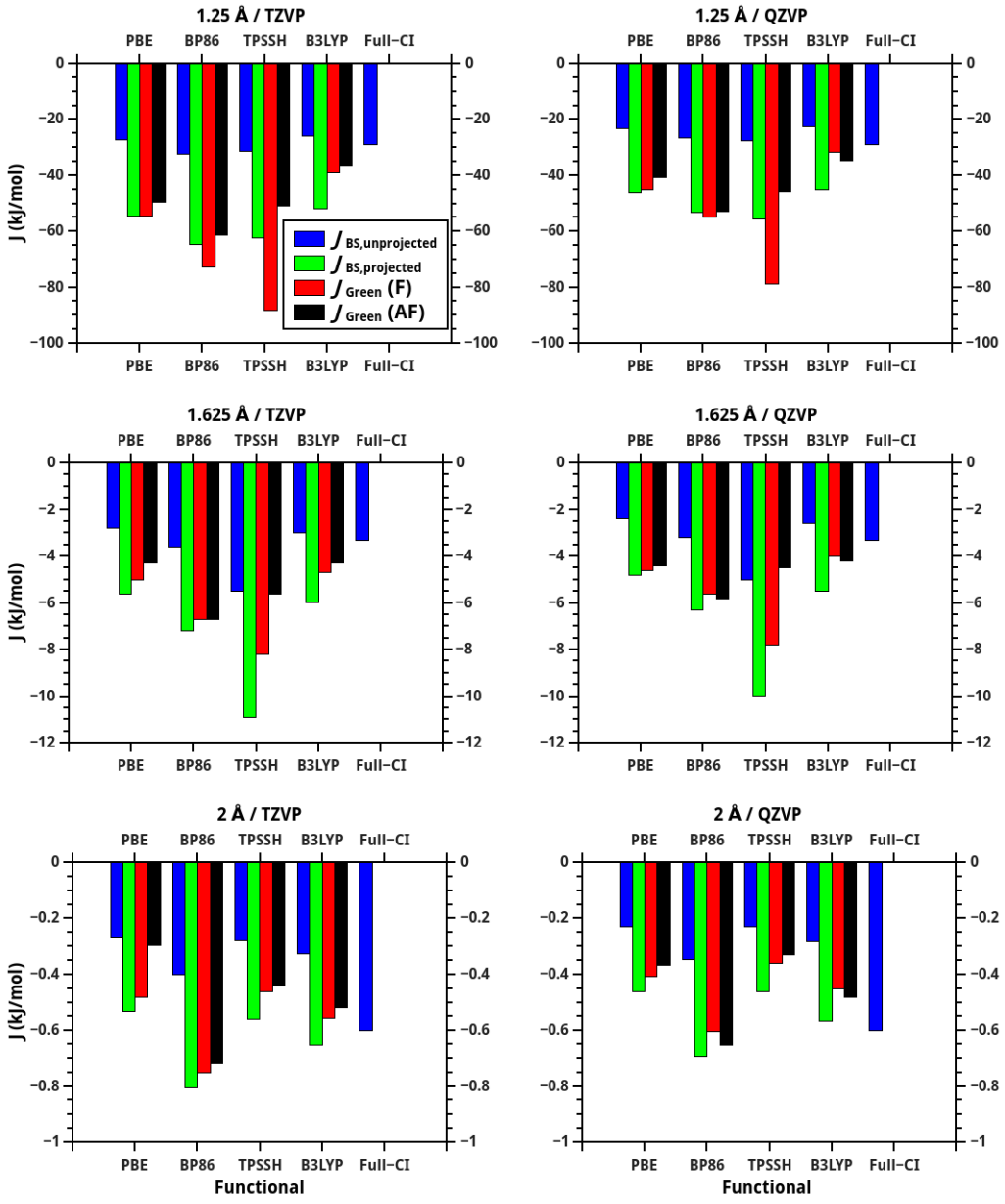

Figure A.2: Coupling constants calculated with different exchange-correlation functionals using the def-TZVP and the def-QZVP basis set.

A.3 Larger Systems with Localized Spins

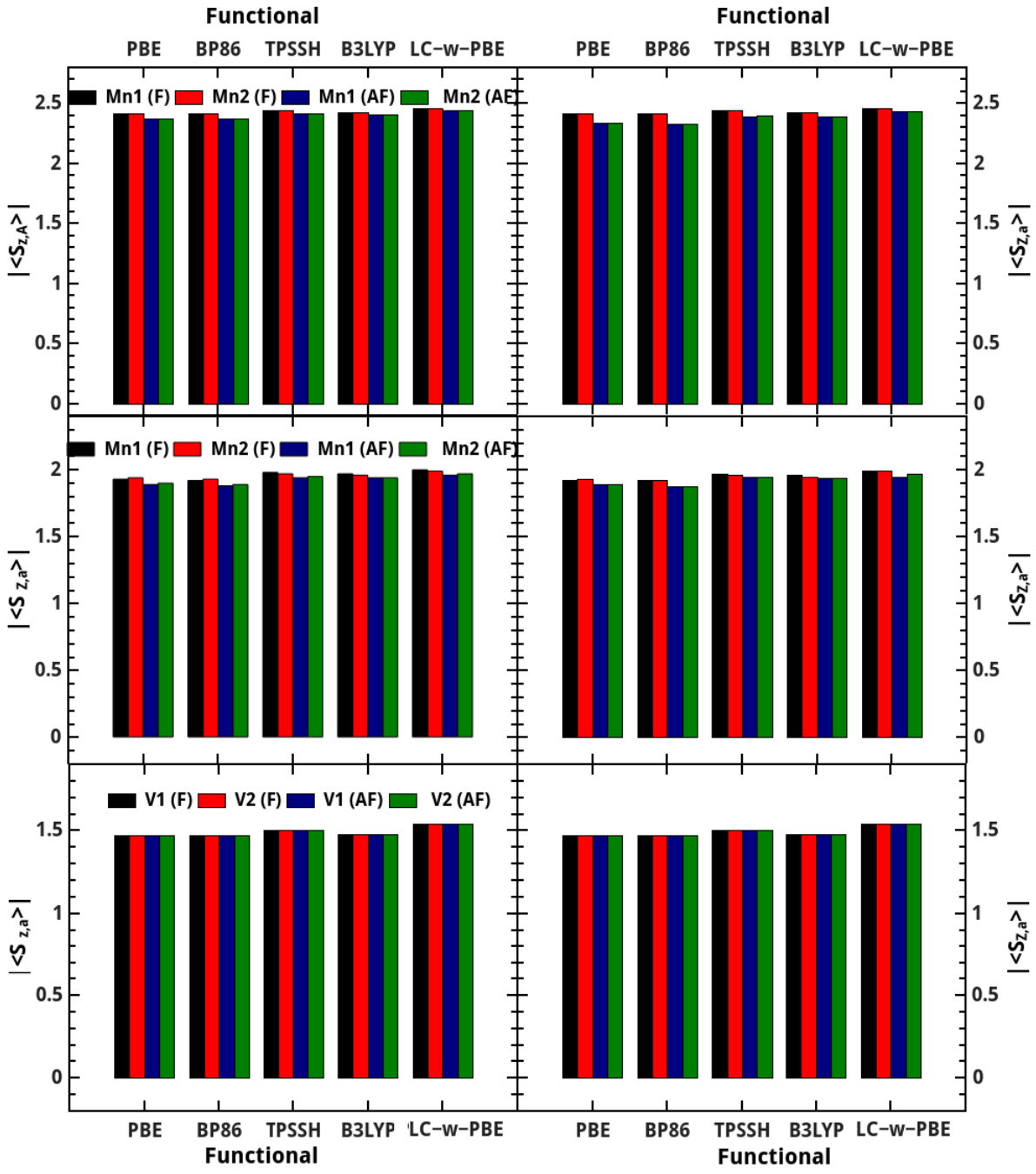

Figure A.3: Local spins for $[Mn_2(Ac)_4(H_2O)_2]$ (upper row), $[Mn_2(\mu-OMe)_2(HL)_4]$ (middle row) and $\left[V_2\left(\eta^5-Cp\right)_2\left(\mu-\eta^5-1,8-DCN\right)\right]$ (lower row) calculated with different exchange-correlation functionals for the high-spin structure (left column) and the BS structure (right column).

A.4 Larger Systems with Delocalized Spins

Table A.1: Magnetic coupling constants calculated with the Broken-Symmetry approach from the optimized spin-state structures of $\left[\mathrm{Co_2}\left(\eta^5-\mathrm{Cp}\right)_2\left(\mu-\eta^5-1,8-\mathrm{DCN}\right)\right]$. All values are given in kJ/mol. Basis set: def-TZVP.

Functional	$J_{\mathrm{BS,unprojected}}$	$J_{\mathrm{BS,projected}}$
PBE	0.69	1.37
BP86	0.72	1.43
TPSSH	−0.22	−0.43
B3LYP	0.47	0.94
LC-ωPBE	23.02	46.04

A.5 Non-Collinear DFT Calculations

Table A.2: Coupling constants J for the high-spin structures of all compounds (except for the $[\mathrm{Cu_2\,(Ac)_4\,(H_2O)_2}]$ complex and the dihydrogen molecule) obtained with PBE by employing the OpenMX program and pseudopotentials provided by the program for the core electrons. The coupling constants obtained with PBE/def-TZVP by employing the Gaussian09 program are given for comparison. The values are given in kJ/mol.

H−He−H model system		
Compound	J^{OpenMX}	$J^{\mathrm{Gaussian09}}$
H−He−H (1.25 Å)	−49.3	−54.4
H−He−H (1.625 Å)	−5.0	−5.6
H−He−H (2 Å)	−0.5	−0.5
Larger systems with localized spins		
$[\mathrm{Mn_2\,(Ac)_4\,(H_2O)_2}]$	−0.77	−0.78
$[\mathrm{Mn_2\,(\mu-OMe)_2\,(HL)_4}]$	0.32	0.30
$\left[\mathrm{V_2}\left(\eta^5-\mathrm{Cp}\right)_2\left(\mu-\eta^5-1,8-\mathrm{DCN}\right)\right]$	−0.0074	−0.0075
$[\mathrm{V_2\,(\mu-O\text{-}Me)_2\,(O)_2\,(ma)_2}]$	−2.57	−2.59
para-$\mathrm{C_8H_8}$	−10.58	−11.22
Larger systems with delocalized spins		
$\left[\mathrm{Co_2}\left(\eta^5-\mathrm{Cp}\right)_2\left(\mu-\eta^5-1,8-\mathrm{DCN}\right)\right]$	2.23	1.82
meta-$\mathrm{C_8H_8}$	19.74	19.07

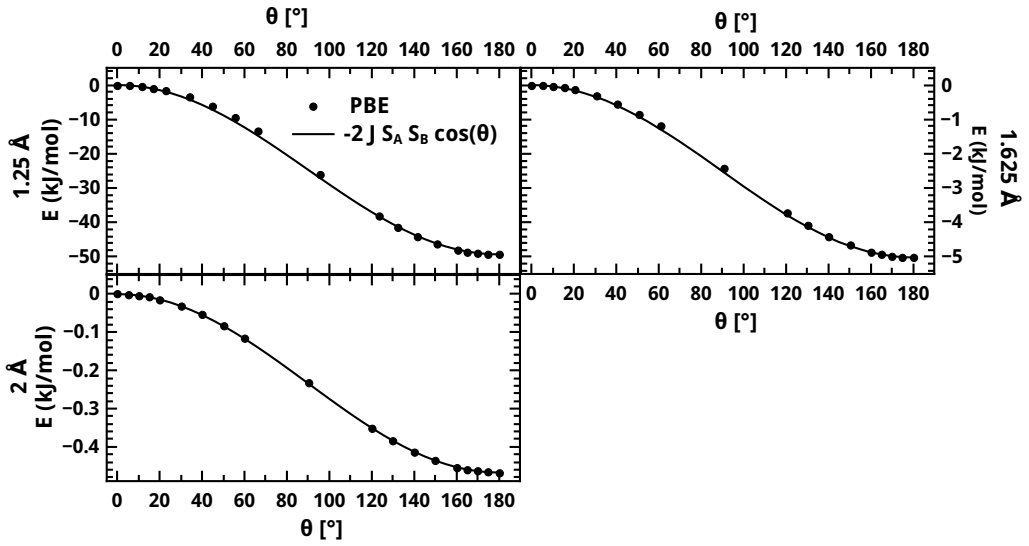

Figure A.4: Non-collinear DFT calculations for the H−He−H system and different bond lengths performed with OpenMX employing the PBE functional (all other parameters are given in the Computational Methodology section).

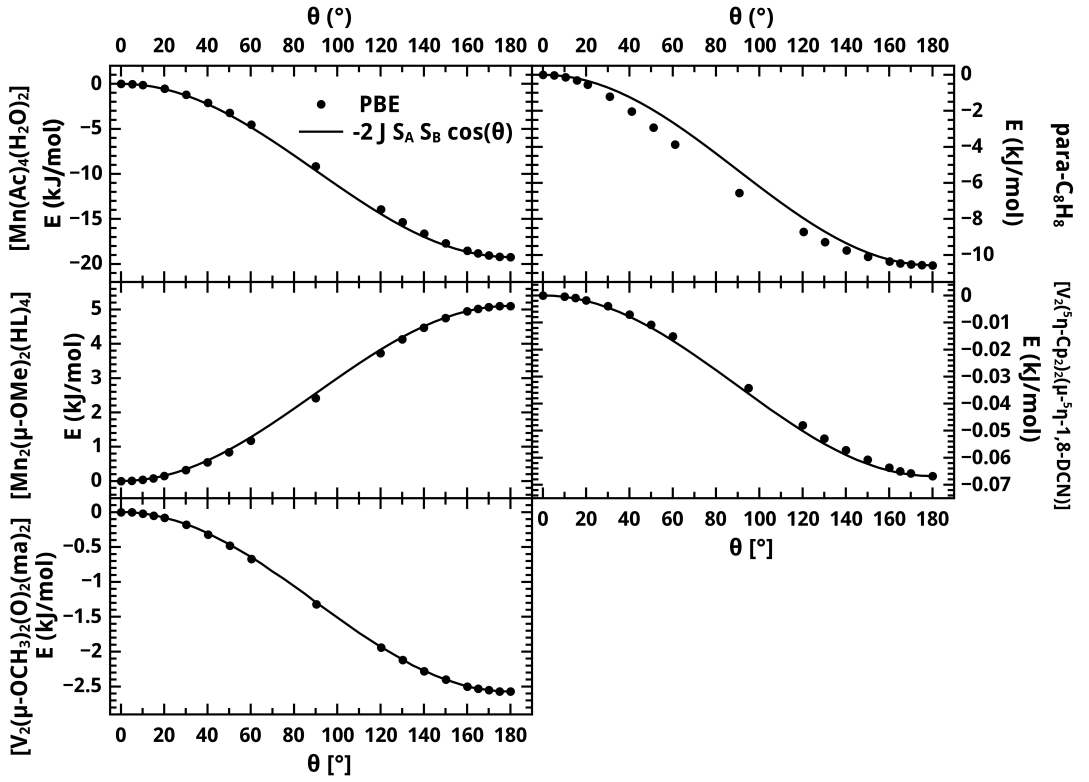

Figure A.5: Non-collinear DFT calculations for the systems with localized spins in the high-spin state performed with OpenMX employing the PBE functional (other parameters are given in the Computational Methodology section).

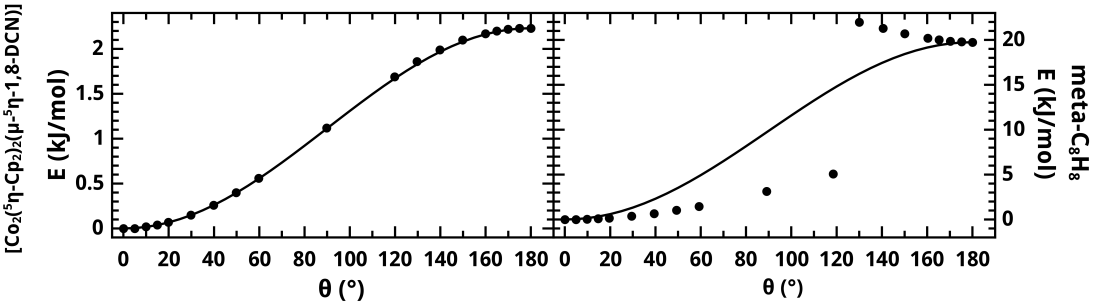

Figure A.6: Non-collinear DFT calculations for the systems with delocalized spins in the high-spin state performed with OpenMX employing the PBE functional (other parameters are given in the Computational Methodology section).

A.6 Structural Differences between Spin States

Table A.3: Structural parameters of the spin-state structures of the $[Mn_2(Ac)_4(H_2O)_2]$ complex.

Parameter	hs structure	BS structure
R(Mn−Mn)	3.024 Å	2.704 Å
R(Mn−O[Ac])	2.124 Å	2.113 Å
∠Mn-O[Ac]-C[Ac]	127.62°	123.86°

Table A.4: Structural parameters of the spin-state structures of the $[Mn_2(\mu-OMe)_2(HL)_4]$ complex.

Parameter	hs structure	BS structure
R(Mn−Mn)	3.170 Å	3.134 Å
∠Mn-O[OMe]-Mn	102.67°	104.78°

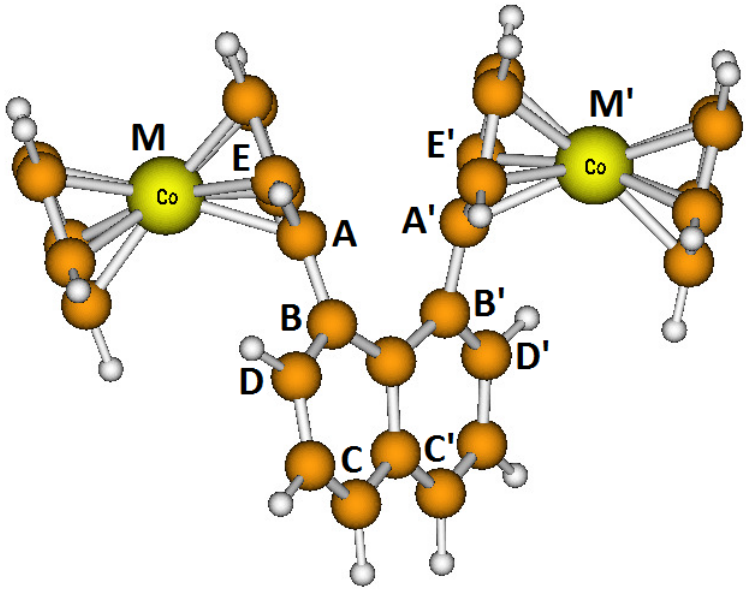

Figure A.7: Structure of the $[Co_2(\eta^5-Cp)_2(\mu-\eta^5-1,8-DCN)]$ complex with declarations of the atoms used to define the parameters given in Table A.5.

Table A.5: Structural parameters of the $\left[\mathrm{Co_2}\left(\eta^5-\mathrm{Cp}\right)_2\left(\mu-\eta^5-1,8-\mathrm{DCN}\right)\right]$ and the $\left[\mathrm{V_2}\left(\eta^5-\mathrm{Cp}\right)_2\left(\mu-\eta^5-1,8-\mathrm{DCN}\right)\right]$ complex in both spin states. The atoms for the definition of parameters are declared in Figure A.7.

	$\left[\mathrm{Co_2}\left(\eta^5-\mathrm{Cp}\right)_2\left(\mu-\eta^5-1,8-\mathrm{DCN}\right)\right]$		$\left[\mathrm{V_2}\left(\eta^5-\mathrm{Cp}\right)_2\left(\mu-\eta^5-1,8-\mathrm{DCN}\right)\right]$	
Parameter	hs structure	BS structure	hs structure	BS structure
R(M−M')	6.822 Å	6.865 Å	7.046 Å	7.046 Å
R(A−A')	2.943 Å	2.990 Å	2.955 Å	2.955 Å
∠ABC	167.88 Å	167.89 Å	170.51 Å	170.52 Å
∠A'B'C'	168.43°	168.30°	170.51°	170.53°
dihedral(DABE)	35.54°	35.05°	45.26°	45.26°
dihedral(DABE)	36.99°	31.04°	45.27°	45.26°

Table A.6: Structural parameters of the spin-state structures of the $[\mathrm{Cu_2}\left(\mathrm{Ac}\right)_4\left(\mathrm{H_2O}\right)_2]$ complex.

Parameter	hs structure	BS structure
R(Cu−Cu)	2.514 Å	2.528 Å
R(Cu−O[Ac])	2.034 Å	2.033 Å
∠Cu-O[Ac]-C[Ac]	120.7°	120.6°

A.7

2-] *Angular Dependence of Exchange Coupling Constants in* $[\mathrm{Cu_2}\left(\mu-\mathrm{OH}\right)_2\mathrm{Cl_4}]^{2-}$

Table A.7: Mulliken local spins for the $[\mathrm{Cu_2}\left(\mu-\mathrm{OH}\right)_2\mathrm{Cl_4}]^{2-}$ complex calculated with PBE and BP86. The values are given in a.u.. Basis set: def-TZVP.

	PBE		BP86	
Angle (°)	high-spin state	BS solution	high-spin state	BS solution
80	0.226	0.202	0.225	0.199
84	0.235	0.208	0.233	0.206
86	0.238	0.210	0.237	0.207
90	0.245	0.210	0.243	0.207
92	0.247	0.208	0.246	0.206
96	0.251	0.200	0.250	0.199
98	0.253	0.198	0.251	0.194
100	0.254	0.192	0.253	0.189
102	0.255	0.186	0.254	0.182
104	0.256	0.178	0.254	0.173
106	0.256	0.169	0.255	0.164
108	0.257	0.159	0.255	0.153
110	0.257	0.147	0.255	0.141

Table A.8: Mulliken local spins for the $[Cu_2(\mu-OH)_2Cl_4]^{2-}$ complex calculated with TPSSH and B3LYP. The values are given in a.u.. Basis set: def-TZVP.

	TPSSH		B3LYP	
Angle (°)	high-spin state	BS solution	high-spin state	BS solution
80	0.259	0.254	0.264	0.262
84	0.268	0.262	0.274	0.271
86	0.271	0.265	0.277	0.274
90	0.278	0.270	0.284	0.279
92	0.280	0.271	0.287	0.281
96	0.285	0.273	0.291	0.284
98	0.287	0.273	0.293	0.284
100	0.288	0.272	0.294	0.285
102	0.289	0.271	0.295	0.285
104	0.290	0.270	0.296	0.284
106	0.291	0.268	0.297	0.283
108	0.291	0.266	0.297	0.282
110	0.291	0.264	0.298	0.281

Table A.9: Mulliken local spins for the $[Cu_2(\mu-OH)_2Cl_4]^{2-}$ complex calculated with LC-ωPBE. The values are given in a.u.. Basis set: def-TZVP.

	LC-ωPBE	
Angle (°)	high-spin state	BS solution
80	0.273	0.273
84	0.282	0.281
86	0.285	0.284
90	0.291	0.289
92	0.294	0.291
96	0.298	0.293
98	0.299	0.294
100	0.301	0.295
102	0.302	0.295
104	0.303	0.295
106	0.304	0.294
108	0.304	0.294
110	0.304	0.293

A.8 Expressions for the Coupling Constants for the Co_4NP_3 Complex

The expressions derived for the coupling constants between the different cobaltocene complexes calculated within the energy-difference based approach using the methodology provided by Ruiz and coworkers [55]:

$$J_{12} = -\frac{E^{\mathrm{tot}}_{(\uparrow\uparrow\uparrow\uparrow)} - E^{\mathrm{tot}}_{(\uparrow\downarrow\downarrow\uparrow)}}{4}, \tag{A.1}$$

$$J'_{12} = -\frac{E^{\mathrm{tot}}_{(\uparrow\uparrow\uparrow\uparrow)} - E^{\mathrm{tot}}_{(\downarrow\uparrow\uparrow\uparrow)}}{2}, \tag{A.2}$$

$$J_{23} = -\frac{E^{\mathrm{tot}}_{(\uparrow\uparrow\uparrow\uparrow)} - E^{\mathrm{tot}}_{(\uparrow\uparrow\downarrow\downarrow)}}{2}, \tag{A.3}$$

$$J'_{23} = \frac{E^{\mathrm{tot}}_{(\uparrow\downarrow\uparrow\uparrow)} - E^{\mathrm{tot}}_{(\uparrow\uparrow\uparrow\uparrow)}}{2} - \frac{E^{\mathrm{tot}}_{(\uparrow\downarrow\downarrow\uparrow)} - E^{\mathrm{tot}}_{(\uparrow\uparrow\uparrow\uparrow)}}{4}. \tag{A.4}$$

A.9 MO Plots for V–NP–V

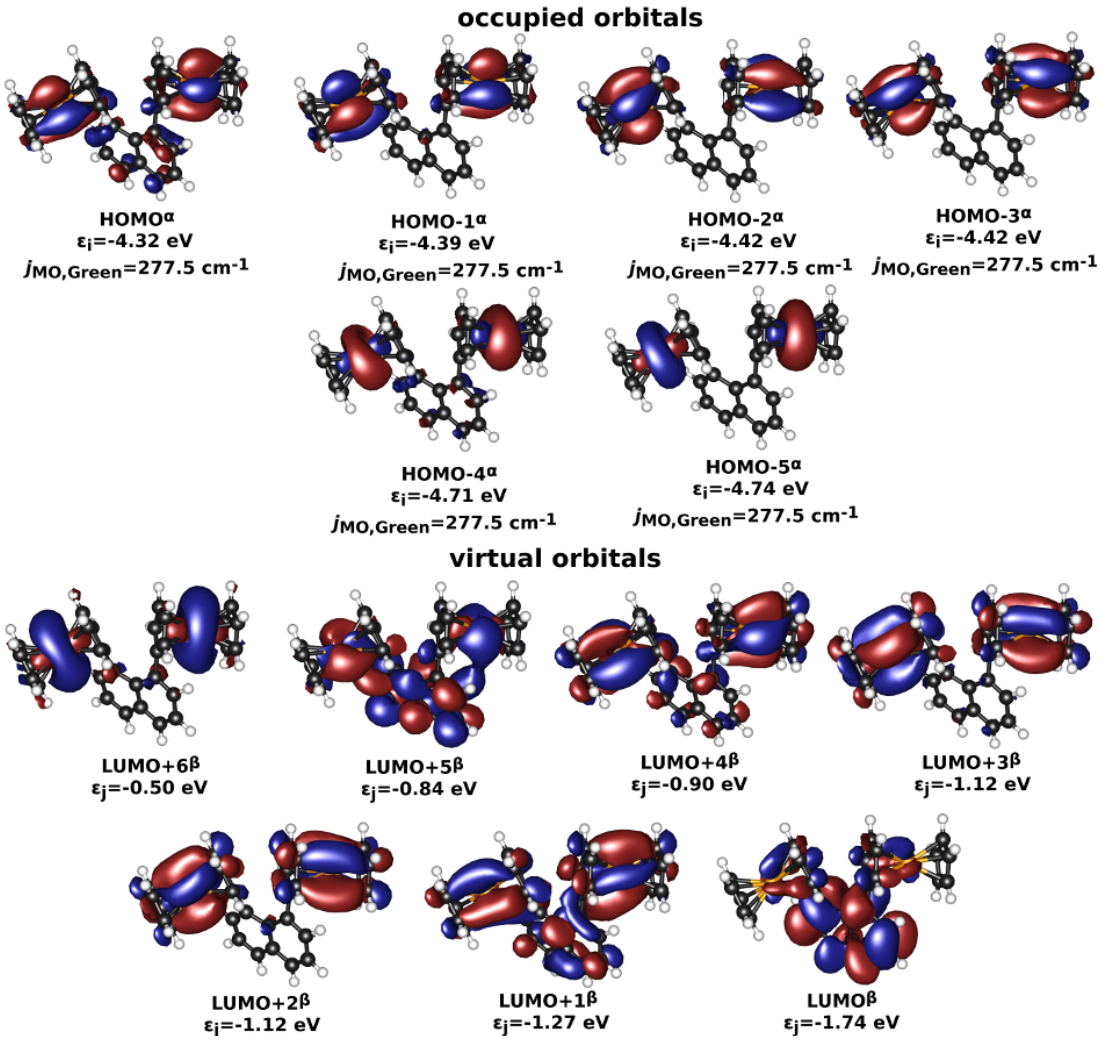

Figure A.8: Molecular orbitals for the high-spin state of V–NP–V calculated with TPSSH / def2-TZVP on the BS structure and contributions from occupied α spin orbitals. Iso-surface value: 0.02.

B. Additional Information for Part II

B.1 Ferrocene-Substituted Switches

B.1.1 Molecular Structures and Energetics

Table B.1: Experimentally and theoretically obtained torsional angles of the ferrocene-substituted cyclopentene and cyclohexene switches (Structures optimized with BP86. Basis set: def-TZVP.) θ_1=C14-C15-C16-C17, θ_2=S1-C15-C16-C20, θ_3= C34-C35-C36-C37, θ_4= S2-C35-C36-C40 (defined according to Figure 10.1).

ferrocene-substituted cyclopentene switch					
Isomeric form	ferrocene orientation	θ_1	θ_2	θ_3	θ_4
open (exp.)	"in"	13.592	9.637	13.592	9.5637
open	"in"	14.002	15.563	15.611	12.923
open	"out"	168.166	170.256	169.631	171.477
closed	"in"	14.854	15.091	15.319	15.800
closed	"out"	164.771	168.836	165.721	169.813
ferrocene-substituted cyclohexene switch					
open (exp.)	"in"	21.745	20.056	10.975	10.406
open	"in"	19.334	20.620	19.966	21.163
open	"out"	162.453	165.135	167.900	170.975
closed	"in"	16.073	16.073	14.932	15.468
closed	"out"	164.314	168.812	163.695	168.047

B.1.2 Molecular Orbital Plots and Optical Properties

Table B.2: Excitation energies and corresponding MO contributions of the open and closed forms of the ferrocene-substituted "in" conformers of the ferrocene-substituted cyclopentene and cyclohexene switch in n-hexane and for the ethynyl-linked switch in acetonitrile by employing the PCM model and the LC-wPBE functional[a].

Open-form "in" conformer State/ λ [nm]/ oscillator strength	Molecular orbital transition	Character	Weight	Closed-form "in" conformer State/ λ [nm]/ oscillator strength	Molecular orbital transition	Character	Weight
ferrocene-substituted cyclopentene switch							
S_{13}/273/0.48	HOMO→LUMO	$\pi-\pi*$	58.8	S_1/547/0.05	HOMO-2→LUMO+4	d−d	15.6
	HOMO-1→LUMO+1	$\pi-\pi*$	21.8		HOMO-5→LUMO+6	d−d	15.6
S_{14}/268/0.07	HOMO→LUMO+1	$\pi-\pi*$	43.3	S_5/480/0.45	HOMO→LUMO	$\pi-\pi*$	76.5
	HOMO-1→LUMO	$\pi-\pi*$/ MLCT	32.7				
S_{15}/250/1.10	HOMO→LUMO+2	$\pi-\pi*$	32.0	S_{14}/299/0.53	HOMO-1→LUMO	$\pi-\pi*$	55.4
	HOMO-6→LUMO	$\pi-\pi*$/ MLCT	14.9		HOMO→LUMO+1	$\pi-\pi*$	22.0
	HOMO-1→LUMO+1	$\pi-\pi*$	13.9		HOMO-5→LUMO	MLCT	12.7
	HOMO-2→LUMO	MLCT/ $\pi-\pi*$	11.3				
				S_{20}/245/0.31	HOMO-4→LUMO	MLCT	27.7
					HOMO-2→LUMO	MLCT	15.2
ferrocene-substituted cyclohexene switch							
S_{13}/267/0.67	HOMO→LUMO	$\pi-\pi*$	54.5	S_1/552/0.08	HOMO-2→LUMO+4	d−d	16.4
	HOMO-1→LUMO+1	$\pi-\pi*$	25.5		HOMO→LUMO	$\pi-\pi*$	12.3
S_{14}/265/0.19	HOMO→LUMO+1	$\pi-\pi*$	50.1	S_5/495/0.42	HOMO→LUMO	$\pi-\pi*$	76.5
	HOMO-1→LUMO	$\pi-\pi*$/ MLCT	32.7				
S_{15}/231/0.40	HOMO→LUMO+2	$\pi-\pi*$	33.2	S_{14}/303/0.57	HOMO-1→LUMO	$\pi-\pi*$	51.4
	HOMO-6→LUMO	$\pi-\pi*$/ MLCT	16.3		HOMO→LUMO+1	$\pi-\pi*$	26.3
					HOMO-5→LUMO	MLCT	12.8
				S_{20}/246/0.30	HOMO-4→LUMO	MLCT	26.2
					HOMO-2→LUMO	MLCT	17.3
ferrocene-substituted cyclopentene switch (with spacer)							
S_{13}/299/1.54	HOMO→LUMO	$\pi-\pi*$	47.9	S_1/559/0.45	HOMO→LUMO	$\pi-\pi*$	47.3
	HOMO-1→LUMO+1	$\pi-\pi*$	33.6		HOMO-2→LUMO+2	d−d/ MLCT	12.1
S_{14}/325/0.69	HOMO→LUMO+1	$\pi-\pi*$	33.6	S_5/495/0.42	HOMO→LUMO	$\pi-\pi*$	46.6
	HOMO-1→LUMO	$\pi-\pi*$/ MLCT	33.6				
S_{15}/253/0.62	HOMO→LUMO+2	$\pi-\pi*$	47.9	S_{14}/325/0.69	HOMO-1→LUMO	$\pi-\pi*$	47.6
	HOMO-2→LUMO	$\pi-\pi*$/ MLCT	33.6		HOMO→LUMO+2	$\pi-\pi*$/ MLCT	28.6
	HOMO-6→LUMO+1	$\pi-\pi*$/ MLCT	47.9		HOMO-5→LUMO	MLCT	12.4
S_{20}/235/0.20	HOMO-2→LUMO+1	$\pi-\pi*$/ MLCT	47.9	S_{17}/271/0.97	HOMO-6→LUMO	MLCT	30.8
	HOMO-6→LUMO+2	$\pi-\pi*$/ MLCT	33.6		HOMO-2→LUMO	MLCT	11.2
					HOMO-1→LUMO+2	$\pi-\pi*$/ MLCT	11.2

[a] Basis set: def-TZVP. The excitation energies were chosen according to their intensity (only oscillator strengths larger than 0.05 are given).

B.2 Cobaltocene-Substituted Systems

Table B.3: Excited states, referring to the excited-state reaction pathways for cyclization in the cyclopentene-bridged Co(I), and Co(II) systems, calculated with B3LYP-D3 / def-TZVP. The C−C distance d is given in Å, the wavelengths, λ, are given in nm, the oscillator strengths f in a.u., and the weights of relevant MO transitions ω are given in percent.

	Co(I) system			Co(II) switch		
d	state / λ / f	MO transition	ω	state / λ / f	MO transition	ω
3.4	S_{17} / 305 / 0.03	HOMO→LUMO+2	65.9	S_{48} / 320 / 0.01	HOMO-1$^{\alpha/\beta}$→LUMO+2$^{\alpha/\beta}$	44.3
3.3	S_{15} / 314 / 0.21	HOMO→LUMO+2	34.5	S_{48} / 324 / 0.01	HOMO-1$^{\alpha/\beta}$→LUMO+2$^{\alpha/\beta}$	39.5
3.2	S_{15} / 319 / 0.14	HOMO→LUMO+2	65.2	S_{38} / 345 / 0.01	HOMO-1$^{\alpha/\beta}$→LUMO+2$^{\alpha/\beta}$	37.7
3.1	S_{15} / 324 / 0.03	HOMO→LUMO+2	54.9	S_{38} / 347 / 0.01	HOMO-1$^{\alpha/\beta}$→LUMO+1$^{\alpha/\beta}$	34.8
3	S_{11} / 339 / 0.01	HOMO→LUMO+2	50.7	S_{38} / 350 / 0.02	HOMO-1$^{\alpha/\beta}$→LUMO+1$^{\alpha/\beta}$	39.8
2.9	S_{11} / 351 / 0.01	HOMO→LUMO+2	78.7	S_{37} / 357 / 0.02	HOMO-1$^{\alpha/\beta}$→LUMO+1$^{\alpha/\beta}$	47.0
2.8	S_{11} / 368 / 0.01	HOMO→LUMO	90.2	S_{30} / 390 / 0.02	HOMO-1$^{\alpha/\beta}$→LUMO+1$^{\alpha/\beta}$	28.9
2.7	S_{11} / 389 / 0.02	HOMO→LUMO	97.8	S_{30} / 398 / 0.07	HOMO-1$^{\alpha/\beta}$→LUMO+1$^{\alpha/\beta}$	57.3
2.6	S_{7} / 417 / 0.03	HOMO→LUMO	96.6	S_{30} / 413 / 0.03	HOMO-1$^{\alpha/\beta}$→LUMO+1$^{\alpha/\beta}$	54.7
2.5	S_{5} / 453 / 0.03	HOMO→LUMO	80.5	S_{27} / 431 / 0.01	HOMO-1$^{\alpha/\beta}$→LUMO+1$^{\alpha/\beta}$	32.8
2.4	S_{3} / 501 / 0.06	HOMO→LUMO	97.9	S_{21} / 520 / 0.00	HOMO-1$^{\alpha/\beta}$→LUMO+1$^{\alpha/\beta}$	30.1
2.3	S_{1} / 567 / 0.07	HOMO→LUMO	94.0	S_{17} / 594 / 0.02	HOMO-1$^{\alpha/\beta}$→LUMO+1$^{\alpha/\beta}$	34.7
2.2	S_{1} / 662 / 0.08	HOMO→LUMO	97.4	S_{15} / 637 / 0.01	HOMO-1$^{\alpha/\beta}$→LUMO$^{\alpha/\beta}$	68.0
2.1	S_{1} / 695 / 0.07	HOMO→LUMO	98.1	S_{13} / 690 / 0.02	HOMO-1$^{\alpha/\beta}$→LUMO$^{\alpha/\beta}$	36.8
2	S_{1} / 804 / 0.03	HOMO→LUMO	98.8	S_{16} / 632 / 0.12	HOMO-1$^{\alpha/\beta}$→LUMO$^{\alpha/\beta}$	71.0
1.9	S_{1} / 576 / 0.17	HOMO→LUMO	90.4	S_{15} / 611 / 0.02	HOMO-1$^{\alpha/\beta}$→LUMO$^{\alpha/\beta}$	68.4
1.8	S_{1} / 623 / 0.13	HOMO→LUMO	97.6	S_{15} / 600 / 0.01	HOMO-1$^{\alpha/\beta}$→LUMO$^{\alpha/\beta}$	65.2
1.7	S_{3} / 522 / 0.28	HOMO→LUMO	97.6	S_{15} / 592 / 0.01	HOMO-1$^{\alpha/\beta}$→LUMO$^{\alpha/\beta}$	61.7
1.6	S_{3} / 509 / 0.30	HOMO→LUMO	96.7	S_{17} / 587 / 0.01	HOMO-1$^{\alpha/\beta}$→LUMO$^{\alpha/\beta}$	39.4
1.5	S_{3} / 501 / 0.31	HOMO→LUMO	96.0	S_{17} / 584 / 0.01	HOMO-1$^{\alpha/\beta}$→LUMO$^{\alpha/\beta}$	56.2
1.4	S_{3} / 496 / 0.31	HOMO→LUMO	95.2	S_{17} / 582 / 0.01	HOMO-1$^{\alpha/\beta}$→LUMO$^{\alpha/\beta}$	65.9

C. Additional Information for Part III

C.1 Local spins

Table C.1: Mulliken local spins summed up over the NNO and SQ radical centers and the bridges including the C≡C spacers for all spin states and functionals under study. X=CH_3 (top) and X=CH_2· (middle, bottom; the results were taken from the author's Bachelor's thesis [35]). Basis set: def-TZVP.

	$\langle\hat{S}_{z,\mathrm{NNO}}\rangle^{\mathrm{uu}}$	$\langle\hat{S}_{z,\mathrm{Br}}\rangle^{\mathrm{uu}}$	$\langle\hat{S}_{z,\mathrm{SQ}}\rangle^{\mathrm{uu}}$	$\langle\hat{S}_{z,\mathrm{NNO}}\rangle^{\mathrm{ud}}$	$\langle\hat{S}_{z,\mathrm{Br}}\rangle^{\mathrm{ud}}$	$\langle\hat{S}_{z,\mathrm{SQ}}\rangle^{\mathrm{ud}}$
BP86	0.52	0.06	0.41	0.53	-0.12	-0.41
TPSS	0.53	0.06	0.41	0.53	-0.12	-0.41
TPSS-D	0.53	0.06	0.41	0.53	-0.12	-0.41
TPSSH	0.53	0.04	0.43	0.54	-0.11	-0.42
B3LYP	0.53	0.04	0.43	0.54	-0.11	-0.43
B2-PLYP	0.54	0.00	0.46	0.55	-0.10	-0.45
	$\langle\hat{S}_{z,\mathrm{NNO}}\rangle^{\mathrm{uuu}}$	$\langle\hat{S}_{z,\mathrm{Br}}\rangle^{\mathrm{uuu}}$	$\langle\hat{S}_{z,\mathrm{SQ}}\rangle^{\mathrm{uuu}}$	$\langle\hat{S}_{z,\mathrm{NNO}}\rangle^{\mathrm{uud}}$	$\langle\hat{S}_{z,\mathrm{Br}}\rangle^{\mathrm{uud}}$	$\langle\hat{S}_{z,\mathrm{SQ}}\rangle^{\mathrm{uud}}$
BP86	0.52	0.57	0.41	0.52	0.40	-0.42
TPSS	0.52	0.57	0.41	0.52	0.40	-0.43
TPSS-D	0.52	0.57	0.41	0.51	0.41	-0.42
TPSSH	0.52	0.56	0.42	0.53	0.41	-0.44
B3LYP	0.53	0.55	0.42	0.53	0.41	-0.44
B2-PLYP	0.53	0.53	0.45	0.53	0.44	-0.47
	$\langle\hat{S}_{z,\mathrm{NNO}}\rangle^{\mathrm{udu}}$	$\langle\hat{S}_{z,\mathrm{Br}}\rangle^{\mathrm{udu}}$	$\langle\hat{S}_{z,\mathrm{SQ}}\rangle^{\mathrm{udu}}$	$\langle\hat{S}_{z,\mathrm{NNO}}\rangle^{\mathrm{duu}}$	$\langle\hat{S}_{z,\mathrm{Br}}\rangle^{\mathrm{duu}}$	$\langle\hat{S}_{z,\mathrm{SQ}}\rangle^{\mathrm{duu}}$
BP86	0.53	-0.45	0.43	-0.50	0.61	0.39
TPSS	0.53	-0.46	0.43	-0.52	0.62	0.40
TPSS-D	0.53	-0.46	0.43	-0.52	0.62	0.40
TPSSH	0.53	-0.48	0.44	-0.54	0.62	0.42
B3LYP	0.54	-0.48	0.44	-0.54	0.62	0.42
B2-PLYP	0.55	-0.52	0.47	-0.55	0.60	0.45

Table C.2: Mulliken local spins summed up over the NNO and SQ radical centers and the bridges including the C≡C spacers for all spin states and functionals under study (the results were taken from the author's Bachelor's thesis [35]). X=NH_2 (top) and X=NH· (middle, bottom). Basis set: def-TZVP.

	$\langle\hat{S}_{z,\mathrm{NNO}}\rangle^{\mathrm{uu}}$	$\langle\hat{S}_{z,\mathrm{Br}}\rangle^{\mathrm{uu}}$	$\langle\hat{S}_{z,\mathrm{SQ}}\rangle^{\mathrm{uu}}$	$\langle\hat{S}_{z,\mathrm{NNO}}\rangle^{\mathrm{ud}}$	$\langle\hat{S}_{z,\mathrm{Br}}\rangle^{\mathrm{ud}}$	$\langle\hat{S}_{z,\mathrm{SQ}}\rangle^{\mathrm{ud}}$
BP86	0.52	0.07	0.41	0.53	-0.12	-0.41
TPSS	0.53	0.06	0.41	0.53	-0.12	-0.41
TPSS-D	0.53	0.06	0.41	0.53	-0.12	-0.41
TPSSH	0.53	0.06	0.42	0.54	-0.11	-0.42
B3LYP	0.53	0.04	0.43	0.54	-0.11	-0.43
B2-PLYP	0.54	0.01	0.46	0.55	-0.10	-0.45
	$\langle\hat{S}_{z,\mathrm{NNO}}\rangle^{\mathrm{uuu}}$	$\langle\hat{S}_{z,\mathrm{Br}}\rangle^{\mathrm{uuu}}$	$\langle\hat{S}_{z,\mathrm{SQ}}\rangle^{\mathrm{uuu}}$	$\langle\hat{S}_{z,\mathrm{NNO}}\rangle^{\mathrm{uud}}$	$\langle\hat{S}_{z,\mathrm{Br}}\rangle^{\mathrm{uud}}$	$\langle\hat{S}_{z,\mathrm{SQ}}\rangle^{\mathrm{uud}}$
BP86	0.52	0.57	0.41	0.49	0.42	-0.41
TPSS	0.52	0.57	0.41	0.53	0.41	-0.42
TPSS-D	0.52	0.57	0.41	0.51	0.41	-0.42
TPSSH	0.53	0.55	0.42	0.53	0.42	-0.44
B3LYP	0.53	0.55	0.43	0.53	0.42	-0.45
B2-PLYP	0.52	0.52	0.46	0.53	0.44	-0.47
	$\langle\hat{S}_{z,\mathrm{NNO}}\rangle^{\mathrm{udu}}$	$\langle\hat{S}_{z,\mathrm{Br}}\rangle^{\mathrm{udu}}$	$\langle\hat{S}_{z,\mathrm{SQ}}\rangle^{\mathrm{udu}}$	$\langle\hat{S}_{z,\mathrm{NNO}}\rangle^{\mathrm{duu}}$	$\langle\hat{S}_{z,\mathrm{Br}}\rangle^{\mathrm{duu}}$	$\langle\hat{S}_{z,\mathrm{SQ}}\rangle^{\mathrm{duu}}$
BP86	0.53	-0.46	0.43	-0.53	0.62	0.41
TPSS	0.54	-0.47	0.43	-0.54	0.63	0.41
TPSS-D	0.54	-0.47	0.43	-0.54	0.63	0.41
TPSSH	0.54	-0.49	0.45	-0.54	0.62	0.42
B3LYP	0.54	-0.49	0.45	-0.55	0.62	0.42
B2-PLYP	0.55	-0.53	0.48	-0.55	0.60	0.45

Table C.3: Mulliken local spins summed up over the NNO and SQ radical centers and the bridges including the C≡C spacers for all spin states and functionals under study (the results were taken from the author's Bachelor's thesis [35]). X=OH (top) and X=O· (middle, bottom). Basis set: def-TZVP.

	$\langle\hat{S}_{z,\mathrm{NNO}}\rangle^{\mathrm{uu}}$	$\langle\hat{S}_{z,\mathrm{Br}}\rangle^{\mathrm{uu}}$	$\langle\hat{S}_{z,\mathrm{SQ}}\rangle^{\mathrm{uu}}$	$\langle\hat{S}_{z,\mathrm{NNO}}\rangle^{\mathrm{ud}}$	$\langle\hat{S}_{z,\mathrm{Br}}\rangle^{\mathrm{ud}}$	$\langle\hat{S}_{z,\mathrm{SQ}}\rangle^{\mathrm{ud}}$
BP86	0.52	0.06	0.41	0.53	-0.12	-0.41
TPSS	0.53	0.06	0.41	0.53	-0.12	-0.41
TPSS-D	0.53	0.06	0.41	0.53	-0.12	-0.41
TPSSH	0.53	0.04	0.43	0.54	-0.11	-0.42
B3LYP	0.53	0.04	0.43	0.54	-0.11	-0.43
B2-PLYP	0.54	0.00	0.46	0.55	-0.10	-0.45
	$\langle\hat{S}_{z,\mathrm{NNO}}\rangle^{\mathrm{uuu}}$	$\langle\hat{S}_{z,\mathrm{Br}}\rangle^{\mathrm{uuu}}$	$\langle\hat{S}_{z,\mathrm{SQ}}\rangle^{\mathrm{uuu}}$	$\langle\hat{S}_{z,\mathrm{NNO}}\rangle^{\mathrm{uud}}$	$\langle\hat{S}_{z,\mathrm{Br}}\rangle^{\mathrm{uud}}$	$\langle\hat{S}_{z,\mathrm{SQ}}\rangle^{\mathrm{uud}}$
BP86	0.53	0.57	0.41	0.45	0.32	-0.26
TPSS	0.53	0.57	0.41	0.48	0.34	-0.32
TPSS-D	0.53	0.56	0.41	0.48	0.34	-0.32
TPSSH	0.53	0.55	0.42	0.53	0.39	-0.42
B3LYP	0.53	0.55	0.42	0.53	0.40	-0.43
B2-PLYP	0.53	0.53	0.45	0.53	0.44	-0.47
	$\langle\hat{S}_{z,\mathrm{NNO}}\rangle^{\mathrm{udu}}$	$\langle\hat{S}_{z,\mathrm{Br}}\rangle^{\mathrm{udu}}$	$\langle\hat{S}_{z,\mathrm{SQ}}\rangle^{\mathrm{udu}}$	$\langle\hat{S}_{z,\mathrm{NNO}}\rangle^{\mathrm{duu}}$	$\langle\hat{S}_{z,\mathrm{Br}}\rangle^{\mathrm{duu}}$	$\langle\hat{S}_{z,\mathrm{SQ}}\rangle^{\mathrm{duu}}$
BP86	0.43	-0.32	0.39	-0.42	0.52	0.41
TPSS	0.46	-0.35	0.40	-0.45	0.55	0.41
TPSS-D	0.46	-0.35	0.40	-0.45	0.55	0.41
TPSSH	0.54	-0.47	0.43	-0.54	0.63	0.42
B3LYP	0.54	-0.48	0.44	-0.55	0.62	0.42
B2-PLYP	0.55	-0.52	0.47	-0.45	0.60	0.45

C.1.1 Towards a realistic molecular system

Mulliken local spins were calculated for the radical moieties (NNO; SQ/SQ(Zn)) and the bridges B of the systems (Figure C.1). For the systems including complexated semiquinone groups SQ(Zn) the local spins were calculated for the semiquinone and the zinc complex separately. The local spin sums for the zinc complex were zero in all cases for the given accuracy (all values were lower than 0.005 a.u.) and are therefore not further considered.

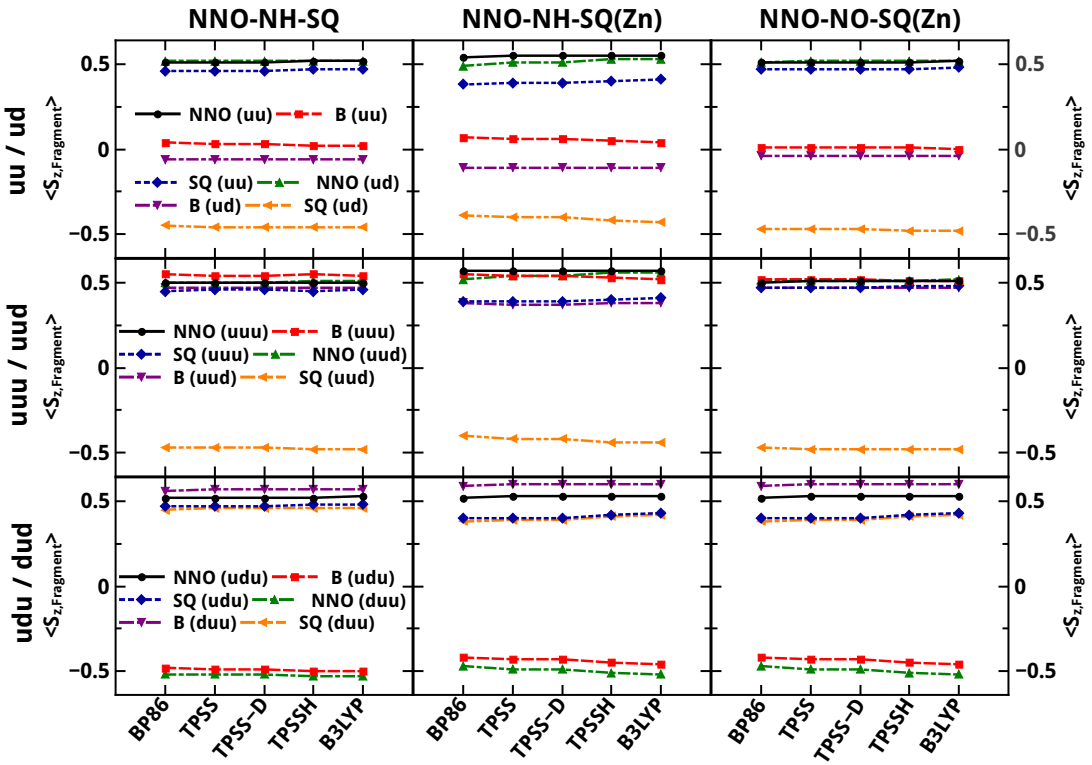

Figure C.1: Mulliken local spins for three model systems and the potentially synthesizable system calculated with different exchange-correlation functionals on the spin-state structures optimized with BP86. Basis set: def-TZVP.

For all spin states delocalization from the SQ or SQ(Zn) moiety onto the bridge is observed for all di- and triradicals. For the uuu and duu spin states this results in a local spin larger than 0.5 a.u. for the bridge. In the udu and the uud spin states the spin's magnitude decreases due to the opposite sign of the local spin sums for the SQ/SQ(Zn) and the bridges.
It is also worth noting that the local spins for the NNO-NO/NOH-SQ(Zn) systems only a very small amount of spin is transferred from the SQ(Zn) to the bridge, while for the NNO-NH/NH2-SQ(Zn) the spin transfer is much higher.

C.2 Spin Contributions of Different Parts of the Bridge in NNO–NH–SQ(Zn) and NNO–NO–SQ(Zn)

Table C.4: Mulliken local spins for the radical group (NH or NO) and the phenyl part (Ph) in atomic units. The numbers in brackets show the contribution of the phenyl part to the total spin sum of the bridge in percent. Basis set: def-TZVP.

NNO–NH–SQ(Zn)								
	uuu		uud		udu		duu	
Functional	$\langle\hat{S}_{z,\mathrm{NH}}\rangle$	$\langle\hat{S}_{z,\mathrm{Ph}}\rangle$	$\langle\hat{S}_{z,\mathrm{NH}}\rangle$	$\langle\hat{S}_{z,\mathrm{Ph}}\rangle$	$\langle\hat{S}_{z,\mathrm{NH}}\rangle$	$\langle\hat{S}_{z,\mathrm{Ph}}\rangle$	$\langle\hat{S}_{z,\mathrm{NH}}\rangle$	$\langle\hat{S}_{z,\mathrm{Ph}}\rangle$
BP86	0.28	0.25 (47)	0.20	0.28 (42)	−0.28	−0.22 (44)	0.29	0.26 (47)
TPSS	0.30	0.23 (43)	0.19	0.29 (40)	−0.30	−0.21 (41)	0.29	0.26 (47)
TPSS-D	0.30	0.23 (43)	0.19	0.29 (40)	−0.30	−0.21 (41)	0.29	0.26 (47)
TPSSH	0.31	0.21 (40)	0.17	0.32 (35)	−0.31	−0.21 (40)	0.31	0.24 (44)
B3LYP	0.31	0.21 (40)	0.17	0.31 (35)	−0.31	−0.21 (40)	0.30	0.25 (45)
NNO–NO–SQ(Zn)								
Functional	$\langle\hat{S}_{z,\mathrm{NO}}\rangle$	$\langle\hat{S}_{z,\mathrm{Ph}}\rangle$	$\langle\hat{S}_{z,\mathrm{NO}}\rangle$	$\langle\hat{S}_{z,\mathrm{Ph}}\rangle$	$\langle\hat{S}_{z,\mathrm{NO}}\rangle$	$\langle\hat{S}_{z,\mathrm{Ph}}\rangle$	$\langle\hat{S}_{z,\mathrm{NO}}\rangle$	$\langle\hat{S}_{z,\mathrm{Ph}}\rangle$
BP86	0.41	0.11 (21)	0.41	0.13 (24)	−0.42	−0.08 (16)	0.41	0.06 (13)
TPSS	0.42	0.10 (19)	0.41	0.13 (24)	−0.42	−0.08 (16)	0.42	0.05 (11)
TPSS-D	0.42	0.10 (19)	0.41	0.13 (24)	−0.42	−0.08 (16)	0.42	0.05 (11)
TPSSH	0.43	0.08 (16)	0.44	0.11 (20)	−0.44	−0.07 (14)	0.44	0.03 (6)
B3LYP	0.44	0.07 (14)	0.44	0.11 (20)	−0.44	−0.07 (14)	0.44	0.03 (6)

C.3 Relative stabilizations of the ground states in the meta-bridged di- and triradicals

Table C.5: Relative stabilization of the "ud" and "duu" di- and triradical ground states against the next spin states X for all systems under study calculated with different functionals. All values are given in kJ/mol. Basis set: def-TZVP.

	NNO-CH_3(Spacer)-SQ				NNO-O(Spacer)-SQ			
Functional	$E_{(\mathrm{uu-ud})}$	X	$E_{(\mathrm{X-duu})}$	$\frac{E_{(\mathrm{X-duu})}}{E_{(\mathrm{uu-ud})}}$	$E_{(\mathrm{uu-ud})}$	X	$E_{(\mathrm{X-duu})}$	$\frac{E_{(\mathrm{X-duu})}}{E_{(\mathrm{uu-ud})}}$
BP86	0.32	uuu	1.98	6.2	0.33	udu	2.56	7.8
TPSS	0.46	uuu	2.03	4.4	0.46	uuu	3.59	7.8
TPSS-D	0.46	uuu	2.01	4.4	0.46	udu	4.24	9.2
TPSSH	0.82	uuu	3.58	4.4	0.81	uuu	3.37	4.2
B3LYP	0.83	uuu	3.77	4.5	0.84	uuu	3.85	4.6
B2PLYP	5.52	uuu	15.07	2.7	5.48	uuu	17.60	3.2
	NNO-NH(Spacer)-SQ				NNO-NH-SQ			
BP86	0.31	uuu	1.52	4.9	0.51	uuu	2.04	4.0
TPSS	0.44	uuu	2.20	5.0	0.73	uuu	2.99	4.1
TPSS-D	0.44	uuu	2.19	5.0	0.74	uuu	3.01	4.1
TPSSH	0.77	uuu	3.91	5.1	1.31	uuu	5.27	4.0
B3LYP	0.80	uuu	4.17	5.2	1.45	udu	5.31	3.7
B2PLYP	5.11	uuu	15.94	3.1	–	–	–	–
	NNO-NH-SQ(Zn)				NNO-NO-SQ(Zn)			
BP86	0.33	uuu	1.87	5.7	0.34	uuu	1.15	3.4
TPSS	0.46	uuu	2.73	5.9	0.47	uuu	1.63	3.5
TPSS-D	0.49	uuu	2.70	5.5	0.56	uuu	1.66	3.0
TPSSH	0.81	uuu	4.88	6.0	0.83	uuu	2.83	3.4
B3LYP	0.88	uuu	5.42	6.2	0.92	udu	2.76	3.0

C.4 Torsional Angles for NNO–NH–SQ(Zn), NNO–NO–SQ(Zn) and NNO–NH–SQ

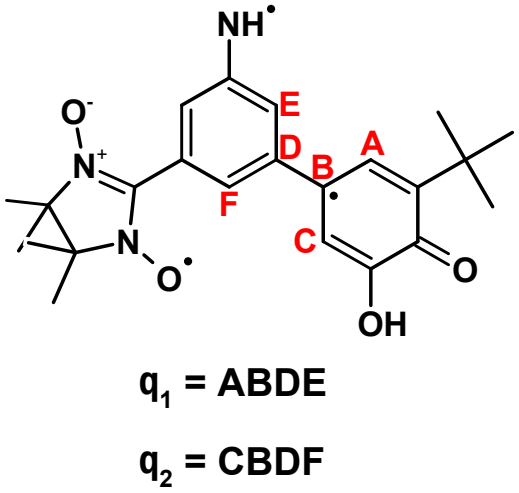

Figure C.2: Definition of the θ_1 and θ_2 angles.

Table C.6: Torsional angles (defined according to Figure C.2). Figure between phenyl bridges and semiquinone moieties for the "duu" spin-state structures optimized with BP86. Basis set: def-TZVP.

Structure	θ_1	θ_2
NNO–CH_2(Spacer)–SQ	0.36	0.22
NNO–O(Spacer)–SQ	4.75	5.30
NNO–NH(Spacer)–SQ	−0.20	−0.17
NNO–NH–SQ	26.38	25.48
NNO–NH–SQ(Zn)	31.36	31.94
NNO–NO–SQ(Zn)	31.55	32.07

C.5 Additional MO Plots for all Spin States

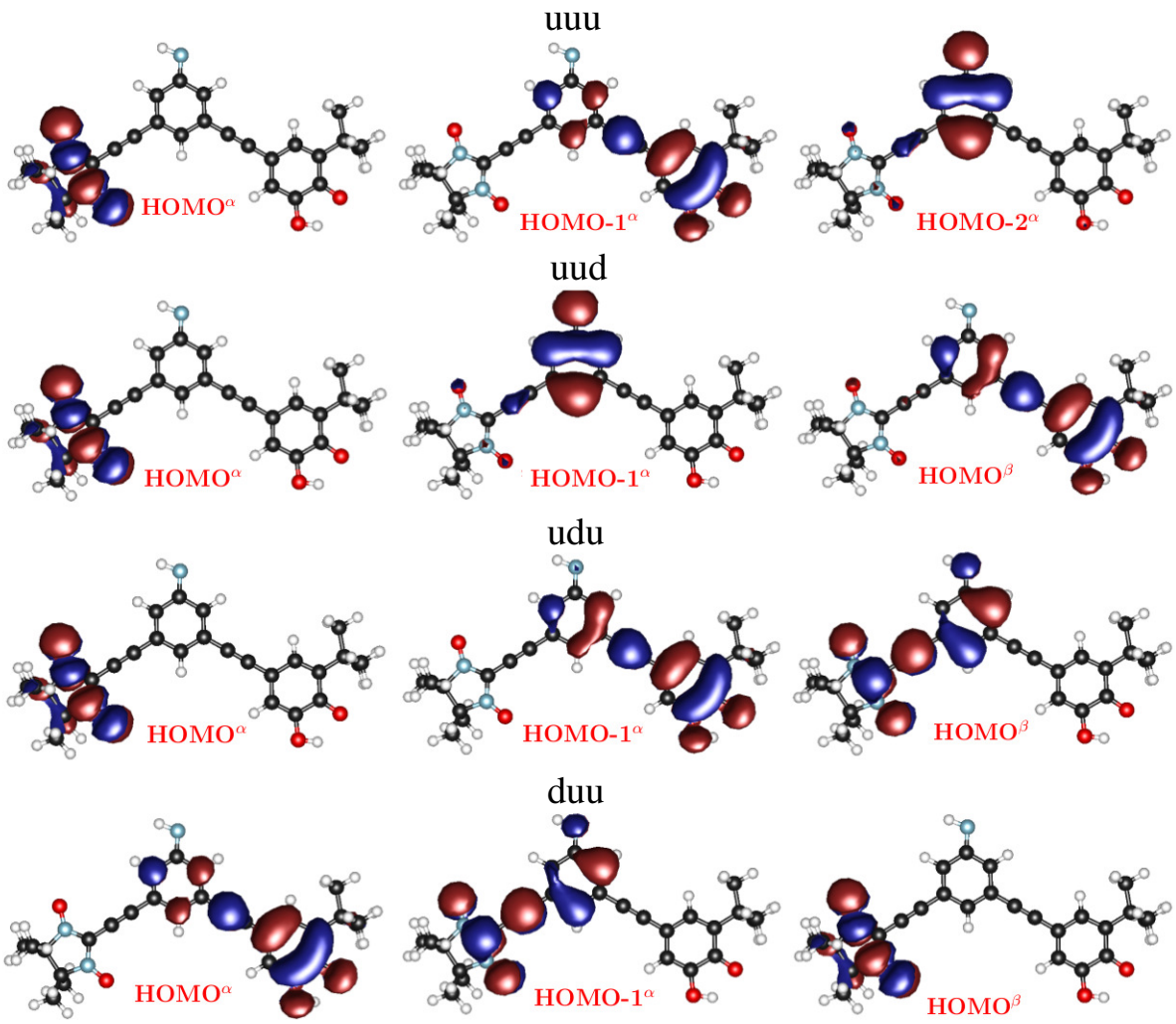

Figure C.3: MOs for the meta-connected X=NH triradical for all spin states. B3LYP/def-TZVP (the results were taken from the author's Bachelor's thesis [35]).

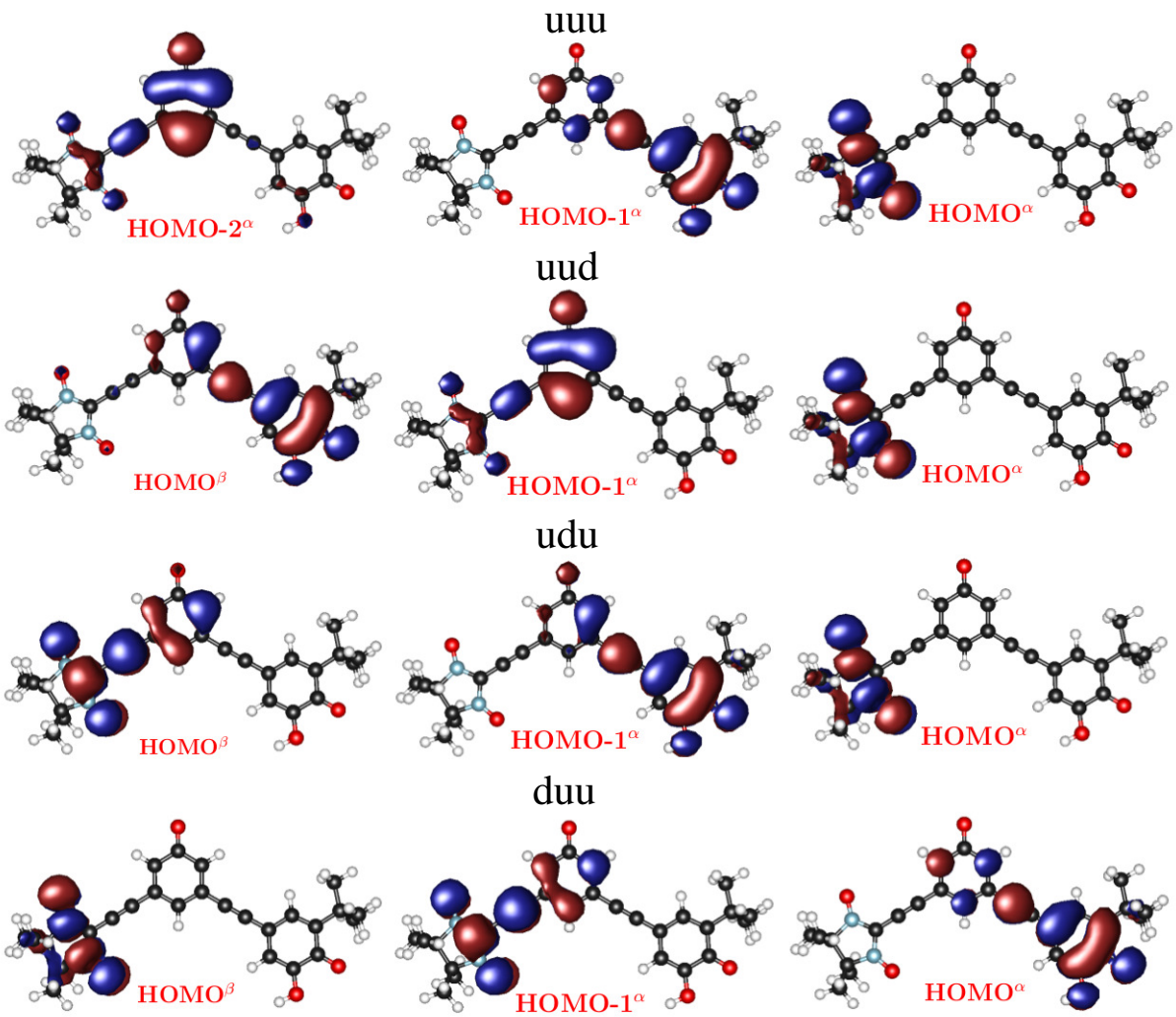

Figure C.4: MOs for the meta-connected X=O triradical for all spin states. B3LYP/def-TZVP (the results were taken from the author's Bachelor's thesis [35]).

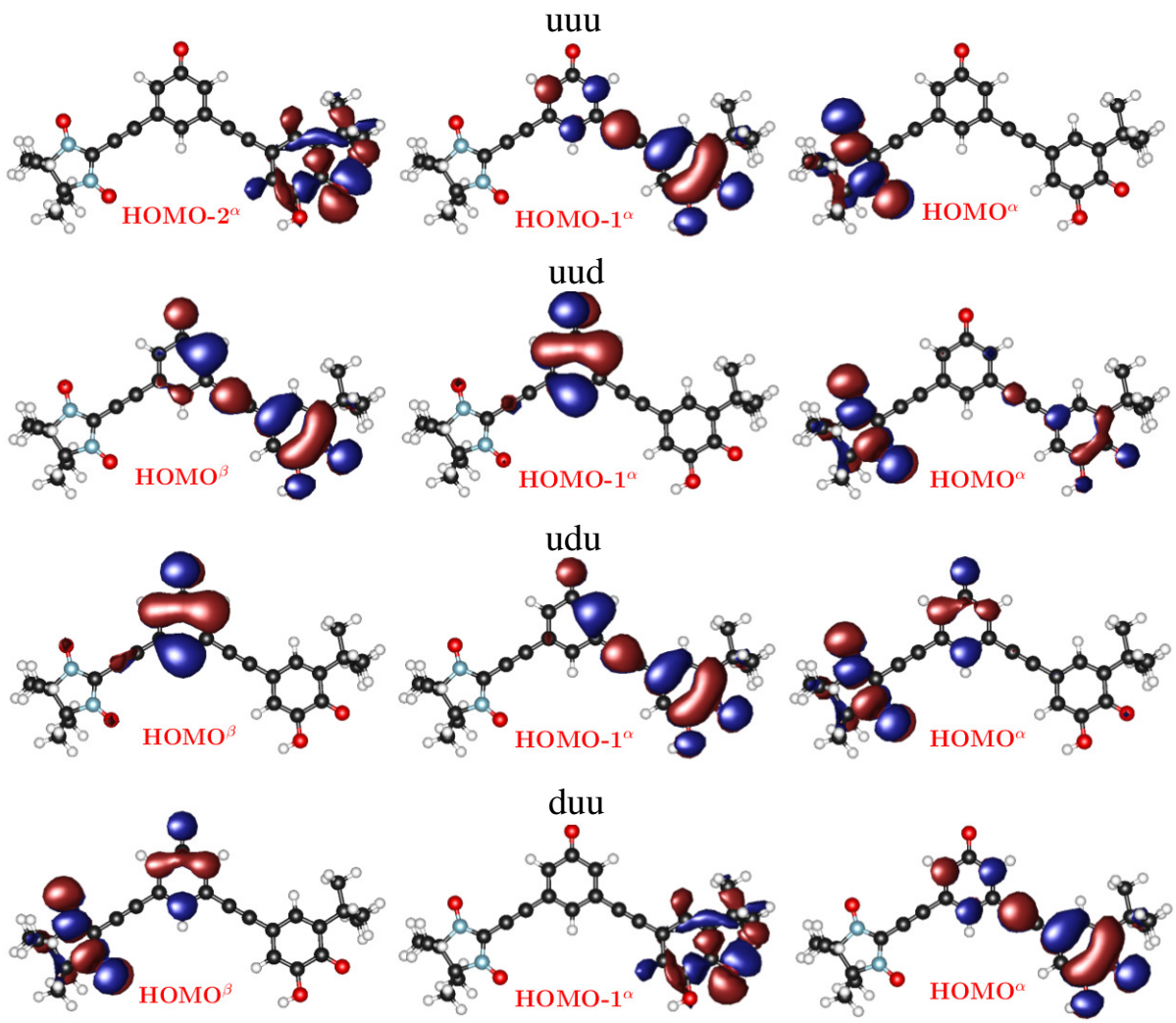

Figure C.5: MOs for the meta-connected X=O triradical for all spin states. BP86/def-TZVP (the results were taken from the author's Bachelor's thesis [35]).

C.6 Spin Densities

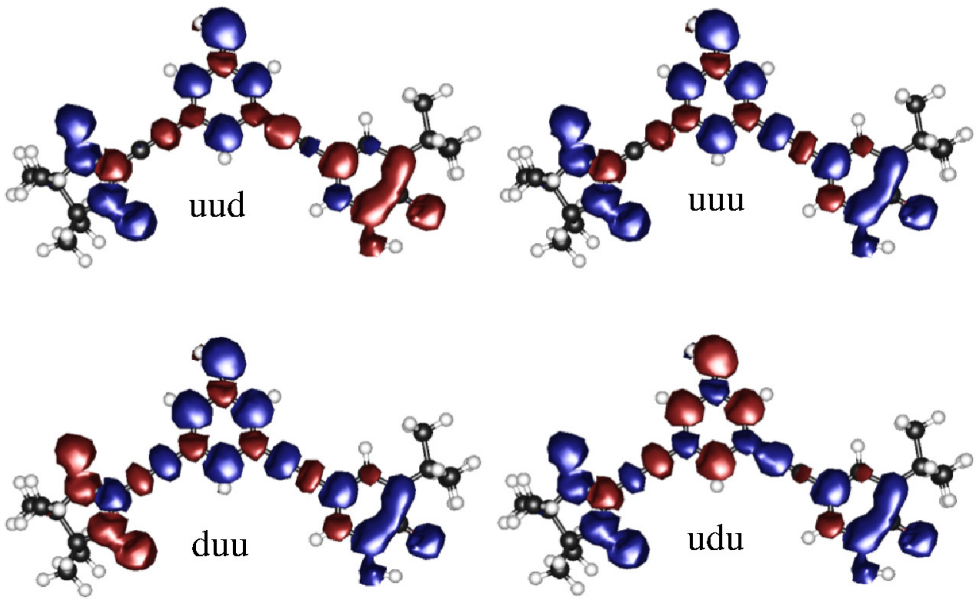

Figure C.6: Spin densities for the meta-connected X=NH triradical for all spin states. B3LYP/def-TZVP (the results were taken from the author's Bachelor's thesis [35]).

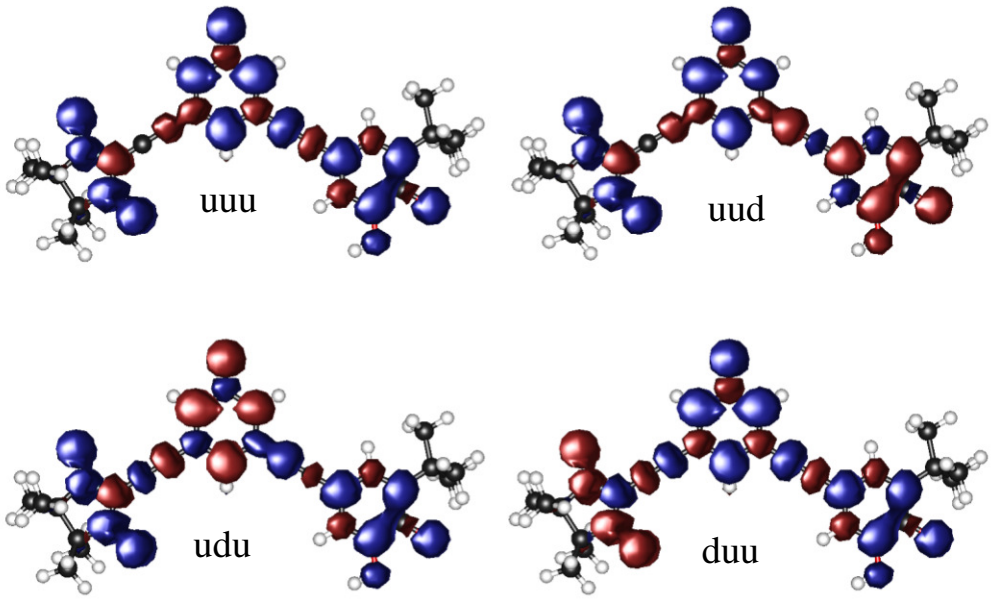

Figure C.7: Spin densities for the meta-connected X=O triradical for all spin states (the results were taken from the author's Bachelor's thesis [35]). B3LYP/def-TZVP.

C.7 Coupling Constants

For the calculation of the coupling constants the following definition of the Heisenberg–Dirac–Van Vleck (HDvV) Hamiltonian was employed:

$$\hat{H}_{\mathrm{HDvV}} = -2J_{AB}\hat{s}_A\hat{s}_A, \tag{C.1}$$

where J_{AB} is the magnetic exchange coupling constant. Its sign gives the kind of coupling in the ground state and its magnitude gives the strength of the coupling. $\hat{s}_A$ and $\hat{s}_B$ are local spin vector operators of the magnetic sites A and B. We employed the unprojected Noodleman formula:

$$J^{\mathrm{Dirad}}_{\mathrm{NNO/SQ}} = \frac{E_{\mathrm{ud}} - E_{\mathrm{uu}}}{2}. \tag{C.2}$$

For the triradicals the following formulas were derived:

$$J^{\mathrm{Trirad}}_{\mathrm{NNO/Br}} = \frac{E_{\mathrm{duu}} - E_{\mathrm{uud}}}{4} + \frac{E_{\mathrm{udu}} - E_{\mathrm{uuu}}}{4}, \tag{C.3}$$

$$J^{\mathrm{Trirad}}_{\mathrm{SQ/Br}} = \frac{E_{\mathrm{uud}} - E_{\mathrm{duu}}}{4} + \frac{E_{\mathrm{udu}} - E_{\mathrm{uuu}}}{4}, \tag{C.4}$$

$$J^{\mathrm{Trirad}}_{\mathrm{NNO/SQ}} = \frac{E_{\mathrm{duu}} - E_{\mathrm{udu}}}{4} + \frac{E_{\mathrm{uud}} - E_{\mathrm{uuu}}}{4}, \tag{C.5}$$

with Br being the bridge (X or X(Spacer)).

Table C.7: Coupling constants for the NNO-NH_2(Spacer)/NH(Spacer)·-SQ, the NNO-OH(Spacer)/O(Spacer)·-SQ, and the NNO-CH_3(Spacer)/NH_2·(Spacer)-SQ di- and triradicals calculated according to Equations (C.2)-(C.5) employing different exchange–correlation functionals. Basis set: def-TZVP.

NNO-CH_3(Spacer)/CH_2·(Spacer)-SQ				
Functional	$J^{\text{Dirad}}_{\text{NNO/SQ}}$	$J^{\text{Trirad}}_{\text{NNO/SQ}}$	$J^{\text{Trirad}}_{\text{NNO/X(Spacer)}}$	$J^{\text{Trirad}}_{\text{X(Spacer)/SQ}}$
BP86	−0.16	−0.27	−0.72	2.53
TPSS	−0.23	−0.18	−0.83	2.77
TPSS-D	−0.23	−0.23	−0.78	2.74
TPSSH	−0.41	−0.30	−1.49	3.37
B3LYP	−0.42	−0.30	−1.59	3.20
B2PLYP		−0.72	2.96	−0.72
NNO-NH_2(Spacer)/NH·(Spacer)-SQ				
BP86	−0.15	−0.06	−0.86	2.44
TPSS	−0.22	−0.15	−0.91	2.97
TPSS-D	−0.22	−0.15	−0.90	2.99
TPSSH	−0.38	−0.25	−1.70	3.70
B3LYP	−0.39	−0.26	−1.83	3.50
B2PLYP	4.12	−0.15	3.12	−0.62
NNO-OH(Spacer)/O·(Spacer)-SQ				
BP86	−0.17	−0.97	−2.87	0.30
TPSS	−0.23	0.14	−1.93	2.25
TPSS-D	−0.23	−0.20	−2.25	1.92
TPSSH	−0.41	0.04	−1.73	4.00
B3LYP	−0.42	0.01	−1.94	4.02
B2PLYP	4.48	0.12	2.95	0.50

Table C.8: Coupling constants for the NNO-NH_2/NH·-SQ, the NNO-NH_2/NH·-SQ(Zn), and the NNO-NH_2/NH·-SQ(Zn) di- and triradicals calculated according to Equations (C.2)-(C.5) employing different exchange–correlation functionals. Basis set: def-TZVP.

NNO-NH_2/NH·-SQ				
Functional	$J^{\text{Dirad}}_{\text{NNO/SQ}}$	$J^{\text{Trirad}}_{\text{NNO/SQ}}$	$J^{\text{Trirad}}_{\text{NNO/X}}$	$J^{\text{Trirad}}_{\text{X/SQ}}$
BP86	−0.26	−0.14	−0.88	2.64
TPSS	−0.37	−0.21	−1.28	3.18
TPSS-D	−0.37	−0.22	−-1.28	3.27
TPSSH	−0.65	−0.37	−2.27	4.01
B3LYP	−0.72	−0.40	−-2.51	3.87
NNO-NH_2/NH·-SQ(Zn)				
BP86	−0.16	−0.10	−0.84	1.58
TPSS	−0.23	−0.13	−1.23	1.94
TPSS-D	−0.25	−0.13	−1.22	2.03
TPSSH	−0.40	−0.22	−2.22	2.51
B3LYP	−0.44	−0.24	−2.47	2.41
NNO-NOH/NO·-SQ(Zn)				
BP86	−0.16	−0.10	−0.84	1.58
TPSS	−0.23	−0.13	−1.23	1.94
TPSS-D	−0.25	−0.13	−1.22	2.03
TPSSH	−0.40	−0.22	−2.22	2.51
B3LYP	−0.44	−0.24	−2.47	2.41
NNO-NOH/NO·-SQ(Zn)				
BP86	−0.17	−0.13	−0.44	0.76
TPSS	−0.23	−0.20	−0.62	0.88
TPSS-D	−0.28	−0.23	−0.60	0.95
TPSSH	−0.42	−0.36	−1.05	1.09
B3LYP	−0.46	−0.38	−1.13	1.00

D. Computational Methodology

In this work different quantum chemical program packages were employed. In all structure optimizations performed in this work, the TURBOMOLE 6.0 [285] and TURBOMOLE 6.5 [286] program packages were employed. In all calculations with TURBOMOLE using pure functionals the resolution-of-identity (RI) approximation [287,288] was taken into account. The convergence criteria for all structure optimizations were set to a gradient norm below 10^{-4} a.u., and for the self-consistent-field (SCF) algorithm, to an energy change below 10^{-7} a.u.. However, single-point calculations with GAUSSIAN09 [289] were performed on top of the optimized structures in all cases where coupling constants were calculated with the Green's-function approach implemented in ARTAIOS [34]. None of the calculations with GAUSSIAN09 were performed within the RI approximation. In these calculations the convergence criterium for the energy change was set to 10^{-6} a.u.. Molecular orbital plots were generated with MOLDEN [290], in all cases employing an iso-surface value of 0.02 a.u., while for the spin density plots a value of 0.002 a.u. was employed. In the following sections the computational methodologies of the three parts are given.

D.1 Part I: Analyzing Spin Coupling Pathways

In Chapter 4, the molecular structures were obtained by defining the structural parameters (small model systems in Section 14.1 and complexes in Section 4.4) or by structure optimizations (all following sections) using TURBOMOLE 6.0 [285] with the BP86 exchange–correlation functional [41, 291] and Ahlrich's triple-zeta def-TZVP basis set [234,235] with polarization functions on all atoms. For the 1,8-bis(vanadocenyl)naphthalene complex we addionally used the empirical dispersion correction of Grimme [236], denoted with "-D" in the structure optimizations.

On top of the structures in Chapter 4, we performed single-point calculations with GAUSSIAN09 [289] using the following exchange–correlation functionals: BP86 [41,291], PBE [42,292–294], TPSSH [42,44,292,293,295], B3LYP [41,45, 292,293,296,297], and LC-ωPBE [298–300]. The convergence criterium for the SCF algorithm was set to an energy change below 10^{-6} a.u. in all single-point calculations.

For the Cu(II) complex in Chapter 5, the structural parameters given in the work of Hay and coworkers [95] were employed (which were identical to that used in Chapter 4). On top of these structures, single-point calculations were performed

with the GAUSSIAN09 program package [289] employing the B3LYP [41,45,292, 293, 296, 297] functional, and Ahlrich's triple-zeta split-valence basis set with polarization functions on all atoms, def-TZVP [234, 235]. For the dinuclear manganese(III) complex, the coordinates were taken from the work of Brunhold et al. [122], and single-point calculations were carried out with the ADF2014 program package [301–303]. Following Ref. [122], we also employed the BP86 [41, 291] functional for this complex in combination with a Slater-type triple-zeta basis set with polarization functions on all atoms, TZP [304]. Brunhold and coworkers carried out calculations using the same program package, basis set, and functional, but in contrast to this work, they used the frozen-core approximation.

Deviating from that scheme, the structure optimizations for the bismetallocene complexes in Chapter 6 were performed with the TPSSH [42, 44, 292, 293, 295] functional and the Ahlrich's triple-zeta def2-TZVP [305, 306] basis set and single-point calculations for both spin states were performed with the GAUSSIAN09 [289] program package for the BS structures using the same parameters. Only for the Co_4NP_3 system, the structure optimizations were performed with BP86 with the RI approximation and the single-point energies were calculated by TPSSH / def2-TZVP.

All coupling constants from the Green's-function approach in this part were calculated with a module JGREEN in our in-house program ARTAIOS [34], which post-processes output from electronic structure codes writing out the relevant matrices and coefficients. For comparison with coupling constants from the BS approach, the obtained J^{unit} was divided by the lengths of the local spin vectors according to Equation (2.4), where we assumed ideal local spins (e.g., one-half per formally unpaired electron). For the exchange pathway analyses, we used our version of the Green's-function approach, as implemented ARTAIOS [34], in which we implemented the contributions from occupied MOs according to Equation (3.27), and the corresponding spin-flip excitations according to Equation (3.26).

The non-collinear DFT calculations (Section A.5) were performed as single-point calculations on the optimized high-spin structures employing the OPENMX 3.7.1 [120] program, the PBE functional, an energy-cutoff value of 250 Ry and an electronic temperature of 300 K in all calculations. The core Coulomb potentials in OPENMX 3.7.1 were described by the tractable norm-conserving pseudopotentials developed by Morrison and coworkers [307]. The following atomic basis functions have been used in the non-collinear calculations: H (H7.0-s2p1), C (C7.0-s2p2d1), O (O7.0-s2p2d1), Mn (Mn10.0-s3p2d2), S (S7.0-s2p2d1), N (N7.0-s2p2d1), Co (Co10.0H-s3p2d2), V (V10.0-s3p2d2)). The Lagrangian multipliers of the penalty functions were increased step by step until a penalty energy lower than 10^{-6} a.u. was achieved. Scalar relativistic effects were considered because of the j-dependence of the pseudopotentials.

D.2 Part II: Controlling Magnetic Properties by Photoswitchable Bridges

In Chapter 9, all-electron electronic structure calculations were carried out using Kohn–Sham density functional theory as implemented in the TURBOMOLE 6.0 program package [285]. The pure BP86 exchange–correlation functional [41,291] and the hybrid functional B3LYP [45,297] were employed in combination with Ahlrichs split-valence basis set of triple-zeta quality with polarization functions on all atoms (def- TZVP) [234,235]. The weights of the molecular orbital excitations of the excitation energies were calculated from the expansion coefficients with the following formula: $weight = 100 \cdot 2 \cdot c^2$.

For the switches considered in Chapter 10, the structure optimizations were performed with the BP86 exchange–correlation functional [41,291] and Ahlrich's def-TZVP basis set [234,235] using the TURBOMOLE 6.5 program package [286]. On top of the optimized structures single-point energies and excitation energies were computed by GAUSSIAN 09 [289] program package by employing the range-separated LC-ωPBE functional, with n-hexane as the solvent for Fe(II)–5DTE–Fe(II) and Fe(II)–6DTE–Fe(II) and Cl–5DTE–Cl, and acetonitrile for Fe(II)–5DTE(Spacer)–Fe(II) using the same basis set. The solvents were considered by applying the polarizable continuum model (PCM) [308–320] and by using a dielectric constant of ϵ=1.8819 for n-hexane and ϵ=35.688 for acetonitrile. For the study on the torsional angle, no solvent effects were considered. The study on the torsional angle was performed by fixing θ angles to certain values and by performing restrained optimizations with the BP86 functional (and single-point calculations with LC-ωPBE functional on top of these structures) for each angle. Calculated optical spectra were broadened by using Gaussian functions with a half width of 40 nm. This was done rather than calculating the full vibronic structure for the sake of computational efficiency while still obtaining an acceptable accuracy (note, however, those more efficient approaches for calculating vibronic structures have recently become available [321]).

The cobaltocene-substituted switches in Chapter 11 were optimized with the B3LYP functional using the empirical dispersion correction of Grimme in third generation ("D3") [248] and Ahlrich's triple-zeta def-TZVP basis set. The Co(II) systems were optimized in both spin states separately. For the calculation of the UV-Vis spectra the same parameters were chosen and the spectra were broadened with a half width of 40 nm.

The structure optimizations in Chapter 12 were carried out with three different functionals (BP86, TPSSH, and B3LYP) in combination with the def-TZVP basis set. On top of these structures, we have performed single-point calculations with GAUSSIAN09 the same exchange–correlation functionals as in the structure optimizations: BP86, TPSSH and B3LYP. The convergence criterium for the SCF algorithm was set to an energy change below 10^{-6} a.u. in all single-point calculations. This was done in order to be able to use the Green's-function approach as implemented JGREEN module of ARTAIOS [34] which was employed

to the electronic high-spin state of the BS structures. The spin center definition was varied in this chapter and is given in more detail in Chapter 12. For the HOMHED values we used the parameters defined in Ref. [79] implemented in a tool written by the author.

D.3 Part III: Increasing Spin Coupling by Radical Bridges

All molecular structures were optimized within spin-unrestricted Kohn–Sham density functional theory for each spin state with the BP86 functional [41, 291], while for all other functionals single-point calculations were carried out on the BP86-optimized structures in the respective spin state. Spin-state energetics were evaluated with six different exchange–correlation functionals: Two pure functionals, BP86 [41, 291] and TPSS [44], one pure functional featuring Grimme's dispersion correction, TPSS-D [248], two hybrid functionals with 10 and 20 percent Hartree–Fock exchange, respectively, TPSSH [42,44,292,293,295] and B3LYP [45,297], and the double hybrid functional B2PLYP [322] which features 53 percent Hartree–Fock exchange and an admixture based on second-order perturbation theory to the correlation functional. Ahlrichs' triple-zeta split-valence basis set with polarization functions on all atoms, def-TZVP [234, 235], was used throughout. The electronic-structure calculations in Section 14.1 were carried out with the TURBOMOLE 6.0 [285] and in Section 14.2 with the TURBOMOLE 6.6 [323] quantum chemistry program packages, respectively. To obtain electronic structures of Broken-Symmetry determinants, a restrained-optimization scheme [324] was used, and to evaluate local spins [58], a local version of TURBOMOLE's MOLOCH, both implemented in a local version of TURBOMOLE at ETH Zurich.
Further single-point calculations were performed on the "duu" spin state structures for all spin-states with GAUSSIAN09 to be able to compare the coupling constants obtained from the BS approach with those obtained from the Green's-function approach for which structure relaxation effects cannot be taken into account.

E. Notation

In this Section, we explain the symbols for the quantities used in this work. In general, matrices are given in bold large letters, vectors are denoted by small bold letters, and scalars are given in italics.

J_{AB} Spin coupling constant.

J_{BS} Coupling constant obtained from the Broken-Symmetry approach.

$\hat{\mathbf{S}}_A$ Local spin vector on magnetic site A.

$\hat{\mathbf{e}}_A$ Unit vector on magnetic site A.

S_A Magnitude of local spin vector on A.

E^{F} Energy of the high-spin state.

E^{BS} Energy of the BS determinant.

ψ_i^σ Space part of σ spin orbital i.

$O_{ij}^{\beta\alpha}$ Overlap between spin orbitals i and j refering to β and α spin orbitals.

$\langle \hat{S}^2 \rangle$ Expectation value of the $\hat{S}^2$ operator.

N^σ Number of σ spin electrons.

$n_{xc,\lambda}(\mathbf{r}, \mathbf{r}')$ Exchange–correlation hole density.

$P_\lambda(\mathbf{r}, \mathbf{r}')$ Pair density.

$n(\mathbf{r})$ Electron density.

$\mathbf{S}$ Overlap matrix.

$\mathbf{P}$ Density matrix.

b_{ij} Transfer integral.

U Hubbard model "U" describing the Coulomb repulsion of electrons on a given spin center.

ϕ Spin orbitals.

J_{AB} and J_{AA} Coulomb repulsion.

K_{AB} Exchange integral.

$\hat{V}_A$ On-site potentials.

$\hat{G}^{\sigma}$ Green's function for σ electrons.

J_{Green} Coupling constant obtained in the Green's-function approach.

ϵ MO energy.

$\hat{p}_A$ Projection operator for atom or fragment A.

μ Chemical potential.

f_i^{α} Fermi distribution function.

$C_{\mu i}^{\sigma}$ MO coefficient for basis function μ and σ spin orbital i.

$F_{\mu\nu}^{\sigma}$ σ Fock matrix element between basis functions μ and ν.

$j_{\text{Green}}(i,j)$ Spin-flip excitations between α spin orbital i and β spin orbital j.

$j_{\text{Green,MO}}^{\sigma}(i)$ Occupied σ spin orbital contribution.

$j_{\text{Green,MO(virt)}}^{\sigma}(i)$ Virtual σ spin orbital contribution.

R_i Bond length of bond i.

$\nu(\mathbf{r})$ External potential (as for example originating from the arrangement of nuclei).

η Global hardness.

IE Ionization energy.

EA Electron affinity.

y Diradical character.

n_i Occupation number of orbital i.

F. List of Abbreviations

ANPA	Acenaphthalene
ANPY	Acenaphthylene
BS	Broken Symmetry
BTF	perfluorated benzothiophene dithienyl switch
BTH	benzothiophene dithienyl switch
Cc	Cobaltocene
DFT	Density functional theory
DTE	Dithienyl ethene
EA	Electron affinity
GGA	Generalized-gradient approximation
HDvV	Heisenberg–Dirac–van Vleck
HOMO	Highest occupied molecular orbital
HF	Hartree–Fock
IE	Ionization energy
KS	Kohn Sham
LDA	Local density approximation
LSD	Local-spin density
LUMO	Lowest unoccupied molecular orbital
MAPE	Mean average percentage error
MO	Molecular orbital
MP2	Møller-Plesset perturbation theory of second order
NNO	Nitronyl nitroxide

NP	Naphthalene
PES	Potential energy surface
RKKY	Ruderman-Kittel-Kasuya-Yoshida
SFB	Sonderforschungsbereich
SQ	Semiquinone
SQ(Zn)	Semiquinone complex
STM	Scanning tunneling microscopy
TDDFT	Time-Dependent Density Functional Theory
TF	perfluorinated dithienylethene switch
TH	dithienylethene switch

G. List of Publications Originated From this Work

1. T. Steenbock, D. A. Shultz, M. L. Kirk, C. Herrmann, *The influence of radical bridges on electron spin coupling*, **2016**, *accepted in J. Chem. Phys. A*.

2. A. Escribano, T. Steenbock, C. Stork, C. Herrmann, J. Heck, *Why are dithienylethene-linked biscobaltocenes so hard to photoswitch?*, **2016**, *accepted in Chem. Phys. Chem.*.

3. T. Steenbock, A. Escribano, J. Heck, C. Herrmann, J. Heck *Photoswitching Behavior of a Cyclohexene-Bridged versus a Cyclopentene-Bridged Dithienylethene System*, **2015**, Chem. Phys. Chem., *16*, 1491–1501.

4. T. Steenbock, J. Tasche, A. I. Lichtenstein, C. Herrmann, *A Green's-Function Approach to Exchange Spin Coupling As a New Tool for Quantum Chemistry*, **2015**, J. Chem. Theory Comput., *11*, 5651–5664.

5. A. Escribano, T. Steenbock, C. Herrmann, J. Heck, *Limits of Molecular Dithienylethene Switches Caused by Ferrocenyl Substitution*, **2016**, Chem. Phys. Chem., *17*, 1881–1894.

H. List of Chemicals

No hazardous compounds according to the GHS (Globally Harmonized System of Classification and Labeling of Chemicals) regulation have been used within the scope of this thesis.

I. Declaration on Oath

I hereby declare, on oath, that I have written the present dissertation by my own and have not used other than the acknowledged resources and aids. I hereby declare that I have not previously applied of pursued for a doctorate (Ph.D. studies).

	09/02/2016
Torben Steenbock	Date

Bibliography

[1] C. Chappert, A. Fert, F. N. V. Dau, *Nat. Mater.* **2007,** *6,* 813–823.

[2] L. Bogani, W. Wernsdorfer, *Nat. Mater.* **2008,** *7,* 1476–1122.

[3] A. A. Khajetoorians, J. Wiebe, B. Chilian, R. Wiesendanger, *Nature* **2011,** *332,* 1062–1064.

[4] F. Troiani, A. Ghirri, M. Affronte, S. Carretta, P. Santini, G. Amoretti, S. Piligkos, G. Timco, R. E. P. Winpenny, *Phys. Rev. Lett.* **2005,** *94,* 207208.

[5] K. Matsuda, M. Irie, *J. Am. Chem. Soc.* **2001,** *123,* 9896–9897.

[6] N. Lorente, C. Joachim, *Architecture and Design of Molecule Logic Gates and Atom Circuits;* Springer: Heidelberg, 2013.

[7] G. Moore, *Electronics* **1965,** *38,* 114–117.

[8] M. Waldrop, *Nature* **2016,** *530,* 144–147.

[9] D. Molka, D. Hackenberg, R. Schone, M. S. Muller, Memory Performance and Cache Coherency Effects on an Intel Nehalem Multiprocessor System. In *Parallel Architectures and Compilation Techniques, 2009. PACT '09. 18th International Conference on*; 2009.

[10] P. Gütlich, A. Hauser, H. Spiering, *Angew. Chem. Int. Ed.* **1994,** *33,* 2024–2054.

[11] J. A. Real, A. B. Gaspar, M. C. Muñoz, *Dalton Trans.* **2005,** 2062–2079.

[12] M. Mannini, *et al. Nat. Mater.* **2009,** *8,* 194–197.

[13] M. Bazarnik, B. Bugenhagen, M. Elsebach, E. Sierda, A. Frank, M. H. Prosenc, R. Wiesendanger, *Nano Lett.* **2016,** *16,* 577–582.

[14] A. J. Heinrich, J. A. Gupta, C. P. Lutz, D. M. Eigler, *Science* **2004,** *306,* 466–469.

[15] T. Balashov, T. Schuh, A. F. Takács, A. Ernst, S. Ostanin, J. Henk, I. Mertig, P. Bruno, T. Miyamachi, S. Suga, W. Wulfhekel, *Phys. Rev. Lett.* **2009,** *102,* 257203.

[16] A. A. Khajetoorians, T. Schlenk, B. Schweflinghaus, M. dos Santos Dias, M. Steinbrecher, M. Bouhassoune, S. Lounis, J. Wiebe, R. Wiesendanger, *Phys. Rev. Lett.* **2013,** *111,* 157204.

[17] Q. Dubout, F. Donati, C. Wäckerlin, F. Calleja, M. Etzkorn, A. Lehnert, L. Claude, P. Gambardella, H. Brune, *Phys. Rev. Lett.* **2015,** *114,* 106807.

[18] C. F. Hirjibehedin, C.-Y. Lin, A. F. Otte, M. Ternes, C. P. Lutz, B. A. Jones, A. J. Heinrich, *Science* **2007,** *317,* 1199–1203.

[19] J. S. Miller, *Inorg. Chem.* **2000,** *39,* 4392–4408.

[20] A. DiLullo, S.-H. Chang, N. Baadji, K. Clark, J.-P. Klckner, M.-H. Prosenc, S. Sanvito, R. Wiesendanger, G. Hoffmann, S.-W. Hla, *Nano Lett.* **2012,** *12,* 3174–3179.

[21] B. Lazarovits, L. Szunyogh, P. Weinberger, *Phys. Rev. B* **2002,** *65,* 104441.

[22] B. Lazarovits, L. Szunyogh, P. Weinberger, B. Újfalussy, *Phys. Rev. B* **2003,** *68,* 024433.

[23] R. itko, T. Pruschke, *New J. Phys.* **2010,** *12,* 063040.

[24] L. Noodleman, *J. Chem. Phys.* **1981,** *74,* 5737–5743.

[25] K. Matsuda, M. Irie, *J. Am. Chem. Soc.* **2000,** *122,* 7195–7201.

[26] A. Bousseksou, G. Molnr, G. Matouzenko, *Eur. J. Inorg. Chem.* **2004,** *2004,* 4353–4369.

[27] S. Ohkoshi, K. Imoto, Y. Tsunobuchi, S. Takano, H. Tokoro, *Nat. Chem.* **2011,** *3,* 564–569.

[28] N. Baadji, M. Piancenza, T. Tugsuz, F. D. Sala, G. Maruccio, S. Sanvito, *Nat. Mater.* **2009,** *8,* 813–817.

[29] M. F. Islam, J. F. Nossa, C. M. Canali, M. Pederson, *Phys. Rev. B* **2010,** *82,* 155446.

[30] M. Chattopadhyaya, M. M. Alam, S. Sen, S. Chakrabarti, *Phys. Rev. Lett.* **2012,** *109,* 257204.

[31] X. Zhang, T. Palamarciuc, J.-F. Letard, P. Rosa, E. V. Lozada, F. Torres, L. G. Rosa, B. Doudin, P. A. Dowben, *Chem. Commun.* **2014,** *50,* 2255–2257.

[32] A. I. Liechtenstein, M. I. Katsnelson, V. A. Gubanov, *J. Magn. Magn. Mater.* **1987,** *67,* 65–74.

[33] T. Steenbock, *Implementation and chemical evaluation of a Green's function based approach to Heisenberg exchange coupling constants;* Master's thesis: University of Hamburg, 2013.

[34] C. Herrmann, L. Groß, T. Steenbock, M. Deffner, B. A. Voigt, G. C. Solomon, "ARTAIOS – a transport code for postprocessing quantum chemical electronic structure calculations, available from `https://www.chemie.uni-hamburg.de/ac/herrmann/software/index.html`", 2016.

[35] T. Steenbock, *Einfluss von radikalischen Brücken auf Spinkopplung: Eine dichtefunktionaltheoretische Studie;* Bachelor's thesis: University of Hamburg, 2011.

[36] S. Blundell, *Magnetism in Condensed Matter;* Oxford University Press: Oxford, 2001.

[37] Z. Sun, Z. Zeng, J. Wu, *Acc. Chem. Res.* **2014,** *47,* 2582–2591.

[38] R. G. Parr, W. Yang, *Density-Functional Theory of Atoms and Molecules;* Oxford University Press: New York, 1989.

[39] C. J. Cramer, D. G. Truhlar, *Phys. Chem. Chem. Phys.* **2009,** *11,* 10757–10816.

[40] P. A. M. Dirac, *Math. Proc. Cambridge* **1930,** *26,* 376–385.

[41] A. Becke, *Phys. Rev. A* **1988,** *38,* 3098.

[42] C. Jacob, M. Reiher, *Int. J. Quantum Chem.* **2012,** *112,* 3661–3684.

[43] D. C. Langreth, M. J. Mehl, *Phys. Rev. B* **1983,** *28,* 1809–1834.

[44] J. Tao, J. Perdew, V. Staroverov, G. Scuseria, *Phys. Rev. Lett.* **2003,** *91,* 146401.

[45] A. Becke, *J. Chem. Phys.* **1993,** *98,* 5648.

[46] R. Baer, E. Livshits, U. Salzner, *Ann. Rev. Phys. Chem.* **2010,** *61,* 85–109.

[47] T. Schwabe, S. Grimme, *Phys. Chem. Chem. Phys.* **2007,** *9,* 3397–3406.

[48] P. W. Anderson, *Solid State Phys.* **1963,** *14,* 1963.

[49] A. I. Liechtenstein, M. I. Katsnelson, V. Gubanov, *J. Phys. F* **1984,** *14,* L125–L128.

[50] V. Antropov, M. Katsnelson, B. Harmon, M. van Schilfgaarde, D. Kusnezov, *Phys. Rev. B* **1996,** *54,* 1019–1023.

[51] J. P. Perdew, A. Savin, K. Burke, *Phys. Rev. A* **1995,** *51,* 4531–4541.

[52] D. C. Langreth, J. P. Perdew, *Phys. Rev. B* **1977,** *21,* 5469.

[53] O. Gunnarsson, B. I. Lundqvist, *Phys. Rev. B* **1976,** *13,* 4274–4298.

[54] D. C. Langreth, J. P. Perdew, *Solid State Commun.* **1975,** *17,* 1425.

[55] E. Ruiz, A. Rodriguez-Fortea, J. Cano, S. Alvarez, P. Alemany, *J. Comput. Chem.* **2003,** *24,* 982–989.

[56] P.-O. Löwdin, *J. Chem. Phys.* **1950,** *18,* 365.

[57] R. S. Mulliken, *J. Chem. Phys.* **1955,** *23,* 1833.

[58] C. Herrmann, M. Reiher, B. A. Hess, *J. Chem. Phys.* **2005,** *122,* 034102.

[59] A. Szabo, N. S. Ostlund, *Modern Quantum Chemistry;* Dover Publications Inc.: Mineola, New York, 1996.

[60] A. Minsky, A. Y. Meyer, M. Rabinovitz, *Tetrahedron* **1985,** *41,* 785–791.

[61] O. Sinanoğlu, *Tetrahedron Lett.* **1988,** *29,* 889–892.

[62] C. H. Choi, M. Kertesz, *J. Chem. Phys.* **1998,** *108,* 6681–6688.

[63] R. G. Parr, W. Yang, *J. Am. Chem. Soc.* **1984,** *106,* 4049–4050.

[64] K. Fukui, T. Yonezawa, H. Shingu, *J. Chem. Phys.* **1952,** *20,* 722–725.

[65] P. Fowler, *Nature* **1991,** *350,* 20–21.

[66] J.-i. Aihara, *J. Phys. Chem. A* **1999,** *103,* 7487–7495.

[67] J.-i. Aihara, *Phys. Chem. Chem. Phys.* **1999,** *1,* 3193–3197.

[68] P. W. Ayers, M. Levy, *Theor. Chem. Acc.* **2000,** *103,* 353–360.

[69] H. Jiao, P. v. R. Schleyer, *J. Am. Chem. Soc.* **1995,** *117,* 11529–11535.

[70] P. v. R. Schleyer, C. Maerker, A. Dransfeld, H. Jiao, N. J. v. E. Hommes, *J. Am. Chem. Soc.* **1996,** *118,* 6317–6318.

[71] W. Flygare, *Chem. Rev.* **1974,** *74,* 653–687.

[72] D. Sutter, W. Flygare, *Struc. Bond.* **1976,** 89–196.

[73] H. J. Dauben Jr, J. D. Wilson, J. L. Laity, *J. Am. Chem. Soc.* **1968,** *90,* 811–813.

[74] J. L. Brdas, *J. Chem. Phys.* **1985,** *82,*.

[75] M. Glukhovtsev, *J. Chem. Educ* **1997,** *74,* 132.

[76] L. Nyulászi, P. v. R. Schleyer, *J. Am. Chem. Soc.* **1999,** *121,* 6872–6875.

[77] M. K. Cyraski, T. M. Krygowski, A. R. Katritzky, P. von Ragu Schleyer, *J. Org. Chem.* **2002,** *67,* 1333–1338.

[78] C. S. Wannere, K. W. Sattelmeyer, H. F. Schaefer, P. v. R. Schleyer, *Angew. Chem.* **2004,** *116,* 4296–4302.

[79] C. P. Frizzo, M. A. P. Martins, *Struct. Chem.* **2012,** *23,* 375–380.

[80] F. D. Proft, P. Geerlings, *Chem. Rev.* **2001,** *101,* 1451–1464.

[81] R. G. Parr, R. A. Donnelly, M. Levy, W. E. Palke, *J. Chem. Phys.* **1978,** *68,* 3801–3807.

[82] R. G. Pearson, *J. Am. Chem. Soc.* **1963,** *85,* 3533-3539.

[83] R. G. Pearson, (Ed.), *Hard and Soft Acids and Bases;* Dowden, Hutchinson & Ross: Stroudsburg, PA, 1973.

[84] R. G. Pearson, *Coord. Chem. Rev.* **1990,** *100,* 403-425.

[85] D. Jacquemin, B. Champagne, J.-M. Andr, *Int. J. Quantum Chem.* **1997,** *65,* 679–688.

[86] Y. Jung, M. Head-Gordon, *J. Phys. Chem. A* **2003,** *107,* 7475–7481.

[87] Z. Chen, D.-e. Jiang, X. Lu, H. F. Bettinger, S. Dai, P. v. R. Schleyer, K. N. Houk, *Org. Lett.* **2007,** *9,* 5449–5452.

[88] M. Nakano, S. Ohta, K. Tokushima, R. Kishi, T. Kubo, K. Kamada, K. Ohta, B. Champagne, E. Botek, H. Takahashi, *Chem. Phys. Lett.* **2007,** *443,* 95–101.

[89] A. Ueda, S. Nishida, K. Fukui, T. Ise, D. Shiomi, K. Sato, T. Takui, K. Nakasuji, Y. Morita, *Angew. Chem. Int. Ed.* **2010,** *49,* 1678–1682.

[90] H. Fukui, S. Takamuku, T. Yamada, K. Fukuda, T. Takebayashi, Y. Shigeta, R. Kishi, B. Champagne, M. Nakano, *Inorg. Chem.* **2014,** *53,* 8700–8707.

[91] V. Bachler, G. Olbrich, F. Neese, K. Wieghardt, *Inorg. Chem.* **2002,** *41,* 4179–4193.

[92] D. Herebian, K. Wieghardt, F. Neese, *J. Am. Chem. Soc.* **2003,** *125,* 10997–11005.

[93] E. Ramos-Cordoba, P. Salvador, *Phys. Chem. Chem. Phys.* **2014,** *16,* 9565–9571.

[94] K. Kamada, K. Ohta, A. Shimizu, T. Kubo, R. Kishi, H. Takahashi, E. Botek, B. Champagne, M. Nakano, *J. Phys. Chem. Lett.* **2010,** *1,* 937–940.

[95] P. J. Hay, J. C. Thibeault, R. Hoffmann, *J. Am. Chem. Soc.* **1975,** *97,* 4884–4889.

[96] R. A. Layfield, *Organometallics* **2014,** *33,* 1084–1099.

[97] W. C. Lineberger, W. T. Borden, *Phys. Chem. Chem. Phys.* **2011,** *13,* 11792–11813.

[98] P. W. Anderson, *Phys. Rev.* **1950,** *72,* 350–356.

[99] P. W. Anderson, *Phys. Rev.* **1959,** *115,* 2–13.

[100] J. Lee, E. Lee, S. Kim, G. S. Bang, D. A. Shultz, R. D. Schmidt, M. D. E. Forbes, H. Lee, *Angew. Chem. Int. Ed.* **2011,** *50,* 4414–4418.

[101] A. Pronschinske, Y. Chen, G. F. Lewis, D. A. Shultz, A. Calzolari, M. B. Nardelli, D. B. Dougherty, *Nano Lett.* **2013,** *13,* 1429–1434.

[102] C. Herrmann, L. Yu, M. Reiher, *J. Comp. Chem.* **2006,** *27,* 1223–1239.

[103] J. L. Fillol, Z. Condola, I. Garcia-Bosch, L. Gomez, J. J. Pla, M. Costas, *Nat. Chem.* **2011,** *3,* 807–813.

[104] S. Biswas, A. Dutta, M. Dolai, I. Bhowmik, M. Rouzieres, H. M. Lee, R. Clerac, M. Ali, *Eur. J. Inorg. Chem.* **2013,** *2013,* 4922–4930.

[105] P. Bruijnincx, I. Buurmans, Y. Huang, G. Juhasz, M. Viciano-Chumillas, M. Quesada, J. Reedjik, M. Lutz, A. Spek, E. Münck, E. L. Bominaar, R. K. Gebbink, *Inorg. Chem.* **2011,** *2011,* 9243–9255.

[106] C. Herrmann, J. Elmisz, *Chem. Commun.* **2013,** *49,* 10435.

[107] J. Proppe, C. Herrmann, *J. Comput. Chem.* **2015,** *36,* 201–209.

[108] M. L. Kirk, D. A. Shultz, E. C. Depperman, C. L. Brannen, *J. Am. Chem. Soc.* **2007,** *129,* 1937–1943.

[109] D. Feng, C. Wang, W. Cheng, G. Li, S. Tian, F. Liao, X. Ming, J. Lin, *Solid State Sci.* **2003,** *11,* 845–851.

[110] M. S. E. Fallah, R. Vincente, A. Escuer, F. Badyine, X. Solans, M. Font-Bardia, *Inorg. Chim. Acta* **2008,** *361,* 4065–4069.

[111] S. Trtica, M. H. Prosenc, M. Schmidt, J. Heck, O. Albrecht, D. Goerlitz, F. Reuter, E. Rentschler, *Inorg. Chem.* **2010,** *49,* 1667–1673.

[112] H. R., Khavasi, V. Amani, N. Safari, A. Abedi, *Dalton Trans.* **2011,** *40,* 6877–6885.

[113] F. A. Mautner, M. Navarro, S. Speed, M. S. E. Fallah, M. Font-Bardia, R. Vicente, *Polyhedron* **2013,** *52,* 866–871.

[114] W. A. Gobeze, V. A. Milway, N. F. Chilton, B. Moubaraki, K. S. Murray, S. Brooker, *Eur. J. Inorg. Chem.* **2013,** 1–15.

[115] K. Chlopek, N. Muresan, F. Neese, K. Wieghardt, *J. Eur. Chem.* **2007,** *13,* 8390–8403.

[116] D. Pantazis, V. Krewald, M. Orio, F. Neese, *Dalton Trans.* **2010,** *39,* 4959–4967.

[117] D. P. Bhave, W.-G. Han, S. Pazicni, J. E. Penner-Hahn, K. S. Carroll, L. Noodleman, *Inorg. Chem.* **2011,** *50,* 6610–6625.

[118] K. D. Vogiatzis, W. Klopper, A. Mavrandonakis, K. Fink, *Chem. Phys. Chem.* **2011,** *12,* 3307–3319.

[119] C. Jacob, M. Reiher, *Int. J. Quantum Chem.* **2012,** *112,* 3661–3684.

[120] T. Ozaki, *et al.* "OpenMx: Open source package for Material EXplorer", 2013, http://www.openmx-square.org/.

[121] M. Han, T. Ozaki, J. Yu, *Phys. Rev. B* **2004,** *70,* 184421.

[122] T. C. Brunhold, D. R. Gamelin, E. I. Solomon, *J. Am. Chem. Soc.* **2000,** *122,* 8511–8523.

[123] J. E. Peralta, V. Barone, *J. Chem. Phys.* **2008,** *129,* 194107.

[124] J. J. Philips, J. E. Peralta, *J. Chem. Phys.* **2013,** *138,* 174115.

[125] S. Bornemann, O. Slpr, S. Mankovsky, S. Polesya, J. Staunton, W. Wurth, H. E. A. J. Minar, *Phys. Rev. B* **2012,** *86,* 104436.

[126] H. Ebert, D. Ködderitzsch, J. Minar, *Rep. Prog. Phys.* **2011,** *74,* 096501.

[127] M. J. Han, T. Ozaki, J. Yu, *Phys. Rev. B* **2007,** *75,* 060404.

[128] T. Yildirim, *Phys. C* **2009,** *469,* 425–441.

[129] S. Polesya, S. Mankovsky, O. Sipr, W. Meindl, C. Strunk, H. Ebert, *Phys. Rev. B* **2010,** *82,* 214409.

[130] H. Purdum, P. A. Montano, G. K. Shenoy, T. Morrison, *Phys. Rev. B* **2009,** *25,* 4412–4417.

[131] A. E. Clark, E. R. Davidson, *Int. J. Quantum Chem.* **2003,** *93,* 384–394.

[132] T. R. Felthouse, D. N. Hendrickson, *Inorg. Chem.* **1978,** *17,* 2636–2648.

[133] J. Glerup, P. A. Goodson, D. J. Hodgson, K. Michelsen, *Inorg. Chem.* **1995,** *34,* 6255–6264.

[134] M. Bnard, J. F. Berry, F. A. Cotton, C. Gaudin, X. Lpez, C. A. Murillo, M.-M. Rohmer, *Inorg. Chem.* **2006,** *45,* 3932–3940.

[135] J. Tercero, E. Ruiz, S. Alvarez, A. Rodriguez-Fortea, P. Alemany, *J. Mater. Chem.* **2006,** *16,* 2729–2735.

[136] N. Pagels, O. Albrecht, D. Görlitz, A. Rogachev, M. Prosenc, J. Heck, *Chem. Eur. J.* **2011,** *17,* 4166–4176.

[137] S. Puhl, R. Harms, J. Heck, *in preparation* .

[138] S. L. Lambert, D. N. Hendrickson, *Inorg. Chem.* **1979,** *18,* 2683–2686.

[139] J. Y. Yang, M. P. Shores, J. J. Sokol, J. R. Long, *Inorg. Chem.* **2003,** *42,* 1403–1419.

[140] S. Schwalbe, K. Trepte, G. Seifert, J. Kortus, *Phys. Chem. Chem. Phys.* **2016,** *18,* 8075–8080.

[141] S. Puhl, T. Steenbock, C. Herrmann, J. Heck, *in preparation* .

[142] SFB668, *unpublished results* .

[143] H. A. Kramer, *Physica I* **1934,** 182.

[144] P. W. Anderson, *Phys. Rev.* **1950,** *79,* 350.

[145] J. B. Goodenough, *Phys. Rev.* **1955,** *100,* 564.

[146] J. B. Goodenough, *J. Phys. Chem. Solids* **1958,** *6,* 287.

[147] J. Kanamori, *J. Phys. Chem. Solids* **1959,** *10,* 87.

[148] A. P. Ginsberg, *Inorg. Chim. Acta Rev.* **1971,** *5,* 45–68.

[149] F. Neese, *J. Phys. Chem. Solids* **2004,** *65,* 781–785.

[150] R. S. Mulliken, *J. Chim. Phys.* **1949,** *46,* 497.

[151] C. Adamo, V. Barone, R. Subra, *Theor. Chem. Acc.* **2000,** *104,* 207–209.

[152] V. Antropov, M. Katsnelson, A. Liechtenstein, *Phys. B* **1997,** *237-238,* 336–340.

[153] D. Bovi, L. Guidoni, *J. Chem. Phys.* **2012,** *137,* 114107.

[154] J. I. Melo, J. J. Philips, J. E. Peralta, *Chem. Phys. Lett.* **2013,** *557,* 110–113.

[155] Y. Sun, M. Melchior, D. A. Summers, R. C. Thompson, S. J. Rettig, C. Orvig, *Inorg. Chem.* **1998,** *37,* 3119–3121.

[156] L. Groß, T. Steenbock, C. Herrmann, *Mol. Phys.* **2013,** *111,* 1482–1491.

[157] W. Crawford, H. Richardson, J. Wasson, D. Hodgson, W. Hatfield, *Inorg. Chem.* **1976,** *15,* 2107–2110.

[158] J. Glerup, D. Hodgson, E. Petersen, *Acta Chem. Scand. Ser. A* **1983,** *A37,* 161–164.

[159] R. Mukherjee, T. Stack, R. Holm, *J. Am. Chem. Soc.* **1988,** *110,* 1850–1861.

[160] B. L. Guennic, N. Ferré, *Curr. Inorg. Chem.* **2014,** *3,* 235.

[161] D. Pantazis, V. Krewald, M. Orio, F. Neese, *Dalton Trans.* **2010,** *39,* 4959–4967.

[162] E. Coulaud, J.-P. Malrieu, N. Guihéry, N. Ferré, *J. Chem. Theory Comput.* **2013,** *9,* 3429.

[163] T. Steenbock, J. Tasche, A. I. Lichtenstein, C. Herrmann, *J. Chem. Theory Comput.* **2015,** *11,* 5651–5664.

[164] Y. N. Molin, K. M. Salikhov, K. Zamarev, *Spin Exchange. Principles and Applications in Chemistry and Biology;* Springer: Heidelberg, 1980.

[165] A. H. Goldberg, D. A. Dougherty, *J. Am. Chem. Soc.* **1983,** *105,* 284–290.

[166] H. Atzkern, P. Bergerat, H. Beruda, M. Fritz, J. Hiermeier, P. Hudeczak, O. Kahn, F. H. Köhler, M. Paul, B. Weber, *J. Am. Chem. Soc.* **1995,** *117,* 997–1011.

[167] D. N. Beratan, J. N. Onuchic, J. Hopfield, *J. Chem. Phys.* **1987,** *86,* 4488–4498.

[168] D. N. Beratan, J. N. Onuchic, J. N. Betts, B. E. Bowler, H. B. Gray, *J. Am. Chem. Soc.* **1990,** *112,* 7915–7921.

[169] M. A. Ratner, *J. Phys. Chem.* **1990,** *94,* 4877–4883.

[170] D. N. Beratan, J. N. Betts, J. N. Onuchic, *Science* **1991,** *252,* 1285–1288.

[171] D. N. Beratan, J. N. Betts, J. N. Onuchic, *J. Phys. Chem.* **1992,** *96,* 2852–2855.

[172] M. Bühl*, H. Kabrede, *J. Chem. Theory Comput.* **2006,** *2,* 1282–1290.

[173] M. P. Waller, H. Braun, N. Hojdis, M. Bühl, *J. Chem. Theory Comput.* **2007,** *3,* 2234–2242.

[174] M. Bühl, C. Reimann, D. A. Pantazis, T. Bredow, F. Neese, *J. Chem. Theory and Comput.* **2008,** *4,* 1449–1459.

[175] M. Orio, D. A. Pantazis, F. Neese, *Photosynth. Res.* **2009,** *102,* 443–453.

[176] D. E. Ferreira, W. B. De Almeida, A. Neves, W. R. Rocha, *Comp. Theor. Chem.* **2012,** *979,* 89–95.

[177] M. A. Sainna, D. Sil, D. Sahoo, B. Martin, S. P. Rath, P. Comba, S. P. de Visser, *Inorg. Chem.* **2015,** *54,* 1919-1930.

[178] K. P. Kepp, *Inorg. Chem.* **2016,** *55,* 2717–2727.

[179] S. Trtica, E. Meyer, M. H. Prosenc, J. Heck, T. Bhnert, D. Grlitz, *Eur. J. Inorg. Chem.* **2012,** *2012,* 4486–4493.

[180] T. Steenbock, A. Escribano, J. Heck, C. Herrmann, *Chem. Phys. Chem.* **2015,** *16,* 1491–1501.

[181] H. Tian, S. Wang, *Chem. Commun.* **2007,** 781–792.

[182] M. Irie, *Chem. Rev.* **2000,** *100,* 1685–1716.

[183] P. A. Liddell, G. Kodis, A. L. Moore, T. A. Moore, D. Gust, *J. Am. Chem. Soc.* **2002,** *124,* 7668–7669.

[184] A. C. Whalley, M. L. Steigerwald, X. Guo, C. Nuckolls, *J. Am. Chem. Soc.* **2007,** *129,* 12590–12591.

[185] E. V. Brown, G. R. Granneman, *J. Am. Chem. Soc.* **1975,** *97,* 621–627.

[186] D. T.-L. Chen, H. Morawetz, *Macromolecules* **1976,** *9,* 463–468.

[187] D. K. Joshi, M. J. Mitchell, D. Bruce, A. J. Lough, H. Yan, *Tetrahedron* **2012,** *68,* 8670–8676.

[188] I. V. Zavarzin, N. G. Smirnova, V. N. Yarovenko, M. M. Krayushkin, *Russ. Chem. B.* **2004,** *53,* 1353–1354.

[189] A. A. Shimkin, V. Z. Shirinian, D. M. Nikalin, M. M. Krayushkin, T. S. Pivina, N. A. Troitsky, L. G. Vorontsova, Z. A. Starikova, *Eur. J. Org. Chem.* **2006,** *2006,* 2087–2092.

[190] V. Z. Shirinian, S. O. Besugliy, A. V. Metelitsa, M. M. Krayushkin, D. M. Nikalin, V. I. Minkin, *Photochem. Photobiol. A: Chem.* **2007,** *189,* 161–166.

[191] B. L. Feringa, *Molecular Switches;* Wiley-VCH Verlag GmbH: Weinheim, 2001.

[192] T. B. Norsten, N. R. Branda, *J. Am. Chem. Soc.* **2001,** *123,* 1784–1785.

[193] H.-L. Wong, W.-T. Wong, V. W.-W. Yam, *Org. Lett.* **2012,** *14,* 1862–1865.

[194] C. Li, W.-L. Gong, Z. Hu, M. P. Aldred, G.-F. Zhang, T. Chen, Z.-L. Huang, M.-Q. Zhu, *RCS Ad.* **2013,** *3,* 8967–8972.

[195] C. Li, H. Yan, L.-X. Zhao, G.-F. Zhang, Z. Hu, Z.-L. Huang, M.-Q. Zhu, *Nat. Commun.* **2014,** *5,*.

[196] K. Sumi, T. Kaburagi, M. Morimoto, K. Une, H. Sotome, S. Ito, H. Miyasaka, M. Irie, *Org. Lett.* **2015,** *17,* 4802–4805.

[197] D. Sud, T. B. Norsten, N. R. Branda, *Angew. Chem.* **2005,** *117,* 2055–2057.

[198] Y. Wei, S. Han, J. Kim, S. Soh, B. A. Grzybowski, *J. Am. Chem. Soc.* **2010,** *132,* 11018–11020.

[199] B. M. Neilson, C. W. Bielawski, *J. Am. Chem. Soc.* **2012,** *134,* 12693–12699.

[200] H. Iida, N. Umebayashi, E. Yashima, *Tetrahedron* **2013,** *69,* 11064–11069.

[201] J. Park, D. Feng, S. Yuan, H.-C. Zhou, *Angew. Chem. Int. Ed.* **2015,** *54,* 430–435.

[202] V. Guerchais, L. Ordronneau, H. Le Bozec, *Coord. Chem. Rev.* **2010,** *254,* 2533–2545.

[203] C.-G. Liu, Z.-M. Su, X.-H. Guan, S. Muhammad, *J. Phys. Chem. C* **2011,** *115,* 23946–23954.

[204] L. Ordronneau, H. Nitadori, I. Ledoux, A. Singh, J. A. G. Williams, M. Akita, V. Guerchais, H. L. Bozec, *Inorg. Chem.* **2012,** *51,* 5627–5636.

[205] M.-Y. Zhang, C.-H. Wang, W.-Y. Wang, N.-N. Ma, S.-L. Sun, Y.-Q. Qiu, *J. Phys. Chem. A* **2013,** *117,* 12497–12510.

[206] J. Boixel, V. Guerchais, H. L. Bozec, D. Jacquemin, A. Amar, A. Boucekkine, A. Colombo, C. Dragonetti, D. Marinotto, D. Roberto, S. Righetto, R. D. Angelis, *J. Am. Chem. Soc.* **2014,** *136,* 5367–5375.

[207] K. J. Chen, A. D. Laurent, D. Jacquemin, *J. Phys. Chem. C* **2014,** *118,* 4334–4345.

[208] N. Katsonis, T. Kudernac, M. Walko, S. J. van der Molen, B. J. van Wees, B. L. Feringa, *Adv. Mater.* **2006,** *18,* 1397–1400.

[209] K. Matsuda, H. Yamaguchi, T. Sakano, M. Ikeda, N. Tanifuji, M. Irie, *J. Chem. Phys. C* **2008,** *112,* 17005–17010.

[210] K. Matsuda, *Pure Appl. Chem.* **2008,** *80,* 555–561.

[211] T. Kudernac, N. Katsonis, W. R. Brown, B. L. Feringa, *J. Mater. Chem.* **2009,** *19,* 7168–7177.

[212] C. P. Harvey, J. D. Tovar, *Polym. Chem.* **2011,** *2,* 2699–2706.

[213] C.-T. Poon, W. H. Lam, H.-L. Wong, V. W.-W. Yam, *J. Am. Chem. Soc.* **2010,** *132,* 13992–13993.

[214] A. Perrier, F. Maurel, J. Aubard, *J. Photochem. Photobiol. A* **2007,** *189,* 167 - 176.

[215] K. A. Belfon, J. D. Gough, *Chem. Phys. Lett.* **2013,** *585,* 63–68.

[216] A. Fihey, F. Maurel, A. Perrier, *Phys. Chem. Chem. Phys.* **2014,** *16,* 26240–26251.

[217] A. Staykov, K. Yoshizawa, *J. Phys. Chem. C* **2009,** *113,* 3826–3834.

[218] D. Guillaumont, T. Kobayashi, K. Kanda, H. Miyasaka, K. Uchida, S. Kobatake, K. Shibata, S. Nakamura, M. Irie, *J. Phys. Chem. A* **2002,** *106,* 7222–7227.

[219] M. N. Roberts, J. K. Nagle, J. G. Finden, N. R. Branda, M. O. Wolf, *Inorg. Chem.* **2009,** *48,* 19–21.

[220] M. T. Indelli, S. Carli, M. Ghirotti, C. Chiorboli, M. Ravaglia, M. Garavelli, F. Scandola, *J. Am. Chem. Soc.* **2008,** *130,* 7286–7299.

[221] A. E. Sanvicente, *1,2-Diarylethene molecular switches connecting cobalt and iron metallocenes;* University of Hamburg: Hamburg, 2015.

[222] A. Escribano, T. Steenbock, C. Herrmann, J. Heck, *Chem. Phys. Chem.* **2016,** *17,* 1881–1894.

[223] G. Guirado, C. Coudret, J.-P. Launay, *J. Phys. Chem. C* **2007,** *111,* 2770–2776.

[224] M. Reiher, O. Salomon, B. A. Hess, *Theor. Chem. Acc.* **2001,** *107,* 48–55.

[225] R. B. Woodward, R. Hoffmann, *J. Am. Chem. Soc.* **1965,** *87,* 395–397.

[226] H. C. Longuet-Higgins, E. W. Abrahamson, *J. Am. Chem. Soc.* **1965,** *87,* 2045–2046.

[227] R. B. Woodward, R. Hoffmann, *Angew. Chem. Int. Ed.* **1969,** *8,* 781–853.

[228] P. Geerlings, P. W. Ayers, A. Toro-Labb, P. K. Chattaraj, F. D. Proft, *Acc. Chem. Res.* **2012,** *45,* 683–695.

[229] S. Nakamura, M. Irie, *J. Org. Chem.* **1988,** *53,* 6136–6138.

[230] N. J. Turro, *Modern Molecular Photochemistry;* University Science Books: Sausalito, 1991.

[231] J. P. Perdew, *Phys. Rev. B* **1986,** *34,* 7406–7406.

[232] K. Kim, K. D. Jordan, *J. Phys. Chem.* **1994,** *98,* 10089–10094.

[233] P. J. Stephens, F. J. Devlin, C. F. Chabalowski, M. J. Frisch, *J. Phys. Chem.* **1994,** *98,* 11623–11627.

[234] A. Schfer, H. Horn, R. Ahlrichs, *J. Chem. Phys.* **1992,** *97,* 2571–2577.

[235] A. Schfer, C. Huber, R. Ahlrichs, *J. Chem. Phys.* **1994,** *100,* 5829–5835.

[236] S. Grimme, *J. Comput. Chem.* **2006,** *27,* 1787–1799.

[237] S. Kobatake, K. Uchida, E. Tsuchida, M. Irie, *Chem. Commun.* **2002,** 2804–2805.

[238] L. Lucas, J. Jong, J. Esch, R. Kellogg, B. Feringa, *Eur. J. Org. Chem.* **2003,** *2003,* 155–166.

[239] Y. Asano, A. Murakami, T. Kobayashi, A. Goldberg, D. Guillaumont, S. Yabushita, M. Irie, S. Nakamura, *J. Am. Chem. Soc.* **2004,** *126,* 12112–12120.

[240] M. Öki, *Topics in Stereochemistry, Vol. 14: Recent Advances in Atropisomerism;* (Eds.: N. L. Allinger, E. L. Eliel, S. H. Wilen), Wiley: Hoboken, NJ, 1983.

[241] H. Friebolin, *Ein- und zweidimensionale NMR-Spektroskopie. Eine Einführung;* VCH Verlagsgesellschaft: Weinheim, 1992.

[242] E. Masson, *Org. Biomol. Chem.* **2013,** *11,* 2859–2871.

[243] J. Sancho-Garca, A. Karpfen, *Chem. Phys. Lett.* **2005,** *411,* 321–326.

[244] Y. Tawada, T. Tsuneda, S. Yanagisawa, T. Yanai, K. Hirao, *J. Chem. Phys.* **2004,** *120,* 8425–8433.

[245] M. Kamiya, H. Sekino, T. Tsuneda, K. Hirao, *J. Chem. Phys.* **2005,** *122,* 234111.

[246] B. Kaduk, T. Van Voorhis, *J. Chem. Phys.* **2010,** *133,* 061102.

[247] S. Prager, I. Burghardt, A. Dreuw, *J. Phys. Chem. A* **2014,** *118,* 1339–1349.

[248] S. Grimme, *Wiley Interdisciplinary Reviews: Computational Molecular Science* **2011,** *1,* 211–228.

[249] A. Escribano, T. Steenbock, C. Stork, C. Herrmann, J. Heck, *to be submitted to Chem. Phys. Chem.* .

[250] F. H. Köhler, *Molecules to Materials. Models and Experiments;* (Eds.: J.S. Miller, M. Drillon), 1st Edition, Wiley-VCH GmbH and Co. KGaA: Weinheim, 2001.

[251] I. Gattinger, M. A. Herker, W. Hiller, F. H. Köhler, *Inorg. Chem.* **1999,** *38,* 2359–2368.

[252] O. Kahn, *Molecular Magnetism;* Wiley VCH: New York, 1993.

[253] S. Sanvito, *Chem. Soc. Rev.* **2011,** 3336–3355.

[254] T. Terencio, R. Bastardis, N. Suaud, D. Maynau, J. Bonvoisin, J. P. Malrieu, C. J. Calzado, N. Guihery, *Phys. Chem. Chem. Phys.* **2011,** *13,* 12314–12320.

[255] M. L. Kirk, D. A. Shultz, D. E. Stasiw, G. F. Lewis, G. Wang, C. L. Brannen, R. D. Sommer, P. D. Boyle, *J. Am. Chem. Soc.* **2013,** *135,* 17144–17154.

[256] S. K. Hoffmann, W. Hilczer, J. Goslar, *Applied Magnetic Resonance 7,* 289–321.

[257] R. E. Coffman, G. R. Buettner, *J. Phys. Chem.* **1979,** *83,* 2387–2392.

[258] J. D. Rinehart, M. Fang, W. J. Evans, J. R. Long, *Nat. Chem.* **2011,** *3,* 538–542.

[259] J. D. Rinehart, J. R. Long, *Chem. Sci.* **2011,** *2,* 2078.

[260] J. D. Rinehart, M. Fang, W. J. Evans, J. R. Long, *J. Am. Chem. Soc.* **2011,** *133,* 14236–14239.

[261] S. Demir, I.-R. Jeon, J. R. Long, T. D. Harris, *Coord. Chem. Rev.* **2015,** *289290,* 149–176 Progress in Magnetochemistry.

[262] S. Demir, J. M. Zadrozny, M. Nippe, J. R. Long, *J. Am. Chem. Soc.* **2012,** *134,* 18546–18549.

[263] X. Mei, X. Wang, J. Wang, Y. Ma, L. Li, D. Liao, *New. J. Chem.* **2013,** *37,* 3620–3626.

[264] R. Liu, C. Zhang, L. Li, D. Liao, J.-P. Sutter, *Dalton Trans.* **2012,** *41,* 12139–12144.

[265] I.-R. Jeon, J. G. Park, D. J. Xiao, T. D. Harris, *J. Am. Chem. Soc.* **2013,** *135,* 16845–16848.

[266] P. Dechambenoit, J. R. Long, *Chem. Soc. Rev.* **2011,** *40,* 3249.

[267] Y.-n. Wu, M. Zhou, S. Li, Z. Li, J. Li, B. Wu, G. Li, F. Li, X. Guan, *Small* **2014,** *10,* 2927–2936.

[268] D. J. Tranchemontagne, J. L. Mendoza-Cortes, M. O'Keeffe, O. M. Yaghi, *Chem. Soc. Rev.* **2009,** *38,* 1257–1283.

[269] S. Kaskel, (Ed.), *The Chemistry of Metal-Organic Frameworks: Synthesis, Characterization, and Applications;* Wiley VCH: New York, 2016.

[270] T. B. Faust, D. M. D'Alessandro, *RSC Adv.* **2014,** *4,* 17498.

[271] F. Xu, H. Xu, X. Chen, D. Wu, Y. Wu, H. Liu, C. Gu, R. Fu, D. Jiang, *Angew. Chem. Int. Ed.* **2015,** *54,* 6814–6818.

[272] S. D. J. McKinnon, B. O. Patrick, A. B. P. Lever, R. G. Hicks, *Inorg. Chem.* **2013,** *52,* 8053–8066.

[273] B. Sarkar, S. Patra, J. Fiedler, R. B. Sunoj, D. Janardanan, G. K. Lahiri, W. Kaim, *J. Am. Chem. Soc.* **2008,** *130,* 3532–3542.

[274] E. T. Chernick, Q. Mi, R. F. Kelley, E. A. Weiss, B. A. Jones, T. J. Marks, M. A. Ratner, M. R. Wasielewski, *J. Am. Chem. Soc.* **2006,** *128,* 4356–4364.

[275] E. T. Chernick, Q. Mi, A. M. Vega, J. V. Lockard, M. A. Ratner, M. R. Wasielewski, *J. Phys. Chem. B* **2007,** *111,* 6728–6737.

[276] M. L. Kirk, D. A. Shultz, R. D. Schmidt, D. Habel-Rodriguez, H. Lee, J. Lee, *J. Am. Chem. Soc.* **2009,** *51,* 18304–18313.

[277] M. Reiher, O. Salomon, B. A. Hess, *Theor. Chem. Acc.* **2001,** *107,* 48–55.

[278] J. N. Harvey, *Struc. Bond.* **2004,** *112,* 151–184.

[279] C. Herrmann, G. C. Solomon, M. A. Ratner, *J. Am. Chem. Soc.* **2010,** *132,* 3682–3684.

[280] P. Bertrand, *Chem. Phys. Lett.* **1985,** *113,* 104–107.

[281] T. C. Brunold, D. R. Gamelin, E. I. Solomon, *J. Am. Chem. Soc.* **2000,** *122,* 8511–8523.

[282] F. Neese, *J. Phys. Chem. Sol.* **2004,** *65,* 781-785.

[283] M. L. Kirk, D. A. Shultz, D. E. Stasiw, D. Habel-Rodriguez, B. Stein, P. D. Boyle, *J. Am. Chem. Soc.* **2013,** *135,* 14713–14725.

[284] T. Hahn, S. Liebing, J. Kortus, M. R. Pederson, *J. Chem. Phys.* **2015,** *143,* 224104.

[285] "TURBOMOLE V6.0, a development of University of Karlsruhe and Forschungszentrum Karlsruhe GmbH, 1989-2007, TURBOMOLE GmbH, since 2007; available from `http://www.turbomole.com`.", 2009.

[286] "TURBOMOLE V6.5 2013, a development of University of Karlsruhe and Forschungszentrum Karlsruhe GmbH, 1989-2007, TURBOMOLE GmbH, since 2007; available from `http://www.turbomole.com`.", .

[287] K. Eichkorn, O. Treutler, H. Ohm, M. Haser, R. Ahlrichs, *Chem. Phys. Lett.* **1995,** *240,* 283–289.

[288] K. Eichkorn, F. Weigend, O. Treutler, R. Ahlrichs, *Theor. Chem. Acc.* **1997,** *97,* 119–124.

[289] M. J. Frisch, *et al.* "Gaussian09 Revision E.01", Gaussian Inc. Wallingford CT 2009.

[290] G. Schaftenaar, http://www.cmbi.kun.nl/~schaft/molden/molden.html.

[291] J. P. Perdew, *Phys. Rev. B* **1986,** *33,* 8822–8824.

[292] P. Dirac, *Proc. Royal Soc. (London) A* **1929,** *123,* 714.

[293] J. Slater, *Phys. Rev.* **1929,** *123,* 714.

[294] J. Perdew, K. Burke, M. Ernzerhof, *Phys. Rev. Lett.* **1996,** *77,* 3865.

[295] V. Staroverov, G. Scuseria, J. Tao, J. Perdew, *Phys. Rev. Lett.* **2003,** *119,* 12129.

[296] S. Vosko, L. Wilk, M. Nusair, *Can. J. Phys.* **1980,** *58,* 1200.

[297] C. Lee, W. Yang, R. Parr, *Phys. Rev. B* **1988,** *37,* 785.

[298] O. Vydrov, G. Scuseria, *J. Chem. Phys.* **2006,** *125,* 234109.

[299] O. Vydrov, J. Heyd, A. Krukau, G. Scuseria, *J. Chem. Phys.* **2006,** *125,* 074106.

[300] O. Vydrov, G. Scuseria, J. Perdew, *J. Chem. Phys.* **2007,** *126,* 154109.

[301] G. te Velde, F. M. Bickelhaupt, E. J. Baerends, C. Fonseca Guerra, S. J. A. van Gisbergen, J. G. Snijders, T. Ziegler, *J. Comput. Chem.* **2001,** *22,* 931–967.

[302] C. Fonseca Guerra, G. J. Snijders, G. te Velde, J. E. Baerends, *Theoretical Chemistry Accounts* **1998,** *99,* 391–403.

[303] "ADF2014", SCM, Theoretical Chemistry, Vrije Universiteit, Amsterdam, The Netherlands, http://www.scm.com.

[304] E. Van Lenthe, E. J. Baerends, *J. Comput. Chem.* **2003,** *24,* 1142–1156.

[305] F. Weigend, R. Ahlrichs, *Phys. Chem. Chem. Phys.* **2005,** *7,* 3297–3305.

[306] F. Weigend, *Phys. Chem. Chem. Phys.* **2006,** *8,* 1057–1065.

[307] I. Morrison, D. M. Bylander, L. Kleinman, *Phys. Rev. B* **1993,** *47,* 6728.

[308] S. Miertuš, E. Scrocco, J. Tomasi, *Chem. Phys.* **1981,** *55,* 117–129.

[309] S. Miertus, J. Tomasi, *Chem. Phys.* **1982,** *65,* 239–245.

[310] J.-L. Pascual-ahuir, E. Silla, I. Tunon, *J. Comput. Chem.* **1994,** *15,* 1127–1138.

[311] M. Cossi, V. Barone, R. Cammi, J. Tomasi, *Chem. Phys. Lett.* **1996,** *255,* 327–335.

[312] V. Barone, M. Cossi, J. Tomasi, *J. Chem. Phys.* **1997,** *107,* 3210–3221.

[313] E. Cances, B. Mennucci, J. Tomasi, *J. Chem. Phys.* **1997,** *107,* 3032–3041.

[314] B. Mennucci, J. Tomasi, *J. Chem. Phys.* **1997,** *106,* 5151–5158.

[315] B. Mennucci, E. Cances, J. Tomasi, *J. Phys. Chem. B* **1997,** *101,* 10506–10517.

[316] V. Barone, M. Cossi, *J. Phys. Chem. A* **1998,** *102,* 1995–2001.

[317] M. Cossi, V. Barone, B. Mennucci, J. Tomasi, *Chem. Phys. Lett.* **1998,** *286,* 253–260.

[318] V. Barone, M. Cossi, J. Tomasi, *J. Comput. Chem.* **1998,** *19,* 404–417.

[319] R. Cammi, B. Mennucci, J. Tomasi, *J. Phys. Chem. A* **1999,** *103,* 9100–9108.

[320] R. Cammi, B. Mennucci, J. Tomasi, *J. Phys. Chem. A* **2000,** *104,* 5631–5637.

[321] D. Barton, C. König, J. Neugebauer, *J. Chem. Phys.* **2014,** *141,* 164115.

[322] S. Grimme, *J. Chem. Phys.* **2006,** *124,* 034108.

[323] "TURBOMOLE V6.6 2014, a development of University of Karlsruhe and Forschungszentrum Karlsruhe GmbH, 1989-2007, TURBOMOLE GmbH, since 2007; available from `http://www.turbomole.com`.", .

[324] C. Herrmann, M. Podewitz, M. Reiher, *Int. J. Quantum Chem.* **2009,** *109,* 2430–2446.